THESIS FOR THE DEGREE OF DOCTOR OF PHILOSOPHY

Geometry Optimization of an Interior Permanent Magnet Machine for Electric Vehicles - Life Cycle Cost Minimization for City, Rural and Highway Driving

ELISABET JANSSON

Department of Electrical Engineering
Division of Electric Power Engineering
CHALMERS UNIVERSITY OF TECHNOLOGY
Göteborg, Sweden 2023

Geometry Optimization of an Interior Permanent Magnet Machine for Electric Vehicles
- Life Cycle Cost Minimization for City, Rural and Highway Driving
ELISABET JANSSON
ISBN 978-91-7905-937-8

Doktorsavhandlingar vid Chalmers Tekniska högskola
Ny serie nr. 5403
ISSN 0346-718X

Department of Electrical Engineering
Division of Electric Power Engineering
Chalmers University of Technology
SE–412 96 Göteborg
Sweden
Telephone +46 (0)31–772 1000

Printed by Chalmers Digital Printing
Göteborg, Sweden , October 2023

To Simon and Vidar

Geometry Optimization of an Interior Permanent Magnet Machine for Electric Vehicles - Life Cycle Cost Minimization for City, Rural and Highway Driving
ELISABET JANSSON
Department of Electrical Engineering
Chalmers University of Technology

Abstract

This thesis investigates the benefits of customizing an Interior Permanent magnet Machine (IPM) for a specific combination of city, rural and highway driving. Focus lies on the potential to reduce the Life Cycle Cost (LCC) of the IPM and power electronic converter, for an example Battery Electric Vehicle (BEV), by custom-making the IPM.

The IPM customization is done with an optimization work-flow where both the size and shape of the IPM geometry is varied to minimize the LCC for a given driving scenario. The driving is represented with a distribution of energy and time over the entire torque versus speed plane of the IPM, which allows a large number of drive cycles to be aggregated and included without affecting the computational time. The optimization work-flow includes scaling of electromagnetic finite element results, to automatically select the best feasible version of each IPM geometry, considering performance requirements as well as thermal and mechanical constraints. Customized IPM designs are created for city, rural and highway driving and compared with an IPM optimized for mixed driving. The city, rural and highway driving types are represented both with single drive cycles and with large amounts of measured driving.

Customizing the IPM geometry was found to give significant LCC reduction in cases with pronounced city or highway driving. The LCC was found to be 7% lower for a city driving cycle and 1% lower for a highway driving cycle, for the customized IPM compared to the IPM optimized for mixed driving. For the city driving cycle, the optimization results in an IPM design with large slots, high amount of copper and relatively shallow flux barriers which are well-filled with magnets. Comparatively, the IPM custom-made for the highway cycle has smaller slots and lower copper and magnet amounts.

Still, the IPM optimized for mixed driving has a large and well-placed operating region with high efficiency and has a low LCC for most of the included driving scenarios. None of the included driving distributions based on large amounts of measured driving were specialized enough to benefit significantly from customization of the IPM. Overall, the results indicate that the usage that is currently typical for passenger cars can be well met with an IPM optimized for general driving and the potential for further improvement by custom-making the IPM is rather limited. However, the benefit of custom-making the IPM design is likely higher for BEV applications with more specialized driving type and larger amounts of driving.

Keywords: Battery Electric Vehicle, Drive Cycles, Electric Machine Design, Finite Element Analysis, Interior Permanent Magnet Machine, Life Cycle Cost, Optimization

Acknowledgements

First and foremost I would like to thank my main supervisor and examiner Prof. Torbjörn Thiringer and co-supervisor Dr. Emma Arfa Grunditz for their amazing support, feedback and time during the entire project. I also want to thank my co-supervisor at Volvo Cars Dr. Jahirul Islam for his support and encouragement during the finalizing of this thesis.

Additionally, I would like to thank all my colleagues at Volvo Cars, for sharing their knowledge and experience and giving me a valuable industrial perspective. Further, I would like to thank all the talented and interesting people I have had the opportunity to meet and discuss with at the Electric Power Engineering division at Chalmers.

Finally, my deepest thanks to my family for their support and patience over all these years.

The financial support from the Swedish Energy Agency (Energimyndigheten) and Volvo Car Corporation is gratefully appreciated.

Elisabet Jansson
Göteborg, Sweden
August, 2023

Acronyms

BEV	Battery Electric Vehicle
CADC	Common Artemis Driving Cycles
CADC-CC/RC/HWC	City Cycle/Rural Cycle/Highway Cycle from CADC
CFD	Computational Fluid Dynamics
CoP	Coefficient of Prognosis
CPSR	Constant Power Speed Range
DoE	Design of Experiments
EM	Electric Machine
FEA	Finite Element Analysis
FW	Field-Weakening
GA	Genetic Algorithm
IGBT	Insulated-Gate Bipolar Transistor
IPM	Interior Permanent magnet Machine
LCC	Life Cycle Cost
LPN	Lumped Parameter Network
MoP	Meta-model of Optimal Prognosis
MTPA	Maximum Torque Per Ampere
NEDC	New European Driving Cycle
NdFeB	Neodymium Iron Boron
NLPQL	Non-Linear Programming by Quadratic Lagrangian
NPV	Net Present Value
PM	Permanent Magnet
PMSM	Permanent Magnet Synchronous Machine

PWM	Pulse-Width Modulation
RMS	Root Mean Square
SA	Sensitivity Analysis
SCMD	Swedish Car Movement Data
SCMD-CT/RT/HWT/GT	City Type/Rural Type/Highway Type/General Type of driving distribution based on SCMD
SQP	Sequential Quadratic Programming
WLTC	Worldwide Harmonized Light Vehicles Test Cycle

Mathematical symbols

Symbols

A_c	Cross section area (for heat transfer)
$A_{IGBT/diode,tot}$	Total chip areas of the IGBTs/diodes (for converter cost)
A_{front}	Effective cross section area of the vehicle (for aerodynamics)
a	Coefficient in convergence curve
$a_{p,ref/resc}$	Number of parallel winding paths in reference/rescaled IPM
α	Rotor barrier pitch angle
B	Magnetic flux density
B_r	Remanence of magnet
b	Exponent in convergence curve
β	Rotor barrier pitch angle offset (rotor geometry parameter)
C_a	Annual cost
C_i	Investment cost (used with subscript for the component)
$C_{NPV,loss}$	Cost of losses, as NPV
C_{th}	Thermal capacitance
c	Coefficient in convergence curve
$c_{high/low}$	Confidence bands (95%) on the coefficient c
c_q	Constant related to iso-lines of the q-flux (used in rotor parametrization)
c_d	Aerodynamic drag coefficient
c_p	Specific heat
c_r	Rolling resistance coefficient
$D_{o/i}$	Outer/inner diameter (used in thermal context)
D_r	Rotor outer diameter
$D_{r,i}$	Rotor inner diameter

D_s	Stator outer diameter
$d_{b/qf}$	Depth of flux barrier/theoretical q-flux line
$E_{onIGBT/offIGBT/diode}$	Energy dissipation during turn-on and turn-off of the IGBTs and diode turn-off
F_{drag}	Resistive force due to air drag
F_{roll}	Resistive force due to rolling resistance
$F_{trac/res}$	Tractive/resistive force on the vehicle
$\mathbf{F}_{\omega}$	Force due to rotational motion
f	Frequency
f_{air}	Insulation ratio, (rotor geometry parameter)
f_{d}	Barrier depth factor (rotor geometry parameter)
f_{PM}	Magnet fill factor (rotor geometry parameter)
f_{t}	Tooth-width factor (stator geometry parameter)
f_{sw}	Switching frequency in the converter
f_{y}	Yoke factor (stator geometry parameter)
φ_{MTPA}	dq-current angle at peak torque (with MTPA)
G	Geometry of an IPM (used with subscripts for optimization details, and superscript for driving distribution)
g	Gravity constant
H	Magnetic field
H_c	Coercivity of magnet
h	Thermal convection coefficient
h_{tt}	Height of stator tooth tip
I_0	Base value of current (for normalization)
I_{cn}	Nominal collector current of the converter
$I_{em,rms}$	Current rating of the electric machine (RMS-value)
$i_{d/q}$	Phase current in d-axis/q-axis
$i_{d/q,n}$	Normalized phase current in d-axis/q-axis
J	Current density (using RMS value of current)
$\hat{i}_s$	Amplitude of phase current
$K_{i/v}$	Exponent for dependency on current/voltage (for converter switching losses)

k_{b}	Slope of a segment of a flux barrier
k_{gear}	Gear ratio
$k_{h/e}$	Core loss coefficients for hysteresis/eddy loss
$k_{a/r/w}$	Scaling factor for axial dimension/radial dimension/rewinding
$k_{w,c/bb}$	Rewinding factor with number of turns continuous/fixed (using Branch-and-Bound algorithm)
κ	Inverter utilization at base speed (normalized model)
$L_{d/q}$	Inductance in d-axis/q-axis
$l_{arc,s-t}$	Arc length of one stator tooth and slot
$l_{\mathrm{av/PM}}$	Available length/length of magnet in a segment of a flux barrier
$l_{bus-bar}$	Length of the bus-bar
λ	Thermal conductivity
m	Mass (used with a subscript indicating the material or component)
$m_{1/3}$	Modulation index for the fundamental/third harmonic injection
$N_{ref/resc}$	Number of winding turns in reference/rescaled machine
n_{pp}	Number of pole-pairs in the electric machine
n_s	Number of stator slots
ω	Electrical angular speed
ω_0	Base value of electrical angular speed (for normalization)
ω_{em}	Rotational speed of the rotor
ω_n	Normalized electrical angular speed
$P_{cond/sw}$	The conduction loss/switching loss in the converter
P_{cu}	Copper loss
P_e	Electric power
$P_{e,0}$	Base value of electric power (for normalization)
$P_{e,n}$	Normalized electric power
P_{fe}	Core loss
p	Interest rate for LCC calculation
$q_{cond/conv}$	Heat transfer in conductive/convective mode
R_{on}	On-state resistance (used for converter losses)
R_s	Phase resistance of stator winding

R_{th}	Thermal resistance
r	Radial distance
$\mathbf{r_{pole-piece}}$	Vector from rotational axis to center of gravity of the pole front and magnets combined
r_{sr}	Rounding radius of the slots
r_{wheel}	Wheel radius
ρ_{air}	Mass density of air
ϱ_{cu}	Resistivity of copper
$\varrho_{cu,20}$	Resistivity of copper at 20°C
S	Stress
σ	Temperature coefficient for resistivity
Ψ_0	Base value of magnetic flux linkage (for normalization)
Ψ_m	Magnetic flux linkage from permanent magnets
T_{em}	Electromagnetic torque (i.e. torque of the electric machine)
T_{ew}	End-winding temperature
T_{cu}	Temperature of copper
t_b	Thickness of a flux barrier
$\mathbf{t_{rib}}$	Combination of rib thickness, for the different ribs in the rotor
$\mathbf{t^*_{rib}}$	Look-up table of optimized rib thickness
θ_b	Angle spanned by a flux barrier, at the air-gap
U_0	Base value of voltage (for normalization)
$\hat{U}_{ph}$	Amplitude of phase voltage of the electric machine
$u_{d/q}$	Phase voltage in d-axis/q-axis
$u_{d/q,n}$	Normalized phase voltage in d-axis/q-axis
V_{DC}	DC-voltage
V_t	On-state threshold voltage (used for converter losses)
v	Angle taken from the edge of the pole towards the d-axis (i.e. pole midline)
v_b	Angle where a theoretical q-flux line reaches the air-gap
v_{car}	Velocity of the vehicle
$w_{t/y/so/ag}$	Width of the stator teeth/yoke/slot opening/air-gap
ζ	Saliency

Subscripts

0	Indicates base value (for normalization)
$0Y/10Y/\infty Y$	Indicates number of years included in LCC-minimization (used in IPM geometry optimization)
$aw/ew/yo/to/toti/fr$	Nodes for active-winding/end-winding/stator yoke/stator teeth/stator tooth tips/frame, in LPN
$k_{w,c/bb}$	Continuous/fixed (using Branch-and-Bound algorithm) number of winding turns (used in scaling)
car	Refers to the electric vehicle
$cond/conv$	Indicates conduction/convection (thermal context)
$cond/sw$	Indicates conduction/switching in converter
d/q	Indicates direct axis (d-axis)/quadrature axis (q-axis)
$em/conv/em+conv$	Indicates electric machine/power electronic converter/both electric machine and converter
$fe/cu/PM$	Indicates laminated core material (i.e. iron)/copper/magnet
$motor/regen$	Indicates motoring/regenerative operation
n	Indicates base normalized value
$pole-piece$	Pole front and magnets (for one rotor pole)
$ref/resc$	Indicates reference/rescaled version

Superscripts

$*$	Indicates optimized value(s)
$CC/RC/HWC$	Indicates city cycle/rural cycle/highway cycle, from CADC (used in IPM geometry optimization)
$CT/RT/HWT/GT$	Indicates city type/rural type/highway type/general type, driving distribution from SCMD (used in IPM geometry optimization)

Contents

Chapter 1

Introduction

1.1 Background

Following the increased environmental awareness, concerns regarding global green-house-gas emissions and recent cost reductions on batteries and power electronics, the road transportation system is currently undergoing a transition towards electric propulsion. The use of BEVs as private passenger cars have increased dramatically during the last decade and BEVs reached 14% of the global market annual sales in 2022 [1]. Governmental policies also promote the transition to electric transportation. Recently, a ban on new petrol and diesel cars from 2035 was announced in the EU [2]. Among the milestone vehicles, that have been forerunners for the BEV development seen now, are Toyota Prius (2007), Nissan Leaf (2011) and Tesla model S (2013). Today, almost all car manufacturers have fully electric vehicles in their portfolio. With higher voltages, currents and electric energy storage for automotive applications coming at a more reasonable cost and size, high performance BEVs are available.

Propulsion of BEVs is a demanding application for electric machines, as they operate over a wide range of torques and speeds. High peak torque is required, also at high speed, to meet acceleration performance requirements. High efficiency is also called for in BEVs, to increase the driving range. This has a high priority, since the size and cost of the battery is a significant limitation for BEVs. Furthermore, small and lightweight components are also desirable for BEV applications. This results in rather challenging restrictions on size and weight of the electric machine, which calls for machine designs with higher rotational speed and current densities which in turn gives challenges in terms of cooling and mechanical strength. Altogether, the electric machines in BEVs are pushing boundaries in several ways. Extensive development takes place in the field of electric machine design for automotive applications and the market has not yet converged to a predominant solution. Instead, several types of electric machines, positioning themselves differently in the many trade-off's, are available. This thesis focuses solely on design Electric Machines (EMs) of the type IPMs, which is the most commonly used machine type for BEVs thanks to their ability to reach both comparatively high efficiency and performance over a wide range of speeds [3], [4].

Furthermore, there is a spread in the use of passenger cars. One aspect of the spread is the type of driving, for example city driving dominates for some vehicles while highway driving dominates for others. These different types of driving are associated with different combinations of operating torque and speed values for the electric traction machine. In order to reduce the energy losses during driving, it is desired to operate as much as possible in the high efficiency area of the electric machine. It is also, to a certain extent, possible to adjust the high-efficiency area by the design of the electric machine. In light of this, it is anticipated that the driving energy losses can be reduced if the electric machine is custom-made for a given driving type.

1.2 Previous work

Customizing an EM for BEV propulsion is a challenging optimization problem and there are many possible alternatives when it comes to choice of objectives, design variables, modelling approach as well as optimization algorithms [5]. Targeting a specific driving type, i.e. a certain combination of city- rural- and highway driving, adds further complexity to the optimization problem. Several interesting examples of IPM design optimization for BEV applications are available in literature, such as [6–11]. However, room for further improvement remains within this complex research field.

The research gaps, related to design and optimization of IPMs, identified within this thesis are:

I In some cases, such as [11], drive cycles are not directly included in the IPM optimization but instead several drive cycles are used to make the final decision among a few promising IPM designs. In other cases, when drive cycles are included in IPM optimization, it is usually with a single cycle that aims to represent general driving, for example Worldwide Harmonized Light Vehicles Test Cycle (WLTC) or New European Driving Cycle (NEDC), such as in [6–8]. Further, optimization objectives formulated from a system perspective, for example cost or driving energy losses of the BEV or a combination thereof (i.e. LCC) are seldom used. Instead, several component level objectives, such as volume, cost and efficiency of the IPM alone, are typically combined using weighting factors that are not straightforward to motivate. Thus, missing in available literature is an investigation of the system level improvement potential associated with optimizing the IPM geometry specifically for several different combinations of drive cycles.

II For the purpose of IPM design optimization, driving is typically included as a low number of relatively short drive cycles (often a single one), that are further simplified into a few representative operating points (i.e. combinations of torques and speeds of the IPM) using a clustering approach, as done in [6–10]. The number of representative operating points is a trade-off between accuracy and computational time [6]. Naturally, including a larger number of drive cycles with a higher resolution, in terms of the operating points, in the IPM optimization would be beneficial as it gives a more realistic representation of the versatile driving application. Overall, there is a lack of demonstrated work-flows that allow several drive cycles to be included in the IPM optimization.

III Recently, fast and accurate scaling laws for IPMs, including radial- and axial scaling as well as rewinding based on Finite Element Analysis (FEA) results for a reference version of the IPM, have been derived [12]. Since these scaling laws are created to preserve electromagnetic aspects, they need to be extended with consideration of thermal and mechanical aspects, for example as shown for a few selected IPMs in [13] and [14]. Scaling, including both IPM and converter, has been used for optimal sizing of components in BEV powertrains in [15] and [16]. However, the use of scaling combined with IPM geometry changes, for the purpose of optimizing not only the size but also the geometry of the IPM, remains to be explored.

IV Considering the computational demands related to EM design optimization, it is important to keep the number of variables low. Both multi-layer IPMs and synchronous reluctance machines share the challenge of representing the rotor geometry with a low number of variables and avoid infeasible geometries (i.e. overlapping flux barriers). Methods to improve the share of feasible geometries in EM optimizations are found in recent literature, such as [17] and [18]. While the choice of number of rotor parameter has been investigated for synchronous reluctance machines, for example in [19], it has not been thoroughly explored for IPMs. Further efforts to reduce the number of rotor parameters would be relevant for the multi-layer IPM topologies that are increasing in BEV applications.

V The rotor topology, i.e. shape and number of flux barriers and magnets, is a design choice for IPMs where a lot of variation is seen both in industry and research [20]. Further, an IPM characteristic that is known to be closely related to the rotor design is the Field-Weakening (FW)-performance [21]. Since FW-performance is highly important for BEV propulsion, there are several investigations of FW-performance for rotor topologies with different shapes of the flux barriers, such as [21–24]. However, the available comparisons covering several shapes of flux barriers are either restricted to single-layer rotor topologies or do not include geometry dependent dimensioning of the ribs (that hold the magnets and the outer part of the rotor pole in place) in the design variations. Thus, there is a lack of flux barrier shape comparisons including combined electromagnetic and mechanical optimization of multi-layer IPM rotors.

VI For an IPM optimization involving electromagnetic FEA, it is important to carefully select the time- and mesh resolution for a desired trade-off between computational burden and numerical accuracy. Investigations of the sensitivity of FEA results to mesh- and time resolution are available in literature, such as [25–28]. However, the existing examples show a relatively wide spread in settings and are typically not focused on core losses, which is of high interest for BEV applications. Overall, there is a lack of guidance on mesh- and time resolution, considering the impact on numerical core loss accuracy, for IPMs with design and sizing that is typical for BEV traction applications.

1.3 Purpose of the thesis and contributions

The purpose of this thesis is to propose a method to custom-make the IPM design towards various BEV-use scenarios, and compare the results of the method for different distributions of city- and highway driving.

The main contributions of this work are:

I Quantification of the potential to reduce life-cycle-cost of the IPM and power electronic converter by custom-making IPM designs for different driving types.

II Proposal, implementation and demonstration of an IPM optimization method where the use case can be represented with an energy or time distribution in the torque versus speed plane, which allows a very high number of drive cycles to be included.

III Demonstration of an approach for IPM scaling, where existing scaling laws for FEA results are extended with mechanical and short-term thermal aspects and also combined with an existing scalable converter model, including both cost and losses. The approach is incorporated in a work-flow for IPM geometry optimization, where it is used to find the optimal scaled version of each given IPM geometry with a chosen objective, in this case life cycle cost, considering both the IPM and the converter.

IV Proposal of a method for rotor geometry parametrization that effectively reduces the number of parameters needed for multi-layer IPM rotors and also allows different flux barrier shapes to be described using the same set of parameters. The method is an extension of the parametrization approaches previously used for synchronous reluctance machines, now for use in IPMs, through the addition of a piece-wise-linear approximation of natural magnetic flux lines and a factor for altering the overall depth of the flux barriers.

V Quantification of the influence of flux barrier shape on field-weakening performance, for a double-layer IPM rotor, including the impact of geometry dependence in the mechanical constraints.

VI Demonstration of a structured method to select mesh and time resolution in the electromagnetic FEA of an IPM. The method is based on estimating convergence curves for the core losses in each part of the IPM geometry. The convergence curve can be used to select a suitable compromise between the numerical accuracy of the core losses and the computational time, depending on the needs of further investigations.

1.4 List of Publications

This thesis is based on the following publications (referred to as Paper I-IV):

I E. Jansson, T. Thiringer, E. Grunditz, "Convergence of Core Losses in a Permanent Magnet Machine, as Function of Mesh Density Distribution, a Case-Study Using Finite-Element Analysis.", *IEEE Transactions on Energy Conversion*, vol. 35, no. 3, pp. 1667-1675, 2020.

II E. Jansson, T. Thiringer, E. Grunditz, "Time Resolution Dependency of Core Loss Accuracy in Finite Element Analysis of a Permanent Magnet Synchronous Machine.", *2020 International Conference on Electrical Machines (ICEM)*, IEEE, 2020.

III E. Jansson, E. Grunditz, T. Thiringer, "Impact of Saturation and Scaling on the Field Weakening Performance of an Interior PM Machine.", *2020 International Conference on Electrical Machines (ICEM)*, IEEE, 2020.

IV E. Jansson, T. Thiringer, E. Grunditz, "Influence of Flux Barrier Shape and Mechanical Constraints on Field-Weakening Performance in Double-Layer Interior Permanent Magnet Machines.", submitted to *IEEE Transactions*, 2023, (under review).

Some contributions have also been made in the following publications. However, these are not directly related to this thesis.

V A. Tokat, T. Thiringer, E. Jansson. "Impact of Stator Slot Geometry on the Performance of a Permanent Magnet Synchronous Generator for Wave Energy Converters.", *2020 International Conference on Electrical Machines (ICEM)*, IEEE, 2020.

VI A. Tokat, E. Jansson, K. Bergsro, T. Thiringer, "Improvement of the Continuous Performance of a Traction Machine for a Battery Electric Vehicle through Magnet Segmentation.", *2022 International Conference on Electrical Machines (ICEM)*, IEEE, 2022.

Chapter 2

Drive system modelling for electric vehicle propulsion and meta-model based optimization

This chapter gives an overview of the theoretical expressions and concepts that are considered fundamental to this thesis. In this thesis, emphasis lies on the electric machine and, in particular, the electromagnetic aspects of it. Therefore, the electromagnetic modelling of the IPM is central here, while the modelling is comparatively more simplified when it comes to other physical aspects (such as mechanical and thermal aspects) or systems that relate the IPM to the BEV application (such as the power electronics converter and the vehicle model). Essentially, the drive system model here is rather an IPM model with a BEV system perspective. This chapter also gives a brief overview of optimizations using meta-models (also known as response surfaces), which is used in the later parts of this thesis.

2.1 Vehicle modelling

For evaluation of vehicle dynamics, the vehicle has been approximated as a rigid body. Such a simplification can be considered reasonable when computation of the energy levels in the propulsion drive train is the main purpose of the model [29], [30]. As in [29], the motion of the vehicle is approximated with a single dimension, the longitudinal direction, assuming that the vehicle remains stable at all times. Thus, the motion of the vehicle can simply be described with Newton's second law, as

$$m_{car}\frac{d}{dt}v_{car} = F_{trac} - F_{res} \tag{2.1}$$

where m_{car} is the mass of the vehicle, v_{car} is the velocity of the vehicle. Forces are denoted with F, and the subscript $_{trac}$ represents tractive forces (that strive to increase the speed of the vehicle) while $_{res}$ represents resistive forces (that strive to reduce the speed of the vehicle).

The influence of road inclination (i.e. road grade) and winds have been neglected here. In practice, there will of course be alternating uphill and downhill driving, where the power from the drive train needs to deliver higher respectively lower power compared to driving on a flat road. Similarly, the wind will lead to either increased of reduced power needed from the drive train, depending on the wind direction relative to the direction of travel of the vehicle [29]. For simplicity, these aspects have not been included in the model here. This leaves the resistive forces acting on the vehicle as the rolling resistance,F_{roll}, and the air drag, F_{drag}, which can be described as

$$F_{res} = F_{roll} + F_{drag} = c_r m_{car} g + \frac{1}{2}\rho_{air} c_d A_{front} v_{car}^2 \tag{2.2}$$

where the coefficients c_r and c_d are the rolling resistance coefficient and aerodynamic drag coefficient respectively, while A_{front} is the effective cross sectional area of the vehicle, g is the gravity constant and ρ_{air} is the mass density of the air. The value of ρ_{air} has been set to 1.225 kg/m^3, i.e. the value for standardized conditions (dry air at 15 °C and atmospheric pressure at sea level) [29]. Here, the value of c_r has been approximated as constant, although it is known to be affected by the tire pressure, temperature and surface of the road [31]. In reality, the value of c_r also increases with vehicle speed, especially at higher speeds [31], but this dependency has not been modelled here. This simplification can be motivated by F_{roll} being a comparatively small part of F_{res} at high speeds, considering the strong speed dependence of F_{drag}.

Furthermore, the transmission has been modelled as lossless which means that the tractive force can be found directly from the output torque of the IPM, the gear ratio and the wheel radius, as

$$F_{trac} = T_{em,motor} \frac{k_{gear}}{r_{wheel}} \tag{2.3}$$

where $T_{em,motor}$ is the torque of the electric machine (in motoring operation), k_{gear} is the gear ratio and r_{wheel} is the radius of the wheel. The electric machine can also perform regenerative braking, where its torque, $T_{em,regen}$, is negative and it then acts as a resistive force. Additional braking capability is of course available through the friction brake in the car [29].

Within this thesis, the vehicle dynamics model described above has been used for the purpose of translating a given "drive cycle" (i.e. a sequence of vehicle speed versus time) into its corresponding operating points for the electric traction machine (i.e. a sequence of torque versus rotational speed of the IPM), which is done in the coming Chapter 3. For this purpose, the torque of the electric machine, T_{em}, has been computed as

$$T_{em} = \frac{r_{wheel}}{k_{gear}} \left(m_{car} \frac{d}{dt} v_{car} + F_{roll} + F_{drag} \right) \tag{2.4}$$

where T_{em} will be either positive (motoring) or negative (regeneration) depending on the sign of the expression on the right hand side, i.e. the balance of the other forces to the velocity profile.

Further, the rotational speed of the electric machine, ω_{em}, has been computed assum-

ing no slip between the tire and the ground, as

$$\omega_{em} = v_{car} \frac{k_{gear}}{r_{wheel}} \tag{2.5}$$

Finally, for the purposes of calculating net driving energy, it has been assumed that braking is done using the electric machine to the largest possible extent (i.e. the friction brakes are only used when the required braking force is beyond the capability of the electric machine). This is rather idealistic for strong decelerations where it might be necessary to distribute the braking force among the wheels. The maximum force that can be applied at the driving wheels, without loosing grip, is limited by the normal force on the wheels with a friction coefficient that goes up to 0.8-1 [29]. The normal force on the driving wheels will depend on the weight distribution of the car, and is also different for accelerations and decelerations [30]. Such aspects have not been considered in the simple vehicle model here. However, operation close to peak torque is rare during driving (seen in Chapter 3) and can therefore be expected to have very limited impact on the driving energy losses.

2.2 Electromagnetic modelling of the IPM

The IPM is a type of synchronous electric machine, where the magnetic flux in the rotor (i.e. rotating part) is created with permanent magnets placed in the interior of the rotor laminate [32]. The magnetic flux in the stator (i.e. stationary part) is created by current-carrying windings, powered by an AC voltage source which, for a BEV typically consists of a battery and a three-phase power electronics converter. The lamination material, mainly iron, in the rotor and stator have a high magnetic permeability and will therefore guide the magnetic flux in the machine.

IPMs are often described with equivalent circuit equations using the dq-reference frame, consisting of the d-axis (direct axis) and q-axis (quadrature axis). The dq-reference frame is rotating at the synchronous speed, with the d-axis aligned with the magnetic flux linkage from the permanent magnets, Ψ_m, and the q-axis leading the d-axis with 90° electrically. Here, amplitude invariant transformation has been used for the transformation from three phase to two phase quantities. Within this thesis, two versions of the circuit equations have been used, both of which are described below. Both models consider electrical steady state. Although BEV propulsion involves operation over a wide range of torque and speed of the IPM (i.e. changes to the IPM operating point), the shift in operating point is associated with the vehicle dynamics which can be considered as rather slow from an electrical point of view. Therefore, the operation of the IPM is here modelled as electrical steady state for each individual operating point.

2.2.1 Model A: normalized dq-model with constant parameters

For the purpose of analysing field weakening, a normalized model with constant circuit parameters has been used. This lossless linear model is referred to as Model A and is

adopted from [33], [34] as

$$u_{d,n} = -\omega_n L_{q,n} i_{q,n} \tag{2.6}$$

$$u_{q,n} = \omega_n L_{d,n} i_{d,n} + \omega_n \Psi_{m,n} \tag{2.7}$$

$$T_{em,n} = \Psi_{m,n} i_{q,n} + (L_{d,n} - L_{q,n}) i_{d,n} i_{q,n} \tag{2.8}$$

where u is voltage, T_{em} is the electromagnetic torque, i is current, ω is angular speed, Ψ_m is magnet flux linkage, L_d and L_q is inductance in d- and q-axis respectively and the subscript $_n$ indicates normalized quantities. The base values, used for the normalization, are the maximum current, I_0, maximum voltage, U_0, and base speed, ω_0. ω_0 is the electrical angular frequency for which the maximum voltage limit is reached in Maximum Torque Per Ampere (MTPA)-operation at peak torque and following [35], it is given by

$$\omega_0 = \left(\left(\frac{I_0 cos(\varphi_{\mathrm{MTPA}}) + \Psi_m / L_d}{U_0 / L_d} \right)^2 + \left(\frac{I_0 sin(\varphi_{\mathrm{MTPA}})}{U_0 / L_q} \right)^2 \right)^{-\frac{1}{2}} \tag{2.9}$$

with φ_{MTPA} as the dq current angle at the MTPA peak torque point (with the angle taken counter clockwise from the positive d-axis).

The normalization of other relevant quantities follows directly from the base values, for example $\Psi_{m,n} = \Psi_m / \Psi_0$, where $\Psi_0 = U_0 / \omega_0$. Here, $L_q < L_d$ and saliency, ζ, is defined as L_q / L_d and is unchanged by normalization. Further, base power, $P_{e,0}$ corresponds to the rated power of the inverter and therefore, normalized power is also referred to as inverter utilization. In particular, the inverter utilization at base speed, $P_{e,n}|_{\omega_n=1}$, is denoted κ. The quantity κ is used further in the analysis of FW operation in the coming section.

2.2.2 Operation boundary of the IPM using Model A

The operation boundary of the IPM consists of the operating points that give the highest available torque at each speed, within selected limits of voltage and current. The operation boundary of an IPM consists of up to three modes, called Mode I-III. However, not all the modes are necessarily used, depending on the IPM design and application. Mode I is MTPA operation, where the IPM produces maximum torque and the maximum voltage is not reached, i.e. up to base speed. Mode II-III are FW modes, where the dq-currents are adjusted to maximize the torque without exceeding the voltage constraint. In Mode II both current and voltage are maximized, but as speed increases further it can lead to Mode III, where voltage remains at the limit while current is below maximum value. Mode I-III are shown in the dq-current plane in Figure 2.1.

As shown in Figure 2.1, torque levels show up as hyperbolae in the dq-current plane of Model A, while the current limit is a circle, $\sqrt{i_{d,n}^2 + i_{q,n}^2} = 1$, and the voltage limit, $\sqrt{u_{d,n}^2 + u_{q,n}^2} = 1$, forms an ellipse that shrinks with increasing speed. The ellipse is given by

$$\left(\frac{i_{d,n} + \Psi_{m,n} / L_{d,n}}{1 / (L_{d,n} \omega_n)} \right)^2 + \left(\frac{i_{q,n}}{1 / (L_{q,n} \omega_n)} \right)^2 = 1 \tag{2.10}$$

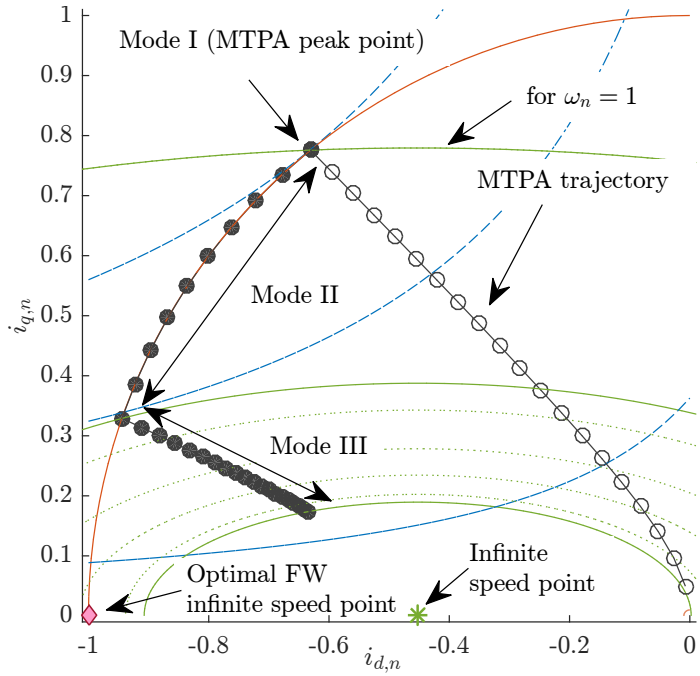

Figure 2.1 Operating points of an IPM in the normalized dq-current plane, Model A. The current limit is the red circle, torque levels are blue hyperbola and the voltage limit is shown as green ellipses for different speeds. Filled round markers indicate points on the operation boundary.

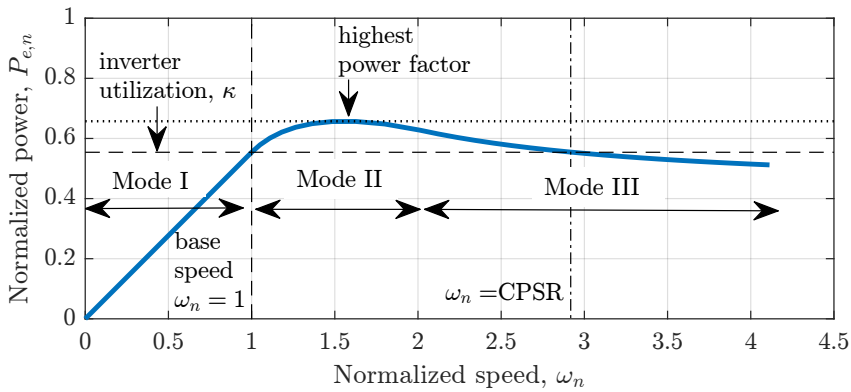

Figure 2.2 The normalized power curve, along the boundary of the operating region, using Model A. The three operating modes, Mode I-III, are marked.

The midpoint of the ellipse, $-\Psi_{m,n}/L_{d,n}$, is called the infinite speed point, since the ellipse reduces to that point as $\omega_n \to \infty$. This value is also known as the characteristic current of the IPM.

Further, FW performance is commonly quantified using Constant Power Speed Range (CPSR) which, in Model A, is the normalized speed where the normalized power drops below κ, see Figure 2.2. As shown by [33], optimal FW performance of an IPM is $\kappa = 0.7$ and a normalized power that increases beyond base speed and approaches 1 as $\omega_n \to \infty$.

The FW performance is often measured using CPSR, which is the value of ω_n where the normalized power drops to a lower value than κ. As shown in [33], the theoretically highest FW performance of an IPM is $\kappa = 0.7$ and infinite CPSR where $P_{e,n} \to \infty$ as $\omega_n \to \infty$. This occurs if $\Psi_{m,n} = L_{d,n}$ (i.e. $\Psi_m = L_d I_0$) which corresponds to the infinite speed point being located on the current limit circle, in other words a characteristic current equal to the rated current.

2.2.3 Model B: dq-model with magnetic saturation of parameters

While Model A is simple and useful for illustrative purposes, it also neglects the influence of magnetic saturation on the circuit parameters which is typically significant for IPMs used for BEV traction applications. Therefore, unless otherwise stated, the results shown within this thesis are made using a model which includes magnetic saturation, referred to as Model B. In Model B, the circuit parameters are computed as a function of d- and q-current, using electromagnetic FEA and the voltage drop due to stator resistance is also included. The circuit equations of Model B are given as

$$u_d = -\omega L_q(i_d, i_q) i_q + R_s i_d \tag{2.11}$$

$$u_q = \omega L_d(i_d, i_q) i_d + \omega \Psi_m(i_q) + R_s i_q \tag{2.12}$$

$$T_{em} = \frac{3 n_{pp}}{2} \left(\Psi_m(i_q) i_q + \left(L_d(i_d, i_q) - L_q(i_d, i_q) \right) i_d i_q \right) \tag{2.13}$$

where R_s is the stator winding resistance and n_{pp} is the number of pole pairs, u is voltage, T_{em} is the electromagnetic torque, i is current, ω is angular speed, Ψ_m is magnet flux linkage, L is inductance and the subscript $_d$ and $_q$ denotes the d- and q-axis respectively.

While the IPM operation could be found analytically when Model A was used, it is not as straightforward when magnetic saturation is included. Here, the circuit equations of Model B has been solved numerically as described further in Chapter 4.

Further, the value of R_s has been taken as the DC-resistance and computed analytically based on the dimensions of the IPM geometry and the winding configuration (considering the number of slots per pole and phase as well as number of turns and parallel branches in the winding). The total copper area in each slot is found from the slot area with a constant fill factor (set to 0.45, which can be regarded as a high but realistic value for a random-wound winding [32]). The active length of one coil (one full turn) in the winding is simply twice the stack length of the IPM. The length of the end winding, on each side of the IPM (i.e. each side of the coil), is approximated using the length of the arc spanning the coil pitch taken at the middle of the slot, with a factor of 1.2 to account for practical routing of the strands in the end winding, plus a constant axial overhang (set

to 25 mm) on each side. The temperature dependence of the copper resistivity, ϱ_{cu} has been modelled as

$$\varrho_{cu}(T_{cu}) = \varrho_{cu,20}(1 + \sigma(T_{cu} - 20)) \tag{2.14}$$

where T_{cu} denotes the copper temperature in °C, $\varrho_{cu,20}$ is the reference resistivity taken as 1.68 $\times 10^{-8}$ Ωm at 20 °C and the coefficient σ is set to 0.003862 K^{-1} [29].

The resistive losses, i.e. copper losses, are then computed based on R_s, as

$$P_{cu} = \frac{3}{2} R_s \left(i_d^2 + i_q^2\right) \tag{2.15}$$

The core losses, i.e. iron losses, albeit not included in the circuit equations are still computed in the FEA using the Bertotti expression, with the volume density of core losses,P_{fe}, given as

$$P_{fe}(B, f) = k_h B^2 f + k_e B^2 f^2 \tag{2.16}$$

where B is the magnetic flux density, f, is the frequency and k_h and k_e are material based coefficients for the hysteresis loss and eddy loss respectively.

2.3 Mechanical modelling of the IPM

For IPMs, the rotor design is a trade-off between the electromagnetic performance and the mechanical integrity of the rotor structure [36]. In particular the sizing of the ribs, i.e. pieces of the rotor laminate that keep the Permanent Magnets (PMs) and outer part of the pole in place during the rotational motion of the rotor, need to be as thin as possible to reduce magnetic flux leakage while still strong enough to maintain structural integrity. Note that the ribs are also known as bridges or posts, but within this thesis they are referred to as ribs. The ribs are marked in Figure 2.3.

The mechanical stress in the ribs of IPMs are typically dominated by the centrifugal force on the outer pole piece (made up by the pole front and the PMs), given as

$$\mathbf{F}_\omega = m_{pole-piece} \mathbf{r}_{\mathbf{pole-piece}} \omega_{em}^2 \tag{2.17}$$

where $\mathbf{F}_\omega$ is the force due to the rotational motion (i.e. centrifugal force) acting on the pole-piece (consisting of the PMs and the pole front), as indicated with the subscript $_{pole-piece}$. m is the mass and $\mathbf{r}$ is the vector from the rotational axis to the center of gravity for the PMs and pole front combined, while ω_{em} is the rotational speed of the rotor.

Further, $\mathbf{F}_\omega$ is distributed among the different ribs in the geometry and the force on each ribs is also distributed over the thickness of the rib itself, i.e. a stress distribution. It is important to round the edges of the flux barriers as corners typically leads to very high local stress [37]. While it is possible to compute the stress distribution and deformation analytically, as shown for an IPM with a single V-shaped flux barrier in [36], it is not a simple task. A fully analytical model also becomes increasingly difficult with more complex rotor structures with several layers of flux barrier and larger number of ribs.

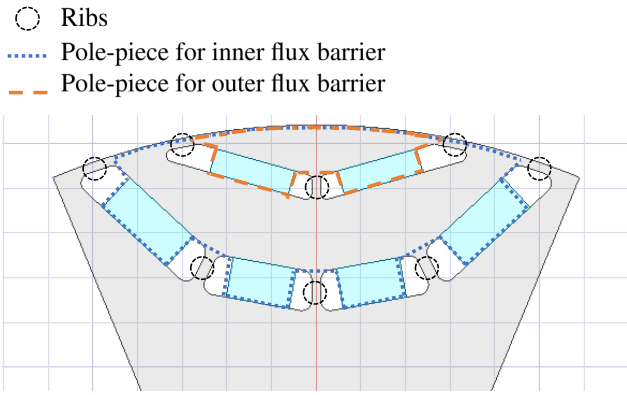

Figure 2.3 Example of an IPM with two layers of flux barriers and PMs, with ribs marked and the pole-pieces for each barrier layer outlined.

Therefore, it is common to compute the von Mises stress in the ribs using structural FEA, which is for example done in [24, 37] as well as within this thesis.

Finally, if deformation is neglected, the stress will scale with rotational speed and rotor diameter, for a radially scaled version of the rotor (keeping the geometrical proportions unchanged), as [37]

$$\frac{S_2}{S_1} = \left(\frac{D_{r,2}}{D_{r,1}}\right)^2 \left(\frac{\omega_{em,2}}{\omega_{em,1}}\right)^2 \tag{2.18}$$

where S is the stress and D_r is the rotor diameter, while the subscript $_1$ and $_2$ denote the rotors with different size and/or rotational speed. While [37] suggests (2.18) to be used with structural FEA results for IPMs, [36] considers it as only approximative since the stress distribution and deformation of the rotor will be load dependent. Still, within this thesis (2.18) was found to have good agreement to structural FEA results, in particular for the inner ribs (which also typically showed the highest stress values), for the limited change in rotor size investigated here.

2.4 Thermal modelling of the IPM

Thermal modelling, describing the heat flows and temperature distribution in the IPM, can be done in several ways with varying degrees of accuracy. Within this thesis, the Lumped Parameter Network (LPN) approach has been used, since priority has been given to simulation speed and simple adaption of the model to different IPM geometries. The accuracy can be improved further by the use of numerical methods, such as thermal FEA, which typically improves the estimation of thermal conduction, or Computational Fluid Dynamics (CFD), which offers improved representation of thermal convection [29].

There are three modes of heat transfer: conduction, convection and radiation, where the two first are typically considered relevant for the thermal situation in electric ma-

chines [29]. **Conductive heat transfer**, which occurs within the solid materials of the IPM, can be described with

$$q_{cond} = \lambda A_c \frac{\Delta T}{l} \tag{2.19}$$

where q_{cond} is the conductive heat flow, λ is the thermal conductivity of the material, A_c is the area of the cross section (perpendicular to the direction of heat flow), l is the thickness of the material (in in the direction of heat transfer) and ΔT is the temperature difference across the distance l. Further, **convective heat transfer**, which occurs between a solid surface and a moving fluid, is given by

$$q_{conv} = hA_c\Delta T \tag{2.20}$$

where q_{conv} is the convective heat flow, h is the thermal convection coefficient, A_c is the area of the cross section (in this case the surface area where convection takes place) and ΔT is the temperature difference between the surface and the fluid. [32].

An LPN for an IPM is a network model that describes the main heat flows in the IPM. Different geometrical parts of the IPM are "lumped" together and described as a node in the LPN. This "lumping" is an approximation, assuming uniform material properties and heat generation (i.e. losses). The nodes are then related to each other with thermal resistances, R_{th}, that describe the relation between heat flow and temperature difference and thermal capacitances, C_{th}, that describe the rate of temperature change depending on heat flow. Thus, a thermal LPN is analogues to an electric circuit, where temperature difference corresponds to voltage and heat flow to current. [29]

The thermal resistance, R_{th}, is given by

$$R_{th} = \frac{\Delta T}{q} \tag{2.21}$$

where q is the heat flow (which can be conductive or convective) between two nodes in the LPN and ΔT is the temperature difference between said nodes.

Further, the thermal resistance can be expressed as [29]

$$R_{th} = \begin{cases} \int_0^l \frac{1}{\lambda A_c(x)} dx & \text{for conduction} \\ \frac{1}{hA_c} & \text{for convection} \end{cases} \tag{2.22}$$

The thermal resistance for radial conduction of heat in a hollow cylinder, which is particularly relevant case here considering the cylindrical shape of the stator and rotor of an IPM, is given by

$$R_{th} = \frac{ln(D_o/D_i)}{\lambda l_{ax}\theta} \tag{2.23}$$

where D_o and D_i is the outer and inner diameter of the hollow cylinder respectively, l_{ax} is the axial length (i.e. perpendicular to the direction of heat transfer) and θ is the angle which the hollow cylinder spans. [29]

Finally, the thermal capacitance of the node is computed as

$$C_{th} = \sum_{i=1}^{N} m_i c_{p,i} \tag{2.24}$$

where C_{th} is the total thermal capacitance of the node, m and c_p denotes mass and specific heat respectively and N is the total number of geometrical parts lumped together in the node [29].

2.5 Scaling of the IPM

Analytical scaling laws, where changes in axial and radial dimension as well as rewinding of an IPM can be implemented while still preserving the magnetic field picture in the IPM, are presented in [12] [38]. This allows a scaled version of an IPM to be evaluated very fast, based on the electromagnetic FEA results of a reference version of the IPM geometry.

The scaling factors, illustrated in Figure 2.4, consist of

- Axial scaling factor, k_a, given as the ratio of a length, in axial direction, of the scaled machine and the corresponding length of the reference machine
- Radial scaling factor, k_r, given as the ratio of a length, in radial direction, of the scaled machine and the corresponding length of the reference machine
- Rewinding factor, k_w, computed as $(N_{resc}a_{p,ref})/(N_{ref}a_{p,resc})$ where N and a_p are the number of turns and parallel paths in the winding respectively and the subscripts $_{ref}$ and $_{resc}$ denote quantities for the reference and rescaled IPM respectively.

Here, the scaling laws from [12] have been used in 2D, neglecting electromagnetic end effects, as

$$I_{resc} = \frac{k_r}{k_w} I_{ref} \tag{2.25}$$

$$L_{d/q,resc} = k_w^2 k_a L_{d/q,ref} \tag{2.26}$$

$$\Psi_{m,resc} = k_w k_r k_a \Psi_{m,ref} \tag{2.27}$$

$$T_{em,resc} = k_r^2 k_a T_{em,ref} \tag{2.28}$$

$$P_{fe,resc} = k_r^2 k_a P_{fe,ref} \tag{2.29}$$

where I, $L_{d/q}$, Ψ_m, T_{em} and P_{fe} denote, in order, the current, inductance (in d- or q-axis), magnet flux linkage, torque and core losses. The subscripts $_{ref}$ and $_{resc}$ denote quantities for the reference and rescaled IPM respectively.

The stator resistance, R_s, is re-computed analytically for the rescaled IPM, with the same approach as in Section 2.2.3. The copper area in each slot will change with k_r^2, as a constant fill factor of 0.45 is assumed here. The active length of each coil in the winding will change as k_a while the end winding changes with k_r (except for the overhang of

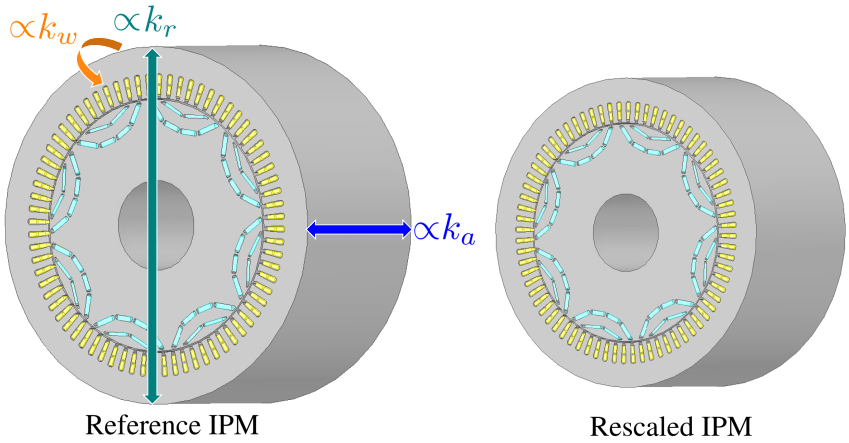

Figure 2.4 Illustration of rescaling an IPM and the involved scaling factors, k_a (axial scaling factor), k_r (radial scaling factor) and k_w (rewinding factor).

25 mm, which has been kept constant here). The combination of changes in copper area per slot, changes to coil length and the change in number of turns and/or parallel paths (as given by k_w) together affect the resistance of the rescaled IPM, $R_{s,resc}$.

Since the scaling laws preserve the field picture, the results for the scaled machine will have the same accuracy as if a new FEA was done on the machine with the new dimensions [12], [38]. This allows significant reduction of the computational time, as the scaling laws are far faster to evaluate than additional FEAs.

2.6 Scalable converter model

Within this thesis, the term converter refers to the power electronics device that converts the DC-voltage from the battery in the BEV into three phase AC-voltage supply for the EM. During motoring operation, power is supplied from the battery to the EM through the converter, while in regenerative operation the direction of power-flow is reversed, with the EM charging the battery through the converter. Typically, the energy losses in the converter are lower than those in the EM. However, as described further within this section, the losses in the converter, for each operating point, will be dependent on the corresponding currents of the EM. Since the currents in the IPM will be affected by the IPM geometry as well as scaling of the IPM, as shown in Section 2.2 and Section 2.5, the losses in the converter will be affected by the IPM design.

The losses in the converter has been modelled with an analytic converter model that includes scaling for different current ratings, readily available in [39]. The model concerns three phase converters with Insulated-Gate Bipolar Transistors (IGBTs) and the scaling is done with empirical formulas based on data sheet information for Infineon FS200/400/600/800, meaning automotive converters with 650 V IGBT modules with different current ratings. The voltage rating can be considered suitable for a BEV power-

train with DC-voltage around 400 V and the range of values of nominal collector current, I_{cn}, covered is 50-800 A [16]. In this model, the converter losses are modelled for Pulse-Width Modulation (PWM) operation with third harmonic injection, based on [40] [41]. The conduction losses are modelled as

$$P_{cond,IGBT} = 6\left(\frac{1}{2\pi} + \frac{m_1 cos\vartheta}{8}\right) V_{t,IGBT}\hat{i}_s + \left(\frac{1}{8} + \frac{m_1 cos\vartheta}{3\pi} - \frac{m_3 cos3\vartheta}{15\pi}\right) R_{on,IGBT}\hat{i}_s^2 \tag{2.30}$$

$$P_{cond,diode} = 6\left(\frac{1}{2\pi} - \frac{m_1 cos\vartheta}{8}\right) V_{t,diode}\hat{i}_s + \left(\frac{1}{8} - \frac{m_1 cos\vartheta}{3\pi} + \frac{m_3 cos3\vartheta}{15\pi}\right) R_{on,diode}\hat{i}_s^2 \tag{2.31}$$

where P_{cond} denotes conduction (indicated by the subscript) power loss of the six switches in the converter, for the component indicated with the additional subscript $_{IGBT}$ or $_{diode}$. m_1 is the fundamental modulation index, while m_3 is the modulation index for the third harmonic injection (as in [39] the value of m_3 is set to $m_1/6$). $\hat{i}_s$ is the amplitude of the phase current and ϑ is the phase angle between current and voltage, both based on the operating point of the EM. V_t and R_{on} are the on-state threshold voltage and resistance respectively, for the component indicated with the second subscript.

Further, the switching losses in the converter are modelled as

$$P_{sw} = \frac{f_{sw}}{\pi} E_{onIGBT/offIGBT/diode} \left(\frac{\hat{i}_s}{I_{ref}}\right)^{K_{i,IGBT/diode}} \left(\frac{V_{DC}}{V_{ref}}\right)^{K_{v,IGBT/diode}} \tag{2.32}$$

where f_{sw} is the switching frequency, which has been set to 10 kHz here, and V_{DC} is the DC-voltage. $E_{onIGBT/offIGBT/diode}$ is the energy dissipation during turn-on and turn-off of the IGBTs and diode turn-off, for a reference case in which the DC-voltage has the value V_{ref} and the amplitude of the phase current is I_{ref}. The exponents K_i and K_v describe the current- and voltage dependency of the switching losses, respectively, for the IGBT or the diode.

Note that the converter loss model here does not include losses related to reverse blocking in the IGBTs, turn on of the diodes or parasitic effects. Losses in driver and snubber circuits are also neglected. Symmetry among the switches, i.e. a balanced load, is also assumed. [39]

Furthermore, the parameters in (2.30)-(2.32) that depend on the converter components can be approximated for different current ratings using the expressions for 125°C

from [39], as

$$V_{t,IGBT} = 0.695 \tag{2.33}$$
$$V_{t,diode} = 0.797 \tag{2.34}$$
$$R_{on,IGBT} = 990.07 I_{cn}^{-1.003} \tag{2.35}$$
$$R_{on,diode} = 675.61 I_{cn}^{-1.004} \tag{2.36}$$
$$K_{v,IGBT} = 1.35 \tag{2.37}$$
$$K_{v,diode} = 0.6 \tag{2.38}$$
$$E_{onIGBT} = 9.964 \times 10^{-6} \hat{i}_s^2 + 0.0156 \hat{i}_s + 0.6221 \tag{2.39}$$
$$E_{offIGBT} = 2.4259 \times 10^{-8} \hat{i}_s^3 - 5.7183 \times 10^{-6} \hat{i}_s^2 + 0.0357 \hat{i}_s + 1.8700 \tag{2.40}$$
$$E_{diode} = 2.8029 \times 10^{-6} \hat{i}_s^2 + 0.0139 \hat{i}_s + 0.9973 \tag{2.41}$$

where threshold voltages, $V_{t,IGBT}$ and $V_{t,diode}$ are given in V, the resistances, $R_{on,IGBT}$ and $R_{on,diode}$, are given in mΩ. $K_{v,IGBT}$ and $K_{v,diode}$ are given for $V_{ref} = 300$ V. Note that the current dependency of the switching losses is not expressed using I_{ref} here, instead this dependency is included in the polynomial for $E_{onIGBT/offIGBT/diode}$, each given in mJ based on $\hat{i}_s$ in A.

The value of I_{cn} can be approximated based on the current rating of the EM, [16], as

$$I_{cn} = 1.092 I_{em,rms} - 6.05 \tag{2.42}$$

where I_{em} is the current rating of the EM, in A (rms). The linear relation is found through simulations of the IGBT chip temperature for three sizes of an example IPM, using a switching frequency of 10 kHz.

The DC-voltage has been approximated as constant for the evaluation of the IPM and converter operation, although it does in principle depend on the state of charge of the battery as well as the resistive voltage drop during operation [29]. With third harmonic injection, the upper limit of the voltage of the EM is given by [29]

$$\hat{U}_{ph} = \frac{V_{DC}}{\sqrt{3}} \tag{2.43}$$

where $\hat{U}_{ph}$ is the maximum amplitude of the AC phase voltage.

Overall, the converter model presented in this section is a simple semi-analytical model that allows the losses in the converter to be approximated with both the influence of both the operating point and current rating of the IPM reflected.

2.7 Cost models for converter and IPM

The term LCC typically refers to the total costs related to a product during the course of its lifetime, including investment cost, operational cost and end-of-life costs [42]. Within this thesis the LCC of the IPM and power electronic converter has been approximated with estimated investment costs, following [16], and energy losses, as described further below.

The investment cost of the IPM has been estimated as

$$C_{i,em} = 1.8m_{fe} + 10.0m_{cu} + 47.3m_{PM} \tag{2.44}$$

where $C_{i,em}$ is the investment cost of the IPM, where the subscript $_i$ indicates investment and the subscript $_{em}$ indicates the electric machine. The cost coefficients used with the weight of the laminations (electro-steel), m_{fe}, winding (copper), m_{cu}, and PM (sintered NdFeB with low Dy), m_{PM}, are based on the cost per kg of the respective raw materials with a manufacturing factor of 1.5. Further description of the cost coefficients can be found in [16].

The investment cost of the power electronics converter is approximated with the cost of the power module, DC-capacitor and bus bar, using the approximations based on data sheets for automotive converters with 650 V IGBT modules with different ratings for nominal collector current, I_{cn}, (using Infineon FS200/400/600/800) presented in [16]. The value of I_{cn} is based on the rated current of the IPM as in (2.42) in the previous section. There are other costs related to the converter, for example related to the housing, controller board and electronics. However, focus here lies on the costs that have a close dependency on the IPM design, i.e. current rating. Therefore, the costs that have low dependency on I_{cn} [16] have not been included here. Overall, the converter cost is here approximated as

$$C_{i,conv} = C_{i,pow-mod}(I_{cn}) + C_{i,DC-cap}(I_{cn}) + C_{i,bus-bar}(I_{cn}) \tag{2.45}$$

where $C_{i,conv}$ is the investment cost of the converter, where the subscript $_i$ indicates investment and the subscript $_{conv}$ indicates the converter. $C_{i,pow-mod}$, $C_{i,DC-cap}$ and $C_{i,bus-bar}$ denote, in order, the investment cost of the power module, the DC-capacitor and bus bar, all of which are taken as function of the nominal collector current I_{cn}.

The costs of the different components included for the converter are estimated, based on [16]. The cost of the power module is here estimated with

$$C_{i,pow-mod} = 5.52A_{IGBT,tot} + 2.46A_{diode,tot} + C_{pack} + C_{heatsink} \tag{2.46}$$

$C_{i,pow-mod}$ is the estimated cost of the power module, in EUR. $A_{IGBT,tot}$ and $A_{diode,tot}$ are the total chip areas for the IGBTs and diodes in the converter respectively, as indicated by the subscript, both in cm^2. C_{pack} and $C_{heatsink}$ are the estimated costs of the power module packaging and heat sink respectively.

Further, each of the costs in (2.46) are related to I_{cn}. For the chip areas, the relation used is

$$A_{IGBT,tot} = 6(0.49I_{cn} + 8.5)/100 \tag{2.47}$$

$$A_{diode,tot} = 6(0.24I_{cn} + 3.9)/100 \tag{2.48}$$

where the areas are given in cm^2 and I_{cn} in A. While the packaging and heat sink costs, in EUR, are approximated based on I_{cn} (in A) with the linear relations

$$C_{i,pack} = 0.1316I_{cn} - 4.83 \tag{2.49}$$

$$C_{i,heatsink} = 0.0011I_{cn} + 1.227 \tag{2.50}$$

Furthermore, the cost of the DC-capacitor is estimated with a polynomial [16], as

$$C_{i,DC-cap} = -3 \times 10^{-7} I_{cn}^3 + 0.0006 I_{cn}^2 + 0.0009 I_{cn} + 18.235 \tag{2.51}$$

where $C_{i,DC-cap}$ is the investment cost of the DC-capacitor in EUR, with I_{cn} in A.

The cost of the bus bar is estimated as

$$m_{bus-bar} = 5\rho_{cu} \frac{I_{cn}}{J_{bus-bar}} l_{bus-bar} 10^{-9} \tag{2.52}$$

$$C_{i,bus-bar} = 20.0 m_{bus-bar} \tag{2.53}$$

where $m_{bus-bar}$ is the mass of the bus bar (in kg), ρ_{cu} is the mass density of copper (8933 kg/m^3), the bu bar has five conductors, each with a length $l_{bus-bar}$ (in mm), here taken as 300 mm. $J_{bus-bar}$ is the nominal current density in the bus bar (in A/mm^2), here set to 20 A/mm^2. The coefficient for the cost is based on the copper cost per kg with a manufacturing factor of 3. [16]

Together, (2.46)-(2.50) give an estimation of the power module cost, while (2.51) and (2.53) estimates the costs for the DC-capacitor and the bus bar respectively. These equations, which are all based on I_{cn}, form the estimated converter cost in (2.45). Note that the converter cost estimates presented here are empirically made based on data sheets for automotive converters with 650 V IGBT modules with different I_{cn} ratings, in the range 50-800 A, and it is not recommended to use them outside that scope.

The investment costs of other parts of the BEV have not been included, as they have been approximated as independent of the IPM design. Costs related to driving of the BEV, i.e. driving energy losses, have been determined as their Net Present Value (NPV), which can be calculated using

$$C_{NPV,loss} = \sum_{i=1}^{N_y} \frac{C_a}{(1+p)^i} \tag{2.54}$$

where $C_{NPV,loss}$ is the NPV of losses, C_a is the annual cost of the losses, p is the interest rate and N_y is the total number of years considered. If C_a is considered constant, the expression is a geometrical sum and can be simplified to

$$C_{NPV,loss} = \frac{C_a}{p} \left(1 - \frac{1}{(1+p)^{N_y}} \right) \tag{2.55}$$

The cost C_a can be computed based on driving energy losses for a chosen set of drive cycles combined with a cost of energy and an annual driving distance. While it would be possible to include the total modelled driving energy losses in the NPV of losses, for the purpose of IPM evaluation in this thesis, typically only the losses in the IPM and converter during driving has been included. Naturally, there is a certain energy corresponding to air drag and rolling resistance, but for a given set of drive cycles used with the vehicle model here, this merely gives an offset to the driving energy loss. Of course, the air drag and rolling resistance will still have an impact on the operating points of the IPM and converter during driving, and subsequently on the losses in those components.

Finally, the LCC of the IPM and converter, $LCC_{em+conv}$, including their investment cost and losses during driving is computed as

$$LCC_{em+conv} = C_{NPV,loss,em+conv} + C_{i,em} + C_{i,conv} \tag{2.56}$$

where $C_{NPV,loss,em+conv}$ is the NPV of the losses and the subscripts denote, in order, that the cost corresponds to the NPV, of the losses, in both the EM and converter. The values of $C_{NPV,loss,em+conv}$ is computed with (2.55) with C_a taken as the cost related to the losses in the IPM and converter per year of driving. $C_{i,em}$ and $C_{i,conv}$ are the investment costs of the EM and converter, computed as described above, in (2.44) and (2.45) respectively.

2.8 Optimization with genetic algorithms and meta-models

This section gives a brief overview of the most central optimization-related concepts used in the later parts of this thesis.

2.8.1 Introduction to optimization

By definition, optimization, means to bring something towards its best possible state [43]. Let's consider a simple example of an optimization problem, as

$$minimize\ y_1(x_1) = x_1^2 + 1 \tag{2.57}$$

where the objective is to find the smallest value of y_1. Further, y_1 is called the objective function and it depends on the variable x_1. The value of x_1 that gives the optimal objective value is denoted x_1^* and referred to as the optimal solution. Here, the optimal solution is simply $x_1^* = 0$ (assuming $x_1 \in \mathbb{R}$), as illustrated with a star in Figure 2.5.

The problem in (2.57) is called an unconstrained optimization problem. If we add a constraint to our optimization problem, as

$$minimize\ y_1(x_1) = x_1^2 + 1 \qquad \text{objective} \tag{2.58}$$
$$subject\ to\ 1 \leq x_1 \leq 3 \qquad \text{constraint} \tag{2.59}$$

the optimal solution will change to $x_1^* = 1$, also marked in Figure 2.5.

So far, only one objective was considered but there are naturally also multi-objective optimization problems. A simple example of an optimization problem with two objectives is

$$minimize\ y_1(x_1) = x_1^2 + 1 \qquad \text{objective 1} \tag{2.60}$$
$$minimize\ y_2(x_1) = (x_1 - 2)^2 + 1 \qquad \text{objective 2} \tag{2.61}$$
$$subject\ to\ 1 \leq x_1 \leq 3 \qquad \text{constraint} \tag{2.62}$$

there is no longer a single optimal solution. Instead there is a set of pareto-optimal solutions, also known as the **pareto-front**, shown in Figure 2.5.

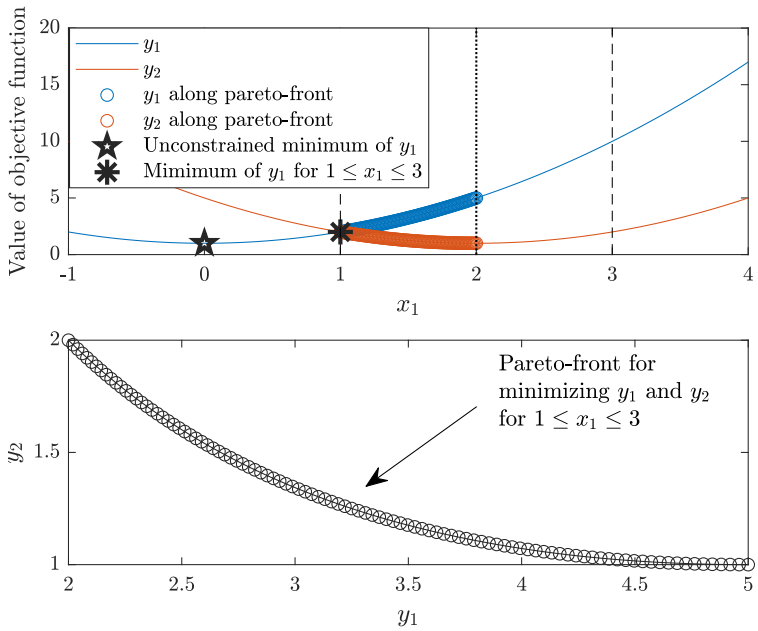

Figure 2.5 Example of unconstrained optimal solution minimizing $y_1 = x_1^2 + 1$ as well as the optimal solution for the same objective function with constraints $1 \leq x_1 \leq 3$ (top). The pareto-front for the multi-objective case, minimizing y_1 and y_2 with constraints $1 \leq x_1 \leq 3$, are shown both as function of x_1 (top) and as y_2 versus y_1 (bottom).

2.8.2 Genetic algorithms and meta-models

In the simple examples above, the optimal solution(s) were straightforward to find. However, it is not typically so for optimization problems with larger number of variables and more complex relations between the variables and the objective function(s). There are a large number of optimization algorithms available, that suit different types of optimization problems [43]. For single-objective optimization, there are several algorithms, referred to as gradient-based algorithms, where the convergence towards the optimum is based on local derivatives of the objective function [44]. A commonly used type of gradient based algorithms are Sequential Quadratic Programming (SQP), for example Non-Linear Programming by Quadratic Lagrangian (NLPQL) [45]. Another type of algorithm, which can be used for multi-objective optimization, is the Genetic Algorithm (GA) [46].

The GA is a nature-inspired algorithm, that mimics the evolution process, that can be used to solve complicated engineering problems [46]. Essentially, a GA starts from a set of possible solutions (referred to as the starting population) that are each given a fitness value, based on the included objectives. Solutions from the starting population are then selected and used as "parents" (mixed using cross-over) to create a new solution, for the next generation of solutions. Natural selection is mimicked, as the chance of using a certain solution as parent depends on the fitness value. It is also common to include some

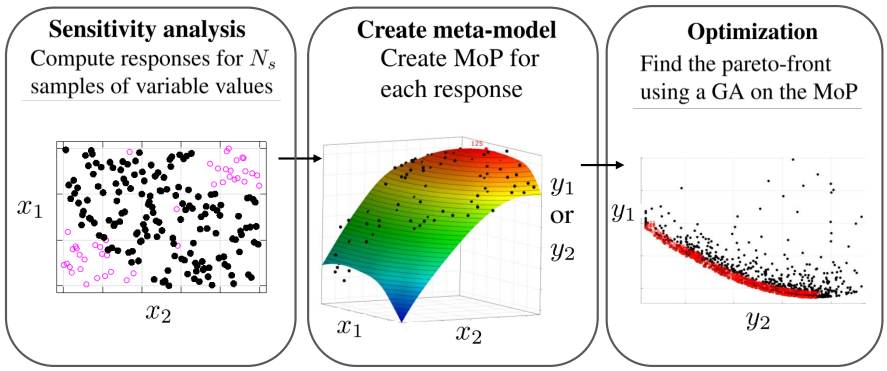

Figure 2.6 Workflow for an example optimization using a GA and meta-models (i.e. MoP), for a case with two variables, x_1 and x_2, and two responses, y_1 and y_2, which are also used as objective functions to be minimized.

extent of random change to the solutions (i.e. mutation) and also to keep a few of the best solutions unchanged (i.e. cloning) for the next generation. Over the generations of the GA, the population of solutions is expected to evolve towards an optimum. However, there is no guarantee that a GA will converge to a globally optimal solution. [46]

Still, the GA is one of the more popular algorithms for EM design optimization [5]. Examples of GAs used for IPM design optimization include [47–49]. When optimization is done directly using FEA for evaluation of objective and/or constraints, the computational time becomes an issue and it is therefore not uncommon to use meta-models (also known as surrogate models or response surfaces) [5, 50] which is, for example, done in [48, 49, 51]. There are several types of meta-models, such as polynomial response surfaces and Kriging models [5]. Within this thesis, the meta-modelling has been done using the commercial software Ansys OptiSLang which offers an automatic selection of the meta-model for each investigated problem, referred to as Meta-model of Optimal Prognosis (MoP) [50].

Prior to the creation of a MoP, a Sensitivity Analysis (SA), also known as Design of Experiments (DoE), must be done. The SA consists of evaluating the responses (i.e. the values of any objective functions or constraints of the coming optimization problem) for several sampled values of the variables. Here, latin hypercube sampling has been used. For example, if we consider an optimization problem with two objectives, y_1 and y_2, that depend on two variables, x_1 and x_2, in some way that can be evaluated using FEA, then the SA with N_s samples means that y_1 and y_2 are evaluated for N_s different combinations of values for x_1 and x_2. Thereafter, a MoP is created based on the N_s results and, finally, an optimization, such as identifying the pareto-front using GA, can be done based on the MoP. This work-flow is illustrated in Figure 2.6.

The SA would require a significant computational effort, as it involves N_s FEA based evaluations of the responses. However, once the MoP is created, the optimization will be fast. Typically, the meta-model based process is expected to be significantly faster than a direct optimization using FEA. Further, there is additional flexibility since the MoP allows the optimization to be repeated quickly for a different version of the objective or

constraints, as long as the responses, variables and variable ranges remain the same. For example, with existing MoPs for y_1 and y_2, depending on x_1 and x_2, it is possible to define a new objective where y_1 and y_2 are combined with certain weighting factors and it can be quickly optimized using the existing MoPs.

Finally, the automatic selection of the MoP in Ansys OptiSLang involves investigation of several types of meta-models that are then compared using a quantity called Coefficient of Prognosis (CoP), which serves as an indication of how well the meta-model is able to predict the response for a new sample point. The CoP, for an example response y_1, is defined as [44, 50]

$$CoP_{y_1} = 1 - \frac{\sum_{i=1}^{N_{test}} (y_{1,i} - \hat{y}_{1,i})^2}{\sum_{i=1}^{N_{test}} (y_{1,i} - \hat{y}_{1,avg})^2} \tag{2.63}$$

where CoP_{y_1} is the CoP for the response y_1. The actual response value for sample i is denoted $y_{1,i}$ while the corresponding value predicted by the meta model is $\hat{y}_{1,i}$ and $y_{1,avg}$ is the average value of the response samples. Note that (2.63) is the square of the linear correlation between the actual and predicted response values. Further, the CoP is evaluated using cross-validation, where the total number of available samples (i.e. N_s samples from the SA) are split into different sets for creating and testing the meta model. Thus, the CoP is evaluated for a set with N_{test} samples that was not used for creating the model. However, while cross validation is used for selecting the meta-model type and for evaluating CoP, the final meta model, i.e. the MoP, is still created using all the available N_s samples. [44, 50]

2.8.3 Discrete variables in optimization

If any of the variables in the optimization is restricted to a set of discrete values (for example integer values), it becomes a discrete optimization problem. Certain design choices of EMs have a discrete nature, for example the number of turns in the winding. However, such design choices need to be treated carefully in optimization procedures, since discrete optimization problems are known to be very challenging to solve to optimality. One approach that can be used for discrete optimizations is the Branch-and-Bound approach. Branch-and-Bound is based on successively adding bounds on variables, thereby splitting the space of solutions into subsets, in a way that allows identifying and ignoring subsets where the optimal solution can not be located [52].

As a simple example of the Branch-and-Bound approach, consider minimization of $y(x)$ where the variable x is required to be an integer. First the integer constraints are relaxed (i.e. x is considered a continuous variable). The optimal solution is then $x^* = 1.6$, with the objective value $y(1.6) = 10$. Since the optimal solution to the relaxed problem is not an integer, the problem is split into two subsets, where the first subset has the bound $x \leq 1$ and the other subset has the bound $x \geq 2$. Solving the problem for the first subset results in $x^* = 1$, with $y(1) = 11$. Solving the problem for the second subset results in in $x^* = 2.3$, with $y(2.3) = 12$. In this case, we do not need to investigate the second subset further, since any integer solution in this subset can not have a lower objective value than $y(2.3) = 12$ and a better integer solution is known $y(1) = 11$. In this simple example, it can then be deduced that $x^* = 1$ is an optimal solution to the discrete problem.

Chapter 3

Driving energy distributions and vehicle performance targets

A BEV will change speed during driving and the EMs used for BEV propulsion will also need to operate over a wide range of speed and torque values, in order for the BEV to follow the velocity profile desired by the driver. A "drive cycle" refers to a sequence of vehicle speed as a function of time. Thus, a drive cycle is an example of driving. A given drive cycle can, together with vehicle parameters, be translated into operating conditions for different components in the vehicle drive system, and in continuation be used to improve the design of the component. Here, focus lies on the operation of the electric traction machine, IPM, where the efficiency during driving is of particular interest. Considering the large variation included in driving, for example city driving is quite different from highway driving, it is not straightforward to select which drive cycles that should be used to represent driving. Here, the aim has been to investigate how strongly the IPM design would be influenced by the drive cycle selection. This also serves to quantify the improvement potential when customizing the IPM design for a specific driving type. To this end, several different sets of drive cycles are chosen and later compared.

3.1 Drive cycles

There are drive cycles created with the aim of representing general driving, such as the current legislative drive cycle WLTC [53], and other drive cycles, for example the Common Artemis Driving Cycles (CADC) [54], that represent different types of driving. There are considerable development efforts behind these drive cycles, and they are significantly closer to real driving compared to the previous legislative cycle NEDC. Still there are differences between WLTC and CADC, for example in the acceleration versus speed distribution, that can lead to different results on vehicle level [55]. The need of keeping the cycles short, to make them usable in certification or practical testing (such as measuring emissions of vehicles with combustion engines and range for BEVs), also leads to limitations in how well the cycles can represent real driving. However, for IPM design evaluation based on simulation models, it is feasible to include a large amount

of driving data. Here, this has been done using a database of real driving data from the "The Swedish Car Movement Data Project" (SCMD) [56]. The CADC have also been included for comparison. The selected drive cycle sets (further described in Section 3.1.1 and 3.1.2), with the abbreviations used for each set, are:

- **CADC-CC**: City cycle from CADC (a.k.a. Artemis Urban cycle, 4.87 km)
- **CADC-RC**: Rural cycle from CADC (a.k.a. Artemis Rural cycle, 17.27 km)
- **CADC-HWC**: Highway cycle from CADC (a.k.a. Artemis Motorway cycle, version with 150 km/h top speed, 29.55 km)
- **SCMD-CT**: City type selected from the database from The Swedish Car Movement Data Project (112 540 km of logged cycles from 178 cars)
- **SCMD-RT**: Rural type selected from the database from The Swedish Car Movement Data Project (155 286 km of logged cycles from 162 cars)
- **SCMD-HWT**: Highway type selected from the database from The Swedish Car Movement Data Project (35 236 km of logged cycles from 42 cars)
- **SCMD-GT**: General type selected from the database from The Swedish Car Movement Data Project (303 062 km of logged cycles from 382 cars, consists of all cycles in SCMD-CT, SCMD-RT and SCMD-HWT combined)

3.1.1 CADC

The CADC consist of the urban cycle, the rural cycle and the motorway cycle [53]. There are two versions of the motorway cycle, with a difference in the maximum speed. Here the more demanding version (150 km/h) of the motorway cycle has been selected. The vehicle speed as function of time for the selected CADC are shown in Figure 3.1.

3.1.2 Real driving data

The real driving data used here comes from a database created in The Swedish Car Movement Data Project [56]. There, driving was measured using GPS-equipment that logged time, position and velocity at 2.5 Hz. The measurements were done in 9 different campaigns, lasting approximately 2 months each, during the years 2010-2012. The measurements were done on privately driven passenger cars, randomly selected from the Swedish motor-vehicle register, with a maximum weight of 3.5 tons and an age of 8 years or younger. BEVs, which at the time were few and quite limited in terms of range, were not included in the vehicle selection. [57].

The analysis database from the The Swedish Car Movement Data Project contains logged data from 714 vehicles, although some of them have a very low number of trips logged. There are 450 vehicles that have 35 or more logged trips with high data quality and out of these 382 vehicles (85%) have been chosen as the vehicle fleet considered here. The selected vehicle fleet (382 vehicles) cover more than 300 000 km of logged driving.

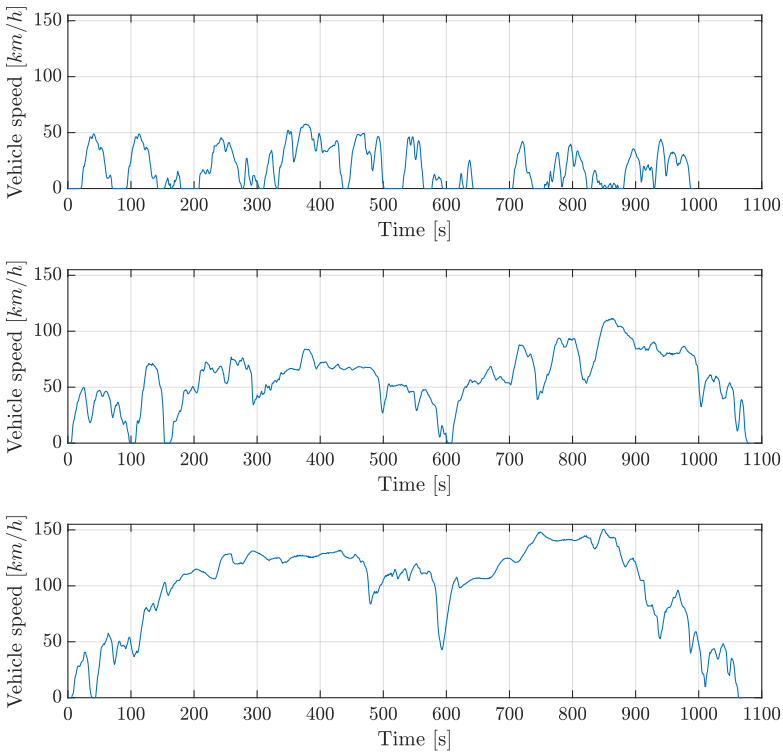

Figure 3.1 The CADC shown as vehicle speed as a function of time, including the urban cycle (here referred to as CADC-CC), top, the rural cycle (CADC-RC), middle, and the 150 km/h version of the motorway cycle (CADC-HWC), bottom.

The initial data selection, resulting in 450 vehicles, also includes filtering and repairing of the data, such as interpolation for short periods of apparently missing data (for example due to temporary loss of satellite connection). Trips with a very low average speed ($<$ 3 km/h) or duration ($<$30 s) have also been removed in the initial data selection. This data repair is similar, but not identical, to the one done in [57]. Here, the data repair has been adapted for the purpose of investigating the relative occurrence of different operating points of the IPM in mind, which is a slightly different use of the data compared to [57] and [58] where focus was on daily driving distances and trip patterns. Further details on the data selection from the database is given in Appendix A.

3.2 Vehicle parameters and performance requirements

The vehicle considered is a passenger BEV with a 2-wheel drive where a single IPM propels the vehicle. The key parameters are as presented in Table 3.1, which is in line with the highway car from [29]. The vehicle parameters in Table 3.1 are henceforth used

Table 3.1 Key parameters of the example vehicle

Parameter	Value
Mass, m_{car}	1700 kg
Front area , A_{front}	2.3 m^2
Drag coefficient, c_d	0.28
Rolling resistance, c_r	0.008
Top speed	160 km/h
Gear ratio, k_{gear}	12
Wheel radius , r_{wheel}	0.34 m

for all the logged cycles in the selected vehicle fleet from the database created in The Swedish Car Movement Data Project, even though the actual driving in the database came form several different vehicles.

When working with IPM operating points based on measured driving data, it is particularly important to remove outliers in acceleration, as that would correspond to an unrealistic value in torque. Apparent outliers, for example related to discontinuous velocity due to missing data, are managed by the data repair (described further in Appendix A). However, driving is an application that inherently has large fluctuations in acceleration and traffic situations can occur where a rather dramatic acceleration or deceleration is requested from the driver. Thus, it is sometimes difficult to judge whether a strong acceleration is related to a measurement issue or an actual result of demanding driving and a high performance vehicle. In such cases, the data was not modified but instead it was decided to select a subset of the vehicle fleet. By selecting 85% of the vehicles, 382 vehicles, the peak torque and power that would be required from the IPM to meet all the logged cycles converged towards values that were considered reasonable for a moderate sized 2-wheel drive passenger vehicle. The resulting performance requirement shown as peak torque and peak power needed as a function of speed is shown in Figure 3.2. The curve in Figure 3.2 describes the performance outline, meaning that all operating points in all logged cycles coming from all vehicles in the fleet are contained below the curve. Regarding the CADC, they are also fully contained below the curve in Figure 3.2.

For the selected vehicle fleet the peak performance, shown in Figure 3.2, is not sensitive to individual vehicles. Thus neglecting any single vehicle in the fleet will not have a large impact on the required peak torque or power from the IPM, since there are other vehicles that also has an operating point at a similar level of torque and speed, which is an indication that it is a performance that can be considered as a reasonable performance requirement for the IPM here. Note that the performance requirement here is simply set as low as possible while still allowing the vehicle to fully follow all drive cycles included in this work. In practice there could be commercial incitements for higher performance, but the influence of such aspects are not covered here. Instead focus lies on loss reduction and LCC, which motivates modest performance requirements.

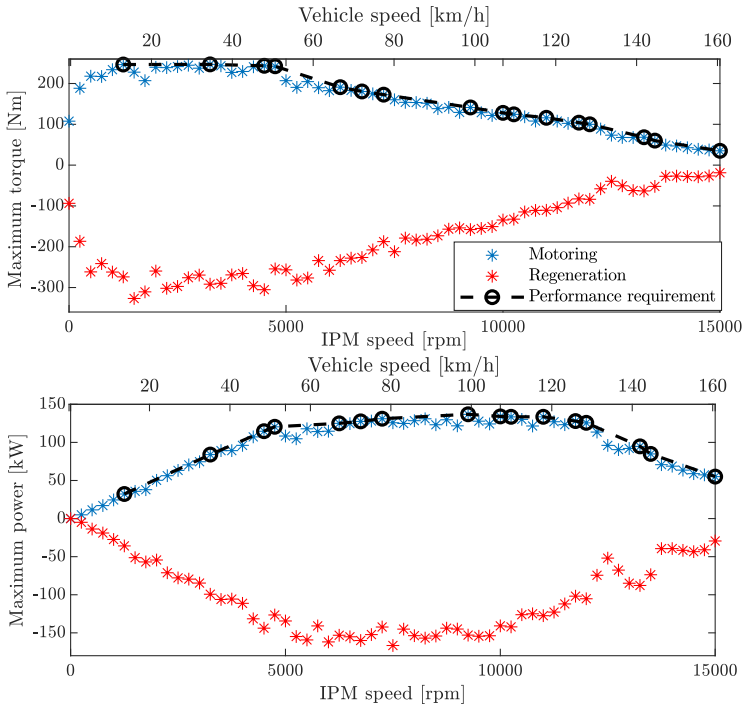

Figure 3.2 Maximum torque (top) and power (bottom) in all the logged cycles of the selected vehicle fleet, for different speeds, together with the motoring outline used as the IPM performance requirement.

3.3 Distribution of energy for different driving types

Considering the vehicle parameters in Table 3.2, a drive cycle can be translated into its corresponding operating points for the IPM. Here, the operating points have been aggregated in a few different ways, to ease the analysis of the data for various purposes, as illustrated in Figure 3.3 using CADC-RC as an example. Predominately, the data has been split into bins of torque and speed, either as time (as in Figure 3.3 b) which is later used together with the loss maps of the IPM to compute losses during driving, or as energy (as in Figure 3.3 c) which can more easily be related to IPM efficiency. The torque and speed regions where most driving energy is spent will be most important in terms of IPM efficiency, to reduce the losses during driving. Note that the energy distribution is simply the time distribution weighted with the power (as torque times speed) of each bin.

The energy distribution versus speed (i.e. summed over the torque dimension), shown in Figure 3.3 d), is later used for classification of driving into different types. The distributions, of driving time and energy, have been normalized with the total driven distance in the cycle to facilitate cycle-to-cycle comparisons.

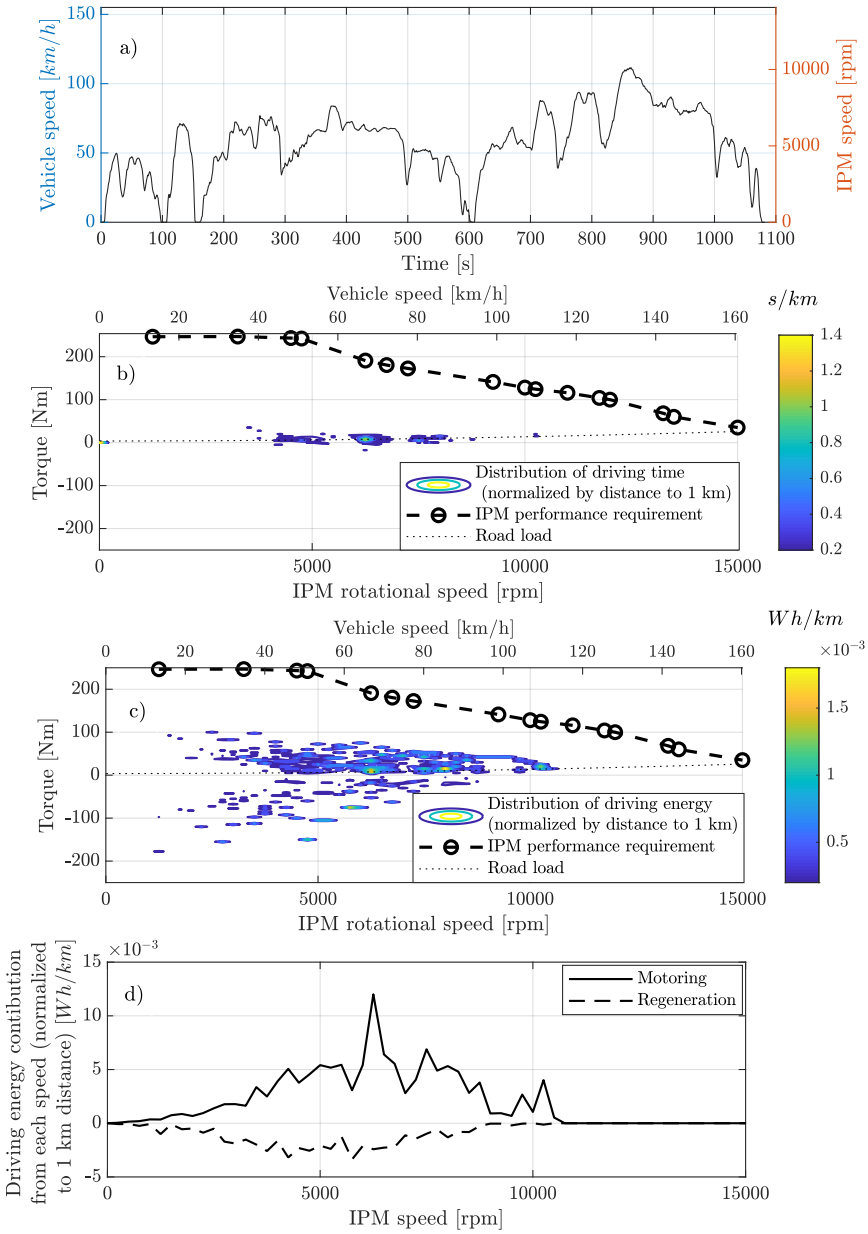

Figure 3.3 The CADC rural (CADC-RC) shown as vehicle speed versus time in a), and related to the example vehicle in different ways (normalizing the driving distance to 1 km) in b)-d). The time spent in different operating points (expressed as bins of torque and speed) of the IPM is shown in b) while c) is the corresponding result for driving energy. Summation in the torque dimension in c) gives the energy distribution versus speed shown in d).

The distributions of time and energy, for each of the considered drive cycle sets, have been normalized with the total driven distance of each set. Then a yearly driving distance of 15 000 km has been used for all sets. In the case of the sets coming from the The Swedish Car Movement Data Project it would have been possible to estimate the yearly driving distances for the different driving types based on the logged driving. However, emphasis here has been placed on the type rather than the amount of driving. Therefore, to isolate the influence of the driving type alone, the driving distance has been kept constant. The selected value of 15 000 km/year lies in-between 17 150 km/year, which is the average value for the data from The Swedish Car Movement Data Project [58], and the national average for Sweden, which has been in the range 13 500-11 000 km/year during the years 1999-2021 [59].

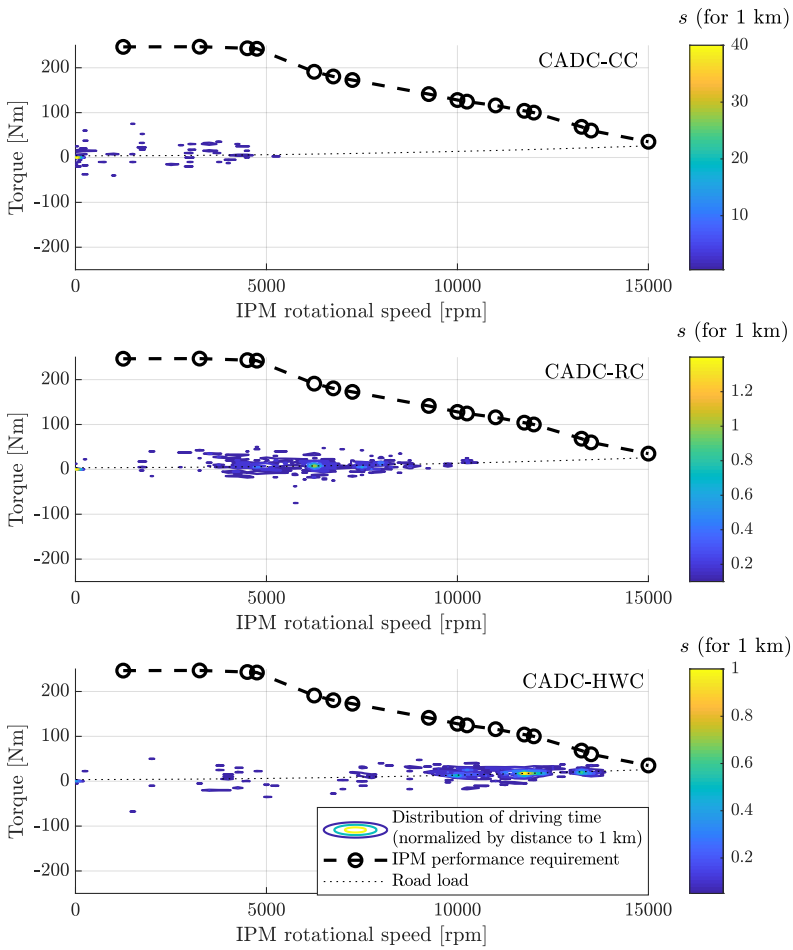

Figure 3.4 Driving time distributed in a grid of torque and speed of the IPM, normalized to a driving distance of 1 km, for each of the CADC.

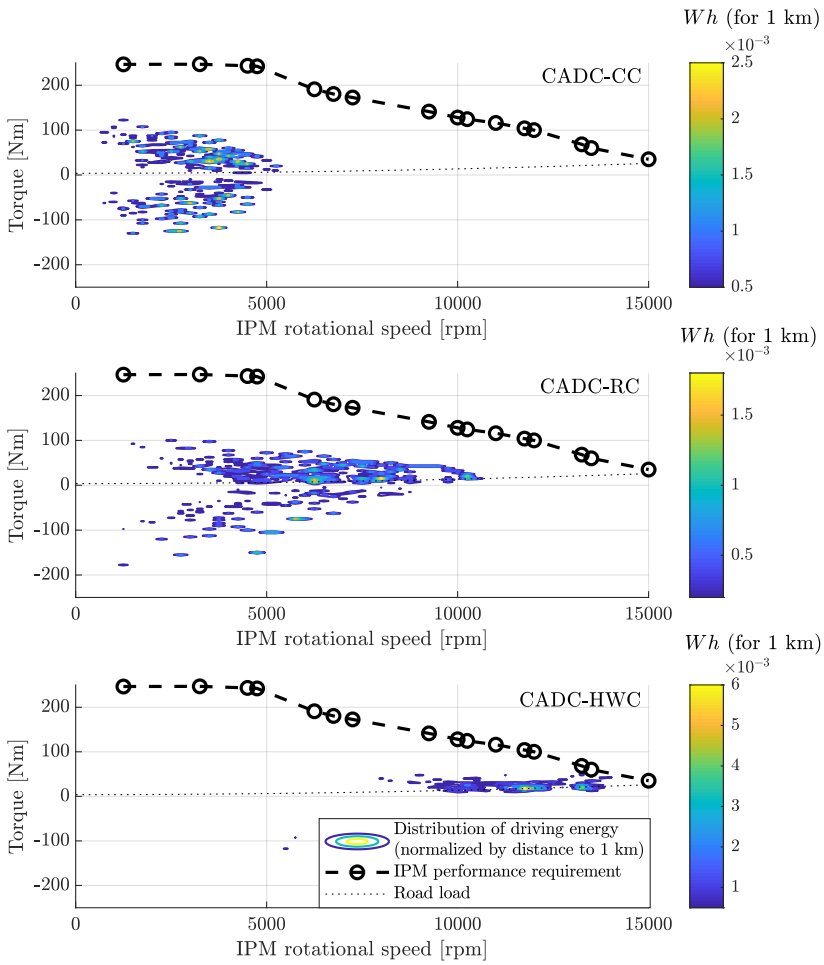

Figure 3.5 Driving energy distributed in a grid of torque and speed of the IPM, normalized to a driving distance of 1 km, for each of the CADC.

3.3.1 Time- and energy distributions for CADC

The distributions, as time and energy, in a grid of torque and speed of the IPM of the three CADC are shown in Figure 3.4 and Figure 3.5. The energy distribution is also shown as power versus speed of the IPM in Figure 3.6. The performance requirement from Section 3.2 and road load of the example vehicle are included for comparison. As shown in Figure 3.5, there is a clear difference between the different cycles in the placement, in terms of torque and speed, of the most energy intense areas.

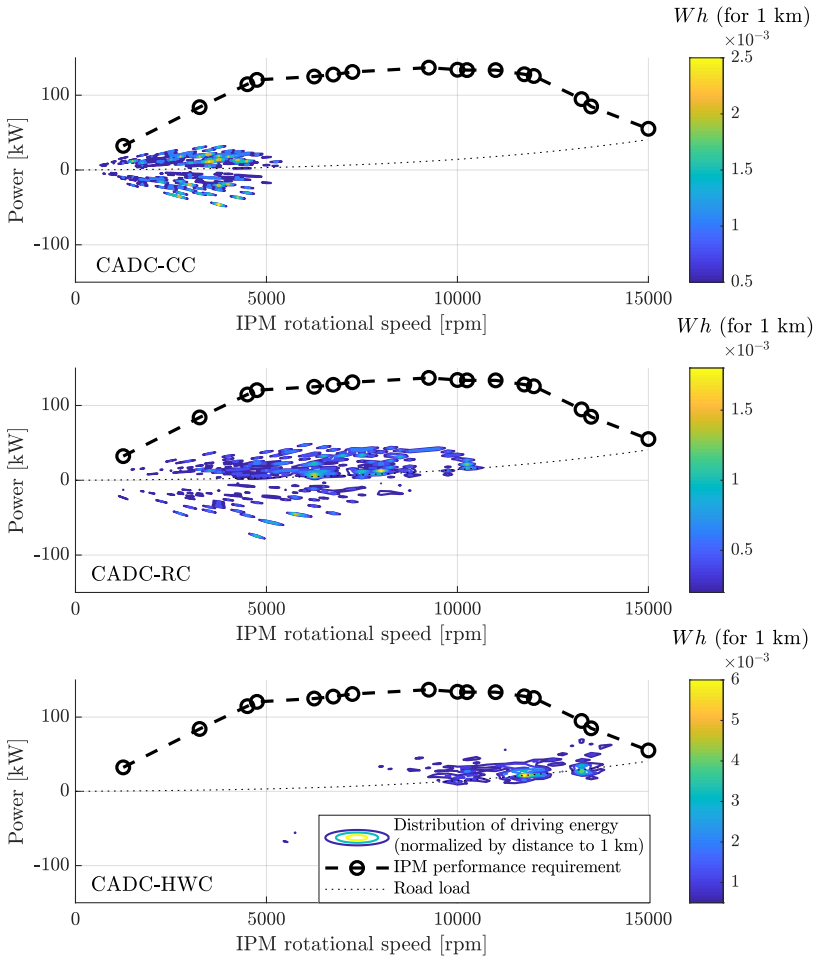

Figure 3.6 Driving energy distributed in a grid of power and speed of the IPM, normalized to a driving distance of 1 km, for each of the CADC.

3.3.2 Separating logged real driving into different types

The drive cycle set corresponding to all logged cycles for the selected vehicle fleet in Section 3.1.2 forms the case referred to as SCMD-GT (which stands for "Swedish Car Movement Data - General Type"). However, the distribution of driving time and energy will look different if a subset of the vehicle fleet is used. Thus, SCMD-GT is a combination of several different driving types. Here, it has been desired to split the set into three subsets, corresponding to a city driving type, SCMD-CT, a rural driving type, SCMD-RT and a highway driving type, SCMD-HWT.

As the driving energy distribution is of high interest here, the driving types have been set based on which speed that contributes most to the driving energy of each individual

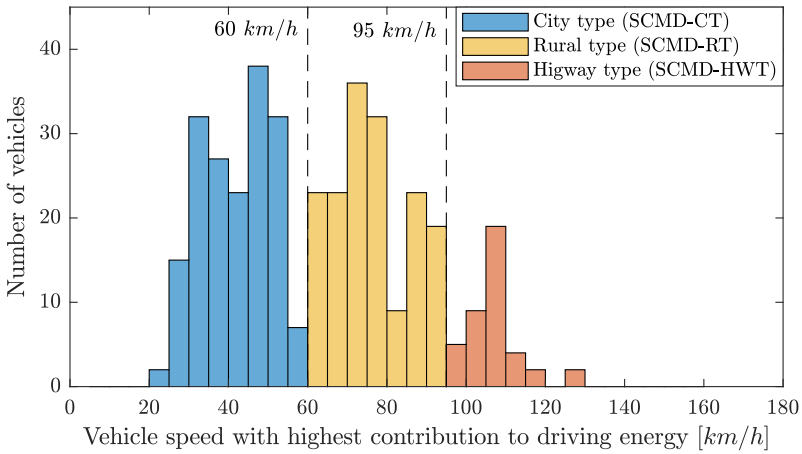

Figure 3.7 Distribution of the vehicles in SCMD-GT based on the speed that contributes most to the driving energy (for motoring operation) for each vehicle.

vehicle in the selected vehicle fleet (SCMD-GT). All the logged cycles for a given vehicle are combined and the driving energy contribution from each speed is computed, to find the vehicle speed with the highest contribution to the energy (in motoring operation). Naturally, the resulting speed varies among the vehicles, as each has their individual combination of logged cycles. The vehicles are then placed in speed bins, based on the speed that contributes the most to their driving energy, as shown in Figure 3.7.

Based on the shape of the histogram in Figure 3.7 there appears to be a natural split around 60 km/h and around 95 km/h. Therefore, it is considered suitable to define the three driving types as: a city type (SCMD-CT) consisting of all logged cycles for the vehicles where the most energy contributing speed is $\leq$ 60 km/h, a rural type (SCMD-RT) consisting of all logged cycles for the vehicles where the most energy contributing speed is $>$ 60 km/h and $<$ 95 km/h and a highway type (SCMD-HWT) consisting of all logged cycles for the vehicles where the most energy contributing speed is $\geq$ 95 km/h.

As the driving types are based on selection of vehicles there is a naturally occurring combination of different driving within each type. For example, the city type (SCMD-CT) has most of the driving energy spent at low speed but still includes some driving at highway speeds. This can be seen in Figure 3.8, which shows the driving energy contribution for the defined driving types. Note that the results in Figure 3.8 are normalized with the total driving distance of each driving type, to allow simple comparison between the types. The corresponding results for CADC are also included for comparison.

It can be seen in Figure 3.8 that the selected driving types emphasise different speed intervals in the energy distribution. The speed intervals also agree relatively well between the driving types created from the logged cycles and the CADC, for example the range 30-50 km/h has highest energy in both SCMD-CT and CADC-CC. However, the driving types based on logged cycles have a notably smoother distribution. This is expected, since larger amounts of data will typically make each individual operating point stand out less, reflecting variations such as similar but not identical trips that occur in real driving.

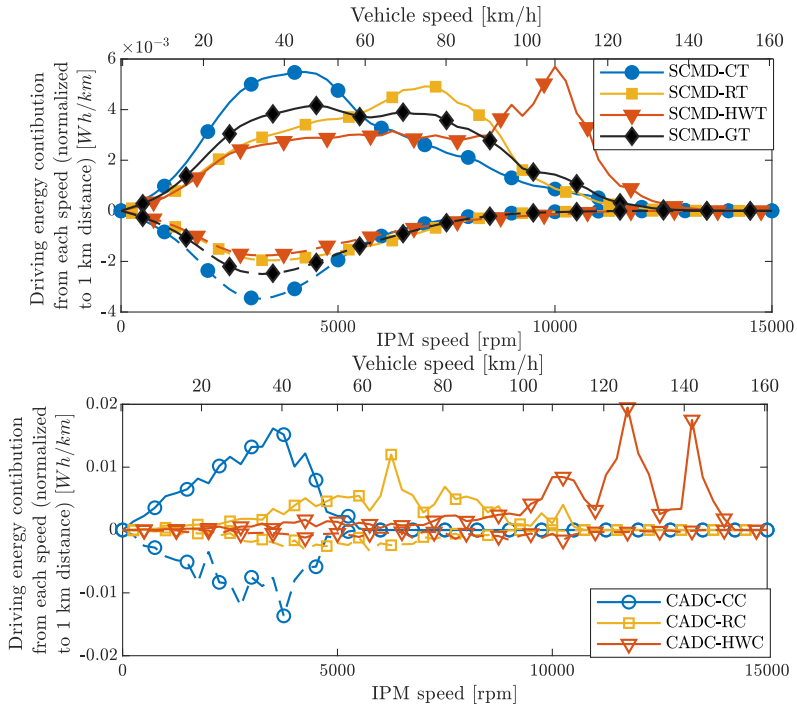

Figure 3.8 Contribution of different speeds to the driving energy, for the driving types based on large amount of real driving data (top) and for the CADC (bottom).

3.3.3 Time- and energy distributions for real driving

The distributions, as time and energy, in a grid of torque and speed of the IPM of the three driving types as well as the entire selected vehicle fleet based on the SMCD, i.e. sets of cycles logged in The Swedish Car Movement Data Project, are shown in Figure 3.9 and Figure 3.10. The energy distribution is also shown as power versus speed in Figure 3.11.

Comparing the results in Figure 3.9-3.11 to the corresponding results for the CADC in Figure 3.4-3.6, shows the distributions for SMCD as significantly smoother than those for CADC. As the CADC city, rural and highway each consist of a single relatively short cycle, the resolution in terms of operating points (combinations of torque and speed) is lower. The SMCD types, on the other hand, each consist of a large amount of driving data and spreads more smoothly over the grid of torque and speed. Here, for consistency, the same high resolution (2.5 Nm steps in torque and 250 rpm steps in IPM speed) has been used for all the drive cycle sets.

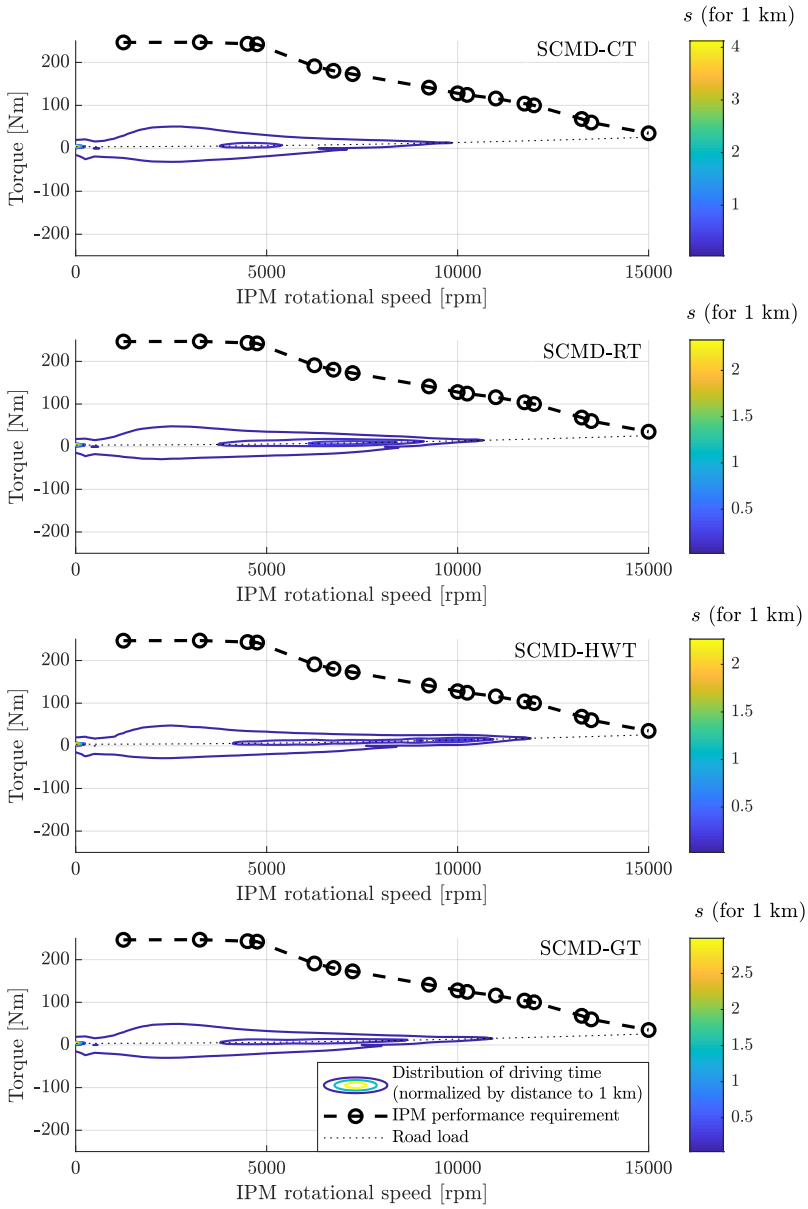

Figure 3.9 Driving time distributed in a grid of torque and speed of the IPM, normalized to a driving distance of 1 km, for each of the drive cycle sets selected from data logged during the Swedish Car Movement Data Project. The driving types, from top to bottom, are city type, rural type, highway type and general type.

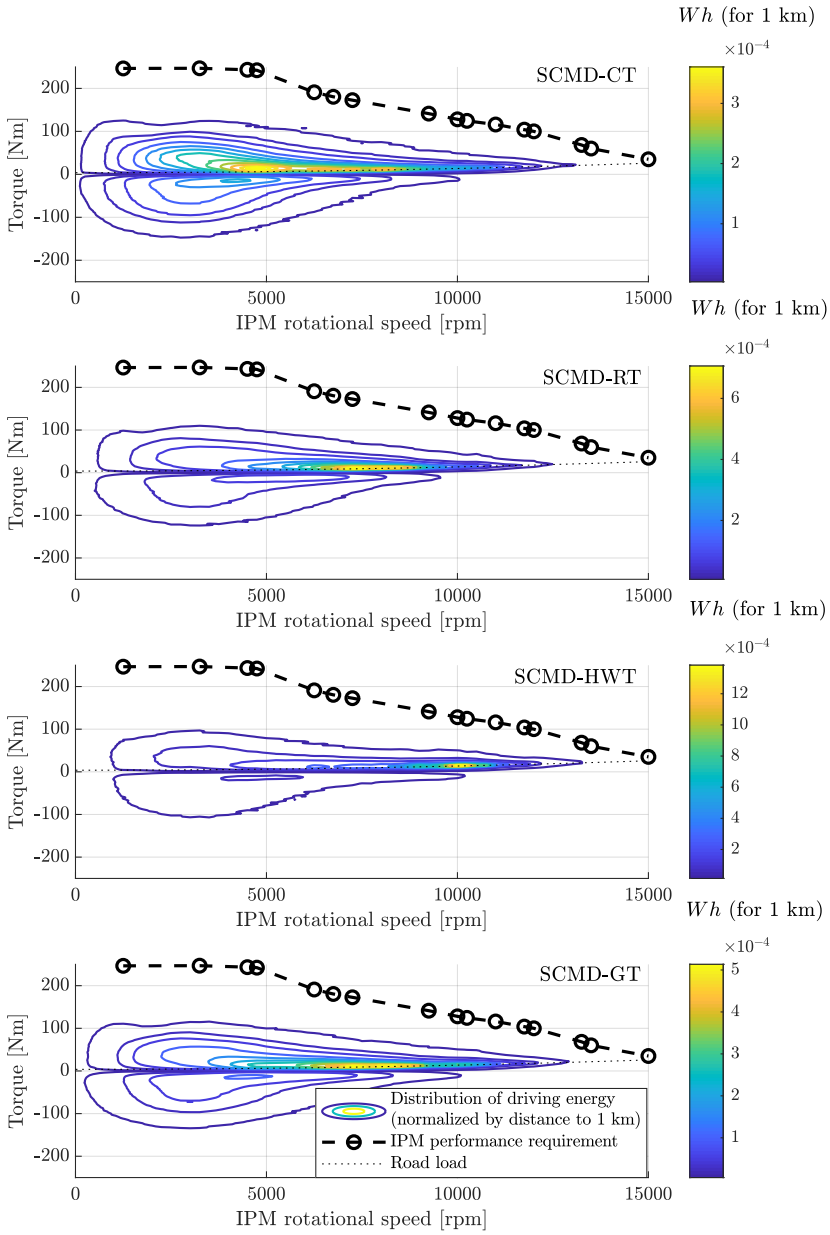

Figure 3.10 Driving energy distributed in a grid of torque and speed of the IPM, normalized to a driving distance of 1 km, for each of the drive cycle sets selected from data logged during the Swedish Car Movement Data Project. The driving types, from top to bottom, are city type, rural type, highway type and general type.

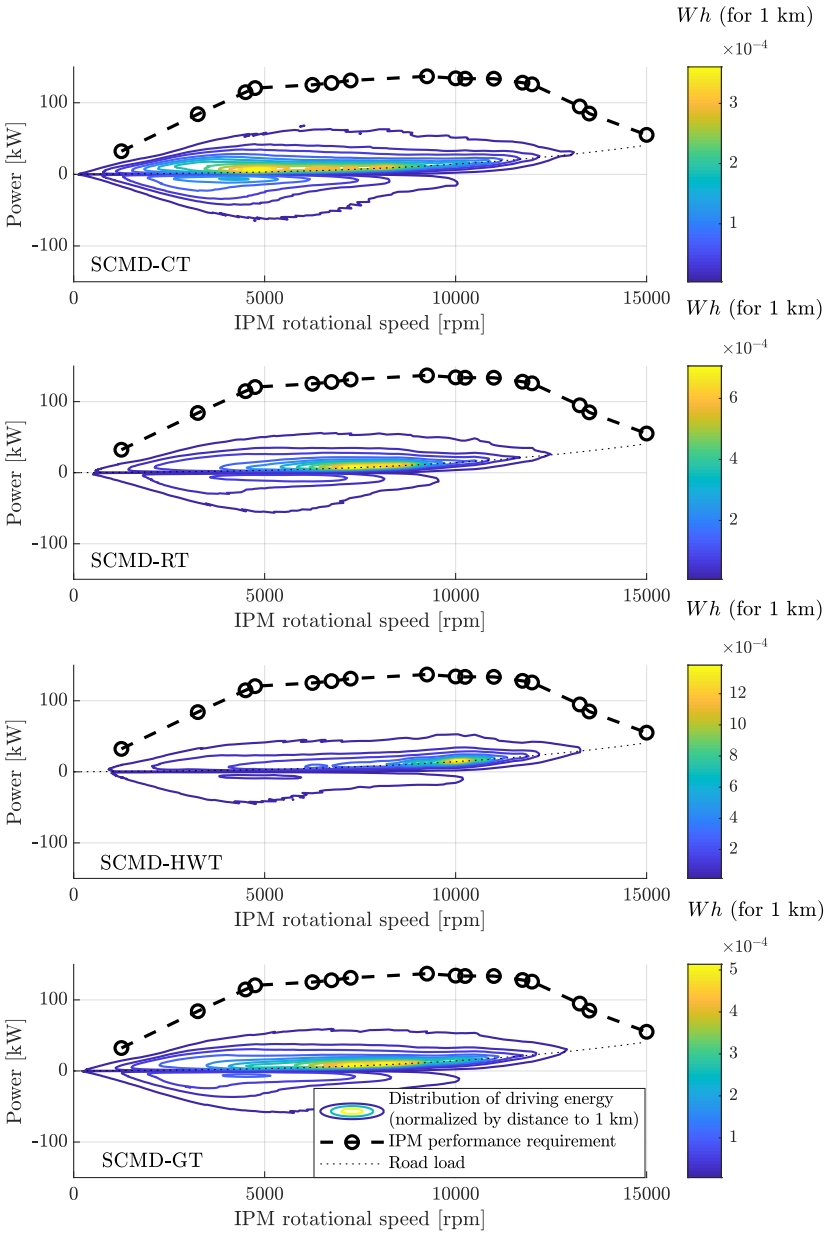

Figure 3.11 Driving energy distributed in a grid of power and speed of the IPM, normalized to a driving distance of 1 km, for each of the drive cycle sets selected from data logged during the Swedish Car Movement Data Project. The driving types, from top to bottom, are city type, rural type, highway type and general type.

Chapter 4

IPM model for evaluation of performance and efficiency

The evaluation of IPM performance and efficiency has, within this thesis, been based on electromagnetic FEA, implemented in the commercial software Ansys Electronics Desktop (sometimes referred to as Ansys Maxwell) as transient 2D FEA with sinusoidal current feeding. While the FEA would be more realistic if the FEA was done in 3D and/or with voltage feeding using switched voltages, it would also lead to a large increase in computational load. Overall, the type of FEA used here has been considered a good compromise between simulation speed and accuracy, for the purposes of IPM design optimization.

4.1 Materials implementation

The IPM model described in this chapter has been used throughout this thesis, for IPMs with random wound copper windings in the stator, a core of non-grain-oriented electrical steel with lamination thickness 0.30 mm (NO30-1600 from the Hi-Lite series, Tata Cogent) [60] and PMs of Neodymium Iron Boron (NdFeB) type.

The core material has been implemented in the FEA with the BH-curve (magnetic flux density, B, versus magnetic field, H) shown in Figure 4.1, which is based on data sheet values of NO30-1600, with extrapolation to extreme values of H using the relative permeability of vacuum. The extrapolated values are mainly needed to model the magnetic saturation in the rotor ribs (see Figure 2.3), since they are designed to saturate very strongly.

The core losses are computed using the loss model available in the FEA software (Ansys Electronics Desktop), where the coefficients of the Bertotti equation (2.16) are identified by the FEA software based on curves of core loss versus B for nine frequencies covering 50 Hz to 10 kHz. The core loss coefficients, k_h, and k_e, are 336.9 $\mathrm{Wsm^{-3}T^{-2}}$ and 0.2644 $\mathrm{Ws^2m^{-3}T^{-2}}$ respectively.

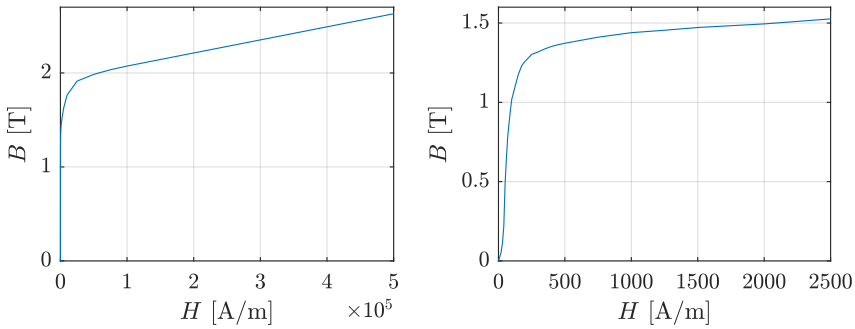

Figure 4.1 BH-curve implemented in the FEA for the core material, based on data sheet with extrapolation to extreme magnetic fields using relative permeability of vacuum, shown in full (left) and zoomed into a more typical range of values (right).

Two variants of the PM-material are included. Initially, in Chapter 6-7, where focus lies on peak performance, a PM of grade N42-SH was considered at a high temperature of 120°C and implemented with a remanence, B_r, of 1.079 T and a coercivity, H_c, of -849.245 kA/m. Later in this thesis, in Chapter 8-10, where focus lies on IPM cost and losses during driving, a PM with low Dy-content (the Hitachi Neomax NMX-37F used in [29]) is used at a lower temperature of 70°C, implemented with a B_r of 1.182 T and a H_c of -902.285 kA/m. This PM also agrees with the cost estimations in [16] that were described in Section 2.7.

4.2 Evaluation of performance and operating region

To determine the performance of the IPM, the FEA has been used together with the equivalent circuit model including magnetic saturation, referred to as Model B and presented in Section 2.2.3. Essentially, the FEA is used to compute the circuit parameters for different values of d- and q-currents, as $\Psi_m(i_q)$, $L_d(i_d, i_q)$ and $L_q(i_d, i_q)$. FEA is done for over 100 combinations of i_d and i_q values, covering the quadrant of motoring operation in the dq-current plane ($i_d \leq 0$ and $i_q \geq 0$), and interpolation is used to evaluate the circuit parameters for any motoring operation point. An example of the circuit parameters from the FEA, for an example IPM, referred to as the intial IPM, is given in Figure 4.2. While the initial IPM, with a current rating of 400 A Root Mean Square (RMS), only serves as an illustrative example here, it is also further presented in the coming Chapter 6.

With the circuit parameters determined, the circuit equations (2.11)-(2.13) can be used to compute torque and voltage for a given combination of i_d and i_q. The DC-resistance of the stator winding is computed analytically, as described in Section 2.2.3, using a fill factor of 0.45 and a winding overhang of 2.5 mm on each side of the stack. An operating point, in this context, refers to IPM operating at a certain torque and speed, which is associated with a certain combination of i_d and i_q and, subsequently, a certain value of the circuit parameters. If the circuit parameters were constant, the operation points would be straightforward to compute analytically, as described in Section 2.2.

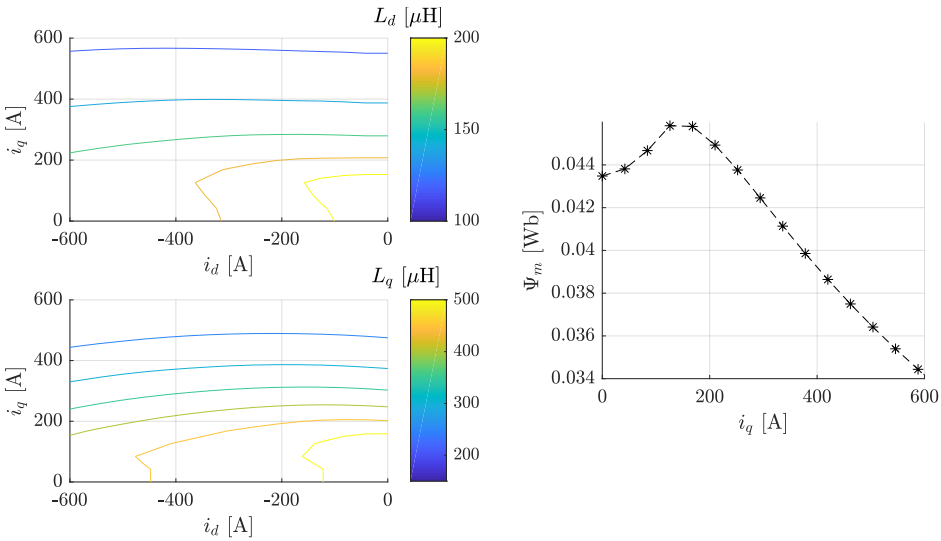

Figure 4.2 Circuit parameters, Ψ_m, L_d and L_q, depending on the currents i_d and i_q based on electromagnetic FEA, using an initial IPM as example.

However, with current-dependent circuit parameters, the operation points have instead been identified numerically.

To account for the current dependence, the circuit equations are solved iteratively. The values of i_d and i_q are changed using a gradient based optimization (using SQP, implemented in the *fmincon* function in Matlab), with the circuit parameters $\Psi_m(i_q)$, $L_d(i_d, i_q)$ and $L_q(i_d, i_q)$ updated in each iteration based on the dq-current values. First the operation boundary, consisting of the highest available torque at each speed (i.e. MTPA and FW for a given voltage, described in Section 2.2) is computed. The i_d and i_q values are then set to maximize the torque, with constraints on current and voltage amplitudes. An example of an operation boundary, for the initial IPM, is illustrated in Figure 4.3, in the dq-current plane (left) and as the torque versus speed curve (right).

With the operation boundary known, a grid of operating points below it is defined to cover the entire operating region. For these points, i_d and i_q are set to reach a desired torque with the smallest current amplitude, of course still within limits of current and voltage. An example of the current combinations for the entire operating region is given in Figure 4.4. This grid of operating points is then used for computing the losses and efficiency of the IPM, as described in the coming section.

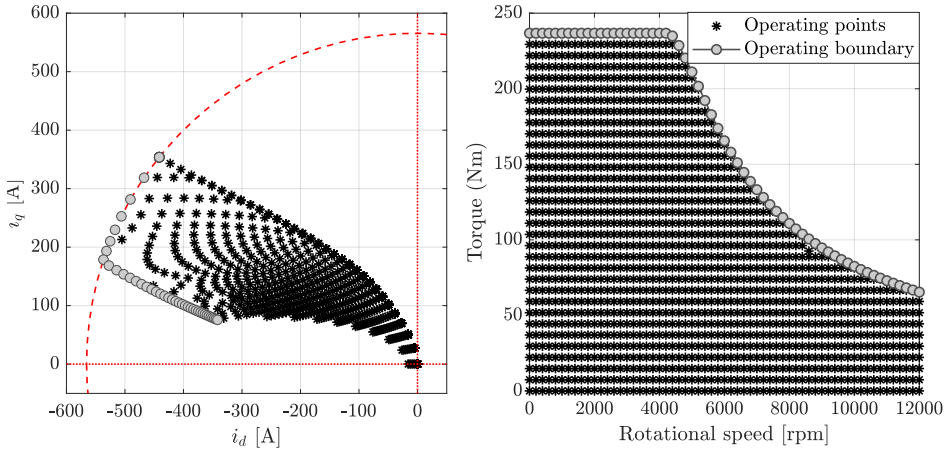

Figure 4.3 Operating boundary with a dense grid of operating points covering the operating region of the initial IPM with a current rating of 400 A (RMS). Operating points are shown in the dq-current plane (left) and as torque versus speed (right).

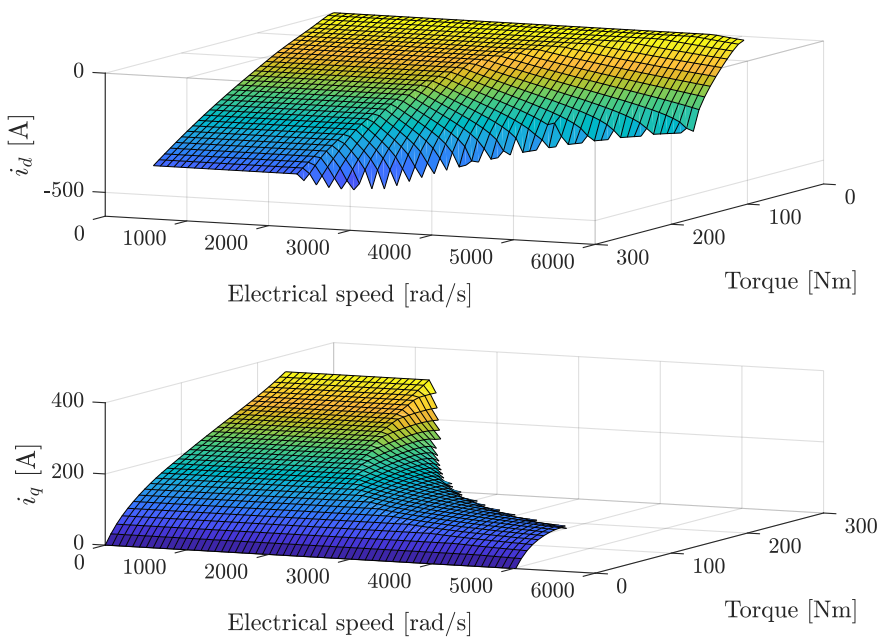

Figure 4.4 Current combinations, i_d and i_q, corresponding to a grid of operating points covering the operating region of the initial IPM with a current rating of 400 A (RMS).

4.3 Evaluation of efficiency and cost of losses

The copper losses over the entire operating region of the IPM can readily be found using (2.15), with the DC-resistance computed analytically (as described in Section 2.2.3) and the dq-currents known for a grid of operating points. The result is referred to as the copper loss map. The corresponding result for the core losses, i.e. the core loss map, is not as straightforward.

Since the FEA here does not include the switched voltage feeding associated with converter driven IPM or the degradation of the core material due to manufacturing of the IPM, a significant under-estimation of the core losses should be expected [61]. Here a factor of 1.7 has been used to scale up the core losses from the FEA, attempting to reflect the core loss increase due to manufacturing effects and impact of converter voltages. Note that this should be seen as a rather strong simplification. However, accurate modelling of core losses in EMs is very challenging and has been considered outside the scope of this thesis.

Further, two approaches for computing the core loss map are used within this thesis, where one approach is fast while the other is more accurate. The core losses, computed with the transient version of the Bertotti equation (2.16), for a given operating point can be obtained from the FEA. The most straightforward approach to finding the core loss map is simply to evaluate all the operating points in the grid using FEA (with the values of i_d, i_q and rotational speed set according to each operating point). This approach is, for example, used in [29]. This approach is here referred to as a full core loss mapping. While full core loss mapping has benefits in terms of accuracy, it is also time consuming which can lead to the need to reduce the resolution of the loss map to avoid overly long computational time.

A faster option for computing the core loss map, referred to as the reduced core loss mapping, is possible if core losses are included in the outputs of the FEAs, covering a grid of i_d- and i_q-values, that is anyway done to identify the performance and operating points (as described in the previous section). As can be seen from (2.16), the core losses are dependent on both frequency and B (which is in turn dependent on the values of i_d and i_q). Interpolation can be used to compute the core losses for a given combination of i_d and i_q. Further, the frequency dependence of the hysteresis loss and eddy losses are known from (2.16) which allows the respective components of the core losses to be scaled with frequency. Thus, if reduced core loss mapping is used, the core losses can be approximated analytically. This allows very dense grid of operating points, like the one shown in Figure 4.4, to be evaluated quickly.

Naturally, the reduced core loss mapping is an approximation of the full core loss mapping. However, if feedback from the core losses on the field solution is neglected in the FEA (which is done within this thesis, to improve computational speed) and the resolution of the dq-current mapping is sufficiently high, then the results of the reduced core loss mapping agrees excellently with those of the full core loss mapping. An example of a comparison of the reduced and full core loss mapping is shown in Figure 4.5, using an IPM from Chapter 7 as example.

Typically, efficiency maps in this thesis have been computed using reduced core loss mapping. However, for more detailed comparisons (as in Section 7.4) the full core loss mapping was used. Core losses for single operating points (as in Section 6.1) are also

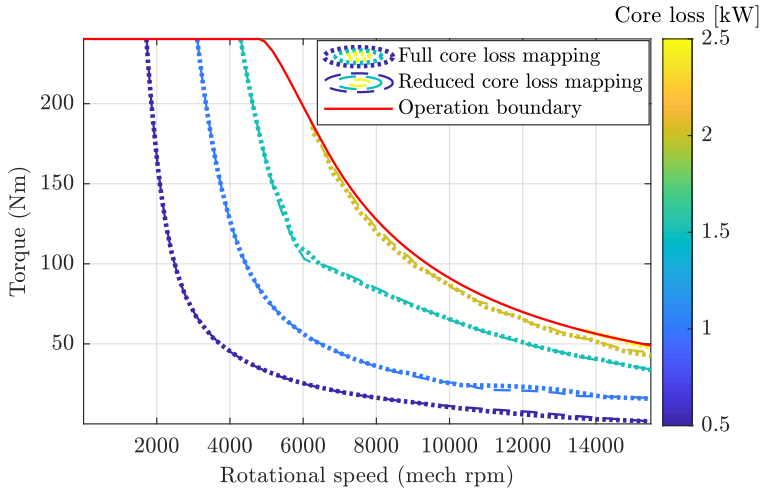

Figure 4.5 Core losses for an example IPM computed using the full and reduced core loss mapping, shown with dotted and dashed contours respectively.

evaluated directly with FEA. When full core loss mapping is used, the eddy current losses in the IPMs are also included. However, in case of reduced core loss mapping, the PM eddy losses, which are typically a comparatively small amount of the total losses for this type of IPMs [29], are neglected.

Furthermore, the efficiency and loss maps have been approximated as symmetric in motoring and regenerative operation (i.e. the loss for a negative torque value is approximated with that of the corresponding positive torque, for the same speed). The loss map of the converter has been computed based on the IPM operating points, as described in Section 2.6. An example of efficiency maps for the IPM and converter (taken from geometry C in Chapter 8), respectively, based on the reduced core loss approach are shown in Figure 4.6.

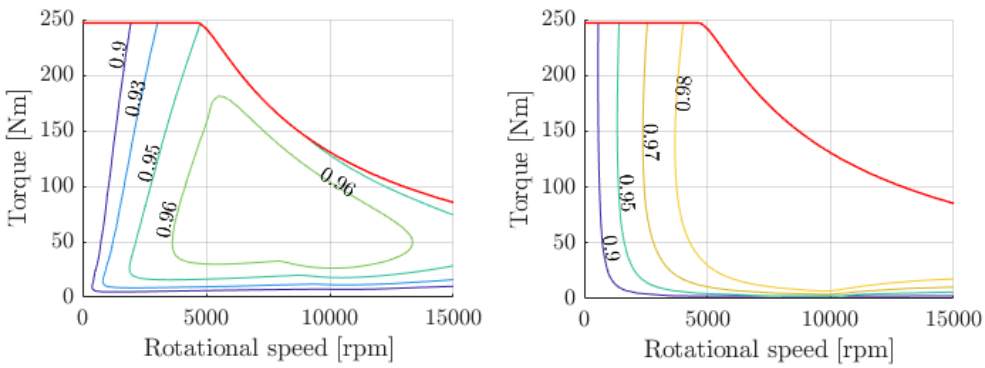

Figure 4.6 Efficiency maps of an example IPM (left) and converter (right).

Finally, the energy loss during driving is computed by weighting the loss map of the IPM and converter with the amount of time in each operating point (i.e. the time distributions for different combinations of driving, described in Chapter 3). Thereafter, the cost of the losses in the IPM and converter during driving has been taken as the NPV of the losses, computed with (2.55), using 15 000 km/year for a selected combination of city- rural- and highway driving as described by the CADC or SCMD, and a cost of 0.27 EUR/kWh (3 SEK/kWh). Further, an interest rate of 5% and 10 years of driving has been considered in the NPV calculation.

4.4 Implementation of IPM scaling

The scaling of the IPM, described in Section 2.5, has been implemented as an optional scaling of the circuit parameters and losses prior to the calculation of operating points. Thus, $\Psi_m(i_q)$, $L_d(i_d, i_q)$ and $L_q(i_d, i_q)$ as well as $P_{fe}(i_d, i_q)$ are rescaled and then the evaluation of performance and losses for the IPM operating region are done as described in the sections above, simply using the rescaled FEA results as inputs instead of direct FEA results.

Examples of the scaling results are presented here, using an initial IPM as example. There are three sets of FEA results, where one is taken as a reference case and the two other sets are scaled versions of the reference corresponding to the scaling factors

- *Case 1*: $k_a = 1.25$, $k_r = 1.00$, $k_w = 0.80$
- *Case 2*: $k_a = 0.69$, $k_r = 1.20$, $k_w = 1.20$

where *Case 1* and *Case 2* have also been computed analytically, using the scaling laws together with the reference set of FEA results.

A comparison of the results from the scaling laws and the actual FEA result for the new size of the IPM that the scaling factors correspond to, for *Case 1* and *Case 2*, are shown in Figures 4.7-4.10. Note that the resolution of d- and q-current here is very low (16 combinations of i_d and i_q) compared to the resolution used for evaluation of the IPM performance and efficiency map (which is >100 combinations of i_d and i_q). However, it still serves the purpose of verifying that the implemented scaling indeed works as expected.

Thus, Figures 4.7-4.10 show that the difference between rescaling the reference FEA results versus running a new FEA for the new size of the IPM is less than a per-mille for the wide range of currents here. Some small difference can be expected due to the numerical aspects of the FEA, like re-meshing the IPM geometry.

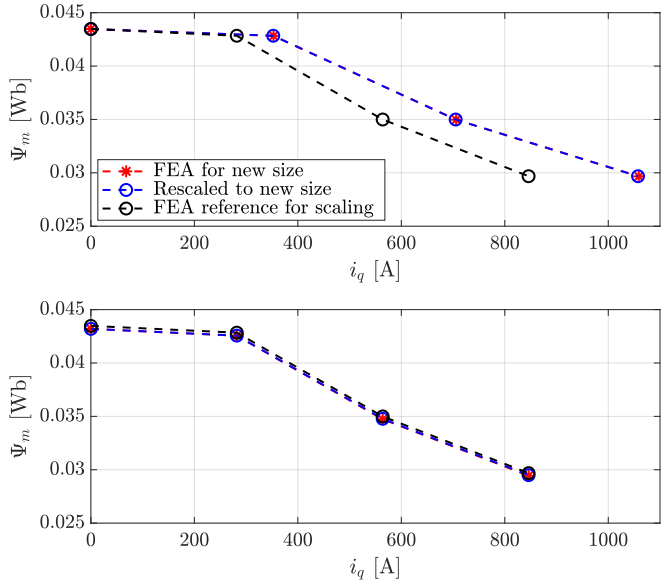

Figure 4.7 Magnet flux linkage, Ψ_m, using FEA for different sizes of an initial IPM geometry and the corresponding result using analytical scaling laws on the FEA results of the reference sized IPM, for *Case 1* (top) and *Case 2* (bottom).

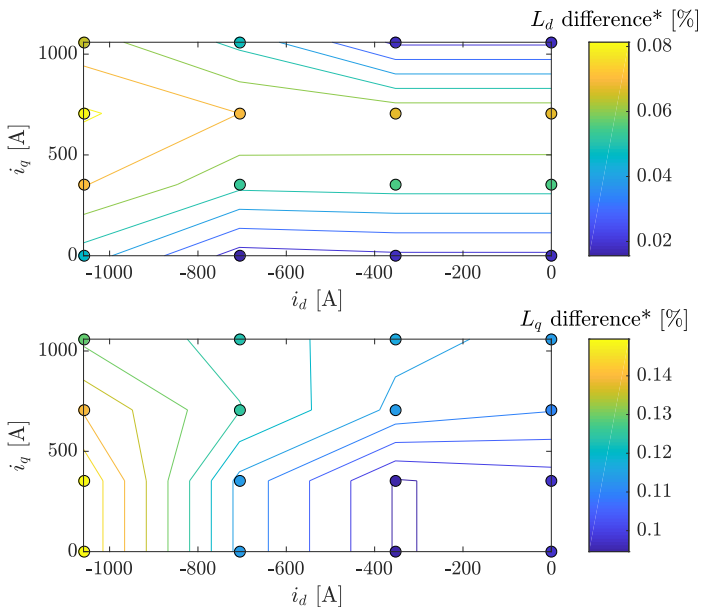

Figure 4.8 Inductance comparison between FEA and analytical scaling laws for an example IPM, for L_d (top) and L_q (bottom), in *Case 1*. *(rescaled result - FEA result)/(FEA result)

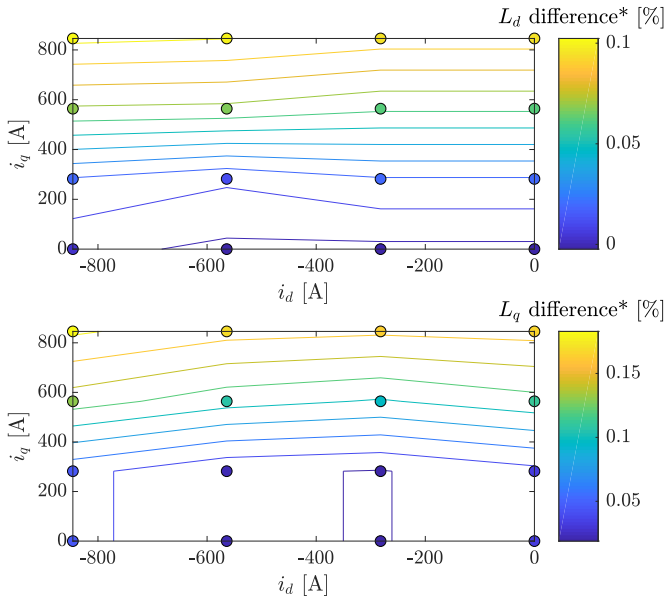

Figure 4.9 Inductance comparison between FEA and analytical scaling laws for an example IPM, for L_d (top) and L_q (bottom), in *Case 2*. *(rescaled result - FEA result)/(FEA result)

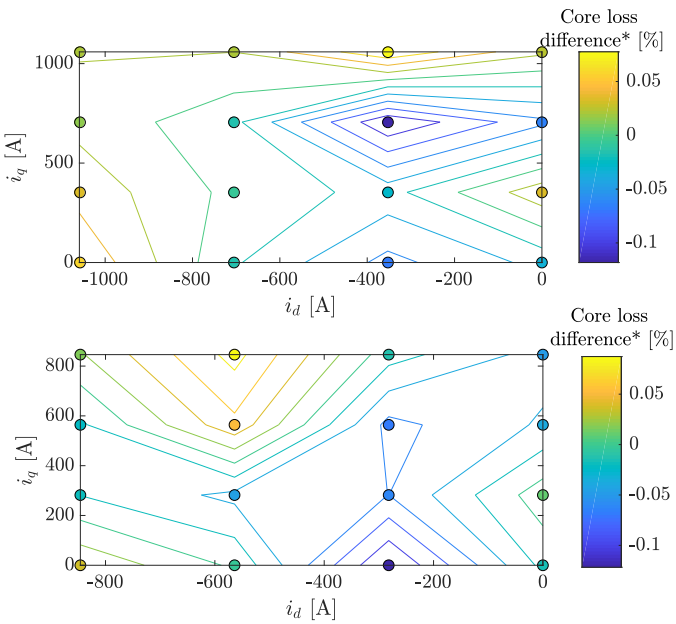

Figure 4.10 Core loss comparison between FEA and analytical scaling laws for an example IPM, for *Case 1* (top) and *Case 2* (bottom). *(rescaled result - FEA result)/(FEA result)

Finally, it is worth to note that a virtually identical power versus speed curve (i.e. operation boundary) can be achieved with different combinations of values for the scaling factors. An example of this is given in Figure 4.11. If we consider the two factors

$$x_1 = k_r^2 k_a \tag{4.1}$$

$$x_2 = k_r k_a k_w \tag{4.2}$$

then rescaled IPMs that come from the same reference (i.e. same geometry and same reference current and voltage rating) and have the same value of x_1 and x_2 will have a close to identical power versus speed curve. In Figure 4.11, $x_1 = 0.83$ (which is also the peak torque factor compared to the reference) and $x_2 = 0.92$ holds for both the scaled versions. This can be understood by (4.1) being the scaling factor for torque and (4.2) being the scaling factor for flux linkage. Essentially, if x_2 is unchanged, the base speed will be almost identical (except for the minor influence of the stator resistance) and, as will be further described in the coming Section 6.2.2, the shape of the power curve will not be altered by the scaling laws. However, the values of x_1 and x_2 for a given peak performance will of course still be dependent on the design of the reference IPM.

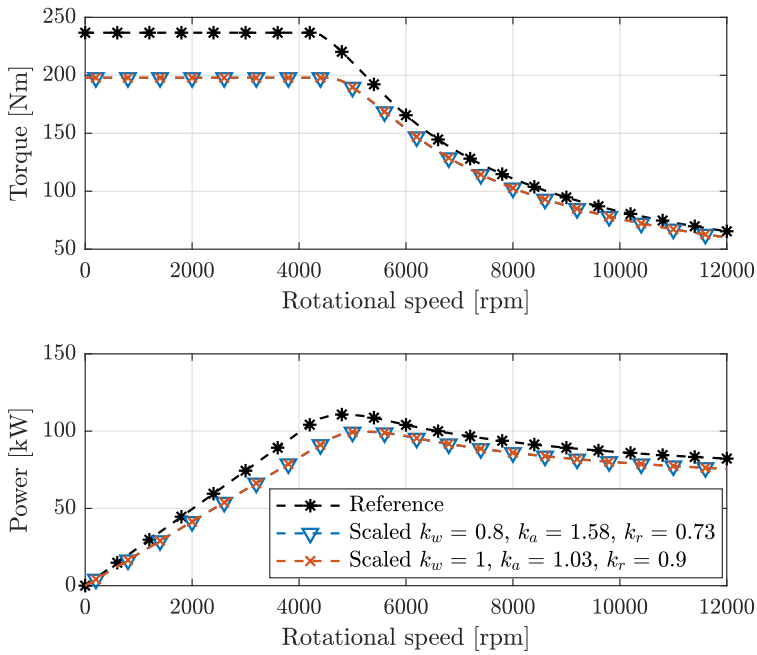

Figure 4.11 Example of two sets of scaling factors that give virtually identical performance (as power versus speed) of the rescaled IPM, using the initial IPM with a current rating of 400 A as reference IPM.

Chapter 5

IPM geometry variations

The aim of the geometry variations presented here is to be used in a workflow for optimizing the IPM geometry against a driving energy distribution (described in Chapter 9). Thus, the geometry parametrization is made with a computationally heavy optimization in mind and therefore the aim is to have a low number of carefully selected IPM design variables that dictate the entire geometry. Further, geometry dependent thermal and mechanical constraints are included in the optimization workflow, so fast estimation of the influence of the geometry on thermal and mechanical aspects are also covered here.

5.1 Geometry parametrization

The IPM geometry is parametrized using eight variables, denoted (β, f_{d}, f_{PM},f_{air}, D_r, D_s, f_{t},f_{y}). The first five variables are related to the rotor and the last three to the stator. The variables have been selected aiming to allow a sufficiently large variation in the geometry while also limiting the risk of infeasible geometries (for example overlapping flux barriers in the rotor). In other words the aim is to effectively focus the geometrical search-space on the most interesting IPM designs.

5.1.1 Stator geometry parametrization

The stator parametrization focuses on balancing the amount of copper and laminate material, which in turn will affect the relative amount of resistive and core losses. The parametrization also includes changing the overall size of the stator, to capture the trade-off between the material cost of the IPM and its efficiency. However, the stator variables do not include the choice of winding configuration. Covering different winding configurations would have caused significant increase in complexity, both in terms of number of variables and in terms of the challenges that integer variables cause in optimizations. Instead, the winding configuration needs to be selected beforehand. The parametrization has been used together with a two-layer winding with one slot short-pitch, on an 8-pole IPM, for a stator with 72 slots in Chapter 9 - 10, and 48 slots in Chapter 6. Here follows an overview of the stator variables and then a step-by-step description of the method.

5.1.1.1 Overview of stator variables

The stator geometry is parametrized using the following variables:

- Stator outer diameter, D_s.
- Tooth-width factor, f_{t}, describes the tooth width as a factor of the available arc-length (taken after the tooth tips, ie. at the smallest radius for which the teeth have constant width).
- Yoke-factor, f_{y}, describes the thickness of the stator yoke as a factor of the stator tooth width.

For a given value of the stator inner diameter (which is set based on the rotor outer diameter D_r and a constant air-gap of 0.8 mm) the variables D_s, f_{t},f_{y} can be used to adjust the split ratio ($\frac{D_r}{D_s}$) as well as the size of the slots relative to the stator lamination material. Therefore, the selected variables allow altering crucial trade-off's such as machine efficiency versus torque density and copper loss versus core loss.

An overview of how the stator geometry is affected by each stator variable individually is shown in Figure 5.1.

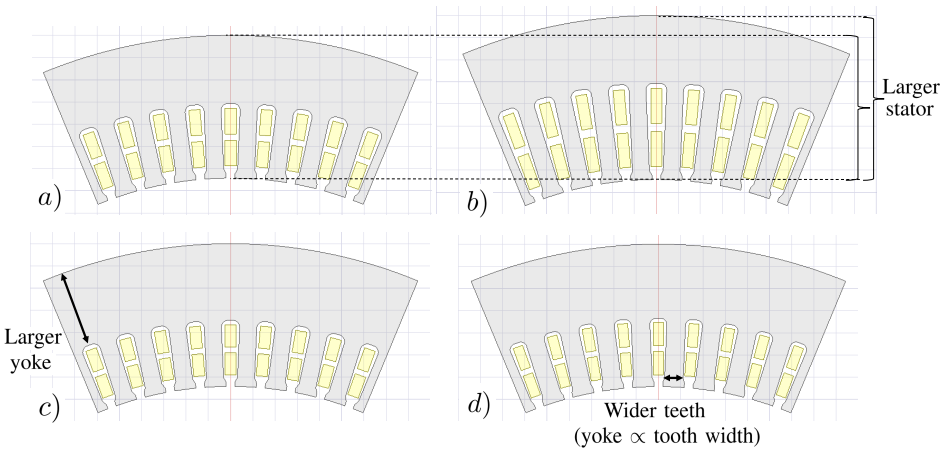

Figure 5.1 Example stator geometry, a) $D_s = 220$ mm, $f_{\mathrm{y}} = 4.0$, $f_{\mathrm{t}} = 0.55$, b) when D_s is increased to 230 mm, c) when f_{y} is increased to 4.5, and d) when f_{t} is increased to 0.6. The inner diameter of the stator is kept at 155.7 mm in a)-d).

5.1.1.2 Step-by-step description of creating the stator geometry

Naturally, with a low number of variables, several assumptions are necessary to fully define the geometrical cross-section of the stator. The main assumptions are keeping the slot openings constant and setting the rounding of the slots proportional to the slot width. Here follows a step-by-step description of how the stator geometry is created based on the variables D_s, f_{t},f_{y}.

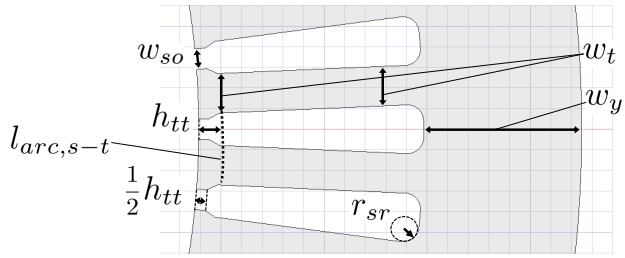

Figure 5.2 Geometrical parameters of the stator laminate, shown on three stator slots.

1. The stator outer diameter is directly set as D_s.

2. The stator teeth have a constant width which is set as

$$w_t = f_{\mathrm{t}} l_{arc,s-t} = f_{\mathrm{t}} \frac{2\pi}{n_s}(D_r/2 + w_{ag} + h_{tt}) \tag{5.1}$$

   where f_{t} is the tooth-width factor and $l_{arc,s-t}$ is the arc-length of one slot and one tooth (shown in Figure 5.2), which is computed using the number of stator slots, n_s, and the innermost radius where the teeth have a constant width which is found using the rotor outer diameter, D_r, width of the air-gap, w_{ag} and the height of the stator tooth tip. The value of w_{ag} has been kept at 0.8 mm and h_{tt} at 2 mm (of which 1 mm is the height of the constant width part of the slot opening).

3. The width of the stator yoke scales with the stator tooth width as

$$w_y = f_{\mathrm{y}} w_t \tag{5.2}$$

   where f_{y} is the yoke-factor. The sizing of the stator yoke based on the tooth width is done with the electromagnetic flux path of the stator in mind. As the flux passes radially through the teeth and then circumferentially through the stator yoke, it can be expected that these parts should scale together to avoid that one of the parts become a bottleneck for the flux. Still, it is possible to get different levels of magnetic saturation in the stator teeth and yoke, since f_{y} is a variable. This was done to not restrict the design freedom too much while still making it easy to focus on IPM designs that have a reasonable balance between the stator yoke and the stator teeth.

4. The slots are rounded on the side facing the stator yoke. The rounding radius of the slots is set as

$$r_{sr} = \frac{1}{2}(1 - f_{\mathrm{t}}) l_{arc,s-t} \tag{5.3}$$

   Thereby, the rounding of the slots is set proportional to the arc length, $l_{arc,s-t}$ minus the tooth width w_t, or, in other words the rounding is proportional to the slot width by the tooth-tip.

5. The slot opening width, w_{so}, has been kept constant, at 2 mm, which together with h_{tt} and w_t from step 2 gives the dimensions of the stator tooth tip.

5.1.2 Rotor geometry parametrization

IPM rotor structures are geometrically complex, in particular for multiple layers of flux barriers and magnets, which is common for IPMs used for BEV applications. Such rotor geometries are challenging to describe with a low number of variables. Here, a particular rotor parametrization method has been developed, which effectively reduces the number of variables and also allows the same set of variables to be used for several different flux barrier shapes. This makes the method especially useful for concept evaluations and system studies. Here, the focus lies on the rotor topology that was selected to use in the optimization presented in Chapter 9 - 10, but the same parametrization is used to compare rotor topologies with different barrier shapes in Chapter 7. Here follows first an overview of the outcome using the rotor parametrization method and then a more thorough description of the method and the logic behind it. Finally, a step-by-step description of how the rotor geometry is created is given.

5.1.2.1 Overview of rotor variables

The rotor geometry is parametrized using the following variables:

- Rotor outer diameter, D_r.
- Rotor barrier pitch angle offset, β, is a ratio that adjusts the barrier span (i.e. the reach of the barrier at the air-gap).
- Barrier depth factor, f_{d}, adjusts the barrier depth (i.e. how far into the rotor the barrier reaches).
- Magnet fill factor, f_{PM}, is the share of available barrier space that is filled with permanent magnet.
- Insulation ratio, f_{air}, adjusts the air-to-iron ratio along the d-axis (pole midline).

The influence of each variable (D_r, β, f_{d}, f_{PM}, f_{air}) on the rotor geometry is illustrated in Figure 5.3. It can be seen that a narrow span of the barrier (low value of β) also automatically gives a more shallow barrier. However, when both β and f_{d} are used, it is possible to create shallow barriers with a wide span as well as deep barriers with a narrow span. Further, Figure 5.3 also shows the "ribs", which are placed in each corner of the piece-wise linear barrier as well as towards the air-gap, to make the rotor structure mechanically feasible. Increasing the size of the rotor, i.e. D_r increased, as shown in Figure 5.3 b), is highly similar to scaling the entire geometry to a larger size. However, it is not a pure scaling since the thickness of the ribs depend on the size of the rotor. The sizing of the ribs is further described in Section 5.2.

5.1.2.2 Barrier shape

Parametrization methods based on natural q-flux lines have previously been used for synchronous reluctance machines in [62] and [63]. Here, the parametrization method has been extended to IPM rotors by the use of a piece-wise linear approximation. In the case of IPM flux barriers, a piece-wise linear curve is strongly preferred as it allows

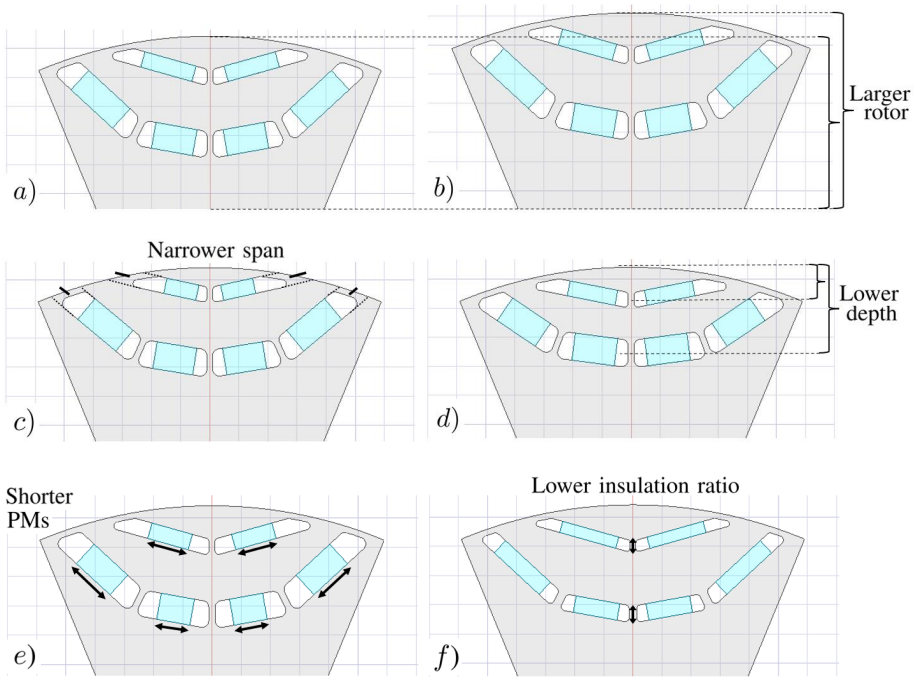

Figure 5.3 Example rotor geometry, showing one pole in an 8-pole IPM, a) $D_r = 154.1$ mm, $\beta = 0.2$, $f_{\mathrm{d}} = 0.75$, $f_{\mathrm{PM}} = 0.75$,$f_{\mathrm{air}} = 0.15$, b) when D_r is increased to 161 mm, c) when β is decreased to 0, d) when f_{d} is decreased to 0.6, e) when f_{PM} is decreased to 0.6, and f) when f_{air} is decreased to 0.1. The rotor topology in a)-f) is referred to as U_4V.

magnets with rectangular cross section to be fitted in the barriers. Further, the factor (f_{d}) is used for adjusting the barrier depth, which gives potential benefits in terms of increased magnet flux linkage and reduced mechanical stress in the rotor laminates.

The shape of the flux barrier is set as a piece-wise linear approximation of a theoretical q-axis flux line, as illustrated in Figure 5.4. The theoretical q-flux curve is matched in two points, at the pole mid-line and at the air-gap. In-between these points, a piece-wise linear approximation is made based on minimization of the average distance to the theoretical curve, as illustrated in Figure 5.4. The number of linear segments used in the approximation results in different barrier shapes. For example, using two segments gives a V-shaped barrier and using four segments results in a more curved shape referred to as U_4. The theoretical q-flux line is described by the Joukowski equation [64] as

$$r(v) = \frac{D_{\mathrm{ri}}}{2} \sqrt[n_{pp}]{\frac{c_q + \sqrt{c_q^2 + 4\sin^2(n_{pp}v)}}{2\sin(n_{pp}v)}} \tag{5.4}$$

where $r(v)$ is the radial distance from the rotor center axis as a function of the mechanical angle, v, which is taken from the edge of the pole towards the pole-midline. D_{ri} is the

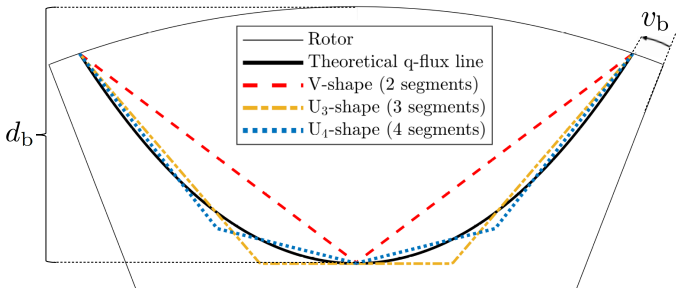

Figure 5.4 A theoretical q-flux line in an 8-pole IPM, for a barrier depth d_b and angle v_b, using piece-wise linear curves with varying number of segments.

rotor inner diameter, p is the number of pole pairs and c is a constant for each iso-line of the q-flux, computed as

$$c_q = \frac{\left(\frac{D_\mathrm{r}/2-d_\mathrm{b}}{D_\mathrm{ri}/2}\right)^{2n_{pp}} - 1}{\left(\frac{D_\mathrm{r}/2-d_\mathrm{b}}{D_\mathrm{ri}/2}\right)^{n_{pp}}} \tag{5.5}$$

where D_r is the rotor outer diameter and d_b is the barrier depth. The angle at which the q-flux curve reaches the air-gap is referred to as v_b, i.e. $r(v_\mathrm{b}) = D_\mathrm{r}/2$. A given angle at the air-gap, v_b corresponds to a certain barrier depth, d_b, and vice versa. As shown by (5.4), the shape of the theoretical q-flux curve changes with the position in the rotor. The smaller the angle v_b, the larger the larger the depth d_b.

The curve obtained by (5.4) and (5.5) has been verified to closely match the magnetic flux lines obtained with FEA when applying pure q-current in the stator with a rotor consisting solely of a laminated core (i.e no barriers or PMs).

It is possible to combine different barrier shapes into a multi-layer IPM rotor, such as the U$_4$V-topology previously shown in Figure 5.3 which has a V-shaped outer barrier and a U$_4$-shaped inner barrier. It can be noted that U$_4$V has a higher number of segments in the inner barrier layer compared to the outer layer which can be expected to be beneficial. A larger number of segments in the piece-wise linear curve results in a better approximation of the theoretical q-flux curve, which in turn is expected to give a higher saliency. However, the deviation between the theoretical q-flux curve and the piece-wise linear approximation of it depends on the depth of the barrier, as shown in Figure 5.5. Furthermore, the quality of the approximation is more sensitive to the number of segments if the barrier is deep compared to a shallow barrier. A lower number of segments also gives a simpler structure with a lower number of PMs (one PM per segment was used here) and lower amount of ribs (one rib per corner in the barrier was used here). In particular, the number of ribs in the outer barrier layer can be important if the thickness of the ribs are not limited by the mechanical stress limit but instead by manufacturing aspects (i.e. the smallest punch-able size). This was found to commonly be the case for the IPM designs investigated here (see Section 5.2 for further description of the mechanical aspects).

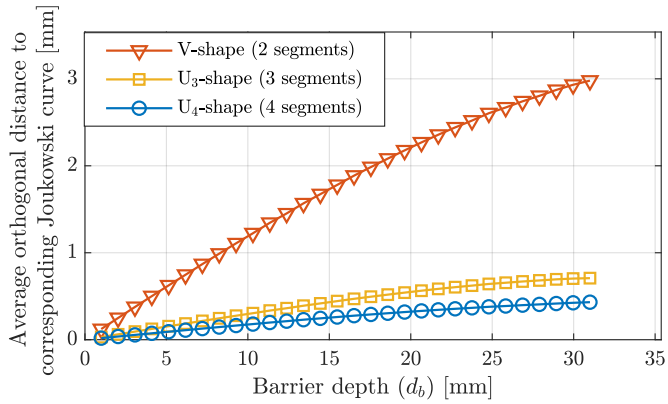

Figure 5.5 Average distance from the adapted piece-wise linear curve to its corresponding theoretical q-flux curve as a function of the barrier depth (d_b), for varying number of segments. For the case of 8 poles with $D_\mathrm{r} = 139.5$ mm and $D_\mathrm{ri} = 50$ mm.

5.1.2.3 Step-by-step description of creating the rotor geometry

In order to reduce the number of variables, several simplifications are made. The most important simplifications are using a constant pitch angle (with an offset) to describe where the flux barriers reach the air-gap, setting the depth of the barriers as a factor of the depth of the theoretical q-flux line with the same entry angle at the air-gap, keeping the barrier thickness constant within each barrier layer, and setting the relative thickness of the barriers based on having the same q-flux per rotor surface at the air-gap (neglecting ribs and assuming a sinusoidal flux distribution). Further description of the implementation and these simplifications are provided below. The topology $\mathrm{U_4V}$ is used as an example here, but the method has also been used for other barrier shapes in Chapter 7. The key geometrical parameters are shown in Figure 5.6.

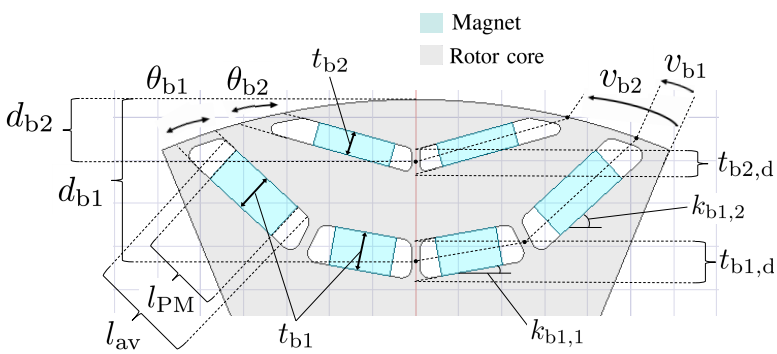

Figure 5.6 Geometrical parameters of the flux barriers, for rotor topology $\mathrm{U_4V}$.

1. The ratio β is used as an offset to the rotor barrier pitch angle, as in [62]. Following [63] one virtual barrier in the pole center is considered, and therefore the rotor barrier pitch angle, α, for two layers of flux barriers is

$$\alpha = \frac{90°(1-\beta)}{3n_{pp}} \tag{5.6}$$

   The angle at the air-gap is set as $v_{\mathrm{b1}} = 0.5\alpha$ and $v_{\mathrm{b2}} = 1.5\alpha$, for the inner and outer flux barrier respectively.

2. The theoretical q-flux line can be found for v_{b1} and v_{b2}, using (5.4)-(5.5). The shape of each barrier is then found as the piece-wise linear approximation of the corresponding theoretical q-flux line, as described in section 5.1.2.2.

3. The barrier depth factor, f_{d}, is used to provide freedom in the depth of the barriers. Let $d_{\mathrm{qf}}(v)$ be the depth of the theoretical q-flux line entering the outer rotor surface at angle v. The depth of the barriers are set as $d_{\mathrm{b1}} = f_{\mathrm{d}} d_{\mathrm{qf}}(v_{\mathrm{b1}})$ and $d_{\mathrm{b2}} = f_{\mathrm{d}} d_{\mathrm{qf}}(v_{\mathrm{b2}})$, for the inner and outer flux barrier respectively. For the inner barrier (U_4-shape) the corner located off the pole midline (see Figure 5.6) is adjusted to maintain the same relation of the slopes of the different segments ($k_{\mathrm{b1,2}}/k_{\mathrm{b1,1}}$ unchanged). If $f_{\mathrm{d}} = 1$, the depth is the same as that of the corresponding theoretical q-flux line. In particular, more shallow barriers ($f_{\mathrm{d}} < 1$) should be anticipated for IPMs, to improve the magnet flux linkage and the mechanical integrity of the rotor.

4. All segments in the barrier have the same thickness, t_{b1} for the inner barrier and t_{b2} for the outer barrier. Extending the barriers all the way to the d-axis (i.e. neglecting ribs) gives $t_{\mathrm{b1,d}}$ and $t_{\mathrm{b2,d}}$ for the inner and outer barrier respectively. The insulation ratio (f_{air}) is taken along the d-axis, as of the available rotor core, thereby $t_{\mathrm{b1,d}} + t_{\mathrm{b2,d}} = f_{\mathrm{air}}(D_{\mathrm{r}}/2 - D_{\mathrm{ri}}/2)$. Further, the relative thickness of the barriers are set based on having the same q-flux per surface area at the air-gap. Assuming a sinusoidal q-flux at the air-gap and neglecting ribs, an even magnetic loading of the rotor surface around the two barriers corresponds to

$$\frac{\int_0^{v_{\mathrm{b1}}} cos(v)dv}{v_{\mathrm{b1}} - 0.5\theta_{\mathrm{b1}}} = \frac{\int_{v_{\mathrm{b1}}}^{v_{\mathrm{b2}}} cos(v)dv}{\alpha - 0.5\theta_{\mathrm{b1}} - 0.5\theta_{\mathrm{b2}}} \tag{5.7}$$

   where θ_{b1} and θ_{b2} are the barrier span at the air-gap, for the inner and outer barrier respectively, see Figure 5.6. A numeric approach was taken, where a small $\Delta\theta_{\mathrm{b1}}$ is added to θ_{b1}, then θ_{b2} can be found using (5.7). Since the shape of the barrier curve is known, the angles (θ_{b1},θ_{b2}) can be translated to barrier thickness (t_{b1},t_{b2}) with corresponding $t_{\mathrm{b1,d}}$,$t_{\mathrm{b2,d}}$. The procedure is repeated, by adding $\Delta\theta_{\mathrm{b1}}$, until $t_{\mathrm{b1,d}} + t_{\mathrm{b2,d}}$ matches the desired insulation ratio.

5. If mechanical constraints are included, ribs are added and the barrier ends are rounded. The rounding radius at each corner of the barrier is set to 1/4 of the corresponding barrier thickness.

6. Finally, the magnet fill factor, f_{PM}, is used to set the length of the magnets, l_{PM}, as a ratio of the available length in the barrier, l_{av}. Thus $l_{\mathrm{PM}} = f_{\mathrm{PM}} l_{\mathrm{av}}$.

5.2 Geometry dependent rib thickness

The thickness of the ribs required to keep a given mechanical stress level in the rotor laminate depends on the size and geometry of the rotor (i.e. the rotor radius as well as the size and position of the flux barriers and magnets). Thick ribs will severely reduce the electromagnetic performance of the IPM and it is therefore crucial to keep the ribs as thin as possible. While it is possible to include a stress constraint in IPM geometry optimization, it becomes cumbersome for multi-layer rotor topologies since the number of ribs significantly increases the size of the optimization problem. Therefore, it is common that ribs are simply kept constant in IPM optimizations. However, that neglects the dependency between the required rib thickness and the rotor geometry, which can cause the resulting geometry to differ from its true optima.

Here, the sizing of the ribs has been treated as a separate optimization problem, referred to as the mechanical sub-problem. In the mechanical sub-problem, the maximum stress in each rib is described based on the rotor variables (β, f_{d}, f_{PM},f_{air}, D_r) as well as the thickness of all individual ribs. The aim is to find a set of rib thicknesses, that minimizes the total rib thickness while meeting the stress constraint in all ribs. The set of required rib thicknesses will depend on the rotor variables as

$$\mathbf{t}^*_{\mathbf{rib}} = f(\beta, f_{\mathrm{d}}, f_{\mathrm{PM}}, f_{\mathrm{air}}, D_r) \tag{5.8}$$

where $\mathbf{t}^*_{\mathbf{rib}}$ is a vector containing the thickness of each rib and * denotes optimized values that meet the stress constraint with the lowest sum of rib thickness.

Once $\mathbf{t}^*_{\mathbf{rib}}(\beta, f_{\mathrm{d}}, f_{\mathrm{PM}}, f_{\mathrm{air}}, D_r)$ has been found, it can be used to set appropriate ribs in a larger IPM optimization covering both the rotor and the stator. This allows mechanical stress constraints to be indirectly included in a full IPM optimization without additional variables. However, pre-computing $\mathbf{t}^*_{\mathbf{rib}}(\beta, f_{\mathrm{d}}, f_{\mathrm{PM}}, f_{\mathrm{air}}, D_r)$ requires effort.

Here, $\mathbf{t}^*_{\mathbf{rib}}(\beta, f_{\mathrm{d}}, f_{\mathrm{PM}}, f_{\mathrm{air}}, D_r)$, has been approximated as a 5-dimensional look-up table that is used with interpolation to cover the entire variable space. Each entry in the look-up table is the result of minimizing the total rib thickness while keeping the von Mises stress below 330 MPa at the maximum operational speed of 15 000 rpm. The look-up table is made on a grid of:

- $\beta \in \{0, 0.1, 0.2, 0.3\}$
- $f_{\mathrm{d}} \in \{0.6, 0.75, 0.9\}$
- $f_{\mathrm{PM}} \in \{0.6, 0.75, 0.9\}$
- $f_{\mathrm{air}} \in \{0.1, 0.15, 0.2\}$
- $D_r \in \{147.2, 154.1, 161\}$ mm

The workflow for evaluating the mechanical stress, given a set of values for the rotor geometry variables and thickness of the ribs, is shown in Figure 5.7. The geometry is created, based on the inputs, in Ansys Maxwell and then exported to Ansys Mechanical where the mechanical stress (von Mises stress) was computed with static structural FEA. For simplicity, only forces related to the rotational motion have been included for the stress calculation. Since the stress evaluation is intended for sizing the ribs in the

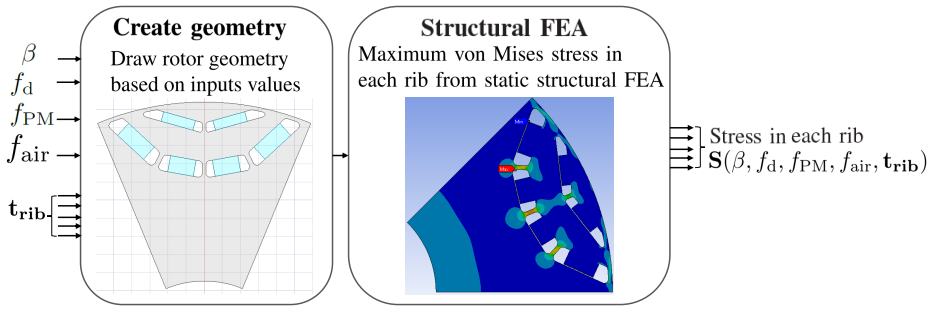

Figure 5.7 Evaluation of the stress in each rib, $\mathbf{S}(\beta, f_{\mathrm{d}}, f_{\mathrm{PM}}, f_{\mathrm{air}}, \mathbf{t_{rib}})$ based on geometrical inputs, for the U_4V-topology with a given D_r.

laminate, the PMs have been modelled in a simple and somewhat precautionary way, as additional weight on the outer edge of the barriers. The laminate material is modelled with a yield strength of 440 MPa, Young's modulus of 185 GPa, poisson's ratio of 0.3 and a mass density of 7600 kgm^{-3}.

The stress evaluation in Figure 5.7 is included in a larger workflow, shown in Figure 5.8, where the look-up-table of required rib thickness is created. The response surface approach in Ansys OptiSLang was used to describe the stress in the ribs as a function of the rib thickness ($\mathbf{t_{rib}}$) and the rotor geometry variables ($\beta, f_{\mathrm{d}}, f_{\mathrm{PM}}, f_{\mathrm{air}}$). The response surface was created separately for three different values of rotor diameter (D_r). Once the response surface has been created it allows optimizations to be done quickly. Here, the optimization has the objective to minimize the total rib thickness ($\sum_{i=1}^{N_{ribs}} t_{\mathrm{rib},i}$) with constraints of each rib having a stress below 330 MPa and a minimum rib thickness of 1 mm. This optimization is repeated for each combination of ($\beta, f_{\mathrm{d}}, f_{\mathrm{PM}}, f_{\mathrm{air}}$) in the defined grid. As a large number of optimizations are needed to fill the look-up table, the speed of the algorithm was important and therefore the NLQP-option in OptiSLang was used. The procedure is repeated for the three values of D_r and thus the look-up table of the required rib thickness is created.

Linear interpolation is used for the first four dimensions, while the last dimension (related to D_r) has a customized cubic interpolation. Based on (2.18), the stress in the ribs is excepted to change quadratically with the size of the rotor (when the entire rotor is scaled), which was also verified using in static structural FEA in Figure 5.9. The rib thickness can therefore be expected to change approximately cubically to keep the stress level unchanged while the rotor diameter changes. However, in case the rib thickness was set to the minimum value (1 mm) the cubic behaviour will be distorted, since there is some margin to the stress limit in that rib that can be reduced. Hence a customization is done as follows. For a given value of D_r, the rib thickness is computed for the closest higher and lower value of rotor diameter in the look-up table (linear interpolation is used in the other dimensions of the table). These two values are then weighted together based on their difference between their corresponding D_r values and the desired value of D_r. If the rib thickness corresponding to the lower rotor diameter is at 1 mm, its weight is set to 0. Once the weighted average has been computed, the minimum rib thickness condition is re-applied, resulting in the interpolated rib thickness.

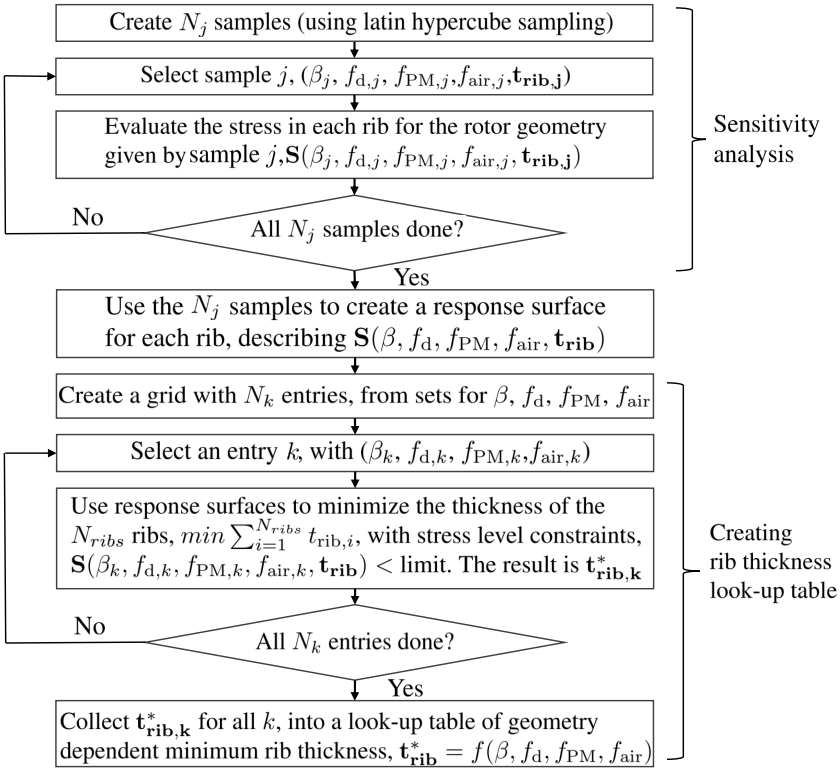

Figure 5.8 Workflow of the mechanical sub-problem, identifying the required rib thickness depending on the rotor geometry variables. This workflow was repeated for different D_r.

Ideally, the stress should be kept exactly at the specified limit (330 MPa) over the entire variable range (except when the minimum rib thickness of 1 mm is active). However, due to imperfections in the response surface, the stress will vary somewhat. Aiming to get a high-quality response surface, the sensitivity study was first done over a broader range in variable values from which the relevant variable ranges was found. A second sensitivity study was then done in the identified variable range. It was noted in the first round of sensitivity study that the outermost ribs (by the air-gap) were best kept at the minimum value of 1 mm, so these were not varied further in the second round of the sensitivity study. The sensitivity studies were done with 200 samples (using advanced latin hypercube sampling) and the CoP of the resulting response surface was 95% or higher for all ribs. To further enhance the quality of the look-up table, the actual stress is computed for each point in the specified grid. A linear correction of the rib thickness is done based on the stress, for points that deviate more than 15 MPa from the target stress level. Two rounds of correction were made before the quality of the look-up table was considered sufficient. Figure 5.10 shows the maximum stress for all points in the look-up table (D_r = 147.2 mm, 154.1 mm, 161.0 mm) as well as results using interpolated rib thickness for two other rotor diameters (D_r = 150.7 mm, 157.6 mm).

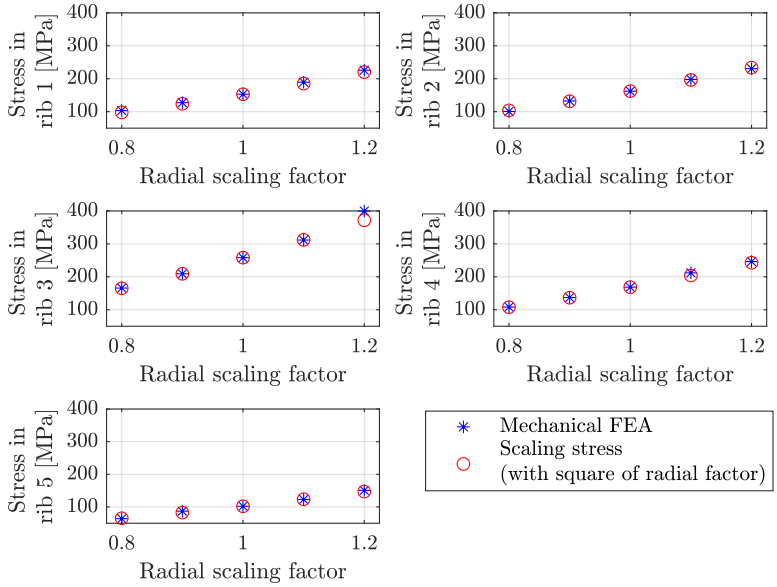

Figure 5.9 Mechanical stress in rib 1 (inner layer, on pole midline), rib 2 (outer layer, on pole midline), rib 3 (inner layer, off pole midline), rib 4 (inner layer, by the air-gap) and rib 5 (outer layer, by the air-gap), when scaling of the entire rotor geometry. Results from structural FEA show good agreement with scaling the stress with the square of the rotor scaling factor.

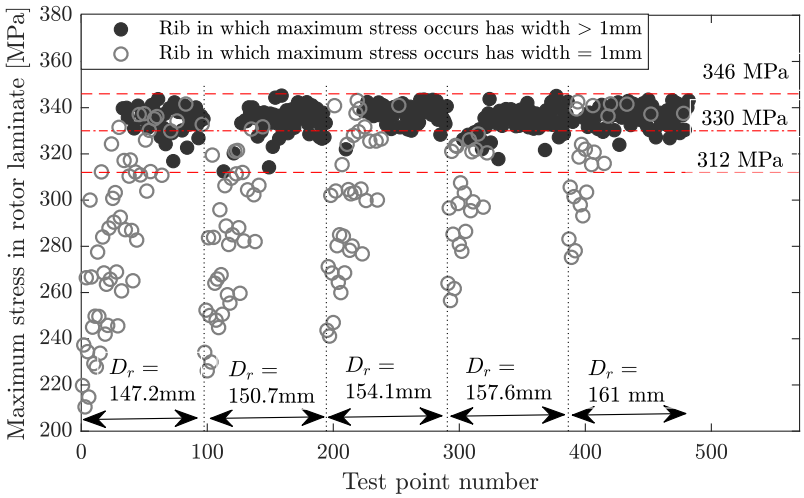

Figure 5.10 Mechanical stress evaluated with FEA using the look-up table of rib thickness over a grid of rotor geometry variables ($\beta \in [0, 0.1, 0.2, 0.3]$, $f_{\mathrm{d}} \in [0.6, 0.75, 0.9]$, $f_{\mathrm{PM}} \in [0.6, 0.75, 0.9]$, $f_{\mathrm{air}} \in [0.1, 0.15, 0.2]$) for rotor diameters $D_r \in [147.2, 150.7, 154.1, 157.6, 161.0]$ mm.

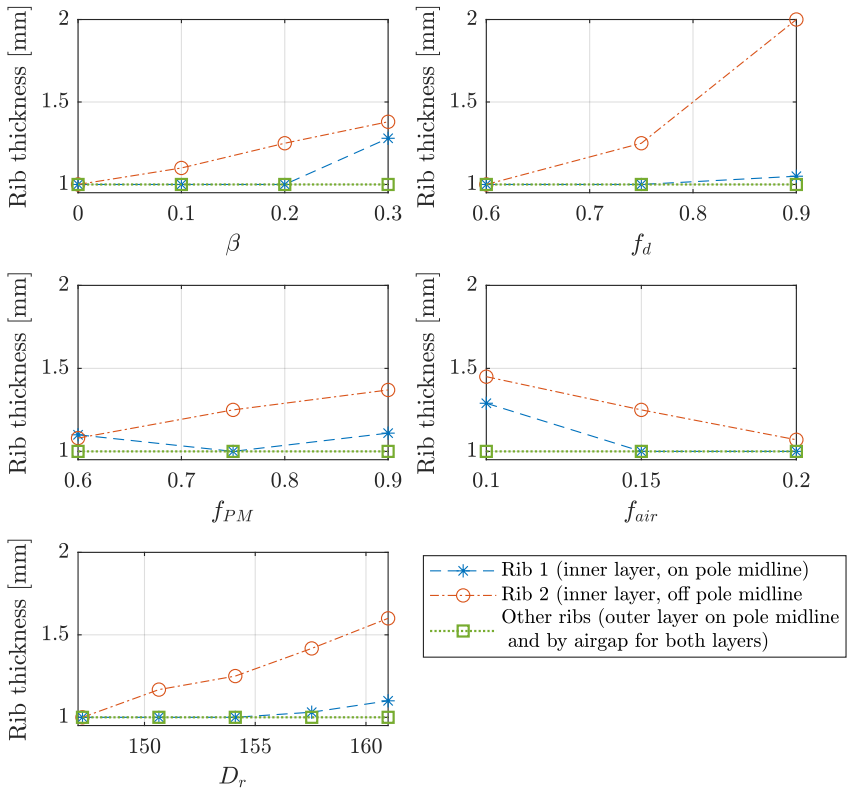

Figure 5.11 Required rib thickness using the look-up table, for variation in each rotor variable, starting from $\beta = 0.2$, $f_{\mathrm{d}} = 0.75$, $f_{\mathrm{PM}} = 0.75$, $f_{\mathrm{air}} = 0.15$ and $D_r = 154.1$ mm.

It can be seen that the look-up table keeps the stress within 312-346 MPa (about $\pm 5\%$ from the stress target), except when the stress drops due to the minimum rib thickness of 1 mm. The stress results for the interpolated values in Figure 5.10 can be seen to be similar to the non-interpolated cases, which indicates that the interpolation works sufficiently well.

Naturally, the entire look-up table is not easily illustrated, but some examples of the variation in rib thickness with rotor geometry is given in Figure 5.11. It shows the rib thickness in the look-up table for changes in one dimension (rotor geometry variable) at a time, from a starting point of ($\beta = 0.2$, $f_{\mathrm{d}} = 0.75$, $f_{\mathrm{PM}} = 0.75$, $f_{\mathrm{air}} = 0.15$ and $D_r = 154.1$ mm). It can be seen that the three innermost ribs (i.e. the ribs not facing the air-gap in the inner flux barrier layer) are adjusted to compensate for the changes in rotor geometry, while the other ribs are kept at the minimum limit of 1 mm (in this part of the look-up-table). The rib thickness variation with D_r has an approximately cubic shape distorts somewhat as the ribs approach 1 mm, in accordance with the interpolation approach used for that dimension. As indicated by Figure 5.11, rib 2 (located off the pole midline in the inner layer) is thicker than rib 1 (located on the pole midline in the inner layer) for most points in the look-up table. However, it is not so throughout the entire

look-up table. The relative size of the ribs change with the rotor geometry and for more mechanically demanding cases (high D_r, high f_{d} and low f_{air}) rib 1 is thicker than rib 2.

Finally, it should be highlighted that there is no guarantee that the values in the look-up table are optimal solutions to the mechanical sub-problem of dimensioning the ribs. It's rather the contrary, that some deviation should be expected due to the complexity of the problem and the simplifications made. Still, it is a structured method that serves the purpose of keeping the stress variations sufficiently small during rotor geometry variations. Further, the scattered points in Figure 5.10 does not show any clear repetitive patterns (except for the points where the minimum rib thickness of 1 mm is active). This indicates that the deviation from the target stress does not have a strong correlation with the rotor geometry variables $(\beta, f_{\mathrm{d}}, f_{\mathrm{PM}}, f_{\mathrm{air}}, D_r)$. This lack of correlation is a benefit when the look-up table is used to set mechanical constraints in optimization of the entire IPM geometry, since it avoids introducing incorrect geometrical dependencies in the optimization problem.

The 5-dimensional look-up table described here has only been created for the rotor topology referred to as $\mathrm{U_4V}$ (illustrated in Figure 5.8), which is the topology used in the optimization described in Chapters 9 - 10. However, reduced look-up tables covering only three dimensions $(\beta, f_{\mathrm{d}}, f_{\mathrm{PM}})$ have been made for four different double-layer rotor topologies. These reduced look-up tables are used in Chapter 7.

5.3 Geometry dependent end-winding temperature

For IPMs used for BEV propulsion, the occurrences of high power are related to the acceleration/deceleration of the vehicle and therefore have a fairly short time duration. According to [29], where several commercial drive cycles as well as logged real world driving are included, most acceleration events last less than 6 seconds. Therefore, the IPMs in BEVs do not need to sustain peak operation continuously but the machine needs to manage peak operation for shorter time periods without overheating.

Typically, the end winding temperature is the thermal limitation during peak operation at lower speeds. At higher speeds, the limitation is usually the PM temperature. The PM temperature is more challenging to capture with a simple model and can also be handled by segmentation of the PMs, to reduce the losses in the PMs (for example shown in [65]). Therefore, the optimization constraint has been aimed solely at end winding temperature.

The thermal modelling of the IPM has been done using an LPN, which is commonly done when high simulation speed is essential. Here, emphasis has been put on simplicity of the model and the intended use of the LPN is only to approximate the temperature rise in the end winding during strong accelerations that last for a short period of time. A simple option is to put a constraint on current density. However, that would not capture the dependency between the machine design and thermal characteristics, such as the thermal buffering capacity of the stator laminations and winding. Therefore, a simplistic LPN is used to create a geometry dependent thermal constraint concerning the end-winding for use in IPM optimization. This LPN, modelling the end-winding temperature (T_{ew}), is therefore referred to as the end-winding-LPN.

Table 5.1 Material properties used in the end-winding-LPN

Material	Density $[kg/m^3]$	Thermal conductivity $[W/mK]$	Specific heat capacity $[J/kgK]$
Core lamination	7600	31	557
Winding (copper)	8933	401	385
Slot impregnation	1350	0.2	1700
Frame (Aluminium)	2790	168	883
Air	0.9458	0.03095	-

The end-winding-LPN is shown in Figure 5.12. The thermal capacitances, thermal resistances and power losses (i.e. heat sources) are denoted with C_{th}, R_{th} and P respectively. Additionally, the node is indicated with subscripts, where $_{aw}$, $_{ew}$, $_{yo}$, $_{to}$, $_{toti}$ and $_{fr}$ correspond to the nodes for the active-winding, end-winding, stator yoke, stator teeth, stator tooth tips and frame respectively.

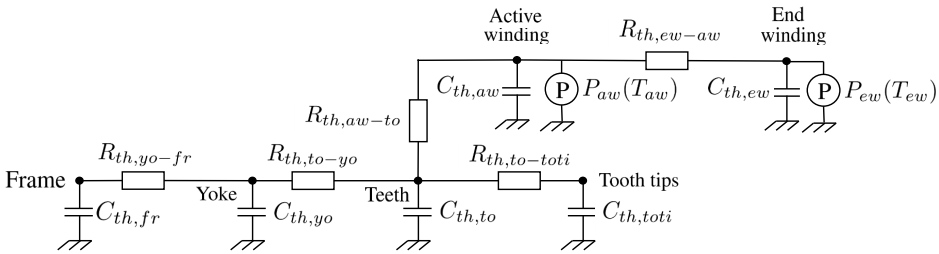

Figure 5.12 End-winding LPN used to model the end-winding temperature during maximum current operation for short periods of time.

The material properties used for the end-winding-LPN are shown in Table 5.1. The material properties are set as in [29], with a slight modification of the mass density of the lamination to match NO30-1600 in [60]. The LPN considers the material properties constant, at values corresponding to 100°C. The geometrical parameters (distances, areas and volumes) needed for the calculation of the thermal resistances and capacitances are simply exported from the geometry used for the FEA calculations (using Ansys Maxwell). The power loss in the active- and the end-winding are included, with a temperature dependent resistance. However, for simplicity, the core losses are neglected in the end-winding-LPN. Following [29], the frame has been modelled as a hollow cylinder with a thickness of 11 mm and a contact air-void of 10 μm is assumed in the contact between the stator yoke and the frame as well as between the stator teeth and the active winding material. The active winding is modelled as a mix of copper and impregnation material, referred to as the winding mix, as was done in [29]. For further description see Appendix B.

The end-winding-LPN was implemented in Matlab Simscape, which offers the flexibility to easily add/remove nodes or to integrate the end-winding-LPN into a larger LPN.

The end-winding-LPN includes strong simplifications and it is important to highlight that it is very limited in terms of the scenarios for which it can be used with sufficient

accuracy. The end-winding-LPN was created based on comparisons with a more detailed LPN described further in Appendix B. In short, the LPN-modelling here was done following [29], with minor modifications to allow two layers of flux barriers and also using separate nodes for the stator tooth and the stator tooth tip. The detailed LPN was then simplified as far as possible while limiting the deviation in end-winding temperature during the first 20 seconds for peak torque operation, simulated as a load step. A comparison of the detailed LPN and the end-winding-LPN, for the intial IPM at 4000 rpm and a current of 400 A, is shown in Figure 5.13. Both LPNs start from 70°C in all active parts of the IPM and the detailed LPN has a cooling jacket in the stator housing (also referred to as the stator frame) with coolant (at 50°C) pumped at 10 litres/min. The steady state temperatures in Figure 5.13 are very high. However, this is expected, since the IPM here is designed to operate very shortly at peak torque. Most importantly, the comparison between the detailed LPN and the end-winding-LPN in the bottom plot of Figure 5.13 shows that the difference in end-winding temperature is small (around 3°C) after 20 seconds of operation.

It would be possible to include a more detailed LPN in the optimization workflow, while still keeping the computational time manageable. Still the end-winding-LPN in Figure 5.12 was settled upon both for its simplicity and robustness. There are significant uncertainties when it comes to heat transfer coefficients and empirical expressions for convection to air that are necessary in more detailed LPNs. Such uncertainties are not relevant for the end-winding-LPN, since it only includes the temperature dependent resistive losses and thermal buffering capacity of the stator laminate and winding. Thus, the thermal constraint is put on a very basic level, estimating if the temperature rise due to resistive losses at peak torque operation can be limited sufficiently by the stator material itself.

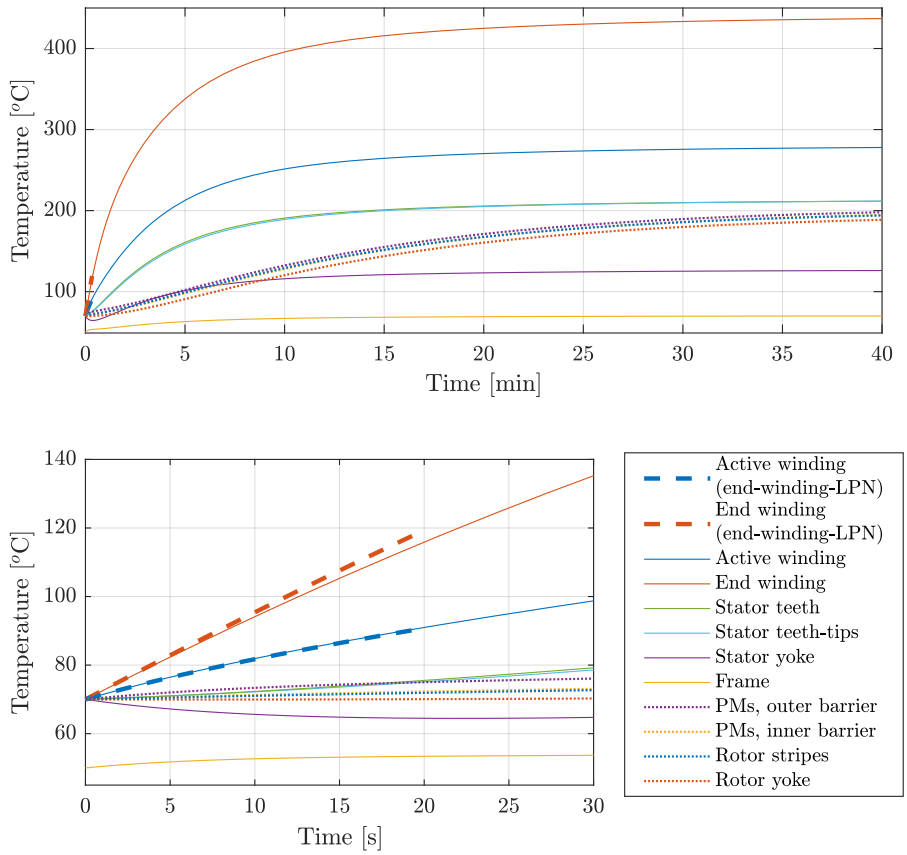

Figure 5.13 Load step to peak torque operation at base speed, starting from thermal equilibrium at 70°C, for an example IPM over a longer period of time (top plot) and zoomed into the first 30 s (bottom plot). Winding temperatures from both the detailed LPN and the simple end-winding-LPN are included.

Chapter 6

Investigations on an initial IPM design

Before moving on to comparisons of different IPM geometries in terms of peak performance and losses in drive cycles, which is the central topic for the work as a whole, a number of investigations are done on an initial IPM deign. These investigations have, in different ways, enabled the geometry optimization that follows in Chapters 9 - 10. First, the mesh- and time resolution in the FEA was investigated in relation to the numerical accuracy of the core losses, as presented further in Section 6.1. This allowed an efficient compromise between numerical accuracy and computational time to be made for the following investigations in this work. Thereafter, the flexibility offered within a given IPM geometry was investigated. Different FW performance can be obtained from the same IPM geometry depending on the current rating and, when combined with changing the size of the IPM through scaling of the FEA results, the same set of peak requirements can be met in different ways, as shown in Section 6.2. The approach of scaling each given IPM geometry to comply with the peak performance requirements is an important feature of the optimization in Chapters 9 - 10.

The initial IPM design serving as the example in this chapter is shown in Figure 6.1 and its key parameters are given in Table 6.1.

Table 6.1 Key parameters of the initial IPM

Maximum speed	12 000 rpm
DC voltage	350 V
Maximum current	different values investigated
Number of poles	8
Number of slots	48
Stator outer diameter	210 mm
Rotor outer diameter	139.5 mm
Air-gap width	0.8 mm
Stack length	135 mm

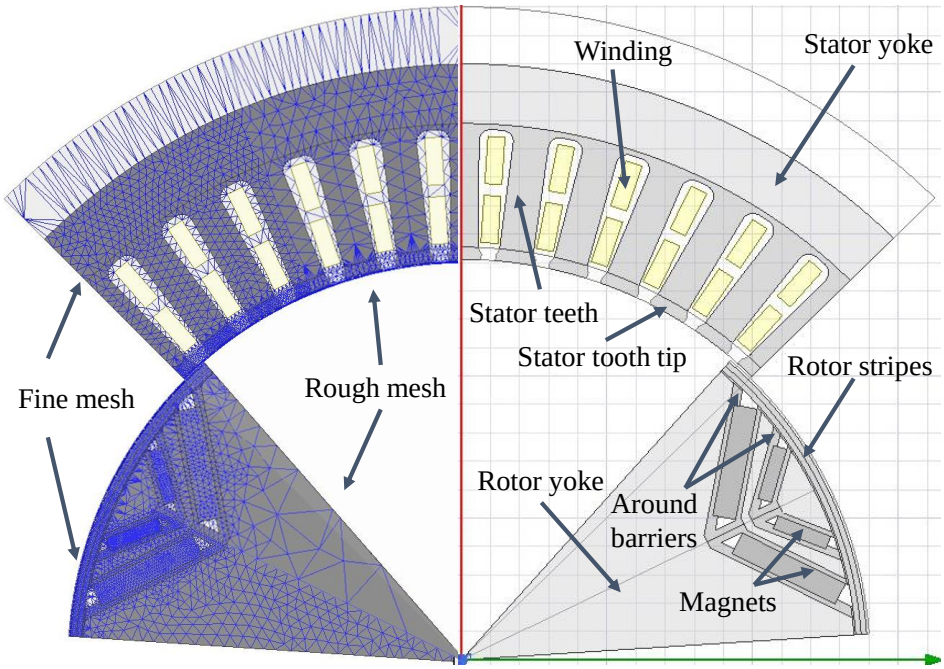

Fig. 6.1 Geometry cross section of the initial IPM, showing the geometrical parts (right half) and the fine and rough mesh (left half).

6.1 Mesh and time resolution in the FEA

The results presented here are extracted from Paper I and Paper II, and further details are given in the appended papers.

Using electromagnetic FEA in an optimization is computationally heavy, and even more so if the FEA needs to be run many times per function evaluation (as is the case in the optimization of the IPM geometry towards an entire driving energy distribution, in Chapter 9). This raises the need for careful selection of the mesh and time resolution in the FEA, to keep the computational load manageable while still keeping the numerical accuracy of the results high enough. The main focus here has been on the convergence of the core losses. This was both due to the importance of core losses during operation and also because the core losses were found to be particularly sensitive to mesh- and time resolution.

Two operating points have been considered for the investigations of mesh- and time resolution. The operating points are taken from the operation boundary of the initial IPM with a current rating of 500 A (RMS). As illustrated in Figure 6.2, the operating points P1 and P2 correspond to peak torque at base speed and available torque at top speed respectively.

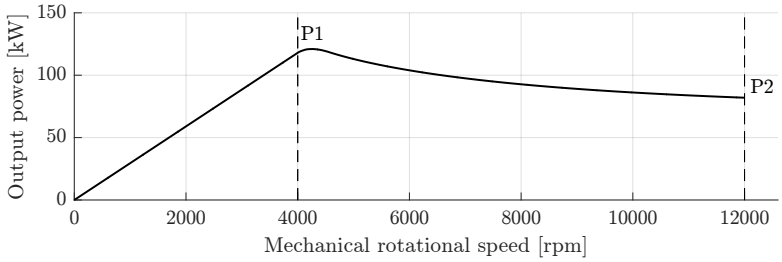

Figure 6.2 Power capability curve of the initial IPM (with a current rating of 500 A), with operating points P1 and P2 indicated.

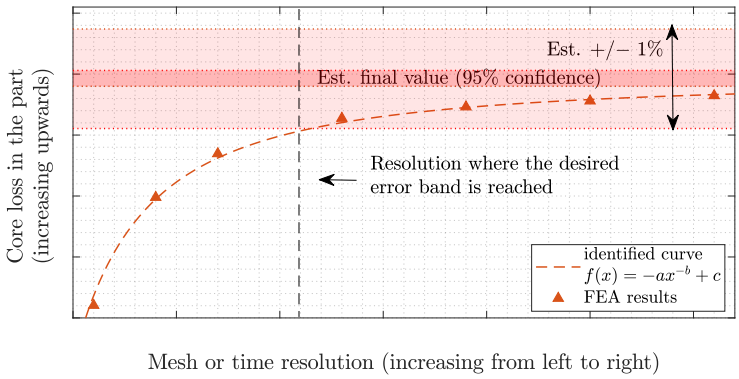

Figure 6.3 Convergence curve, with 95% confidence band and selected 1% error band.

In principle, the numerical accuracy of an electromagnetic FEA increases until the mesh elements and time steps are infinitesimal, which is naturally not realizable in practice. Instead, both the investigation of mesh and time step resolution here are based on estimating a convergence curve for the core losses, in order to estimate the fully converged core loss value which is then used to estimate the core loss error. This approach has previously been used by [27] and has been developed further here by including confidence bands on the coefficient of the convergence curve. Further, the approach has been applied to both time resolution and mesh resolution in different regions of an IPM geometry. Once the convergence curve has been identified, it allows the machine designer to select time and mesh settings to reach a quantified level of convergence in the core losses.

An example of a convergence curve with error bands are given in Figure 6.3. The convergence curve is given by the expression

$$f(x) = -ax^{-b} + c \tag{6.1}$$

where x is the mesh density or time steps per electric period for the mesh and time resolution investigation respectively. The values of coefficients a, b and c, with 95% confidence bands, are found using the Matlab Curve Fitting Tool (Mathworks) for results

from FEA with different values of x. The theoretical value at full convergence is c, for which the identified 95% confidence band is referred to as $[c_{low}, c_{high}]$. The 1% error band consists of the values that are at least 99% of c_{high} and simultaneously not more than 101% of c_{low}, i.e. the values that are within 1% of the entire confidence band of c.

Here, the convergence of the core losses has been investigated as a function of mesh density and time resolution in two separate studies. While it would be an improvement to investigate both mesh and time resolution aspects simultaneously, this was deemed overly complex. For the investigation of mesh density dependency of core losses, the time resolution was kept at 120 steps per electric period. The investigation of time resolution dependency of core losses was then done for two different versions of mesh settings, corresponding to a rough and fine mesh from the mesh investigation.

6.1.1 Sensitivity of core losses to mesh density

The mesh density has been controlled for the different geometrical parts defined in Figure 6.1, meaning that the mesh resolution is controlled by six variables. However, there is an interdependence between the parts, where the mesh density in one part will affect the overall magnetic field solution and, subsequently, the core loss in another part. The interdependence makes it more challenging to set up the convergence analysis. Initially, an approach that neglected interdependence was tested but it was found to result in premature convergence of the core losses and underestimation of the fully converged core loss value in all parts of the geometry. Therefore, an approach that captures interdependence, referred to as the "iterative approach", was developed which is the approach described in this section. Still, the approach that neglects interdependence is considerably easier for the user to implement and the underestimation of the fully converged core losses was not too severe (about 1% compared to the iterative method). A description and a comparison of both approaches are presented in the appended Paper I.

The iterative approach involves several iterations in which the mesh density in all parts increase simultaneously, with a specific distribution of the mesh elements among the parts. The first iterations sets the same mesh density in all parts (i.e. the distribution of mesh elements is based on the area of the different parts). A convergence curve is then fitted to the FEA results for core loss in each part. The convergence curve is then used to find the mesh density at which the core loss in the part reaches within 1% of its fully converged value (with 95% confidence). The resulting mesh densities for all the included parts will give a new distribution of the mesh elements among the parts, which will be the distribution used for the next iteration. This procedure is then repeated until the change in mesh distribution from one iteration to the next is considered small enough. The challenging part, which requires some pre-knowledge from the user, is controlling the mesh to maintain the desired distribution of mesh elements among the parts while the total number of mesh elements increase.

The simultaneous convergence of core loss in all included parts is shown in Figure 6.4. For brevity, only the results for P2 are shown here, but the results for P1 have similar appearance. The aim is to reach a synchronized convergence, where all parts reach their respective error bands simultaneously. Figure 6.4 shows how the convergence synchronization improves with each iteration, until it was considered sufficient at the third iteration. The convergence curve for the core losses in each part are shown in Figure 6.5.

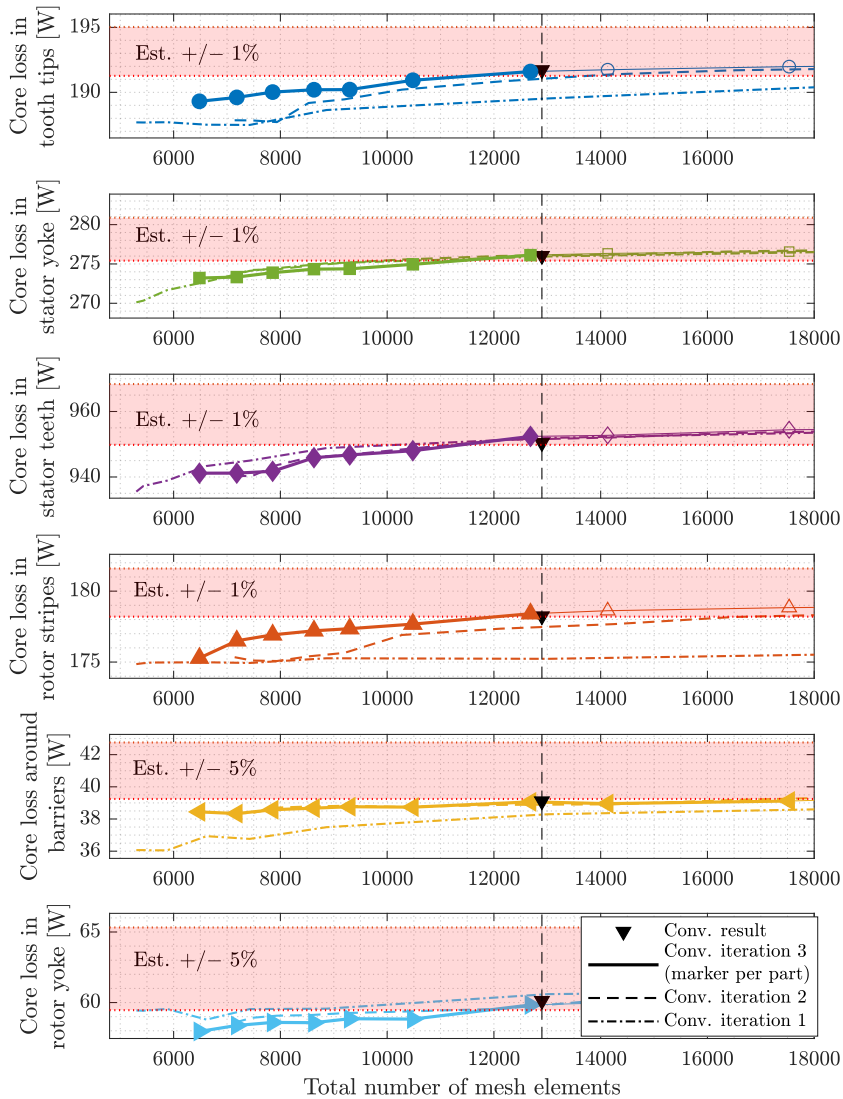

Figure 6.4 Overall core loss convergence, using the iterative approach, for operating point P2. Filled markers indicate values until the error band is reached.

It should be noted that the curve fitting is based on a wider range of mesh densities than what is covered in Figure 6.4 - 6.5. Further, the target here has been to reach within 1% of the fully converged core loss value, regardless of where in the estimated confidence band it may lie. While this is possible for most parts, there are some parts where the difference between the upper and lower value of the confidence band itself is more than 1%. In such cases, the quality of the estimated curve is not high enough to allow such a low error with 95% confidence and higher error margins need be accepted. Therefore 5% error bands are used for the rotor yoke and the part around the flux barriers.

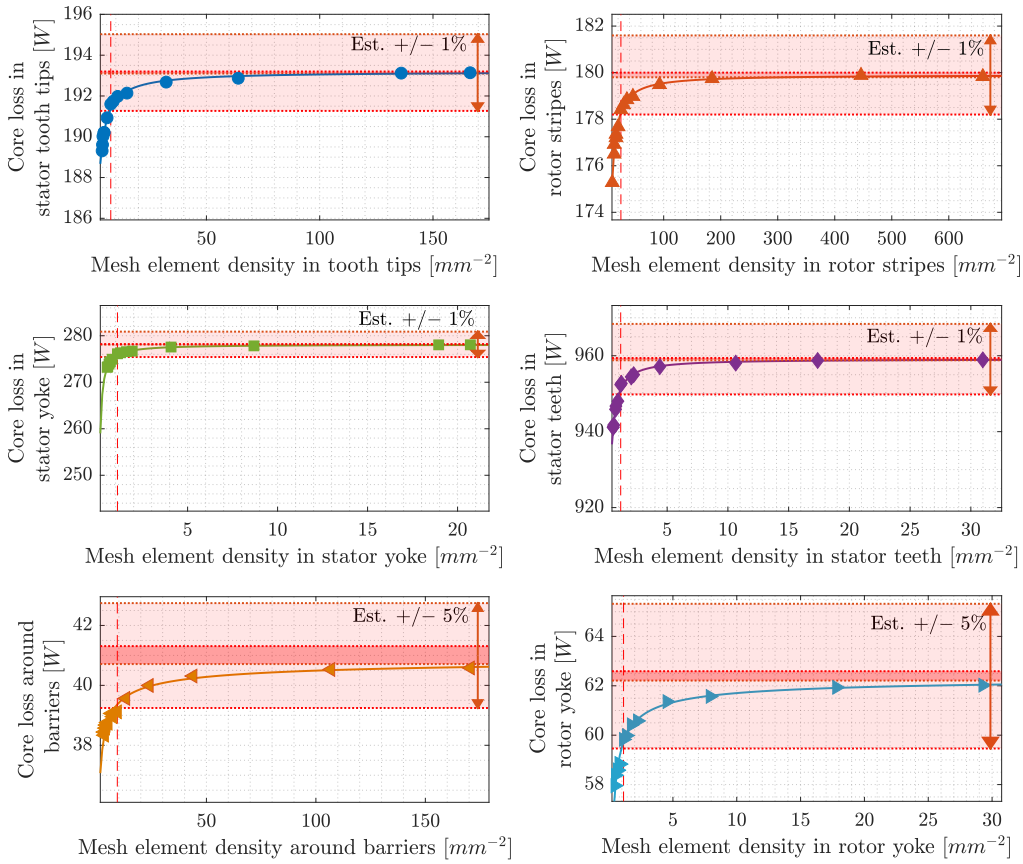

Figure 6.5 Core loss convergence, per IPM part, for operating point P2. The estimated final values, with 95% confidence bands, are shown (thin red band) together with their respective error bands (thick red band, with arrows). Vertical lines indicate where the curve enters its respective error band.

The convergence analysis has been done for both operating points, P1 and P2, and the final set of mesh settings are then chosen as the finest of the mesh densities needed to reach the desired error band, in either P1 or P2. Overall, the mesh settings for the stator parts were driven by the results in P1, while P2 was driving the settings in the rotor parts. The final mesh settings and their associated estimated core loss errors are presented in Table 6.2. The error estimates here are somewhat precautionary, using the desired error band from the convergence analysis as the level of underestimation of the core losses. The other side of the error band is set to 0, considering that the convergence analysis here was done on demanding operating points, on the border of the operating region, while the core losses in other operating points might converge faster. Table 6.2 cover three different mesh versions, referred to as the fine, medium and rough mesh. These different sets of mesh settings have been found by using the identified core loss convergence curve with

Table 6.2 Mesh densities and estimated core loss error bands, per IPM part, for the fine, medium and rough mesh

Part	Fine mesh		Medium mesh		Rough mesh	
	Mesh density [mm^{-2}]	Est. core loss error [%]	Mesh density [mm^{-2}]	Est. core loss error [%]	Mesh density [mm^{-2}]	Est. core loss error [%]
Stator tooth tips	14.2	[-1, 0]	6.3	[-2, 0]	4.9	[-3, 0]
Rotor stripes	22.3	[-1, 0]	13.2	[-2, 0]	9.8	[-3, 0]
Stator yoke	1.0	[-1, 0]	0.5	[-2, 0]	0.4	[-3, 0]
Stator teeth	1.2	[-1, 0]	0.8	[-2, 0]	0.6	[-3, 0]
Around barriers	11.9	[-5, 0]	5.4	[-6.3, 0]	4.0	[-7.5, 0]
Rotor yoke	1.1	[-5, 0]	0.7	[-6.3, 0]	0.5	[-7.5, 0]
Air-gap	32.8	-	32.8	-	32.8	-

Table 6.3 Trade-off between computational load and core loss convergence, for the fine, medium and rough mesh

Mesh	Number of mesh elements	Simulation time* [min]	Estimated error in total core loss [%]
Fine	15 500	14.5	[1.2, 0]
Medium	9 200	10.0	[2.3, 0]
Rough	7 200	8.6	[3.3, 0]

* Non-parallel simulation covering two electrical periods with 120 time steps/period (and saving of the field solution), on a PC with 3.2 GHz processor and 64 GB RAM.

different error bands and they offer different compromises between core loss convergence level and computational time, as summarized in Table 6.3. Here, the core losses and error bands for each part in the IPM have been combined to an estimated error for the total core loss. The fine mesh consists of 15 500 mesh elements (modelling an angular segment of the IPM covering one pole) and has an estimated total core loss error of 1.2 %. Reducing the number of mesh elements to 7 200, as in the rough mesh, gives an estimated error of 3.3% but also nearly cuts the FEA simulation time in half.

6.1.2 Sensitivity of core losses to time resolution

The investigation of core loss convergence with time resolution has been done for the same operating points, P1 and P2, that were used for the mesh analysis. Further, the influence of time resolution has been analysed for both the fine and the rough mesh, presented in the previous section. The investigated range of time resolutions are 6-360 steps per electric period. However, considering that the IPM here has six slots per pole, going below 24 steps per electric period violates the Nyquist criteria for the first space harmonic caused by the stator slots. Below 24 steps per electric period, both the core losses in the rotor parts and the torque ripple falls to almost 0. The impact on time resolution on the average torque and torque ripple for P1 is shown in Figure 6.6, which shows the issue at very low time resolutions. Figure 6.6 also shows that the average torque converges relatively quickly and remains virtually unchanged after 60 steps per electric period. The torque ripple converges slower and reaches a good level of convergence around 120-180 steps per electric period.

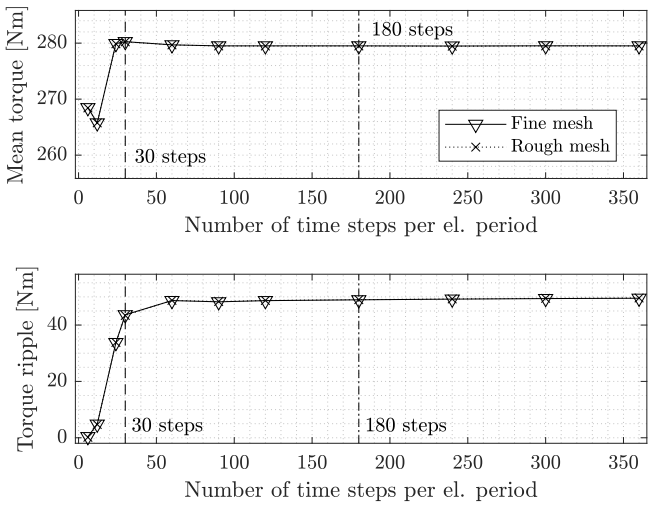

Figure 6.6 Average torque (top) and torque ripple (bottom) for different time resolutions, for P1.

Due to the issues at very low time resolution, the core losses are investigated for 30-360 steps per electric period. The core loss convergence in each IPM part, for P2, are shown in Figure 6.7. The core losses in the rotor parts show a notably slower convergence compared to the stator parts. Reaching a 1% error band for the rotor parts would require a very fine time resolution, which is associated with increased simulation time. Instead, larger estimated errors, up to 5% is accepted for the rotor parts while a 1% error band is used for the stator parts. A time resolution of 180 steps per electric period is considered as a good compromise between computational load and the level of core loss convergence in the different parts of the IPM. Comparing the core loss convergence for the fine and rough mesh, in Figure 6.7, it is found that the lower mesh resolution gives lower core losses in general, but the time dependent characteristics is very similar to those at finer mesh resolution.

Finally, the possibility of reducing the number of time steps in the first of the two simulated periods was investigated. It was found that using 60 steps in the first period and 180 steps in the second period (240 steps in total) reduced the simulation time with 30% without any significant impact on the core losses in the second period, compared to using 180 steps in each of the periods (360 steps in total). Further description of using different time resolutions in the first versus second electric period is included in the appended Paper II. However, within this work the more straightforward approach of using the same time resolution in both periods has been used.

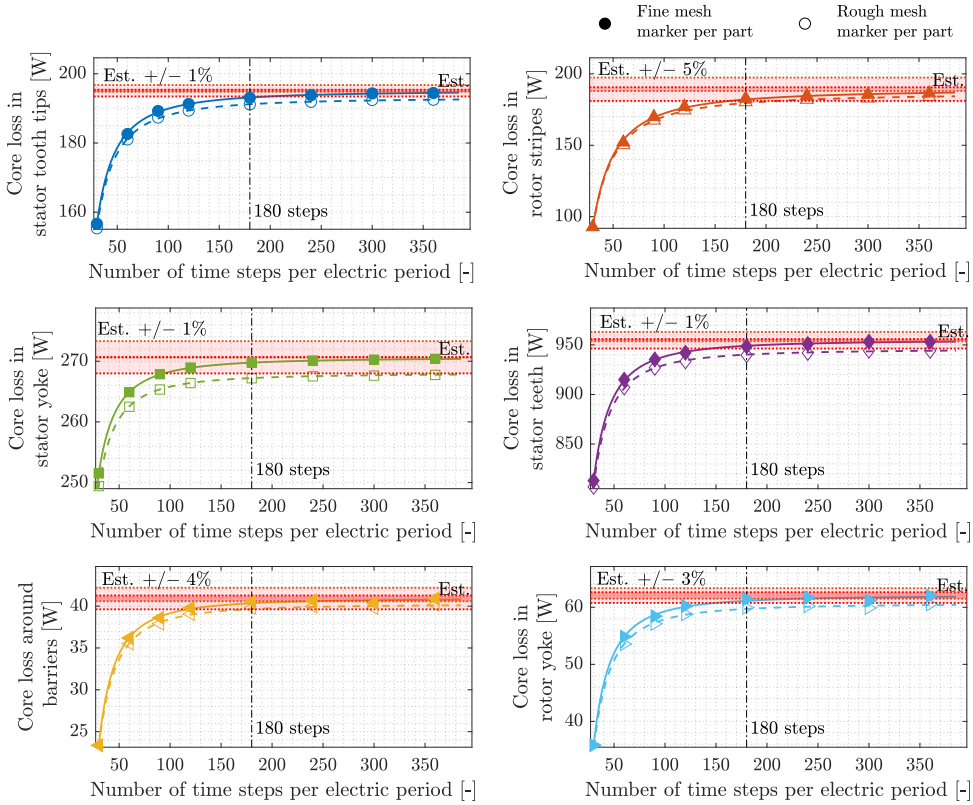

Figure 6.7 Core loss in P2, per IPM part, as a function of time resolution, with the fine mesh and rough mesh. The estimated fully converged value, with 95% confidence band, is shown (thin red band) with the corresponding error band (thick red band). The chosen error band varies among the parts.

6.1.3 Purpose dependent mesh and time resolution settings

The quantification of convergence of core losses, torque and torque ripple depending on mesh and time resolution in the FEA presented in above offer the flexibility to select different trade-off's between numerical accuracy and computational load depending on the type of investigation at hand. Such flexibility has been an important enabler for the results that are presented in Chapter 7 and, especially, in Chapter 10.

The selection of mesh and time resolution was based both on the importance of reducing simulation time and how sensitive the output quantities of interest are to the mesh and time resolution. For example, optimization of the IPM geometry involves a large number of simulations which makes it necessary to reduce the mesh and time resolution as far as possible. Contrastingly, when comparing a few selected IPMs, the mesh and time resolution can be increased for better numerical accuracy in the comparison. Further, the average torque from the FEA converges relatively fast so if that is the main quantity of

interest, a relatively low mesh and time resolution is sufficient. Core losses, on the other hand, converge slower and thus a higher mesh and time resolution is called for when core losses play a major role in the outcome.

Within this work, the investigations involving core losses has been done with the medium mesh settings (for optimizations) and the fine mesh settings (for detailed comparisons) and the investigations that do not cover core losses have been done with the rough mesh settings (for optimizations) and the medium mesh settings (for detailed comparisons). As the coming investigations in Chapter 7 and Chapter 10 include changes in the IPM geometry, it will inevitably alter the mesh. It should be noted that the mesh density has not been kept constant during geometry variations. Instead, the length of the mesh elements has been adjusted based on the size of the different geometrical parts in the IPM. For example, the length of the mesh elements in the stator teeth scale with the tooth width and the length of mesh elements in the stator yoke scale with the thickness of the yoke (in radial direction). This is done considering that thinner stator teeth are likely associated with stronger magnetic saturation which could require a higher mesh density. However, it should be noted that a deeper evaluation of the adopted approach for adjusting mesh settings for different geometries has been considered out of scope for this work. Further, the time resolution (in detailed comparisons) is set to 180 steps/electric period for the IPMs with 48 slots and 270 steps/electric period for the IPMs with 72 slots. Thus, the time resolution has been scaled based on the frequency of the slot harmonics.

6.2 Impact of saturation and current rating on field-weakening performance

The results presented here are extracted from Paper III, and further details are given in the appended paper.

This section presents an analysis of the FW performance of the initial IPM design, shown in Figure 6.1, for a range of current ratings. The fine mesh presented in the previous section is used with a time resolution of 180 steps per electric period. In short, the FW performance of an IPM can be explained as its capability to maintain the power output, with a limited voltage, when the rotational speed increases. Considering the shape of the required power versus speed from Chapter 3, where the curve is quite flat over a wide speed range and the highest power lies at a high speed, it is clear that high FW-performance will be important for this application.

6.2.1 Interpretation of FEA results in the IPM parameter plane

FW performance is a characteristic of the IPM that depends on the balancing between the flux linkage of the PMs, the inductances and the rated current. Here, the FW performance has been analysed using a normalized dq-model referred to as Model A, which is adopted from [33] - [34] and described in Section 2.2. Model A is a lossless linear model that uses $\Psi_{m,n}$, $L_{d,n}$, $L_{q,n}$ as constant circuit parameters. The normalized speed, ω_n, is a ratio of the base speed (i.e. the speed at which the voltage limit is reached at peak torque operation). The normalized power, $P_{e,n}$, is the IPM output power as a ratio of the rated converter power. In particular, the inverter utilization, κ, is given as $\kappa = P_{e,n}|_{\omega_n=1}$.

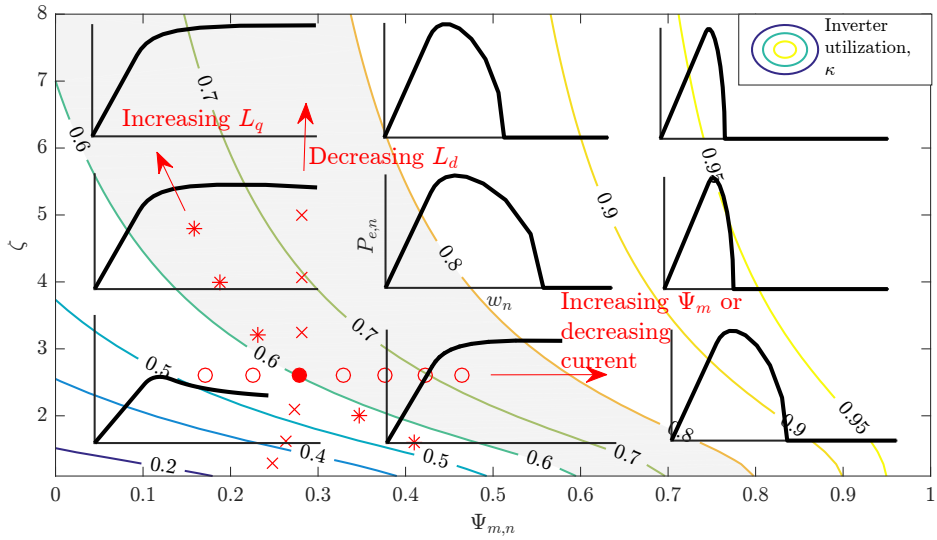

Figure 6.8 The IPM parameter plane, using Model A, spanned by saliency, ζ, and normalized magnet flux linkage, $\Psi_{m,n}$. Optimal FW performance lies along an inverter utilization, κ, of 0.7 (middle of the shaded area). Power curve shapes are shown for $\Psi_{m,n} = 0.2, 0.5, 0.8$ and $\zeta = 3, 5, 7$. Trajectories for changing circuit parameters (Ψ_m, L_d, L_q) are marked (circles, crosses and stars respectively), from an example initial point (filled red circle).

The FW performance is then quantified using CPSR, which is the value of ω_n where the normalized power drops to a lower value than κ. As shown in [33], the theoretically highest FW performance of an IPM is $\kappa = 0.7$ and infinite CPSR (where $P_{e,n} \to 1$ as $\omega_n \to \infty$). This occurs if $\Psi_{m,n} = L_{d,n}$ (i.e. $\Psi_m = L_d I_0$), i.e. with the infinite speed point located on the current limit circle.

The IPM parameter plane, introduced by [33], is a powerful graphical tool for analysing FW performance in IPMs. The plane is spanned by $\zeta = L_q/L_d$ and $\Psi_{m,n}$ and the shape of the power curve (i.e. the CPSR) of a given IPM is entirely dependent on its position of this plane. Figure 6.8 shows the IPM parameter plane, with examples of the power curve shapes for nine selected points in the plane. Trajectories for how the position in the IPM parameter plane is affected by changes in the circuit parameters Ψ_m, L_d, L_q (non-normalized) are shown, from an example starting point in the plane.

While the IPM parameter plane can be a great aid in understanding the FW performance and how it is affected by the IPM design, the use of the IPM parameter plane is also associated with the limitations of Model A. As a lossless linear mode, Model A neglects winding resistance, iron losses and magnetic saturation effects. As shown in [66], the impact of neglecting winding resistance and iron loss is relatively minor, but the FW performance is heavily dependent on magnetic saturation effects. This is an issue, in particular for BEV applications where a high FW performance is desired while the IPM is also, typically, pushed relatively far into magnetic saturation. Electromagnetic FEA is commonly used to account for magnetic saturation in IPMs, and therefore it would be a benefit to be able to interpret such results using the IPM parameter plane.

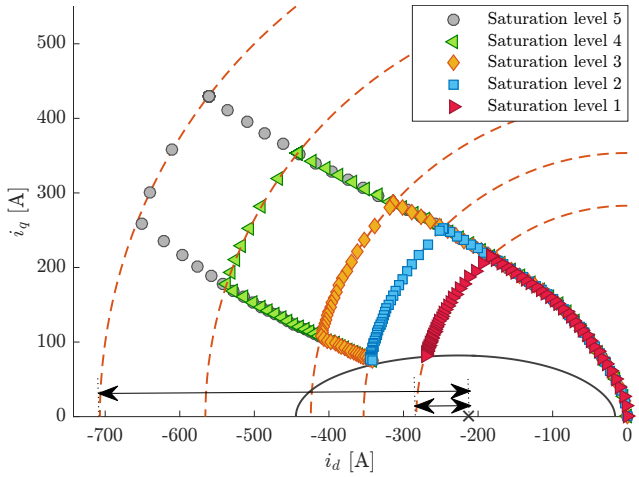

Figure 6.9 Operating boundary and MTPA trajectory, using Model B, in the dq-current plane. Traces are given for saturation levels 1-5, corresponding to increasing maximum stator current. Current limits are indicated (red dashed circles) along with voltage limit at maximum speed (black ellipse) and the infinite speed point inside (black cross).

A model that includes magnetic saturation of the circuit parameters is Model B, described in Section 2.2, where FEA is used to compute $\Psi_m(i_q)$, $L_d(i_d, i_q)$ and $L_q(i_d, i_q)$. Model B has been used for the initial IPM with five optional settings for the rated stator current. These current values are 200 A, 250 A, 300 A, 400 A and 500 A, referred to as saturation level 1-5 respectively (reflecting the severity of the magnetic saturation at peak torque operation). The resulting operation boundary, for each of the five saturation levels, are shown both as traces in the dq-current plane in Figure 6.9 and as power curves in Figure 6.10. Note that the difference between the power curves reduces as the speed increases. This occurs as the higher saturation levels come far into Mode III, in which the maximum current can no longer be utilized, and eventually end up at the same dq-current values as the lower saturation levels. There is a clear difference between the FW performance among the saturation levels, both due to the difference in overall balance between Ψ_m and $L_d I_0$ and due to the difference in severity of the magnetic saturation effects.

The results of Model B are further interpreted using Model A. This is done by representing each point along the operating boundary of Model B with a constant circuit parameter set, which in turn corresponds to a normalized Model A result. In other words, the circuit parameters, Ψ_m, L_d and L_q, for a given operating point on the operating boundary (i.e. a given i_d, i_q combination) are normalized into $\Psi_{m,n}$, $L_{d,n}$ and $L_{q,n}$. Doing so for all points along the operation boundary creates a series of parameter sets, where the first set in the series consists of circuit parameters for peak torque operation, i.e. the MTPA peak point, and the last set in the series consists of parameters from top speed operation (at 12 000 rpm). Thus, a single FEA result, where circuit parameters vary due to saturation, is here represented as a series of normalized results based on constant circuit parameter sets. This allows the results to be interpreted in the IPM parameter plane as shown in Figure 6.11.

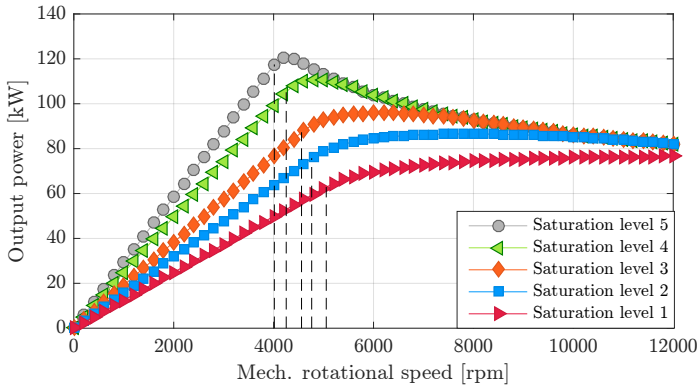

Figure 6.10 Operating boundary, as maximum output power versus speed, from Model B. Five saturation levels, corresponding to increasing maximum stator current, are included along with the base speeds (dashed lines).

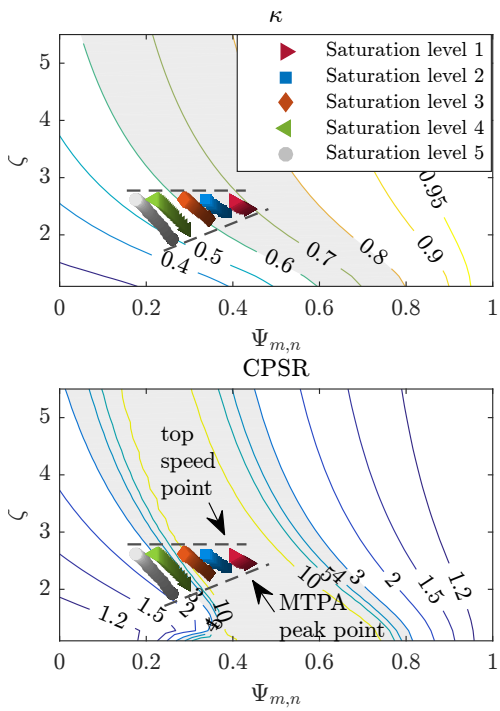

Figure 6.11 IPM parameter plane, with representation of an IPM, using Model A based on FEA results for saliency (ζ) and normalized magnet flux linkage ($\Psi_{m,n}$) along the operation boundary from Model B. Traces, ranging from MTPA peak point at base speed, to operation at mechanical top speed, are given for five saturation levels in the same machine geometry. The shaded areas are considered desirable areas of κ and CPSR.

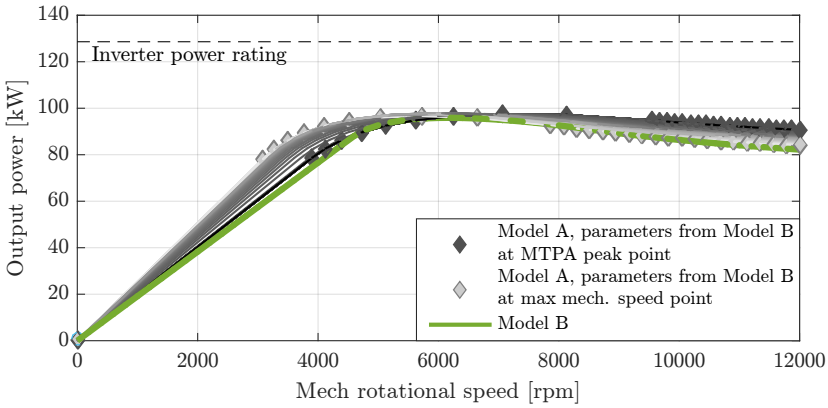

Figure 6.12 Peak power curve using Model B, for saturation level 3, (dashed green curve) and how it compares to the set of Model A solutions (grey curves) taken along the Model B power curve. Constant circuit parameter combinations from higher speeds have a lighter shade. As the speed increases the Model B power curve shifts from matching the low speed parameter lines to matching the high speed parameter lines.

Figure 6.11 shows both an overall drift in position toward the right (i.e. towards higher CPSR and κ) with lower saturation level, which is due to the change in balance between $\Psi_m$and $L_d I_0$, and a spread within each saturation level, which is caused by the impact of saturation on the circuit parameters. Further, by comparing the spread due to saturation with the impact of changing each circuit parameter (see Figure 6.8), it can be seen that the influence of saturation is mainly in the direction of reduced L_q. Thus, the dominating saturation effect, for the FW performance of the investigated IPM, is saturation of L_q.

Further analysis of the saturation effects, including their influence on the i_d, i_q combinations along the operation boundary, are given in the appended Paper III. Especially, it should be noted that although the power along the operation boundary of Model B is indeed a combination of all curves in the series of Model A results, it does not mean that the FW of Model B matches that of any of the Model A results in the series. Instead, the Model B results exhibits a lower CPSR than all Model A results in the series. As shown in Figure 6.12, the power of Model B reduces as for a machine with higher $\Psi_{m,n}$ at high speeds while, at low speeds, the power rises as for a machine with lower $\Psi_{m,n}$. Therefore, the CPSR of Model B is consistently lower than that of all its corresponding Model A results, for all included saturation levels, as shown in Table 6.4.

Overall, FEA results can be interpreted in the using the IPM parameter plane, which gives an indication of the overall FW performance and how severely it is affected by magnetic saturation, as well as which saturating circuit parameter that has the strongest impact on the FW performance. However, the exactness of the IPM parameter plane for quantification of the FW performance is not preserved when used with FEA results including saturation. Still, it can be used as an indicative tool for improved understanding of the FW performance in IPMs operating under significant magnetic saturation. While only one IPM design has been investigated here, the FW performance also changes with

Table 6.4 FW performance, as CPSR and κ, of Model A and Model B, with and without rescaling, for five saturation levels

Sat. level	Model A (constant parameter sets)		Model B (FEA result)		Model B (rescaled FEA result)		
	CPSR	κ	CPSR	κ	CPSR	κ	Scaling factors (k_r,k_a) **
1	∞	0.68 - 0.69	∞ *	0.73	∞ *	0.73	(1.06,1.47)
2	∞	0.64 - 0.65	**3.87***	0.71	**3.87***	0.71	(1.00,1.31)
3	7.1 - 43.2	0.60 - 0.61	**2.12**	0.68	**2.12**	0.68	(0.96,1.18)
4	3.0 - 3.3	0.55 - 0.57	**1.37**	0.61	**1.37**	0.61	(0.90,1.03)
5	2.2 - 2.4	0.50 - 0.53	**1.16**	0.55	**1.16**	0.54	(0.87,0.95)

*The CPSR ends outside the mechanically feasible range. **All have $k_w = 1$

the IPM design. In particular the influence of the shape of the flux barriers in the rotor on the FW performance is investigated in the coming Chapter 7.

6.2.2 Field-weakening performance of rescaled FEA results

While the difference in the shape of the power curves, and hence difference in FW performance, was the focus of the previous section, the different current ratings associated with each saturation level naturally also affects the maximum torque and power from the IPM as can be seen in Figure 6.10. This means that the results for different saturation levels can not be considered as alternatives for the same application. However, that discrepancy can be accounted for by using scaling laws, presented in [12]- [38] and described in Section 2.5. The scaling laws can be used with FEA results (i.e. Model B) to adjust the torque and power. However, the scaling leaves the CPSR unchanged, as shown in Table 6.4 and further motivated in the appended Paper III.

The combination of variation in current rating with scaling allows a given application to be met with different FW performances, for a given IPM geometry. Here, this is demonstrated for an example vehicle with rolling resistance coefficient 0.008, wheel radius 0.36 m, gear ratio 9, weight of 2000 kg and air drag coefficient times front area of 0.72. Note that this is an initial vehicle, which has somewhat different parameters compared to the example vehicle specified in Section 3.2 which is used in the remainder of this thesis. Still, the initial vehicle serves the demonstration purposes here. The power requirement as function of speed is set to meet the CADC, with the addition of the road load at the vehicle top speed of 180 km/h. Here, $k_w = 1$ was selected, then k_r was minimized numerically, with k_a calculated for each given k_r and the ratio of the required torque and the peak torque of the IPM with the given current rating (prior to scaling). The resulting power curves are shown in Figure 6.13.

After scaling, the same power requirement curve can indeed be met with all the saturation levels. However, both the current rating and size of the IPM varies with the saturation levels in the rescaled results. The trade-off between inverter current rating (and power considering that the voltage is unchanged) and IPM volume is shown in Figure 6.14. The volume of the IPM has been normalized with the volume for saturation level 5 and the inverter power has been normalized with the highest required power (81 kW).

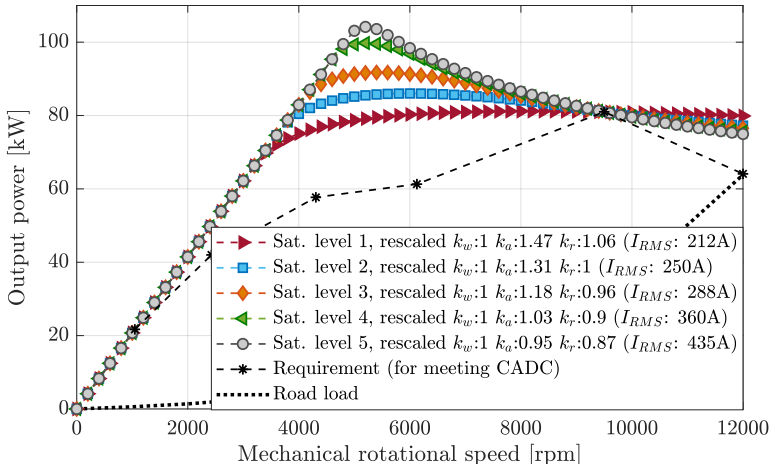

Figure 6.13 Maximum output power as a function of rotational speed, using Model B with scaling. Traces are given for the five saturation levels. Each saturation level has been scaled to precisely meet the power versus speed requirement.

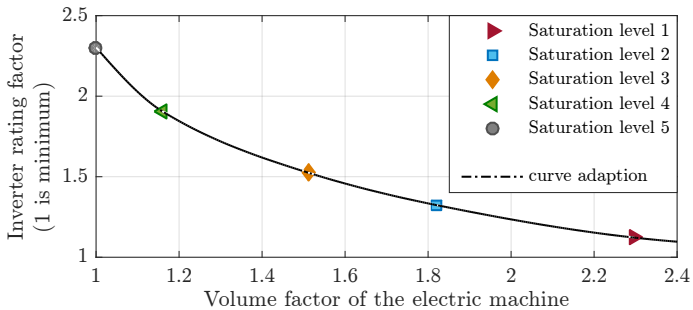

Figure 6.14 Trade off between inverter rating and IPM volume. The inverter rating factor is the inverter rating divided by the highest power in the requirements and the volume factor is the volume of the IPM divided by that of saturation level 5.

As shown in Figure 6.14, the CADC can be met with a low volume IPM if the inverter rating is high. This corresponds to high currents, strong saturation and poor FW performance. Alternatively, a smaller inverter can be used which gives better FW performance, at the expense of a larger IPM volume. Qualitatively, this trade-off is well known. Here it has been demonstrated how this trade-off can be effectively identified, for a specific requirement and IPM design, with FEA accuracy. The presented approach would also be valuable to combine with variations in the IPM design, to improve the solution further. This is done in the coming Chapters 8-10.

Chapter 7

Field-weakening potential of different flux barrier shapes

The results presented in this chapter are largely extracted from Paper IV, and further details are given in the appended paper.

This chapter investigates the influence of barrier flux shape on the FW-performance, with particular attention to the impact of mechanical constraints. While the influence of current rating on the FW-performance was investigated for a given IPM geometry in Section 6.2, the results will also depend on the IPM geometry. Here, the rotor parametrization method from Chapter 5 is used for different flux barrier shapes and the results serve as support for selecting a rotor topology for further investigation in Chapter 9-10.

7.1 Investigated case

The investigation here has been restricted to IPM rotors with two layers of flux barriers and magnets. Three different flux barrier shapes are combined into four two-layer rotor topologies. The rotor parametrization from Section 5.1.2 has been used with different barrier shapes, referred to as V, U_3 and U_4 (shown in Figure 5.4 in Section 5.1.2). Examples of geometries of each topology is given among the coming results here, in Figure 7.6. The two-layer topologies included here are denoted as VV, $\mathrm{U}_3\mathrm{U}_3$, $\mathrm{U}_4\mathrm{U}_4$ and U_4V, where the notation describes the shapes used in the respective flux barrier, from the innermost to outermost barrier layer. Thus, the first three topologies have the same barrier shape in both layers while U_4V has the U_4-shape in the innermost barrier and V-shape in the outermost barrier. Together, the four topologies allow a comparison of the different flux barrier shapes as well as view of the possibility to combine different barrier shapes.

A geometry optimization of the flux barriers has been done, for each rotor topology, within the variable space spanned by $\beta \in [-0.2, 0.3]$, $f_{\mathrm{d}} \in [0.6, 1.2]$ and $f_{\mathrm{PM}} \in [0.3, 0.9]$, where β is the rotor barrier pitch angle offset factor, f_{d} is the barrier depth factor and f_{PM} is the PM fill factor. The insulation ratio, f_{air}, has been kept at 0.1 and the rotor diameter, D_r has been kept at 139.5 mm. Further description of the different rotor parameters and their influence on the rotor geometry can be found in Section 5.1.2. The

Table 7.1 Key parameters of the IPM geometry

	Stator I	Stator II
DC voltage [V]	400	360
Max current (RMS) [A]	400	444
Number of slots	48	72
Number of poles	8	
Stator outer diameter [mm]	210	
Max speed [rpm]	15 500	
Rotor outer diameter [mm]	139.5	
Rotor inner diameter [mm]	50	
Air-gap [mm]	0.8	
Stack length [mm]	135	

use of these particular rotor parameters, and their associated parametrization method, allows the comparison of the included rotor topologies to be done using the exact same variable space.

The stator geometry and overall machine parameters are not varied during the optimization. However, two stator versions, referred to as Stator I and Stator II and specified in Table 7.1, are included in the investigation. Stator II can be considered an approximation of Stator I, but with nine slots per pole instead of six. Stator II has a 50% lower tooth width, but also 50% more teeth compared to Stator I. Additionally, the current and voltages for Stator II are altered somewhat, to account for an inevitable difference in number of winding turns when going from six to nine slots with a two-layer winding. Both stators have one slot short pitch.

The optimization aims to improve the FW performance, by means of the dual-objective of increasing both saliency, ζ, and normalized magnet flux linkage $\Psi_{m,n}$. The IPM parameter plane, which is spanned by ζ and $\Psi_{m,n}$, can be used to analyse FW performance of IPMs, as shown in Section 6.2 (see Figure 6.8 in particular). Due to magnetic saturation, the values of saliency and normalized magnet flux linkage will vary along the operation boundary, for a given IPM geometry and current rating. Here, ζ and $\Psi_{m,n}$ refers to the average values taken along the operation boundary. Essentially, the objective is to improve the average position in the IPM parameter plane. Overall, the selected objective enables an optimized field-weakening performance, were the balancing of the reluctance characteristic (ζ) and the permanent magnet characteristic ($\Psi_{m,n}$) of the IPM can directly be assessed.

To evaluate ζ and $\Psi_{m,n}$, each IPM is characterized over its full operating range, using electromagnetic FEA. This makes each evaluation of the objective function rather time consuming and, therefore, the approach of creating a response surface (also known as meta-model of optimal prognosis [50], further described in Section 2.8) is used. The overall work-flow of the optimization is shown in Figure 7.1.

In short the work-flow consists of three steps. The first step is a sensitivity analysis (SA), where the outputs (ζ and $\Psi_{m,n}$) are evaluated for different combinations of values of the input variables (β, f_{d} and f_{PM}). The combinations are created using latin hypercube sampling (200 samples).

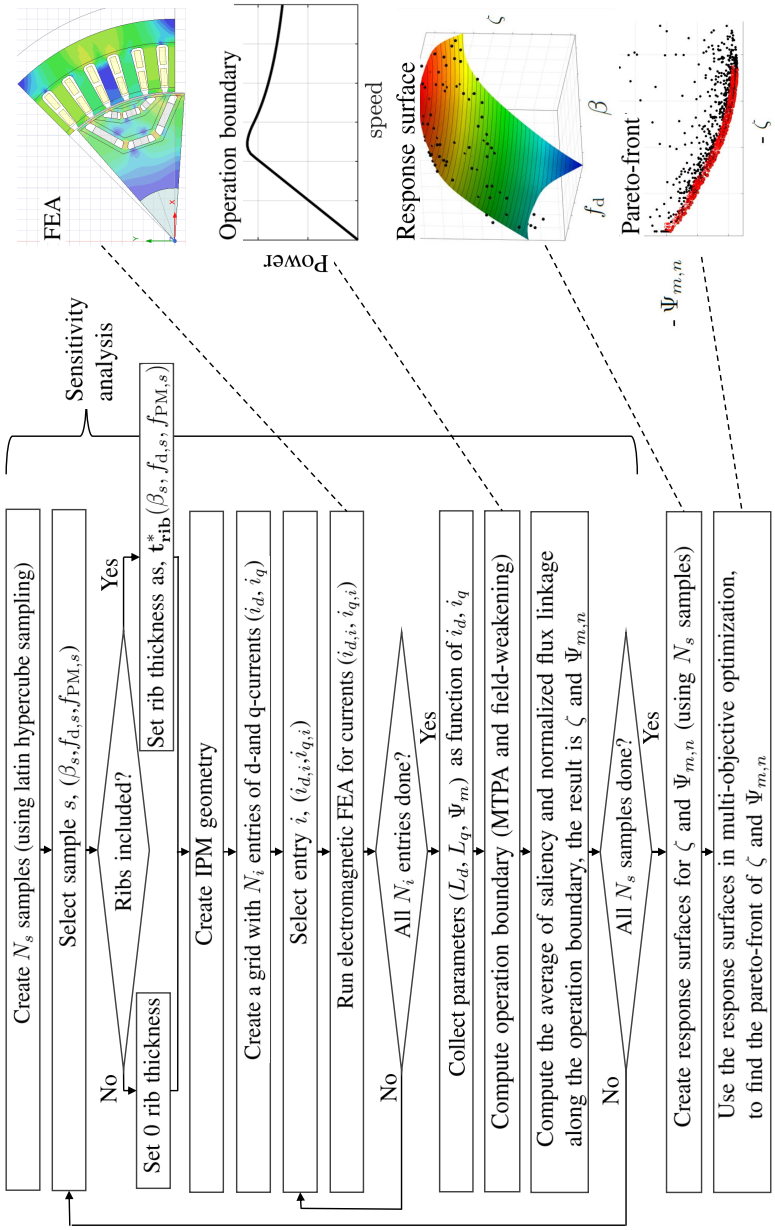

Figure 7.1 Optimization work-flow, showing sensitivity analysis of the IPM responses (evaluated using electromagnetic FEA), followed by response surface approximation and multi-objective optimization.

In the second step, a multi-dimensional response surface (RS) is fitted to the results of the SA. The coefficient of prediction was 98% or higher for the RS's of all rotor topologies included in this study. In the last step, the created RS is used together with an optimization algorithm to find an optimal solution, given an objective involving the outputs described by the RS. A function evaluation using the RS is very fast, which allows generous settings in the optimization algorithm. Here, a genetic algorithm has been used, with a population size of 20 and a maximum number of generations set to 100. For reference, each SA done in this investigation took around 100 hours of simulation time (running 6 simulations in parallel on a PC with a 3.00 GHz processor) while an optimization, using the genetic algorithm and the created RS, took about 10 minutes.

Finally, the work-flow in Figure 7.1 has been done both with and without mechanical constraints (i.e. with and without including the ribs that hold the outer part of the rotor pole and PMs in place). This is done in order to quantify the influence of mechanical constraints on the FW potential of each rotor topology, since the different flux barrier shapes can be expected to have differences from a mechanical perspective. Geometry versions with and without ribs can be seen in the coming Figure 7.6. When ribs are included, their sizing is done using the approach described in Section 5.2. However, there are some difference in the settings here compared to Section 5.2. Here, the look-up table of required rib thickness is 3-dimensional (i.e. dependent on β, f_{d} and f_{PM}) over a somewhat wider variable space. Further, the look-up table is created in four different versions, one for each rotor topology investigated here, with the constraint on von Mises stress set to 300 MPa.

7.2 Pareto fronts for ζ and $\Psi_{m,n}$

The pareto front for ζ and $\Psi_{m,n}$ for each of the four included rotor topologies, for the case without mechanical constraints, are shown in Figure 7.2. Since ribs are absent, these IPMs are naturally not realizable in practice. Still, they can be viewed as an ideal situation with perfectly saturated ribs and allows the purely electromagnetic potential of the rotor topologies to be compared. Figure 7.2 shows that the values of ζ are higher, overall, for the topologies with more arc-like barriers (i.e. $\mathrm{U_4U_4}$ and $\mathrm{U_3U_3}$). On the other hand VV has a higher value of $\Psi_{m,n}$ for each given PM amount (indicated by the color along the pareto fronts). For each topology, there is an additional marker for the IPM version with a PM weight of 1.25 kg. These additional markers correspond to IPM geometries created using the values from the pareto front and then re-evaluated using FEA. Considering that the pareto front is based solely on the response surface, the additional markers give an indication of the quality of the response surface. The good agreement between the additional markers and the pareto fronts in Figure 7.2 indicate a high quality response surface.

The pareto fronts resulting from optimization with mechanical constraints, where the ribs are sized with dependency on the rotor geometry (using look-up tables depending on β, f_{d} and f_{PM}), are also included in Figure 7.2. The agreement between the additional markers (at 1.25 kg magnet) and the pareto-front is not as good as without ribs. This can be expected, since the inclusion of mechanical constraints increases the complexity of the problem. The agreement is still considered sufficient for a comparison of the flux

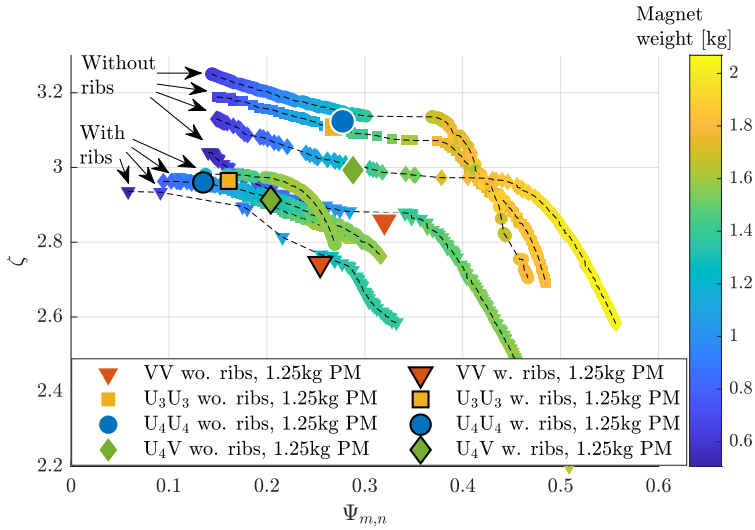

Figure 7.2 Pareto front of saliency, ζ, and normalized magnet flux linkage, $\Psi_{m,n}$ with and without mechanical constraints (w./wo. ribs), for the rotor topologies VV (triangles), U_3U_3 (squares), U_4U_4 (circles) and U_4V (diamonds), all with Stator I. The color along the pareto fronts corresponds to the PM weight. The pareto front designs with 1.25 kg PM weight, evaluated using FEA, are shown with additional markers.

barrier shapes. As shown in Figure 7.2, the mechanical constraint have a strong impact on both ζ and $\Psi_{m,n}$

Further, it was found that almost all the IPM designs along the pareto fronts in Figure 7.2, using Stator I, have very high values of torque ripple. Naturally, it is possible to add a torque ripple constraint to the optimization. However, even a torque ripple constraint of 20% at peak torque operation, which is higher than usually seen for BEV applications, leaves the pareto fronts severely compromised, as shown in Figure 7.3. By comparing the pareto fronts for Stator I in Figure 7.3 with their counterparts in Figure 7.2, it is clear that the range of the pareto-front have shrunk significantly and, in particular, the ζ-values are lower.

Torque ripple is known to be sensitive to positions of the flux barrier endings close to the air-gap as well as to the number of slots in the stator [67]. It would be possible to reduce the torque ripple through skewing [68]. Still, the correlation between high ζ and high torque ripple (both mainly dependent on the rotor parameter β) found for the case investigated here is not ideal from the perspective of FW performance. Therefore, a stator with 72 slots (Stator II) has been considered, to greatly reduce torque ripple without sacrificing ζ. The pareto front from optimization using Stator II are shown in Figure 7.4. However, note that the additional markers for Stator II are simply the rotors that were found previously (based on the optimization using Stator I), with the stator replaced to Stator II. Still, these markers are close to the pareto fronts obtained with Stator II, which indicates that the optimal values of the rotor parameters included here are not very sensitive to the number of slots in the stator.

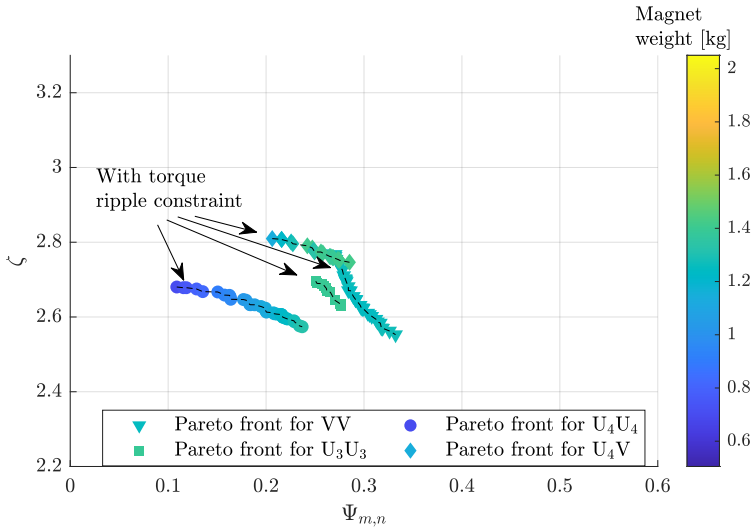

Figure 7.3 Pareto front of saliency, ζ, and normalized magnet flux linkage, $\Psi_{m,n}$ with a 20 % constraint on the torque ripple at peak torque, for the different rotor topologies, with Stator I.

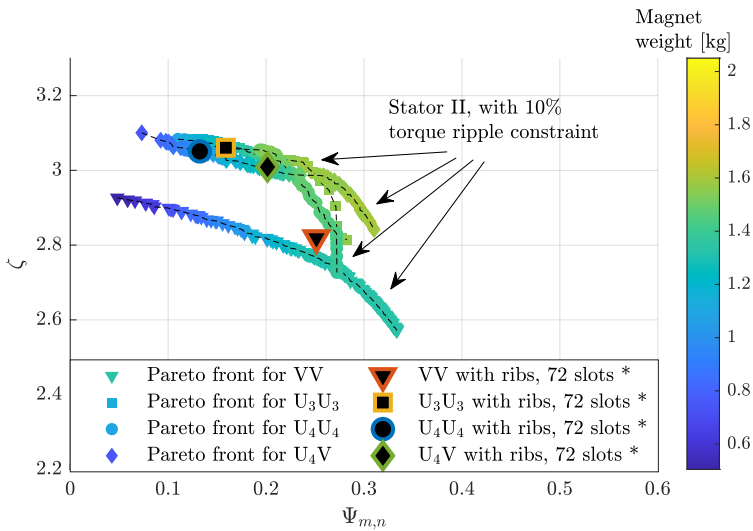

Figure 7.4 Pareto front of saliency, ζ, and normalized magnet flux linkage, $\Psi_{m,n}$ with a 10 % constraint on the torque ripple at peak torque, for the different rotor topologies, with Stator II. * Additional markers are shown for a combination of the rotors with 1.25 kg PM weight from the optimization done with Stator I without torque ripple constraint combined with Stator II instead, which can be seen to agree relatively well with the pareto fronts for the optimization using Stator II.

7.3 Comparison of barrier shapes with the same magnet weight

This section presents a more in-depth comparison of the IPM designs with 1.25 kg PM weight found in the previous section, i.e. those shown with additional markers in Figure 7.2 and Figure 7.3.

The designs include the results of the optimizations with and without mechanical constraints for the included rotor topologies. The designs optimized with mechanical constraints are included with two stator versions (Stator I and II in Table 7.1), keeping the rotor unchanged. Further, a last set of designs are created by adding ribs to the designs optimized without ribs. The thickness of the added ribs are set according to the look-up table, $\mathbf{t}^*_{\mathbf{rib}}$, but using the rotor parameter values from the optimization without ribs. Thus, there are four IPM versions per rotor geometry, all of which are shown in Figure 7.6. An overview of the values of the rotor variables as well as a summary of the performance for each of the geometries is presented in Table 7.2. The mechanical stress levels, shown in Table 7.2, deviate somewhat from the intended limit (300 MPa), since the response surfaces are not exact, but the deviations are considered small enough for the comparisons here.

As shown by the power versus speed curves in Figure 7.5, when ribs are excluded, all the rotor topologies have similar FW performance. This can also be seen from their positions in the IPM parameter plane, shown in Figure 7.7. Although the different IPMs without ribs have a different balance between ζ and $\Psi_{m,n}$, they are still similar in terms of distance to the ideal field-weakening line (i.e. inverter utilization of 0.7).

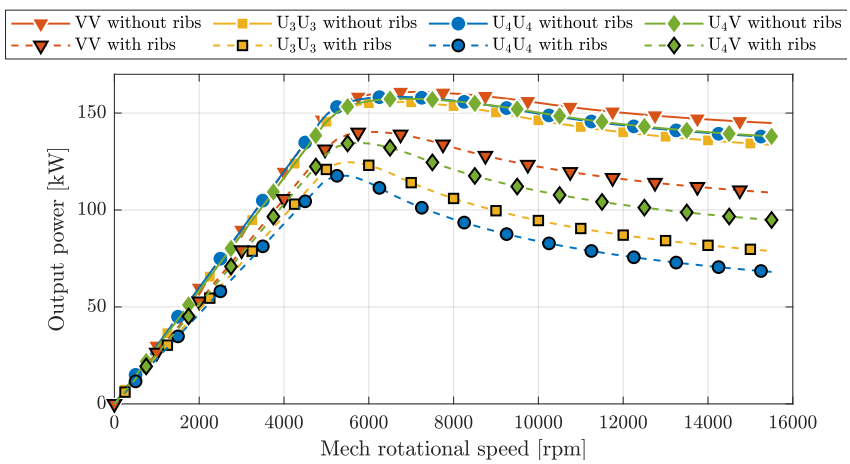

Figure 7.5 Power capability of the machine designs with 1.25 kg magnet weight, from the optimizations with and without ribs (using Stator I). The influence of mechanical constraints on the optimized field-weakening performance is shown, for the different IPM rotor topologies.

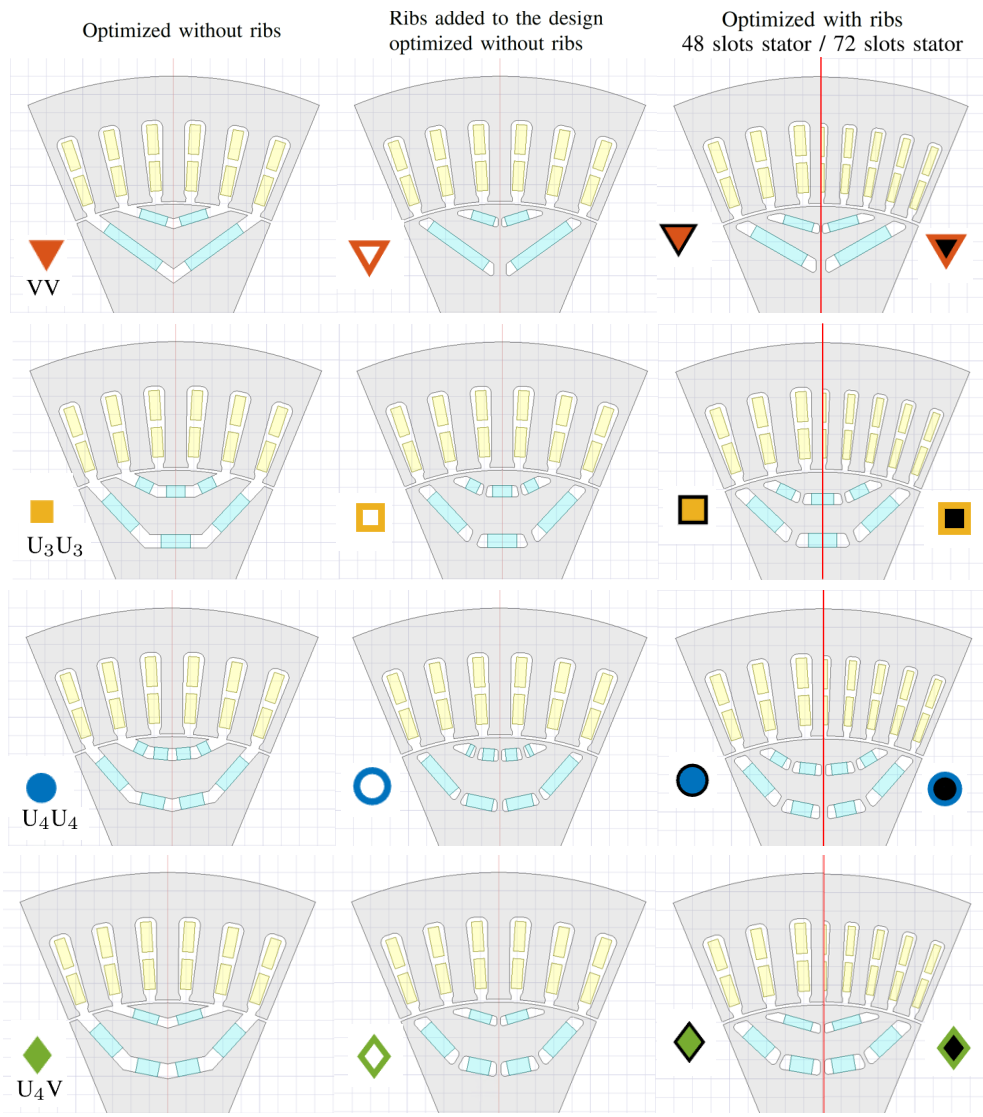

Fig. 7.6 Machines with different rotor topologies, each with 1.25kg magnet. The design versions include optimization without ribs (left column), ribs added to the design optimized without ribs (middle column) and optimization with ribs (right column). The right column shows two stator versions, stator I (48 slots) and stator II (72 slots) with the same rotor. Comparing the middle and right column shows the difference in machine geometry between adding ribs to an electromagnetically optimized design versus multi-physics optimization with mechanical constraints.

Table 7.2 Overview of parameters and results for machine designs with 1.25 kg magnet weight

Rotor topology	Machine version rotor, stator	β	f_{d}	f_{PM}	ζ*	$\Psi_{\mathrm{m,n}}$*	Max torque [Nm]	Max power [kW]	Power at top speed [kW]	Torque ripple ** [%]	Stress at top speed [MPa]	$\sum$ rib thickness inner, outer layer [mm]
VV	Without ribs, I	-0.04	1.01	0.71	2.86	0.32	285.5	160.9	144.8	-	-	-
	Ribs added, I	-0.04	1.01	0.90	2.69	0.23	253.0	133.4	96.3	13.2	302	5.3, 3
	With ribs, I	0.17	0.78	0.79	2.74	0.25	252.3	140.3	109.0	45.9	292	4.8, 3
	With ribs, II	0.17	0.78	0.79	2.82	0.25	260.2	141.8	110.1	6.2	292	4.8, 3
U_3U_3	Without ribs, I	0.03	0.95	0.57	3.11	0.27	278.5	155.8	133.6	-	-	-
	Ribs added, I	0.03	0.95	0.76	2.86	0.15	229.9	119.8	71.0	50.5	281	6.6, 4
	With ribs, I	0.23	0.80	0.69	2.96	0.16	231.5	124.7	78.8	52.7	304	6.2, 4
	With ribs, II	0.23	0.80	0.69	3.06	0.16	240.4	126.7	79.6	11.7	304	6.2, 4
U_4U_4	Without ribs, I	-0.06	0.97	0.63	3.12	0.28	286.1	158.4	137.6	-	-	-
	Ribs added, I	-0.06	0.97	0.89	2.51	0.18	229.4	117.9	69.6	38.1	287	6.3, 5
	With ribs, I	0.28	0.84	0.66	2.96	0.13	221.7	117.7	68.1	71.6	295	6.9, 5
	With ribs, II	0.28	0.84	0.66	3.05	0.13	231.3	120.1	68.7	15.1	295	6.9, 5
U_4V	Without ribs, I	0.02	0.91	0.59	2.99	0.29	278.3	157.4	138.0	-	-	-
	Ribs added, I	0.02	0.91	0.76	2.86	0.18	240.0	126.0	80.9	33.8	278	6.0, 3
	With ribs, I	0.22	0.74	0.70	2.91	0.20	246.1	134.7	94.9	55.8	271	5.1, 3
	With ribs, II	0.22	0.74	0.70	3.01	0.20	254.3	136.4	95.9	1.8	271	5.1, 3

* Average over operation boundary, ** At max torque

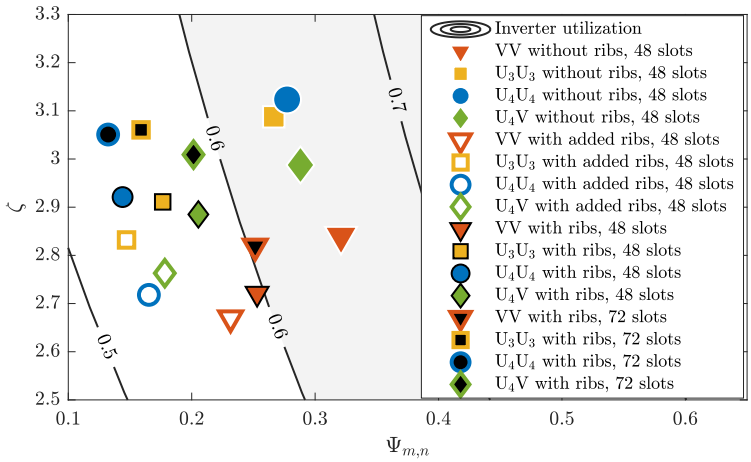

Fig. 7.7 IPM plane with the average position of machines with 1.25 kg magnet weight marked for different IPM rotor topologies. Each topology has four versions: optimized without ribs (stator I), ribs added after the optimization (stator I), optimized with ribs (stator I) and the rotor optimized with ribs together with stator II.

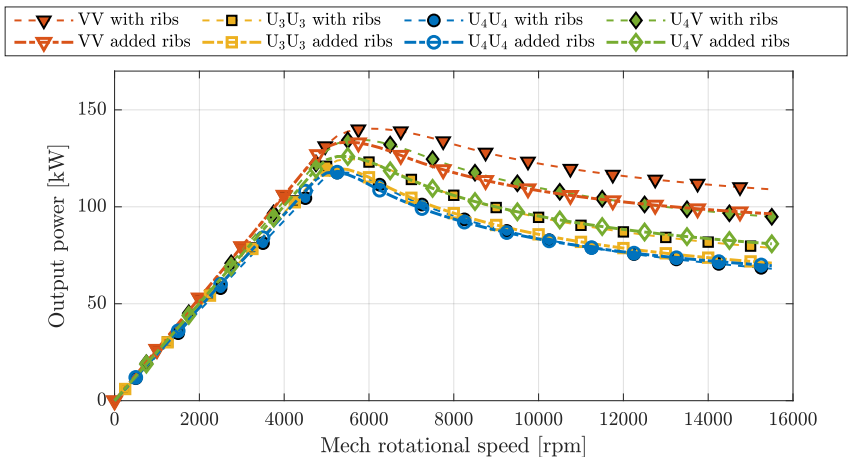

Fig. 7.8 Power capability of the machine designs with 1.25 kg magnet weight (using Stator I). Two versions of each rotor topology are included, one set where ribs were included in the optimization (referred to as "with ribs") and another set where the ribs were added after the optimization (referred to as "added ribs").

When ribs are included, the difference between the rotor topologies increases, as can be seen in both Figure 7.5 and Figure 7.7. The least affected rotor topology is VV, which has the most shallow placement of magnets and the lowest number of ribs among the included topologies. The mechanical constraints have the most severe influence for U_4U_4 while VV is the least affected topology here. Having a low number of ribs in total can

be a benefit considering that each rib is required to be at least 1 mm. For the topologies with the same number of ribs, U_3U_3 and U_4V, the latter is slightly less affected by the mechanical constraints.

Further, the importance of including mechanical constraints in the optimization is analysed. Comparing the middle and right column in Fig. 7.6 shows the difference in machine design between adding ribs to a design optimized without mechanical constraints and multi-physics optimization with mechanical constraints included. The difference can also be seen in the rotor parameter values in Table 7.2. For all rotor topologies, there is a visible difference between including mechanical constraints in the optimization and adding ribs after the optimization (i.e. comparing the middle and right column in Figure 7.6). Overall, the inclusion of geometry dependent mechanical constraints lead to rotor geometries with shallower placement and wider flux barriers.

As shown in Figure 7.8, the FW performance improves significantly when mechanical constraints are included, compared to adding ribs to an electromagnetically optimized design, for all rotor topologies except U_4U_4. Additionally, it is also interesting to note that the power capability of U_4V optimized with ribs is slightly higher than that of VV with ribs added after the optimization, in Fig. 7.8. This shows that careful handling of the mechanical constraints is of similar importance as the choice of rotor topology.

7.4 Choice of rotor topology

Summarized, the previous section showed the IPM rotors with different flux barrier shapes to have different optimal balance between saliency (ζ) and normalized magnet flux linkage ($\Psi_{m,n}$), but their potential for high field-weakening performance is very similar if mechanical constraints are neglected. However, including mechanical constraints in the optimization caused a significant spread among the topologies of different flux barrier shapes. Once mechanical constraints were included, the reduction in $\Psi_{m,n}$ is no longer compensated by the higher ζ associated with more arc-like flux barrier shapes. The topology with V-shaped flux barriers, which had the lowest ζ and highest $\Psi_{m,n}$ among the included topologies, was least affected by mechanical constraints and reached the highest field-weakening performance in the investigated case.

Finally, a view on the difference in losses is given by the efficiency maps. Figure 7.9 shows the efficiency maps for the four IPM designs consisting of Stator II together with the rotors optimized with mechanical constraints (i.e. rightmost column in Figure 7.6). Here, the losses of the IPM include resistive losses, core losses and eddy losses in the PMs based on 2D FEA. For comparison, the road load of the example BEV (specified in Section 3.2) is included. While the IPM with the VV-topology has the highest efficiency for most of the operating region, it also has the lowest efficiency among the included topologies close to the road load at speed above 7000 rpm. This can be explained by the lower ζ associated with the VV-topology.

Considering that operation close to the road load at high speeds is highly important for driving energy losses in rural and highway driving, the U_4V-topology is considered to be preferable in terms of trade-off between efficiency and performance across the speed range, despite the higher FW performance found for the VV-topology. Therefore, U_4V is selected for the coming optimizations in Chapter 9-10.

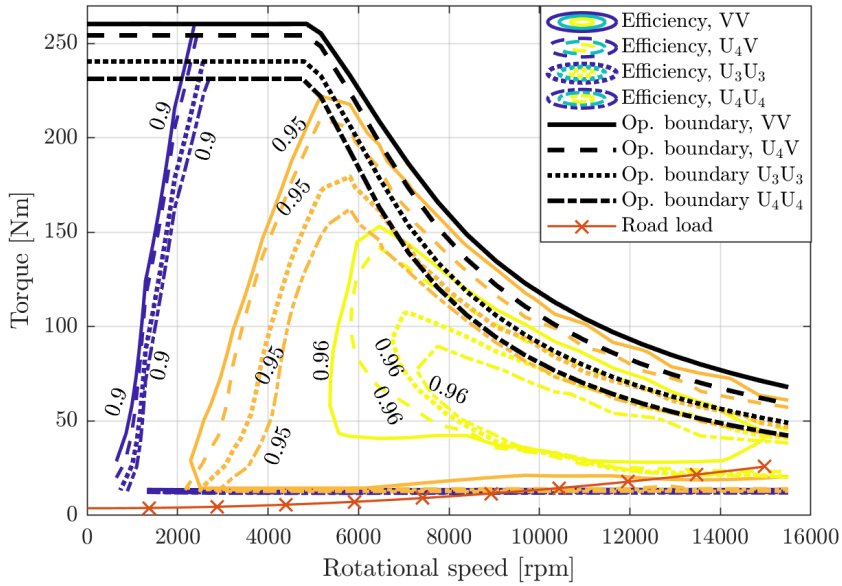

Figure 7.9 Efficiency of the IPMs with 1.25 kg PM and Stator II together with the road load of the considered example BEV.

It should also be noted that the efficiency map can likely be improved further for all the rotor topologies, by altering the IPM design, involving both rotor and stator design features. For example, the core losses during FW are related with harmonics in the d-axis flux density. They can be reduced both by the combination of stator slots and rotor flux barrier numbers, as well as the balance between flux density from the magnets and number of turns in the stator winding [69, 70]. However, these aspects have not been covered in the comparison of rotor topologies here.

Chapter 8

Scaling IPM and converter for minimum life cycle cost

The scaling of FEA results in Section 6.2.2 offer a computationally efficient way to adjust a given IPM design towards a chosen application. Considering the computational load of the FEA, it is highly beneficial to maximize the utilization of the information obtained from the FEA results. The scaling can, in a way, be seen as the identification of all other machines (of different sizes and number of winding turns) whose FEA results you can accurately predict from the set of FEA results for your reference machine. The reference machine and the scaled versions of it will all share the same shape of the geometrical cross section, which is here referred to as the reference geometry. The aim with the scaling is here to select the best scaled version of the given reference geometry. Thus the size of the machine, number of winding turns and current rating should be set to make the best use of the given geometrical cross section. This is done here, based on the scaling approach presented in Section 6.2.2 together with thermal and mechanical constraints. This scaling approach is then combined with variations in the reference geometry in the optimization in Chapters 9 - 10.

The scaling in Section 6.2.2 is made to preserve the magnetic field picture and thereby the validity of the electromagnetic FEA. This means that it is a purely electromagnetic scaling that does not account for thermal or mechanical aspects of the IPM design. This calls for caution when using the scaling in a design process. Here, a scaling approach is defined where the radial scaling is restricted to keep the mechanical stress level close to that of the reference IPM in order to avoid under- or over-dimensioning the ribs in the rotor. Further, the thermal feasibility of the rescaled IPM is evaluated and used to set the current density. From the rescaled IPM versions that are considered thermally and mechanically feasible, the version that is best for a given objective function is selected. Here, focus has been on the objective of minimizing LCC but other objectives would also be possible and here we have included examples of scaling for minimum investment cost or minimum driving energy loss instead.

For all scaling examples showed here, the investment cost and losses of the power electronics converter has been included using the expressions from Section 2.6-2.7. More

detailed modelling of the converter is beyond the scope of this work but it has still been considered important to include the converter in a simplified way, since changing the current rating of the IPM will inevitably affect the cost and losses of the converter.

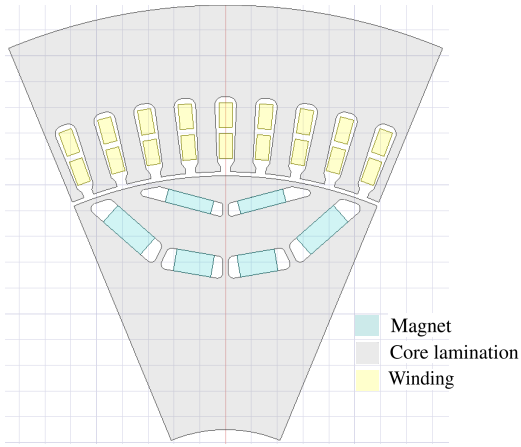

Figure 8.1 Geometrical cross section of the IPM referred to as geometry A.

8.1 Demonstration of the scaling approach for an example IPM geometry

This section describes the scaling approach, using the IPM shown in Figure 8.1 as example. This geometry is referred to as geometry A and was created using the parametrization method described in Chapter 5 with $\beta = 0.188$, $f_{\mathrm{d}} = 0.727$, $f_{\mathrm{PM}} = 0.761$, $f_{\mathrm{air}} = 0.142$, $D_r = 153.5$ mm, $D_s = 219.7$ mm, $f_{\mathrm{t}} = 0.532$, $f_{\mathrm{y}} = 4.81$ and a stack length of 120 mm. This particular geometry was selected because it is one of the more interesting ones from the large set of geometries that are near-randomly generated (using latin hypercube sampling) and used later, in Chapters 9 - 10. Here, it only serves as an example geometry and in principle any IPM geometry could have been used for demonstration of the scaling approach.

The scaling approach, described step by step below, has four degrees of freedom, the three scaling factors k_r (scaling in radial dimension), k_a (scaling in axial dimension) and k_w (rewinding), and the rated current, as described in Section 6.2.2.

1. Let J_{ref} be the current density in the reference IPM (at peak torque operation), which corresponds to a certain rated current in the reference IPM, denoted as I_{ref}. The current density of the rescaled IPM will scale with the inverse of k_r, thus $J_{resc} \propto 1/k_r$. Further, the mechanical stress in the rotor will scale with the square of k_r, thus $S_{resc} \propto k_r^2$. Therefore, in order to avoid that the rescaled IPM deviates too much from the reference IPM in terms of thermal and mechanical aspects, it is important to keep k_r close to 1.

Further, torque scales as

$$\frac{T_{em,resc}}{T_{em,ref}} = k_r^2 k_a = x_1 \tag{8.1}$$

where T_{em} is the peak torque of the IPM and the subscript $_{resc}$ and $_{ref}$ denotes the rescaled and reference IPM versions respectively. This torque ratio is also denoted x_1. Further, the ratio for flux linkage, x_2, which is also closely related to the base speed and high speed power (as described in Section 4.4), is given as

$$x_2 = k_r k_a k_w \tag{8.2}$$

which, if $k_r = 1$ gives

$$k_{w,c} = \frac{x_2}{x_1} \tag{8.3}$$

where $k_{w,c}$ denotes the continuous version of k_w, which is of course a theoretical situation and in practice the value of k_w needs to be restricted to comply with integer number of turns for the given winding configuration. Still, $k_{w,c}$ can be used to identify the closest feasible values of k_w or, if it is of interest to investigate how much the winding configuration restricts the rescaled result, $k_{w,c}$ could be used directly. Note that the ratios x_1 and x_2 can be found by first setting $k_w = 1$ and scaling the reference IPM towards the peak requirements of the chosen application (as done in Section 6.2.2 and also described below).

2. With k_w selected, the values of k_a and k_r can be set in the same way as in Section 6.2.2, by numerical minimization of k_r with k_a automatically set to $\frac{T_{em,resc}}{T_{em,ref} k_r^2}$. The rated current scales as k_r/k_w, so the rated current of the rescaled IPM will be $I_{resc} = \frac{k_r}{k_w} I_{ref}$. Note that the resulting k_r will typically not be exactly 1 even if $k_{w,c}$ is used. This can be explained by (8.3) being a slight approximation, since it neglects that the power in the FW region is also slightly dependent on the scaling of the stator resistance. That could be accounted for but it is not found necessary here, since the deviation is typically less than 1% and $k_r \approx 1$ is considered sufficient.

3. Thereafter, the mechanical stress of the rescaled IPM can be computed based on the stress of the reference IPM and the value of k_r. The stress of the reference IPM (geometry A) is approximately 330 MPa (as it has rotor ribs sized using the method in Section 5.2). The thermal buffering capacity of the rescaled stator and winding is approximated using the end-winding-LPN, described in Section 5.3, for the rescaled IPM. The end winding temperature is computed after running at full current, I_{resc} for the duration of one acceleration from 0-160 km/h (top speed) of the example vehicle from Chapter 3, starting from 70°C. The resulting stress S_{resc} and end-winding temperature T_{ew} can then be compared to the chosen limits for what is considered feasible. Here, the thermal constraint for the end-winding has been set to $T_{ew} < 125$°C. In case of the mechanical constraint it is advised to allow some slack compared to S_{ref}, to give some room for the scaling, at least if k_w is not continuous. Here the mechanical constraint has been set to $S_{resc} < 380$ MPa (i.e. allowing 15% increase from the reference). However, in case $k_{w,c}$ is used, the deviation will be much lower, typically < 10 MPa.

4. In addition to the thermal and mechanical aspects, the rescaled IPM is evaluated based on an objective of choice, for example LCC. For computation of LCC, the driving losses of the IPM and converter are considered. The scaling of the IPM includes core losses and copper losses (as described in Chapter 4). For simplicity and considering that they typically have a marginal influence on the total losses, the eddy losses in the magnets are neglected in the scaling here. Note that the entire loss map of the IPM is not required for the previous steps.

5. Finally, the entire procedure (from the first step) is repeated for different values of J_{ref}. This is done to identify the scaled IPM version that meets the thermal and mechanical constraints with the best objective value (for example lowest LCC). This naturally requires that the FEA results of the reference IPM cover a fairly wide range of currents, so that different values of I_{ref} can be used with sufficient resolution. While the scaling is very fast, the post-processing of FEA results and computation of the IPM efficiency map with high resolution in torque and speed is not negligible time-wise. Therefore, the variation in J_{ref} is done as an adaptive sweep that consists of an **initial sweep** (12 values evenly spaced from 10-30 A/mm^2) followed by **refining the sweep** in the most interesting region. The refinement is done by identifying the point in the sweep which has the best objective value among the feasible options, from that the interval around that point is identified (as the highest and lowest neighbouring point in the sweep) and then additional sweep points are added in that interval. This is repeated until either the change in best objective is less than 0.1 EUR, the change in best value of J_{ref} is less than 0.02 A/mm^2 or the limit of 15 added points is reached. Once any of these criteria is met the scaled version that meets the constraints with the lowest objective value is outputted as the best feasible scaled IPM version of the given geometry.

Using the scaling approach, with $k_{w,c}$ (continuous k_w) for IPM geometry A with the objective of minimizing LCC considering 10 years of driving, at 15 000 km/year of the driving distribution SCMD-GT (Chapter 3) is summarized in Figure 8.2, which shows the points included in the current density sweep in the form of the resulting LCC versus I_{resc} with the thermal constraint evaluation illustrated (the mechanical stress was also evaluated but always feasible). The best feasible version, marked with a star in Figure 8.2, resulting from the scaling approach has the scaling factors $k_w = 1.086$, $k_a = 1.042$ and $k_r = 0.998$ and a current $I_{resc} = 356.2$ A (RMS), which gives a T_{ew} of 122 °C, a stress S_{resc} of 329 MPa and an LCC of 815 EUR. The efficiency maps of the scaled IPM and converter are presented in Figure 8.3, together with the performance requirement and the torque corresponding to the road load of the example vehicle.

If the scaling approach is done with $k_w = 1$, by keeping the number of turns and parallel paths in the winding same as in the reference IPM, the LCC versus I_{resc} curve in Figure 8.4 is obtained. The results for the best feasible version, marked with a star in Figure 8.4, has scaling factors $k_w = 1$, $k_a = 1.222$ and $k_r = 0.939$ and a current $I_{resc} = 351.2$ A (RMS), which gives a T_{ew} of 125 °C, a stress S_{resc} of 291 MPa and a LCC of 817 EUR. These results are quite similar to the results with continuous k_w, which is not unexpected considering that the value of $k_{w,c}$ was relatively close to 1 in the continuous case.

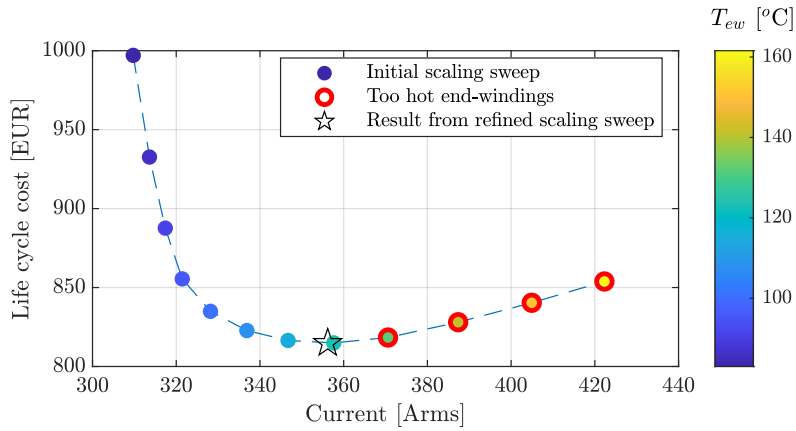

Figure 8.2 The results, including the initial current density sweep and the outcome of the refined sweep, of the scaling approach with continuous k_w, for IPM geometry A with the objective of minimizing LCC (10 years of driving, SCMD-GT driving distribution).

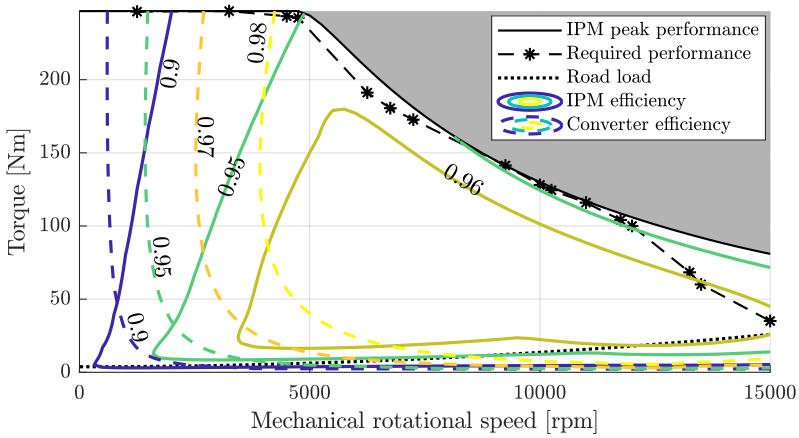

Figure 8.3 Efficiency of the rescaled IPM and converter, resulting from using the scaling approach with continuous k_w on geometry A with minimization of LCC (10 years of driving, SCMD-GT driving distribution) as objective.

However, there are significant differences between continuous k_w and $k_w = 1$ in terms of how well the mechanical stress can be kept close to the stress of the reference IPM. When the flexibility in k_w is restricted it needs to be compensated for by k_r which affects the stress of the rescaled IPM. Scaled versions for which stress constraint set for the scaling, S_{resc} >380 MPa, is violated are indicated with black round markers in Figure 8.4. The size of the round markers also correspond to the stress safety factor (which is inversely proportional to the stress, thus smaller markers mean higher stress).

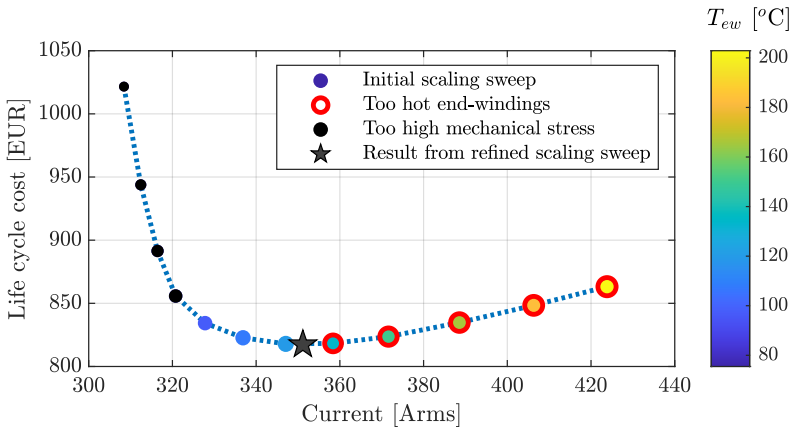

Figure 8.4 The results of the scaling approach, including the initial current density sweep and the outcome of the refined sweep, with $k_w = 1$, for IPM geometry A and minimization of LCC (10 years of driving, SCMD-GT driving distribution) as objective. The size of the round markers indicate the safety factor on mechanical stress.

Figure 8.4 shows that the range of feasible scaled versions is quite limited when both thermal and mechanical aspects are considered and k_w is restricted to 1. Still, feasible range correlates rather well with low LCC values, although the lowest LCC value is found close to the thermal limit, in the case here (with IPM geometry A and the driving distribution SCMD-GT).

If another driving distribution is considered for the LCC, it will naturally affect the results. The results of the scaling with different driving distributions, including the CADC and SCMD (described in Chapter 3), for geometry A are shown in Figure 8.5. Note that the feasible range from the initial current density sweep does not change with the driving distribution, but the LCC values are affected. Overall, there is a spread in the results from different driving distributions shown in Figure 8.5. However, the curves for CADC-RC (Artemis rural cycle), SCMD-RT (rural type from logged cycles) and SCMD-HWT (highway type from logged cycles) are very similar, while CADC-CC (Artemis city cycle) stands out in terms of higher LCC results. Looking at the best feasible scaled version for each driving distribution, marked with stars in Figure 8.5, it can be noted that the two distributions focused at lower speeds (CADC-CC and SCMD-CT) have the lowest current rating, which would help to reduce copper losses. The case with CADC-CC stands out as the LCC values improve all the way to the mechanical constraint. The other included distributions have more high speed content and give better results with a current rating quite close to the thermal constraint used here, which could be related to reducing core losses.

The scaling also offers a view on the trade-off between the investement cost and the NPV of losses in the IPM and converter, as shown in Figure 8.6, and the trade-off between IPM investment cost and converter investment cost, as shown in Figure 8.7. Both the

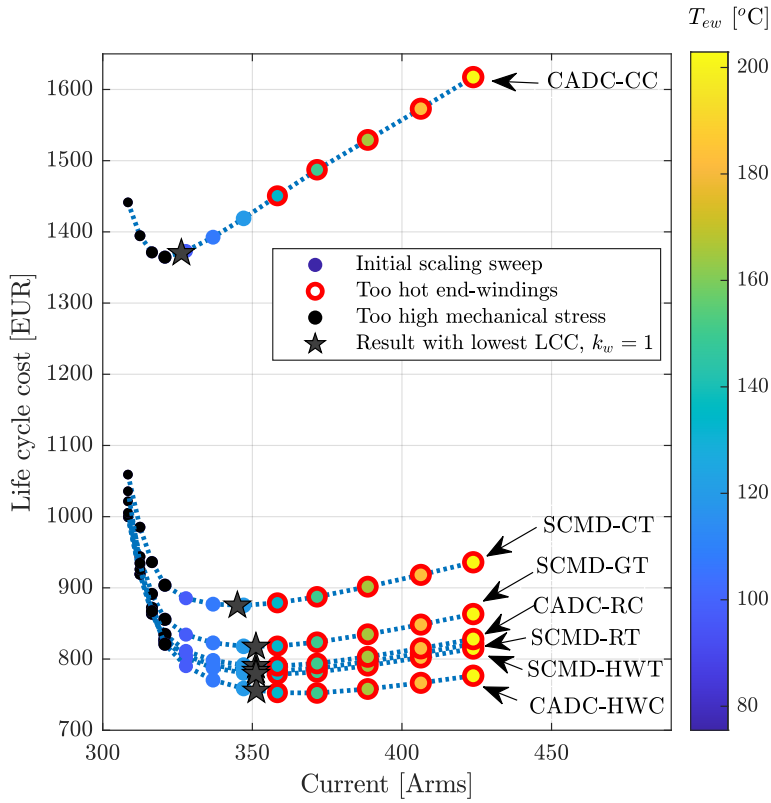

Figure 8.5 The results of the scaling approach with $k_w = 1$, for IPM geometry A and minimization of LCC (10 years of driving) as objective, for the CADC and SCMD driving distributions. The size of the round markers indicate the stress safety factor.

case with continuous k_w (i.e. $k_w = k_{w,c} = 1.086$) and with $k_w = 1$ are included for comparison. The results corresponding to the minimum LCC are also indicated with star markers. The scaling that gives the lowest LCC is not exactly the same as the scaling that gives either the lowest investment cost or the lowest NPV of losses. Thereby, if one of those would have been chosen as objective, the best feasible scaled version of the IPM would be slightly different. Overall, selecting another objective than LCC, or another driving type than SCMD-GT, or another reference IPM than geometry A, would affect the results, and this is investigated for a few selected examples in the next section.

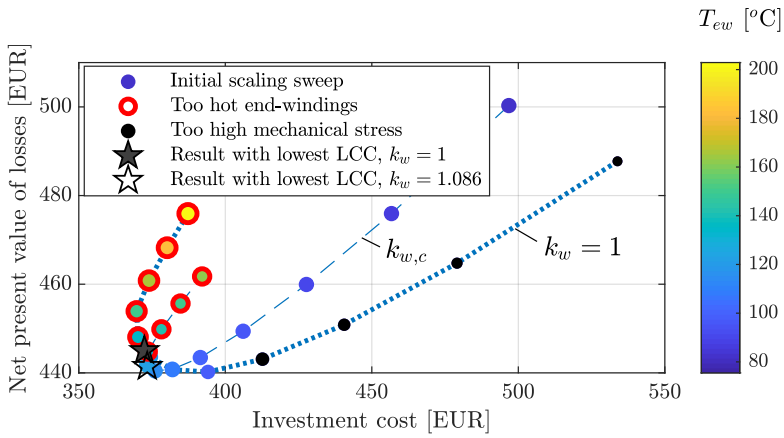

Figure 8.6 Trade-off between NPV of losses and investment cost (including both IPM and converter), when scaling geometry A with 10 years of driving, SCMD-GT driving distribution, in the NPV calculation. The results of the initial current density sweep are shown together with the result of the refined sweep (targeting minimum LCC), for both the case with continuous k_w (dashed curve) and with the restriction $k_w = 1$ (dotted curve).

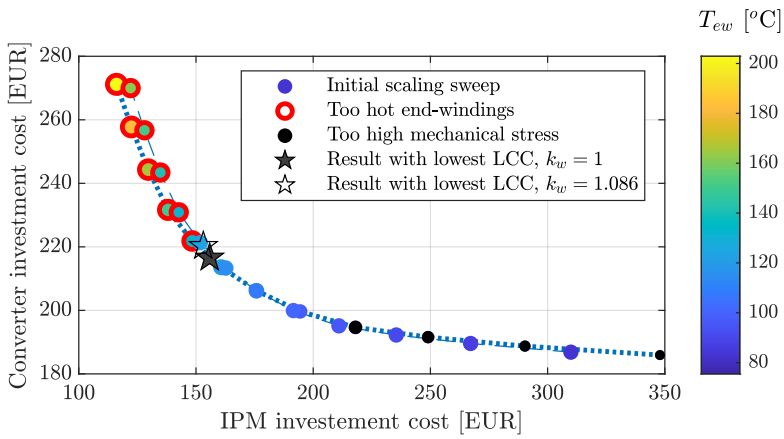

Figure 8.7 Trade-off between investment cost of the IPM and the converter, when scaling geometry A. The results of the initial current density sweep are shown together with the result of the refined sweep (targeting minimum LCC), for both the case with continuous k_w (dashed curve) and with the restriction $k_w = 1$ (dotted curve).

8.2 Combining the scaling approach with geometry changes

This section gives an overview of the results that can be achieved when the scaling approach is combined with geometrical changes in the IPM. The five geometries, referred to as A-E, serving as examples here are shown in Figure 8.8 and their corresponding geometrical variable values (following the parametrization in Chapter 5) are given in Table 8.1. All the geometries A-E have a stack length of 120 mm before scaling. The geometries in this section are all selected from a larger set of designs that is later used for IPM geometry optimization in Chapters 9 - 10. Thus the designs are not optimized but merely interesting randomly generated examples.

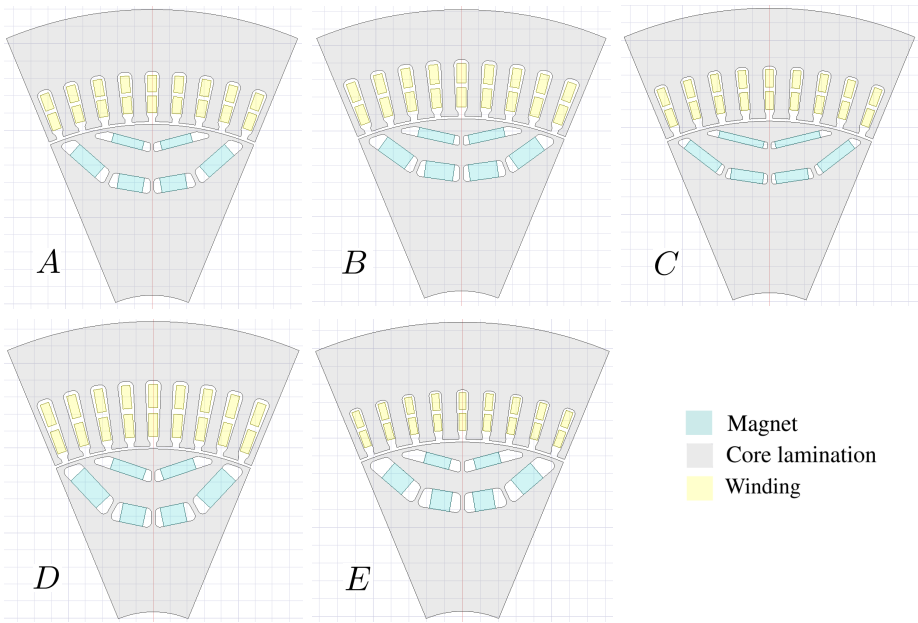

Figure 8.8 Geometrical cross sections of the IPM referred to as geometries A-E.

Each of the geometries A-E are scaled, using the approach described in Section 8.1, for three different objectives: minimize LCC, minimize NPV of losses and minimize investment cost. As the two first objectives depend on the driving type the scaling has been done separately for each of the drive cycle sets described in Chapter 3. In total, each geometry will have 15 scaled versions (although not all are necessarily different). The resulting scaling factors and current ratings for each scaled version are presented in Table 8.2-8.4. The estimated mechanical stress and end-winding temperature of each version are also included in the tables. The investment cost for the versions in Table 8.2, the LCC of the versions in Table 8.3 and the NPV of the versions in Table 8.4 are all shown in Figure 8.9 (top plot).

Figure 8.9 shows that IPM geometry C gives the lowest investment cost (top plot) but its NPV of losses is highest among the included geometries for all the CADC and

Table 8.1 Geometrical variable values for the reference IPMs corresponding to geometries A-E

	A	B	C	D	E
β	0.188	0.248	0.298	0.245	0.254
f_{d}	0.727	0.614	0.629	0.824	0.695
f_{PM}	0.761	0.835	0.895	0.817	0.638
f_{air}	0.142	0.152	0.104	0.194	0.186
D_r [mm]	153.5	157.2	153.5	149.5	147.6
D_s [mm]	219.7	221.3	218.4	224.5	214.8
f_{t}	0.532	0.533	0.592	0.518	0.619
f_{y}	4.81	3.87	4.06	4.94	4.58

Table 8.2 IPM versions scaled for **minimum investment cost** of the IPM and converter, for each of the geometries A-E, using continuous k_w

	A	B	C	D	E
k_r	0.998	0.992	0.998	1.014	1.003
k_a	1.019	0.872	0.974	0.942	1.640
k_w	1.098	1.312	1.101	1.256	0.887
I_{resc} (RMS) [A]	359.8	346.9	338.8	366.3	350.6
S_{resc}* [MPa]	328.5	324.7	328.5	339.2	332.2
T_{ew} [°C]	124.9	121.4	124.8	102.4	124.9

* Using $S_{ref} = 330$ MPa

SCMD driving types (bottom plot). On the other hand, geometries D and E have lower NPV of losses (bottom plot), with D being the best option for the most pronounced city-driving (CADC-CC) and E being the best option for the highway types CADC-HWC and SCMD-HWT. Looking at a compromise between the investment cost and NPV of losses, such as the LCC (middle plot), the best option is either geometry A or B depending on the driving type.

Finally, it can be seen from the middle plot in Figure 8.9 that the balance between investment cost and losses varies with geometry, but it tends to even out somewhat and the LCC does not vary dramatically. Still, the results in Figure 8.9 indicate that there is some potential to improve the LCC and that the most beneficial IPM geometry will depend a bit on the driving type. However, combining scaling with changes in the geometry creates a large and complex computational challenge. So, aiming to improve the IPM geometry further, a meta-model based optimization of the IPM is done in Chapters 9 - 10.

Table 8.3 IPM versions scaled for **minimum LCC** of the IPM and converter, for each of the geometries A-E, using continuous k_w. The LCC considers 10 years of driving at 15 000 km/year for seven different driving distributions (CADC and SCMD)

Drive cycle combination	Scaling	Geometry				
		A	B	C	D	E
CADC-CC	k_r	1.002	0.997	1.001	0.998	1.005
	k_a	1.425	1.090	1.186	1.228	2.08
	k_w	0.901	1.140	0.970	1.113	0.775
	I_{resc} (RMS) [A]	322.9	319.9	318.7	327.6	330.0
	S_{resc}* [MPa]	331.3	328.0	330.7	328.7	333.3
	T_{ew} [°C]	97.5	100.9	106.1	91.2	105.6
CADC-RC	k_r	0.998	0.992	0.998	1.013	1.003
	k_a	1.023	0.872	0.972	0.933	1.640
	k_w	1.096	1.312	1.102	1.262	0.887
	I_{resc} (RMS) [A]	359.0	346.9	339.1	368.6	350.6
	S_{resc}* [MPa]	328.7	324.7	328.7	338.5	332.0
	T_{ew} [°C]	124.0	121.4	125.0	103.2	124.9
CADC-HWC	k_r	0.998	0.992	0.998	0.960	1.003
	k_a	1.019	0.872	0.972	0.971	1.640
	k_w	1.098	1.312	1.102	1.238	0.887
	I_{resc} (RMS) [A]	359.8	346.9	339.1	379.8	350.6
	S_{resc}* [MPa]	328.7	324.7	328.7	304.1	332.0
	T_{ew} [°C]	124.9	121.4	125.0	113.2	124.9
SCMD-CT	k_r	0.999	0.992	0.998	0.994	1.003
	k_a	1.092	0.872	0.973	0.983	1.640
	k_w	1.059	1.312	1.102	1.254	0.887
	I_{resc} (RMS) [A]	349.3	346.9	339.0	358.6	350.6
	S_{resc}* [MPa]	329.3	324.7	328.7	326.1	332.0
	T_{ew} [°C]	116.7	121.4	124.9	104.0	124.9
SCMD-RT	k_r	0.998	0.992	0.998	1.013	1.003
	k_a	1.023	0.872	0.972	0.933	1.640
	k_w	1.096	1.312	1.102	1.262	0.887
	I_{resc} (RMS) [A]	359.0	346.9	339.1	368.6	350.6
	S_{resc}* [MPa]	328.7	324.7	328.7	338.5	332.0
	T_{ew} [°C]	124.0	121.4	125.0	103.2	124.9
SCMD-HWT	k_r	0.998	0.992	0.998	1.013	1.003
	k_a	1.023	0.872	0.972	0.933	1.640
	k_w	1.096	1.312	1.102	1.262	0.887
	I_{resc} (RMS) [A]	359.0	346.9	339.1	368.6	350.6
	S_{resc}* [MPa]	328.7	324.7	328.7	338.5	332.0
	T_{ew} [°C]	124.0	121.4	125.0	103.2	124.9
SCMD-GT	k_r	0.998	0.992	0.998	0.942	1.003
	k_a	1.042	0.872	0.972	1.014	1.640
	k_w	1.086	1.312	1.102	1.256	0.887
	I_{resc} (RMS) [A]	356.2	346.9	339.1	366.3	350.6
	S_{resc}* [MPa]	328.7	324.7	328.7	339.2	332.0
	T_{ew} [°C]	122.0	121.4	125.0	102.4	124.9

* Using $S_{ref} = 330$ MPa

Table 8.4 IPM versions scaled for **minimum NPV of losses** of the IPM and converter, for each of the geometries A-E, using continuous k_w. The LCC considers 10 years of driving at 15 000 km/year for seven different driving distributions (CADC and SCMD)

Drive cycle combination	Scaling	Geometry				
		A	B	C	D	E
CADC-CC	k_r	1.005	1.000	1.002	1.001	1.007
	k_a	2.194	1.284	1.385	1.511	2.799
	k_w	0.659	1.005	0.864	0.967	0.639
	I_{resc} (RMS) [A]	307.3	311.1	311.0	312.9	315.4
	S_{resc}* [MPa]	333.3	330.0	331.3	330.7	334.6
	T_{ew} [°C]	83.3	92.3	96.9	84.3	91.6
CADC-RC	k_r	0.998	0.992	0.998	1.012	1.004
	k_a	1.071	0.872	0.973	0.893	1.784
	k_w	1.070	1.312	1.102	1.276	0.848
	I_{resc} (RMS) [A]	352.0	346.9	339.0	380.3	341.9
	S_{resc}* [MPa]	328.7	324.7	328.7	338.0	332.6
	T_{ew} [°C]	118.8	121.4	124.9	106.4	116.9
CADC-HWC	k_r	0.998	0.992	0.998	0.994	1.003
	k_a	1.019	0.872	0.972	0.889	1.640
	k_w	1.098	1.312	1.102	1.288	0.887
	I_{resc} (RMS) [A]	359.8	346.9	339.1	385.4	350.6
	S_{resc}* [MPa]	328.7	324.7	328.7	326.1	332.0
	T_{ew} [°C]	124.9	121.4	125.0	123.9	124.9
SCMD-CT	k_r	1.001	0.992	0.998	0.995	1.006
	k_a	1.267	0.875	0.974	1.023	2.224
	k_w	0.972	1.310	1.101	1.213	0.742
	I_{resc} (RMS) [A]	332.4	346.4	338.0	356.8	326.4
	S_{resc}* [MPa]	330.7	324.7	328.7	326.7	334.0
	T_{ew} [°C]	104.5	121.0	124.8	100.7	101.6
SCMD-RT	k_r	0.998	0.992	0.998	1.012	1.004
	k_a	1.071	0.872	0.973	0.893	1.784
	k_w	1.070	1.312	1.102	1.276	0.848
	I_{resc} (RMS) [A]	352.0	346.9	339.0	380.3	341.9
	S_{resc}* [MPa]	328.7	324.7	328.7	338.0	332.6
	T_{ew} [°C]	118.8	121.4	124.9	106.4	116.9
SCMD-HWT	k_r	0.998	0.992	0.998	0.998	1.004
	k_a	1.051	0.872	0.972	0.973	1.712
	k_w	1.081	1.312	1.102	1.102	0.867
	I_{resc} (RMS) [A]	354.8	346.9	339.1	339.0	346.0
	S_{resc}* [MPa]	328.7	324.7	328.7	328.7	332.6
	T_{ew} [°C]	121.1	121.4	125.0	124.9	120.5
SCMD-GT	k_r	0.999	0.992	0.998	0.994	1.005
	k_a	1.136	0.872	0.973	0.976	1.945
	k_w	1.036	1.312	1.102	1.259	0.807
	I_{resc} (RMS) [A]	344.1	346.9	339.0	360.0	334.2
	S_{resc}* [MPa]	328.7	324.7	328.7	326.1	333.3
	T_{ew} [°C]	112.9	121.4	124.9	104.8	109.9

* Using $S_{ref} = 330$ MPa

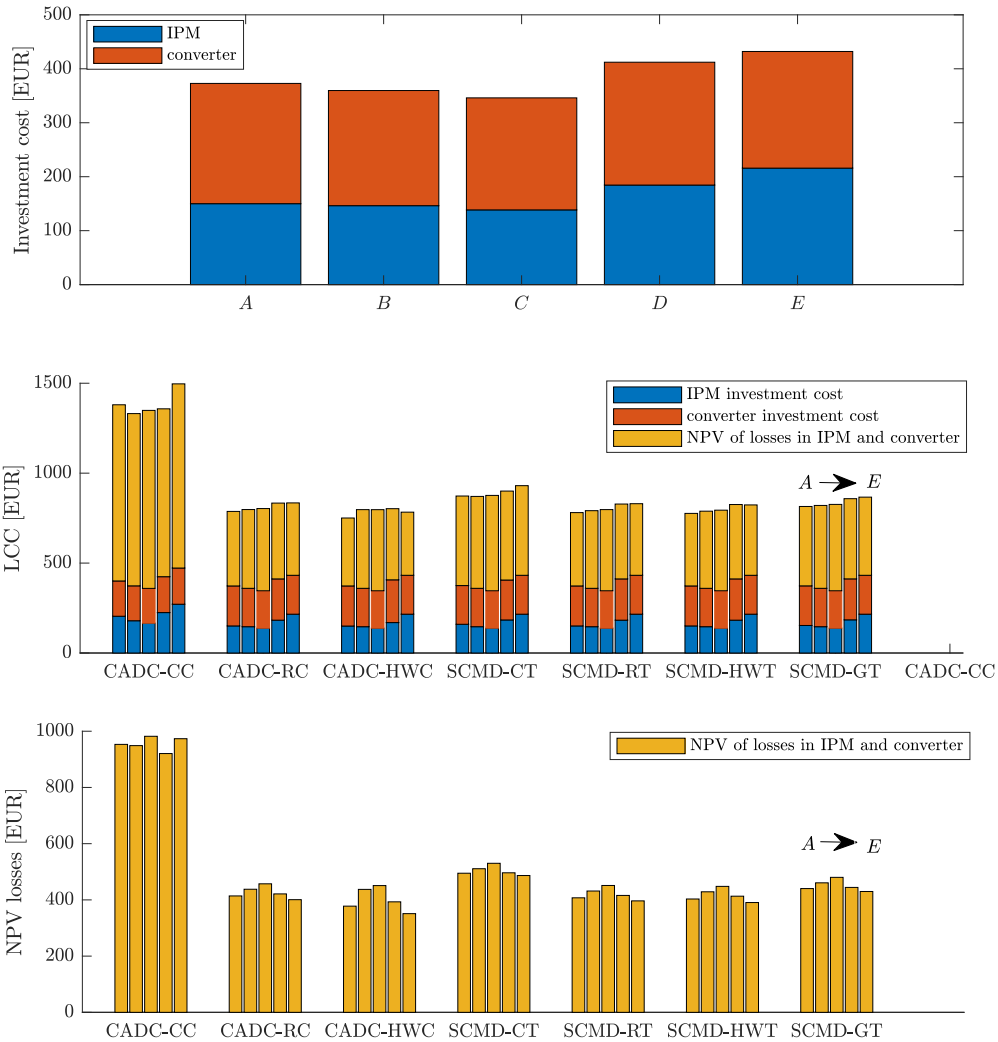

Figure 8.9 Results of scaling for lowest investment cost, top, lowest LCC, middle, and lowest NPV of losses, bottom. The investment cost and losses consider both IPM and converter. Both the middle and bottom plots consider 10 years of driving with 15 000 km/year and the scaling is done individually for each different driving types (CADC and SCMD) and each IPM geometry A-E.

Chapter 9

Procedure for optimization of IPM geometry against driving distribution

9.1 Optimization problem set-up

This section describes the set-up of an optimization problem where the IPM geometry is optimized for an energy distribution corresponding one or more drive cycles.

9.1.1 Optimization objective

The objective in the optimization has been minimization of the LCC of both the IPM and inverter. The optimization is done separately with different life-time values considered in the objective. The life-time affects how the investment cost and the losses during driving are balanced against each other. The LCC is calculated as in Chapter 8, using aggregated driving distributions as described in Chapter 3. Since the driving is aggregated into bins in a torque versus speed grid, any number of drive cycles can be included without increasing the computational cost of the optimization. However, using the entire driving energy distribution also requires computation of the full efficiency map of the IPM in each evaluation of the objective function. That is a significant computational burden, involving >100 electromagnetic FEAs, as described in Chapter 4. Therefore, the optimization problem needs to be set-up carefully when it comes to the choice of variables and handling of constraints, to keep it manageable time-wise.

9.1.2 Choice of variables

The optimization is done on the geometric variables, $(\beta, f_{\mathrm{d}}, f_{\mathrm{PM}}, f_{\mathrm{air}}, D_r, D_s, f_{\mathrm{t}}, f_{\mathrm{y}})$, described in Section 5.1. The ranges of the variables are presented in Table 9.1. The required rib thickness is based on the values of the rotor variables $(\beta, f_{\mathrm{d}}, f_{\mathrm{PM}}, f_{\mathrm{air}}, D_r)$ using the look-up table,$\mathbf{t}^*_{\mathbf{rib}}$, described in Section 5.2.

9.1.3 Function evaluation

An overview of the computational steps involved in each function evaluation (i.e. the computation of LCC for the IPM and inverter based on the IPM geometry variables) is shown in Figure 9.1. Further description of the intermediate steps regarding the electromagnetic FEA, driving distribution and scaling can be found in Chapter 4, Chapter 3 and Chapter 8 respectively.

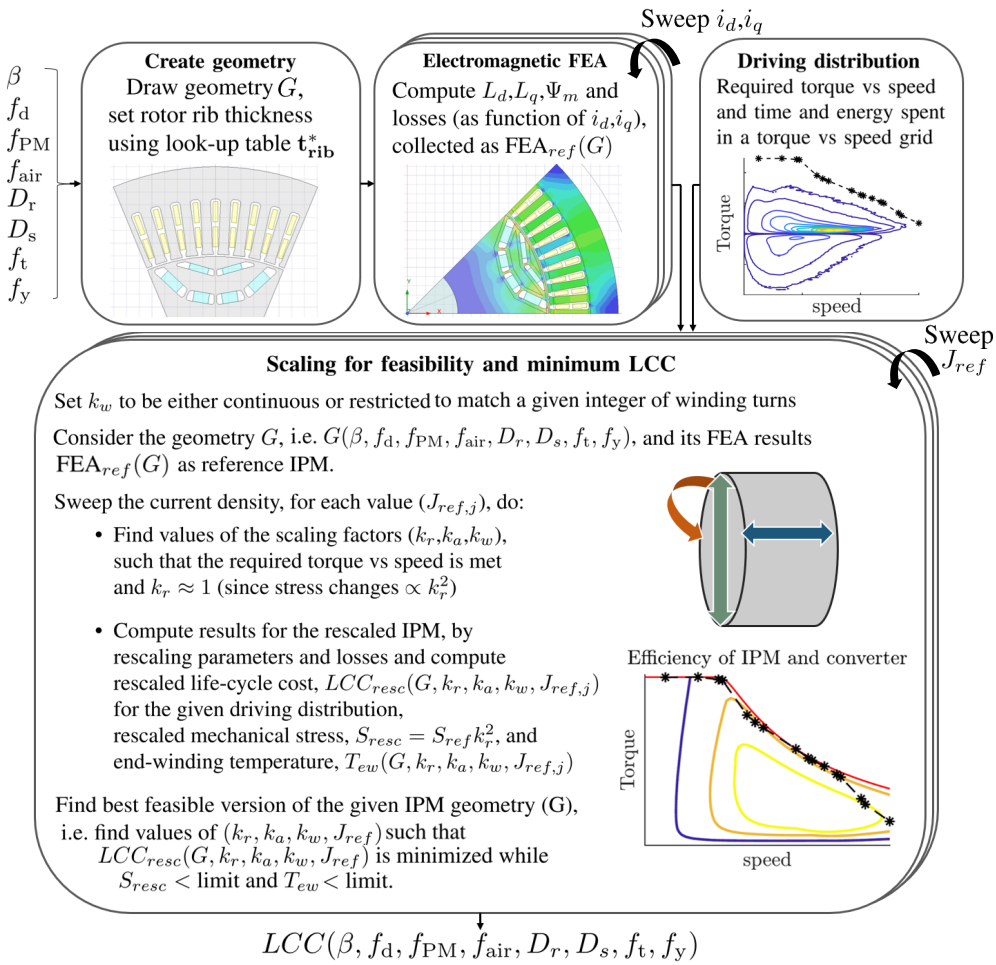

Figure 9.1 Overview of the workflow for computing the LCC potential, given a combination of the geometrical variables $(\beta, f_\mathrm{d}, f_\mathrm{PM}, f_\mathrm{air}, D_r, D_s, f_\mathrm{t}, f_\mathrm{y})$. The electromagnetic FEA and scaling steps in the workflow involve several iterations and are illustrated as stacks.

Table 9.1 Geometrical variables and their ranges used in the optimization

Variable	Minimum	Maximum
β	0	0.3
f_{d}	0.6	0.9
f_{PM}	0.6	0.9
f_{air}	0.1	0.2
D_r	147.2 mm	161 mm
D_s	200 mm	230 mm
f_{t}	0.5	0.62
f_{y}	3.8	5.0

9.1.4 The use of scaling for performance requirements and thermal and mechanical constraints

Thermal and mechanical aspects are considered in the optimization. However, considering that a function evaluation is a substantial computational burden it is crucial to keep the number of variables low and to avoid time-consuming evaluation of infeasible designs. Therefore, performance requirements as well as the thermal and mechanical constraints are managed during the scaling step.

Here scaling has been used with the aim of creating the best feasible version of each IPM geometry. Each IPM geometry is rescaled to precisely meet the peak performance requirements (i.e. a required set of power versus speed values). When the IPM is rescaled, the thermal and mechanical feasibility is also assessed and each given IPM geometry is scaled to minimize the objective function while remaining feasible. The mechanical constraint is solely aimed at limiting the stress in the rotor laminate and the thermal constraint only targets the end-winding temperature during maximum current operation for a time duration corresponding to the vehicle accelerating from standstill to top speed on a flat road. The evaluation of thermal and mechanical feasibility is done as described in Section 5.2 and Section 5.3. Further description of the applied scaling approach is given in Chapter 8. Before scaling, the thickness of the rotor ribs are set for a maximum von Mises stress in the rotor laminate (at top speed) of 330 MPa using the look-up table,$\mathbf{t}^*_{\mathbf{rib}}$. However, to allow some room for changes in the scaling the limit on rotor stress, after scaling, is set to 380 MPa (which corresponds to allowing up to 7.3% increase in radius during scaling). The limit used for end-winding temperature is 125°C (after running full current for the time needed to reach top speed, starting from 70°C).

9.2 Optimization procedure

The overall optimization work-flow is illustrated in Figure 9.2. The evaluation of LCC from geometrical inputs, $LCC(\beta, f_{\mathrm{d}}, f_{\mathrm{PM}}, f_{\mathrm{air}}, D_r, D_s, f_{\mathrm{t}}, f_{\mathrm{y}})$, in Figure 9.2 refers to the procedure in Figure 9.1 although not all intermediate steps are shown here.

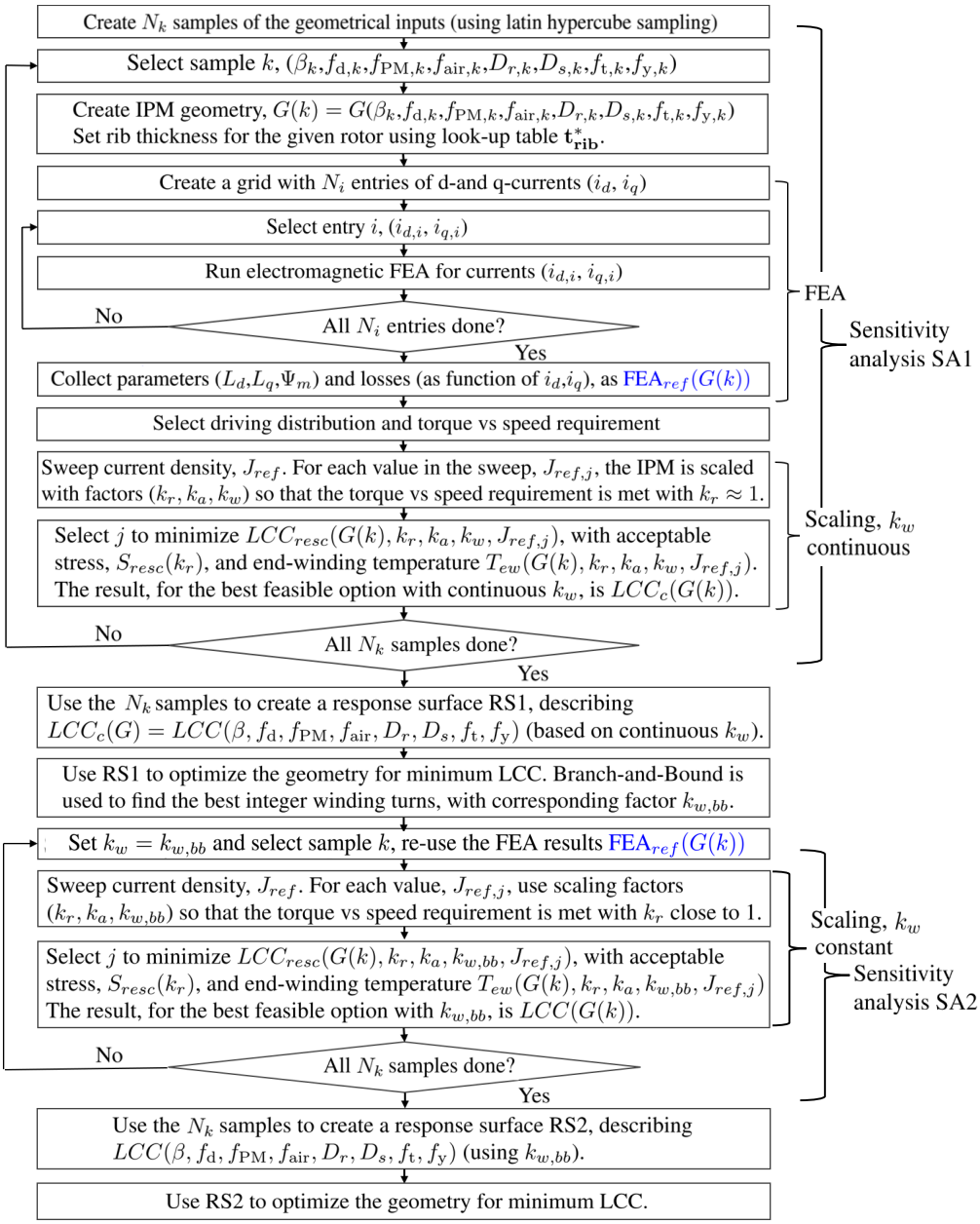

Figure 9.2 Workflow of the LCC minimization problem. This workflow has been used for different driving types (corresponding to different driving energy distributions). The LCC includes investment cost and cost of losses of both IPM and inverter.

The optimization procedure involves two rounds of the sequence: sensitivity analysis (SA) - response surface (RS) creation - optimization using the response surface, these rounds are referred to as 1 and 2 respectively. The difference between the rounds is the handling of the rewinding factor, k_w, used in the scaling. Initially, this optimization was attempted with k_w being selected individually for each geometry from a set of available values corresponding to different integer winding turns. However, that approach led to significant issues with getting a high CoP in the response surface step. These issues appeared to be related to the step-wise changes in k_w since either setting k_w to be continuous or locking k_w to a given value gave substantial improvement in the CoP of the response surface.

This lead to the choice of running the optimization in two rounds, where round 1 is a relaxation of the problem (k_w continuous). Once the response surface RS1 is created it allows several optimizations to be done quickly. This allows the best integer number of turns (with associated value $k_{w,bb}$), to be found using the Branch-and-Bound approach, which is a systematic way of adding constraints and solving the optimization problem until the integer solution is found (see Section 2.8.3 for further description). Thereafter, round 2 is performed to target $k_{w,bb}$ specifically. While the main aim of round 1 is to identify the best integer number of winding turns for use in round 2, it also serves another purpose. Comparing the result of round 1 and 2 gives an indication of how much the selected winding layout compromises the reachable LCC.

9.3 Overview of the applied optimization procedure

This section presents an overview of the optimization procedure applied to a case with 10 years of driving with the SCMD-GT driving type. This example is associated with the IPM design referred to as $G^{GT}_{10Y,bb}$, which is one of the optimized designs presented in the coming Chapter 10.

First, 600 IPM geometries are created, using latin hypercube sampling of the search space spanned by the 8 geometrical variables ($\beta, f_\mathrm{d}, f_\mathrm{PM}, f_\mathrm{air}, D_r, D_s, f_\mathrm{t}, f_\mathrm{y}$). These 600 IPMs are evaluated using electromagnetic FEA, with > 100 combinations of i_d and i_q values for each IPM. Thereafter, each IPM is post-processed using scaling with continuous k_w and the resulting LCC and rewinding factor $k_{w,c}$, for the best feasible version of each IPM geometry, are collected. Based on the collected results, MoPs are created (one for LCC and another for $k_{w,c}$).

These MoPs are used together with a GA, both to find the design $G^{GT}_{10Y,c}$ and to find the most promising rewinding factor, referred to as $k_{w,bb}$. Minimizing LCC based on the MoP, without any constraint on k_w results in the design $G^{GT}_{10Y,c}$. However, the rewinding factor of $G^{GT}_{10Y,c}$ is $k_{w,c} = 1.16$, which can not be realized with the winding configuration used here (two-layer winding with three slots per pole and phase). The reference IPM has 18 turns per pole and phase (4 parallel paths), which corresponds to $k_w = 1$. For example, increasing to 24 turns per pole and phase (4 parallel paths) is feasible, and gives $k_w = 4/3 \approx 1.33$. Overall, respecting the integer nature of the given winding configuration turn the minimization of LCC into a discrete optimization problem. Here, a Branch-and-Bound approach was used with the MoPs for LCC and $k_{w,c}$. Essentially, optimization was repeated twice (using the created MoPs), first minimizing LCC with

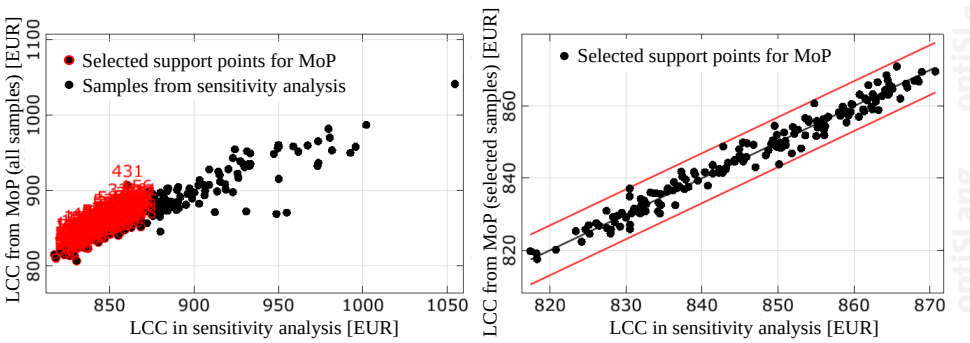

Figure 9.3 Example of selection of support points for MoP creation, for LCC with 10 years of driving (SCMD-GT driving type, 15 000 km/year) and $k_{w,bb} = 1$. The left plot shows the full set of feasible results (black) along with the subset selected for creating the final MoP. The right plot shows the prediction of the final MoP.

the constraint $k_{w,c} \leq 1$ added and then minimizing LCC with the constraint $k_{w,c} \geq 4/3$ added. The first optimization converged to a design with $k_{w,c} \approx 1$ (according to the MoP) and the second optimization converged to a design with $k_{w,c} \approx 1.33$ (according to the MoP). However, the LCC values predicted by the MoP for these two optimization cases are fairly close and, since MoPs are never perfect, it is considered safest to try both $k_{w,bb} = 1$ and $k_{w,bb} = 4/3$. Doing so showed $k_{w,bb} = 1$ to be the better option, while $k_{w,bb} = 4/3$ leads to significant issues with finding feasible versions in the scaling step.

The existing FEA results for the 600 IPM geometries are post-processed again, this time scaling based on $k_w = k_{w,bb} = 1$ and a new MoP is created for LCC. Out of these 600 IPM geometries, nearly 500 are geometrically feasible and, after scaling, 290 meet all constraints (i.e. performance met, with rotor stress and end-winding temperatures below limits). Finally, 165 scaled results with good objective values (i.e. low LCC) are selected for creating the MoP, as illustrated in Figure 9.3.

The creation of the MoP was an iterative process and different selections were tested. While it is possible to create a MoP using nearly all the 290 feasible results (referred to as support points in the software Ansys OptiSLang), it typically leads to a poorer fit for the design with lowest LCC. Here, using around 50%-70% of the feasible results as support points for the MoP gave the best results. A better solution would be to use the adaptive sampling available in OptiSLang, allowing the software to focus the MoP towards the most promising areas of the search space. However, this case is one of several in Chapter 10, where seven different driving distributions are covered (combined with different lifetime values and the options of continuous and discrete k_w in the scaling). Thus, there are many MoPs involved. Therefore, it was considered too time consuming to make adaptive sampling for each individual MoP. Instead the full set of samples (the 600 IPM geometries) is kept the same, but the subset selected for MoP generation is focused on the most promising samples for each individual MoP.

An overview of the MoP used for $G^{GT}_{10Y,bb}$ (with $k_{w,bb} = 1$) is shown in Figure 9.4. This MoP, which has a CoP of 97%, is used together with a GA, for LCC minimization, as shown in Figure 9.5.

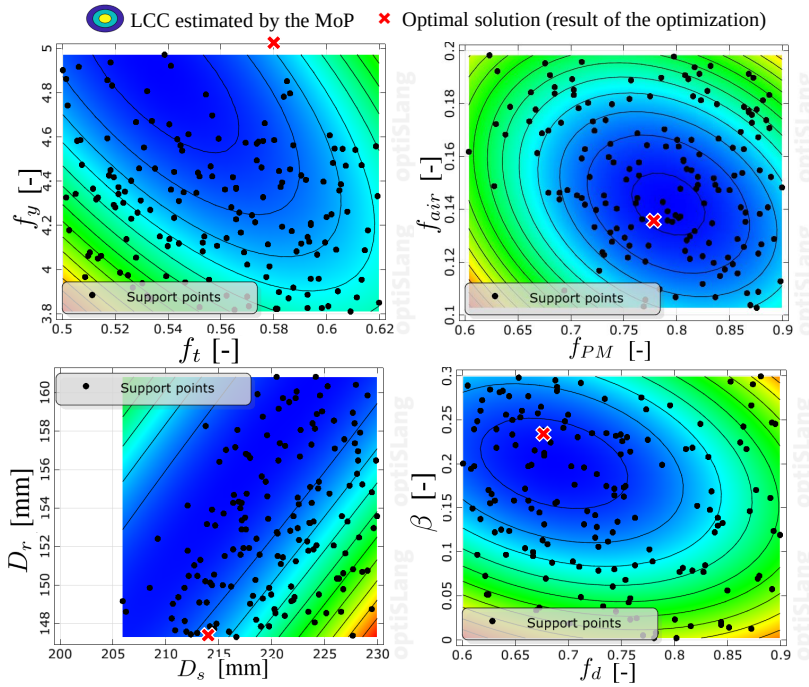

Figure 9.4 MoP describing LCC, for 10 years of driving (SCMD-GT driving type, 15 000 km/year) and $k_{w,bb} = 1$, as function of the input variables (β, f_d, f_PM, f_air, D_r, D_s, f_t, f_y) for the IPM geometry. The MoP, which has eight dimensions, is visualized as four projections, each with two variables.

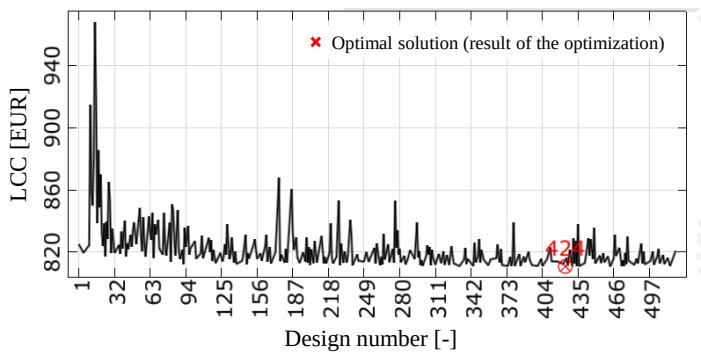

Figure 9.5 Example of GA used for LCC minimization, based on the MoP for the case with 10 years of driving (SCMD-GT driving type, 15 000 km/year) and $k_{w,bb} = 1$.

The population size in the GA is 20, half of the initial population consists of the best designs from the sensitivity analysis (i.e. SA2). The LCC of the final IPM design, $G^{GT}_{10Y,bb}$, is predicted as 810.8 EUR using the MoP and GA. Evaluating the same geom-

etry, using the full process of FEA and scaling, results in an LCC of 812.2 EUR. The design $G^{GT}_{10Y,bb}$ is also indicated with a red cross in Figure 9.4. The eight-dimensional surface of the MoP is, in Figure 9.4, projected to four different planes (sets of two input variables each). Note that these projections are far from all the dependencies in the MoP, and only serve as examples for some selected relations.

For brevity, only the case of $G^{GT}_{10Y,bb}$ is shown here, but the same procedure has been used for all the optimized IPM designs presented in Chapter 10.

The vast majority of the computational time in the optimization procedure is spent in the sensitivity analysis (i.e. evaluation of the 600 IPM geometries). The computational time for one IPM geometry is around 1 hour and 20 minutes, of which around 1 hour consists of FEA (running 12 simulations in parallel) and around 20 minutes consists of the post-processing/scaling (where several driving distributions can be run in parallel), using a PC with 12 cores, 2.1 GHz processor and 128 GB RAM.

Chapter 10

Results of IPM optimization for different types of driving

This chapter presents the results from using the IPM geometry optimization described in Chapter 9 for seven different driving distributions (the CADC and SCMD described in Chapter 3 that represent various combinations of city, rural and highway driving. Further, the optimization is done considering three different values of lifetime in the LCC calculation. Note that the lifetime here should simply be seen as the number of years of driving considered in the IPM optimization, and not necessarily the actual lifetime of the BEV. The number of years has been varied strongly, with 0, 10 and ∞ years included. The extreme cases, with 0 and ∞ years, correspond to minimization of the investment cost of the IPM converter and to minimization of the driving energy loss respectively. The case in-between, with 10 years, serves as a more realistic lifetime value. Naturally, the minimization of investment cost will be independent of driving distribution, while the influence of the driving distribution can be expected to be largest when minimizing the driving energy loss. Together, the results cover the influence of driving type for different balancing between investment cost and driving losses.

While the combination of several different driving distributions and objectives offer a wider scope in the results, it also leads to a large number of resulting IPM geometries. Therefore, the geometries are named systematically, where the notation $G^{GT}_{10Y,c}$ refers to the geometry resulting from the minimization of LCC based on 10 years of driving (indicated by the first subscript) for the drive cycle set SCMD-GT (indicated by the superscript). A second subscript is used, where $_c$ indicates that continuous k_w has been allowed, while $_{bb}$ indicates that k_w has been fixed to the value obtained from Branch-and-Bound (corresponding to a real winding configuration). Note that the letter G indicates both the IPM geometry together with a specific scaling and current rating.

10.1 Optimized IPM geometries for the different driving distributions

10.1.1 IPM geometries with generalized winding configuration

The IPM designs resulting from the LCC minimization where k_w is a continuous variable in the scaling, are shown for CADC in Figure 10.1 and for SCMD in Figure 10.2. For each drive cycle combination, the designs from investment cost minimization (0Y), LCC minimization (10Y) and driving energy loss minimization (∞Y) are shown. The values of the geometry variables as well as scaling factors and current ratings are presented in Table 10.1.

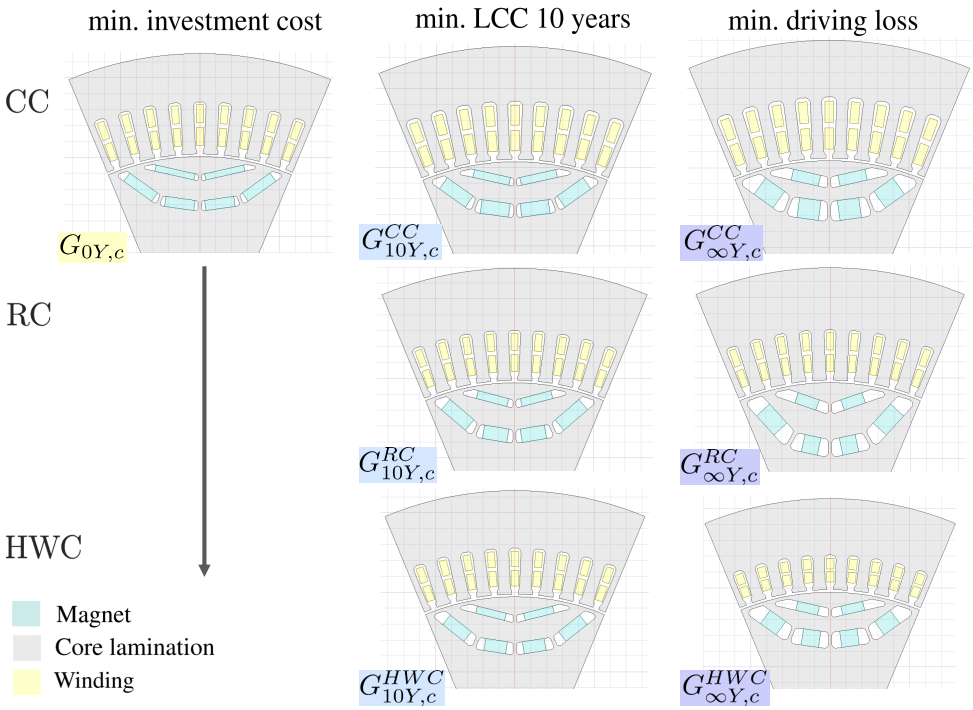

Figure 10.1 IPM geometries resulting from the optimizations with **continuous k_w in the scaling**. The size of each IPM reflects its diameter including scaling. The cases of minimization of investment cost (left column, yellow label), minimization of driving energy loss (right column, purple labels) and minimization of LCC with 10 years of driving (middle column, blue labels), are included for each of the driving distributions in **CADC**.

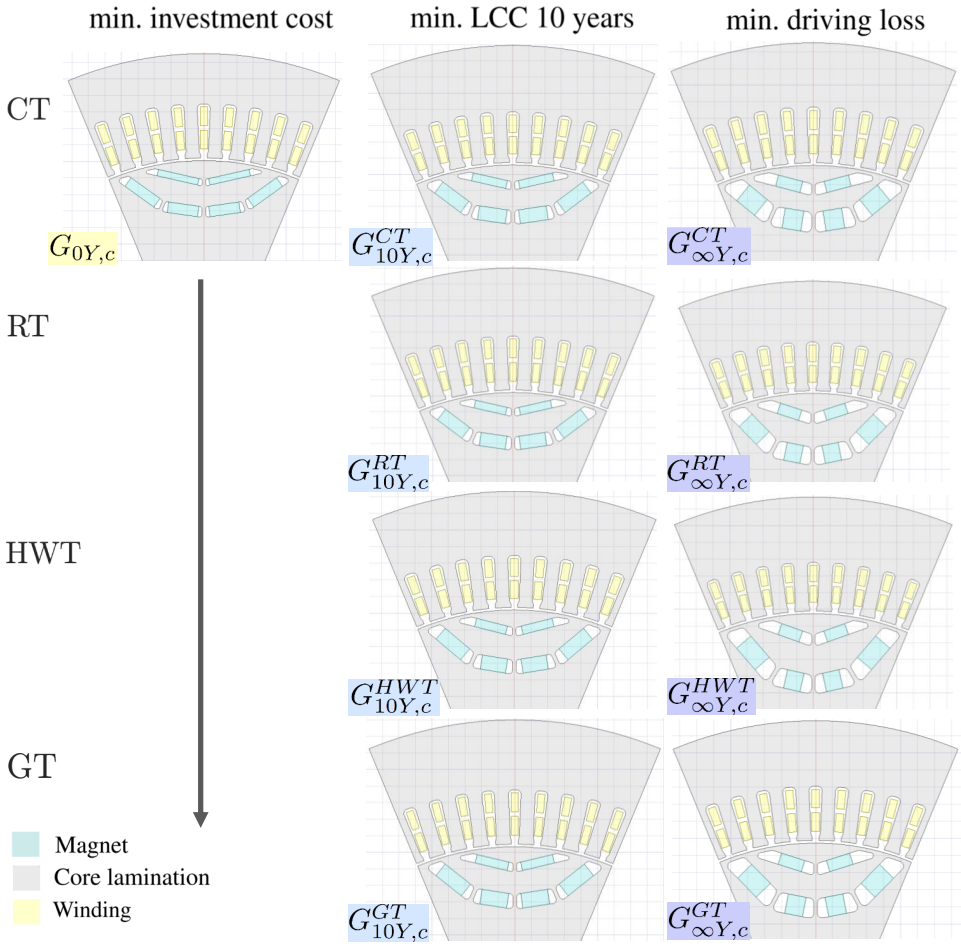

Figure 10.2 IPM geometries resulting from the optimizations with **continuous k_w in the scaling**. The size of each IPM reflects its diameter including scaling. The cases of minimization of investment cost (left column, yellow label), minimization of driving energy loss (right column, purple labels) and minimization of LCC with 10 years of driving (middle column, blue labels), are included for each of the driving distributions in **SCMD**.

Comparing the IPMs in a given column in Figure 10.1 - Figure 10.2 shows the difference with driving type. Overall, the IPM design for the most pronounced city driving type (the CADC-CC) and most pronounced highway driving type (the CADC-HWC) stand out while the IPMs for the other driving types are similar in appearance. Comparing the IPMs in a given row in Figure 10.1 - Figure 10.2 shows the difference with the optimization objective. For all driving types, there is a significant difference in the IPM geometry between investment cost minimization, LCC minimization and driving energy loss minimization. Further analysis of the design features are given in Section 10.2, where results for both continuous and fix k_w are combined.

Table 10.1 Values of geometry variables and scaling factors for the IPM designs resulting from the optimizations with **continuous k_w in the scaling**. The cases of minimization of investment cost (yellow fill), minimization of driving energy loss (purple fill) and minimization of LCC with 10 years of driving (blue fill), are included for seven driving distributions related to CADC and SCMD.

IPM	β [-]	f_d [-]	f_{PM} [-]	f_{air} [-]	D_r [mm]	D_s [mm]	f_t [-]	f_y [-]	k_r [-]	k_a* [-]	k_w [-]	I_{resc} [A]
$G_{0Y,c}$	0.300	0.60	0.90	0.11	150.5	215.2	0.59	3.80	0.997	0.95	1.15	344.6
$G^{CC}_{10Y,c}$	0.275	0.60	0.90	0.14	153.6	227.0	0.50	5.00	0.995	0.99	1.25	322.2
$G^{CC}_{\infty Y,c}$	0.300	0.60	0.73	0.20	154.5	230	0.51	5.00	1.002	1.90	0.87	318.1
$G^{RC}_{10Y,c}$	0.227	0.70	0.84	0.15	147.2	219.3	0.59	5.00	0.997	1.02	1.13	344.6
$G^{RC}_{\infty Y,c}$	0.237	0.84	0.60	0.20	147.2	218.6	0.60	4.81	1.005	2.10	0.75	343.3
$G^{HWC}_{10Y,c}$	0.294	0.65	0.71	0.13	147.2	214.0	0.57	4.75	1.000	1.19	0.99	362.9
$G^{HWC}_{\infty Y,c}$	0.300	0.60	0.60	0.17	147.2	206.3	0.53	5.00	1.006	2.02	0.86	341.2
$G^{CT}_{10Y,c}$	0.249	0.68	0.82	0.14	147.8	220.5	0.59	5.00	0.997	1.04	1.12	345.8
$G^{CT}_{\infty Y,c}$	0.295	0.66	0.63	0.20	151.7	225.4	0.59	4.77	1.002	1.79	0.88	343.3
$G^{RT}_{10Y,c}$	0.216	0.65	0.83	0.14	152.0	230.0	0.62	5.00	0.997	0.94	1.15	352.9
$G^{RT}_{\infty Y,c}$	0.250	0.80	0.60	0.20	147.2	216.9	0.57	4.96	1.004	1.98	0.79	344.9
$G^{HWT}_{10Y,c}$	0.206	0.70	0.80	0.14	151.9	223.2	0.57	4.87	0.997	0.98	1.13	354.4
$G^{HWT}_{\infty Y,c}$	0.193	0.90	0.61	0.20	147.3	217.2	0.61	4.82	1.006	2.12	0.73	341.0
$G^{GT}_{10Y,c}$	0.197	0.67	0.85	0.15	153.3	230.0	0.61	4.97	0.996	0.95	1.16	343.3
$G^{GT}_{\infty Y,c}$	0.247	0.79	0.63	0.20	147.2	218.8	0.58	4.93	1.003	1.78	0.86	346.8

* Using a reference stack length of 120 mm

An overview of the results for each of the IPM designs are shown in Table 10.2. As expected, thanks to the flexibility in k_w, the rotor stress S_{resc} is not strongly affected by the scaling and therefore remains close to the 330 MPa of each reference IPM in all cases. The end-winding temperature (T_{ew}) varies more, with the lowest values seen for the most pronounced city driving type (CADC-CC) and, especially, for the minimization of driving energy losses. As lower T_{ew} can be expected to correlate with larger amount of copper and lower resistive losses, the results agree with resistive loss reduction becoming more important both in case of city driving and if focus is only on the losses.

As expected, the driving energy losses are lowest for the IPM from the loss minimizations. However, the reduction of the losses comes with a rather dramatic increase in investment cost, compared to the IPMs from LCC minimization. Depending on the driving distribution, the reduction in losses (of the IPM and converter during driving) is around 1-6%, while the investment cost (of the IPM and converter) is around 17-40%. Even more dramatic is the increase in IPM weight, and the heaviest IPM in in Table 10.2 ($G^{CC}_{\infty Y,c}$) weighs around three times as much as the lightest IPM ($G_{0Y,c}$). On the other hand, minimizing solely the investment cost gives only a rather small reduction in the investment cost, of 15-20 EUR, compared to the IPMs from LCC minimization.

Table 10.2 Key results for the IPM designs resulting from the optimizations with **continuous** k_w **in the scaling**. The cases of minimization of investment cost (yellow fill), minimization of driving energy loss (purple fill) and minimization of LCC with 10 years of driving (blue fill), are included for seven driving distributions related to CADC and SCMD.

IPM version	Investment cost* [EUR]	Energy loss*,** [EUR]	Efficiency ** [%] IPM	Efficiency ** [%] converter	S_{resc} *** [MPa]	T_{ew} [°C]	Weight**** [kg] PM	Weight**** [kg] Copper	Weight**** [kg] IPM
$G_{0Y,c}$	348.5	-	-	-	327.8	119.7	1.2	3.6	29.0
$G^{CC}_{10Y,c}$	368.9	29.6	94.9	95.5	326.4	96.5	1.6	5.0	33.3
$G^{CC}_{\infty Y,c}$	517.6	29.3	95.2	95.3	331.3	80.9	4.2	6.9	85.8
$G^{RC}_{10Y,c}$	364.8	13.3	95.4	97.8	327.8	124.9	1.5	3.5	32.0
$G^{RC}_{\infty Y,c}$	498.9	12.6	96.0	97.5	333.3	94.4	2.9	5.2	62.7
$G^{HWC}_{10Y,c}$	380.4	11.7	96.2	98.6	330.1	124.9	1.4	3.5	35.3
$G^{HWC}_{\infty Y,c}$	444.4	11.0	96.5	98.6	334.2	124.9	2.4	3.7	53.7
$G^{CT}_{10Y,c}$	366.6	15.9	95.1	96.7	328.0	124.9	1.5	3.5	32.9
$G^{CT}_{\infty Y,c}$	478.4	15.2	95.5	96.6	331.3	96.4	2.7	5.3	56.9
$G^{RT}_{10Y,c}$	364.8	13.2	95.1	97.3	327.8	124.9	1.3	3.5	32.7
$G^{RT}_{\infty Y,c}$	481.5	12.5	95.7	97.0	333.0	97.0	2.7	5.1	58.0
$G^{HWT}_{10Y,c}$	367.9	12.9	95.2	97.5	328.0	124.6	1.4	3.5	31.9
$G^{HWT}_{\infty Y,c}$	499.8	12.3	95.9	97.2	333.8	98.2	3.1	4.7	62.6
$G^{GT}_{10Y,c}$	363.2	14.2	95.0	97.1	327.4	124.9	1.4	3.4	32.8
$G^{GT}_{\infty Y,c}$	467.1	13.6	95.6	96.9	332.2	97.3	2.6	4.9	53.4

* For only IPM and converter, ** Motoring, in the driving distribution in the optimization
*** Using $S_{ref} = 330$ MPa, **** Excluding housing and shaft

10.1.2 IPM geometries with real winding configuration

The IPM designs resulting from the LCC minimization where k_w has a fix value in the scaling, are shown for CADC in Figure 10.3 and for SCMD in Figure 10.4. For each drive cycle combination, the designs from investment cost minimization (0Y), LCC minimization (10Y) and driving energy loss minimization (∞Y) are shown. The values of the geometry variables as well as scaling factors and current ratings are presented in Table 10.3. Note that the value of k_w is set constant within each optimization, but it may vary between different optimizations.

Although, the IPM designs in Figure 10.3 - 10.4 show some differences compared to their counterparts in Section 10.1.1 (for the case of continuous k_w in the scaling), the main trends remain. Again, the CADC-CC and CADC-HWC stand out while the IPM designs for the other driving distributions appear quite similar for the optimization minimizing LCC for 10 years of driving (middle column). The IPM design differences among the driving distributions are largest for the case where the driving energy losses are minimized (rightmost column). Further analysis of the design features are given in Section 10.2, where results for both continuous and fix k_w are combined.

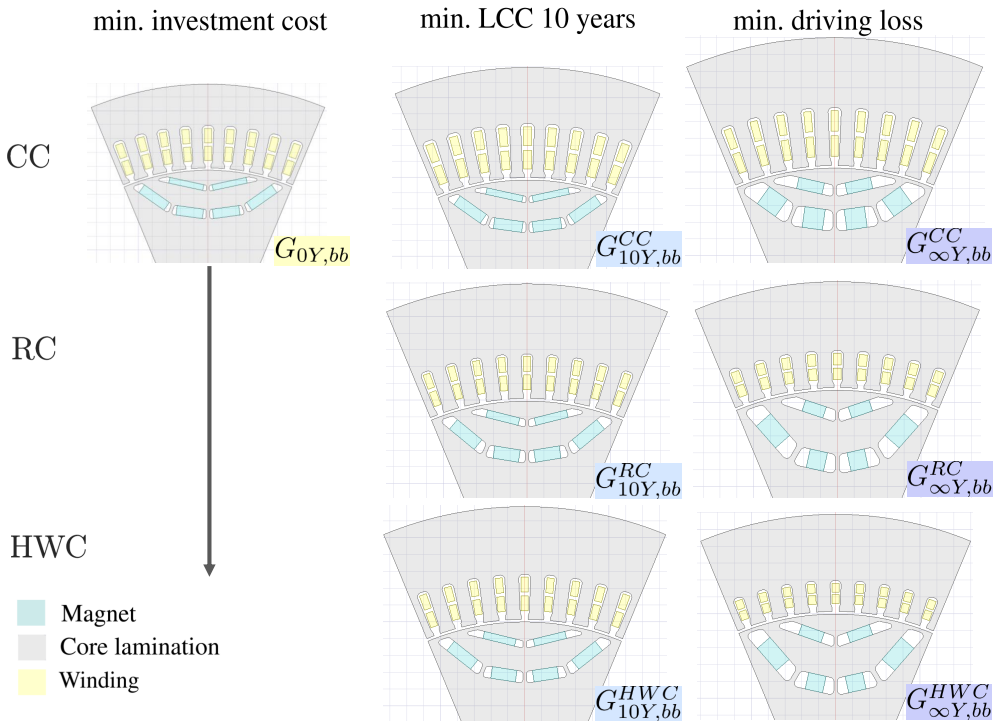

Figure 10.3 IPM geometries resulting from the optimizations with **fixed k_w in the scaling**. The size of each IPM reflects its diameter including scaling. The cases of minimization of investment cost (yellow label), minimization of driving energy loss (purple labels) and minimization of LCC with 10 years of driving (blue labels), are included for each of the driving distributions in **CADC**.

An overview of the results for each of the IPM designs are shown in Table 10.4. The rotor stress S_{resc} varies significantly more here, compared to the case with continuous k_w in the scaling (see Table 10.2). This is expected, since restricting k_w to a fixed value makes larger changes in k_r necessary to match the performance requirements. The larger changes in k_r also gives larger changes in S_{resc}.

It should also be noted that there is no guarantee that the optimization results in a fully feasible design since the MoPs are not exact and there are limitations to the scaling. Therefore, slight violations of constraints can still occur, like S_{resc} for $G^{HWT}_{10Y,bb}$.

There is a notable trend of increased stress, i.e. $k_r > 1$, with several of the designs pushing close to the stress constraint of 380 MPa used for the scaling. On the other hand, the IPM design for minimization of investment cost ($G^{HWC}_{\infty Y,bb}$, yellow fill in Table 10.4) instead shows a significant reduction in stress, i.e. $k_r < 1$. This can also potentially be problematic from a manufacturing perspective since it means that the size of the geometric cross-section is decreased. For example, smaller slot openings can lead to difficulties with inserting the winding and a smaller air-gap is more sensitive to manufacturing tolerances.

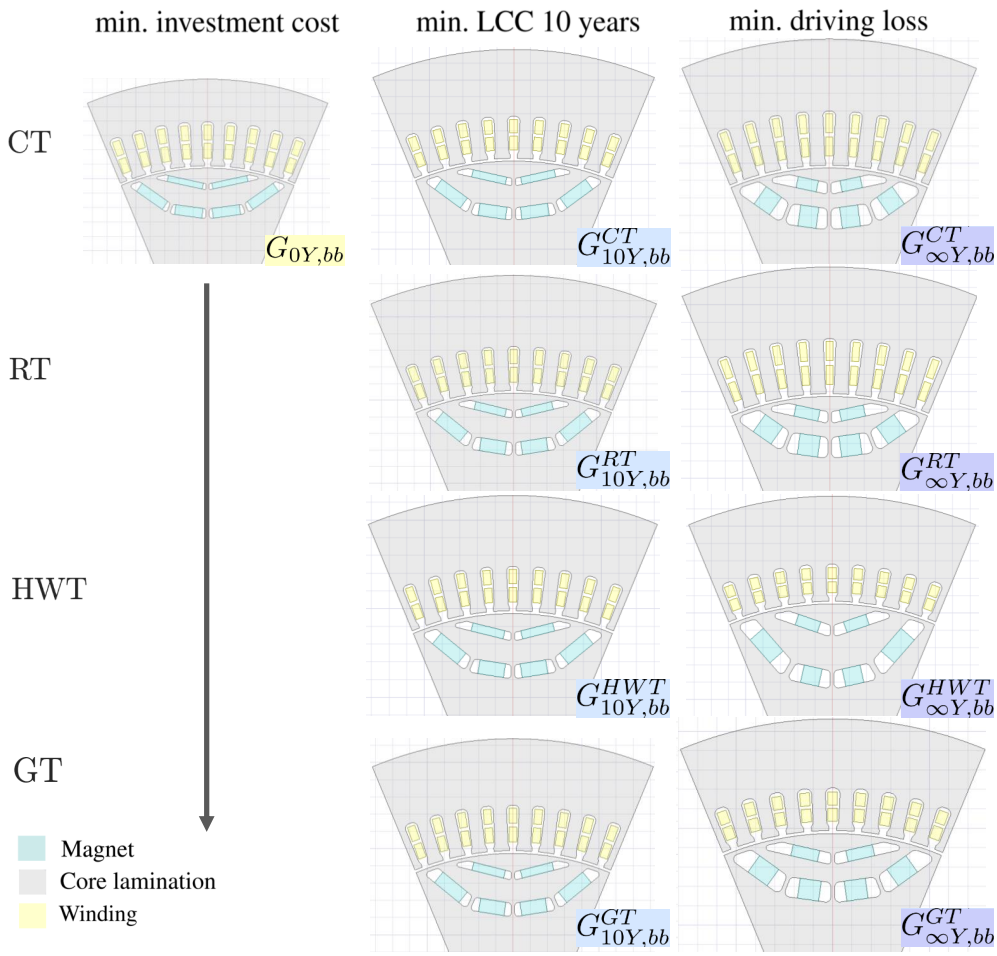

Figure 10.4 IPM geometries resulting from the optimizations with **fixed k_w in the scaling**. The size of each IPM reflects its diameter including scaling. The cases of minimization of investment cost (yellow label), minimization of driving energy loss (purple labels) and minimization of LCC with 10 years of driving (blue labels), are included for each of the driving distributions in **SCMD**.

It was necessary to allow some variation in k_r during the scaling, to reach sufficient number of feasible IPM designs in the optimization procedure. However, it appears that this freedom in k_r is exploited by the optimization algorithm to improve the objective value by pushing the IPM sizes further towards the extremes. An indication of this is that the variation in investment cost and IPM weight is even larger in Table 10.4, compared to Table 10.2. While this is not surprising, it is not a desired effect here. Still, it is considered that the changes in k_r are sufficiently small to be acceptable here.

Table 10.3 Values of geometry variables and scaling factors for the IPM designs resulting from the optimizations with **fix k_w in the scaling**. The cases of minimization of investment cost (yellow fill), minimization of driving energy loss (purple fill) and minimization of LCC with 10 years of driving (blue fill), are included for seven driving distributions related to CADC and SCMD.

IPM	β [-]	f_d [-]	f_{PM} [-]	f_{air} [-]	D_r [mm]	D_s [mm]	f_t [-]	f_y [-]	k_r [-]	k_a* [-]	k_w [-]	I_{resc} [A]
$G_{0Y,bb}$	0.259	0.60	0.90	0.11	157.3	219.0	0.55	3.80	0.881	1.27	1.00	329.2
$G^{CC}_{10Y,bb}$	0.269	0.60	0.90	0.12	148.1	219.2	0.53	5.00	0.983	1.29	1.00	317.2
$G^{CC}_{\infty Y,bb}$	0.300	0.60	0.66	0.20	152.2	230.0	0.61	5.00	1.058	2.69	2/3	317.4
$G^{RC}_{10Y,bb}$	0.236	0.68	0.79	0.13	149.4	219.5	0.62	5.00	1.056	1.11	1.00	336.5
$G^{RC}_{\infty Y,bb}$	0.262	0.60	0.68	0.20	147.2	221.9	0.62	5.00	1.056	2.10	2/3	334.2
$G^{HWC}_{10Y,bb}$	0.257	0.65	0.74	0.12	150.0	218.5	0.61	4.88	1.066	1.08	1.00	352.6
$G^{HWC}_{\infty Y,bb}$	0.199	0.89	0.60	0.18	149.8	208.9	0.60	4.85	1.073	2.16	2/3	335.6
$G^{CT}_{10Y,bb}$	0.237	0.62	0.81	0.12	152.0	218.0	0.57	5.00	1.034	1.16	1.00	328.1
$G^{CT}_{\infty Y,bb}$	0.241	0.60	0.60	0.20	147.2	221.0	0.62	5.00	1.059	2.77	2/3	335.3
$G^{RT}_{10Y,bb}$	0.197	0.68	0.78	0.13	154.2	225.1	0.61	5.00	1.036	1.11	1.00	334.9
$G^{RT}_{\infty Y,bb}$	0.262	0.6	0.68	0.20	147.2	221.9	0.62	5.00	1.062	1.47	1.00	356.2
$G^{HWT}_{10Y,bb}$	0.223	0.64	0.75	0.13	147.2	212.9	0.59	5.00	1.073	1.16	1.00	333.3
$G^{HWT}_{\infty Y,bb}$	0.155	0.90	0.60	0.17	155.1	217.4	0.56	5.00	1.057	2.10	2/3	337.3
$G^{GT}_{10Y,bb}$	0.236	0.68	0.78	0.14	147.2	213.8	0.58	5.00	1.030	1.19	1.00	335.8
$G^{GT}_{\infty Y,bb}$	0.237	0.6	0.68	0.20	150.5	230.0	0.62	5.00	1.065	1.44	1.00	351.0

* Using a reference stack length of 120 mm

Finally, it should be noted that this use of scaling to widen the range of IPM diameters available in the optimization was not possible in the continuous k_w case. In the continuous k_w case, the value $k_{w,c}$ was set to counteract changes in k_r (as described in Chapter 8), which means that it stays close to the stress of the reference IPM and is limited to control the IPM size with only the geometry variables (i.e. D_s and D_r). This also means that it is not guaranteed that the optimal objective value is better in case of continuous k_w (as it has been implemented here) compared to the case of fix k_w. It depends on whether the benefit of increased flexibility in the winding outweighs the drawback of not allowing the scaling to expand the range of reachable IPM sizes, which likely depends on the optimization problem and its objective.

By comparing the results in Table 10.4 and Table 10.2, it can be seen that the more extreme optimizations, minimizing only the investment cost and minimizing only the driving energy losses, typically reach slightly lower objective values with fix k_w. On the other hand, for the more balanced optimization objective, minimization of LCC, the objective values reached are typically lower for the continuous k_w case.

Table 10.4 Key results for the IPM designs resulting from the optimizations with **fix k_w in the scaling**. The cases of minimization of investment cost (yellow fill), minimization of driving energy loss (purple fill) and minimization of LCC with 10 years of driving (blue fill), are included for seven driving distributions related to CADC and SCMD

IPM	Investment cost* [EUR]	Energy loss*,** [EUR]	Efficiency ** [%]		S_{resc} *** [MPa]	T_{ew} [°C]	Weight **** [kg]		
			IPM	converter			PM	Copper	IPM
$G_{0Y,bb}$	343.5	-	-	-	256.0	124.6	1.4	3.2	30.5
$G^{CC}_{10Y,bb}$	373.8	30.2	94.8	95.4	318.7	94.2	1.6	4.7	39.1
$G^{CC}_{\infty Y,bb}$	641.4	28.8	95.5	95.1	369.3	79.9	4.5	8.0	98.7
$G^{RC}_{10Y,bb}$	372.2	13.3	95.5	97.7	367.8	124.9	1.5	3.2	39.2
$G^{RC}_{\infty Y,bb}$	529.0	12.6	96.2	97.3	367.7	98.8	3.5	4.3	72.9
$G^{HWC}_{10Y,bb}$	375.2	11.7	96.2	98.6	374.8	124.9	1.4	3.3	38.2
$G^{HWC}_{\infty Y,bb}$	501.4	10.9	96.6	98.5	379.6	121.6	3.3	3.2	67.2
$G^{CT}_{10Y,bb}$	363.9	16.1	94.9	96.8	353.0	124.8	1.5	3.1	38.2
$G^{CT}_{\infty Y,bb}$	598.8	14.9	95.8	96.5	370.0	86.2	3.7	6.7	93.7
$G^{RT}_{10Y,bb}$	371.6	13.0	95.2	97.2	354.5	124.9	1.5	3.5	39.3
$G^{RT}_{\infty Y,bb}$	456.1	12.3	95.7	97.2	372.5	110.1	2.3	4.6	51.8
$G^{HWT}_{10Y,bb}$	376.3	12.7	95.4	97.5	380.2	125.0	1.6	3.2	39.7
$G^{HWT}_{\infty Y,bb}$	508.6	12.3	96.1	97.1	368.6	100.6	3.2	4.1	68.7
$G^{GT}_{10Y,bb}$	372.0	14.1	95.2	97.1	350.0	124.4	1.6	3.3	37.5
$G^{GT}_{\infty Y,bb}$	466.9	13.3	95.6	97.0	374.3	97.3	2.3	5.4	55.1

* For only IPM and converter, ** Motoring, in the driving distribution in the optimization
*** Using 330 MPa for the reference IPM, **** Excluding housing and shaft

10.2 Influence of driving selection on design features of the IPM

As several optimized IPM geometries have been presented in the previous section, a joint analysis of the observed trends in the optimized IPM geometries depending on driving distribution and objective is given here. A side-by-side comparison of the optimized geometries using continuous and fix k_w in the scaling is given for CADC in Figure 10.5 and for SCMD in Figure 10.6.

Not surprisingly, the difference between IPMs optimized for different objectives (minimization of investment cost versus minimization of LCC versus minimization of driving energy loss), is larger than the difference between different driving distributions of the same objective. Mostly, the IPM geometries agree quite well between the cases with continuous k_w and fix k_w in the scaling (i.e. comparing the right and left side of each geometry in Figure 10.5-Figure 10.6), but the overall size of the IPM cross section changes. In general, there is a trend towards larger IPM diameters with increased importance of the driving energy losses compared to the investment cost (i.e. from left to right).

Minimizing the investment cost of the IPM and converter results in a comparatively small IPM, which makes effective use of the expensive materials copper and PM. For

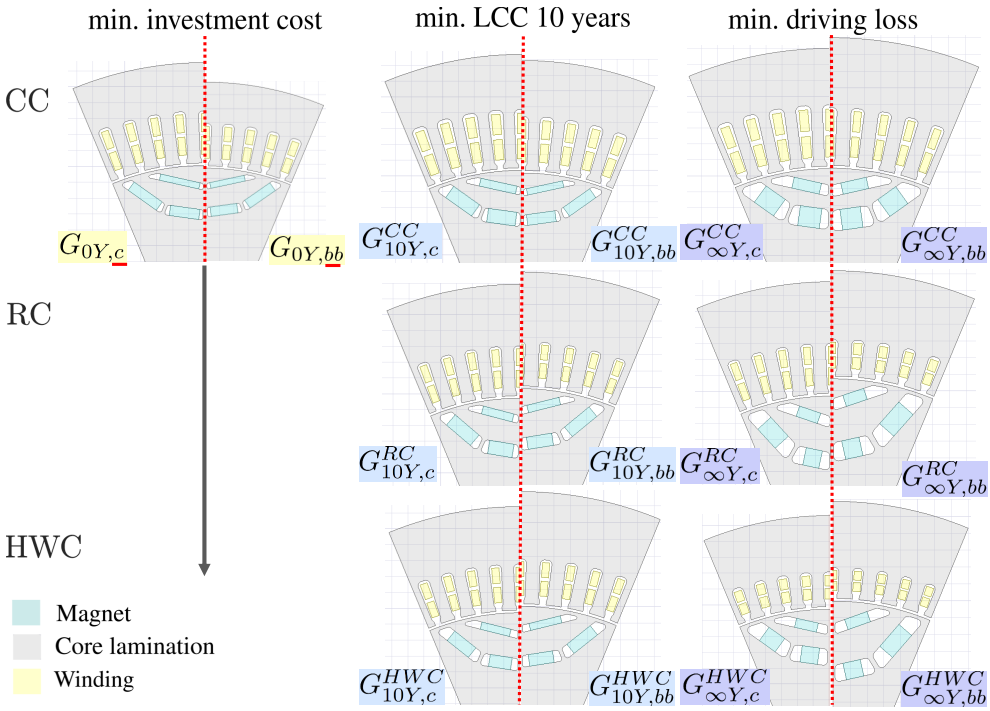

Figure 10.5 Comparison of IPM geometries resulting from the optimizations with **continuous** k_w **(left sides) versus fix** k_w **(right sides) in the scaling**. The size of each IPM reflects its diameter including scaling. The cases of minimization of investment cost (yellow label), minimization of driving energy loss (purple labels) and minimization of LCC with 10 years of driving (blue labels), are included for the **CADC** driving distributions.

the copper amount, having a relatively long active length compared to the stator diameter helps, by reducing the impact of the end-winding. For the PM amount, shallow and wide flux barriers (i.e. close to the air-gap and spanning a large share of the pole) helps to keep the magnet flux linkage high (according to Chapter 7) while thin barriers helps to keep the PM amount down. On the other hand, minimization of the driving energy loss, of the IPM and converter, results in IPMs that are large both in stator diameter and axial length. The rotors of these IPMs have significantly larger but short PMs placed in thick barriers, this can be expected to improve the saliency which (as seen in Chapter 7) helps to improve the IPM efficiency in the operating region of low torques at high speeds.

When it comes to comparison of IPMs with the same optimization objective but different driving distribution (i.e. within the same column in Figures 10.5-10.6), some trends can be seen. There is a clear trend towards larger slot areas for the city driving types (CADC-CC and SCMD-CT) compared to the other driving distributions, especially in case of minimization of driving energy losses but also for the minimization of LCC. For the rural and highway types (CADC-RC, CADC-HWT, SCMD-RT and SCMD-HWT) there is a trend towards deeper flux barriers with a lower share of magnet material compared to the city driving types. These design features can be considered to agree with

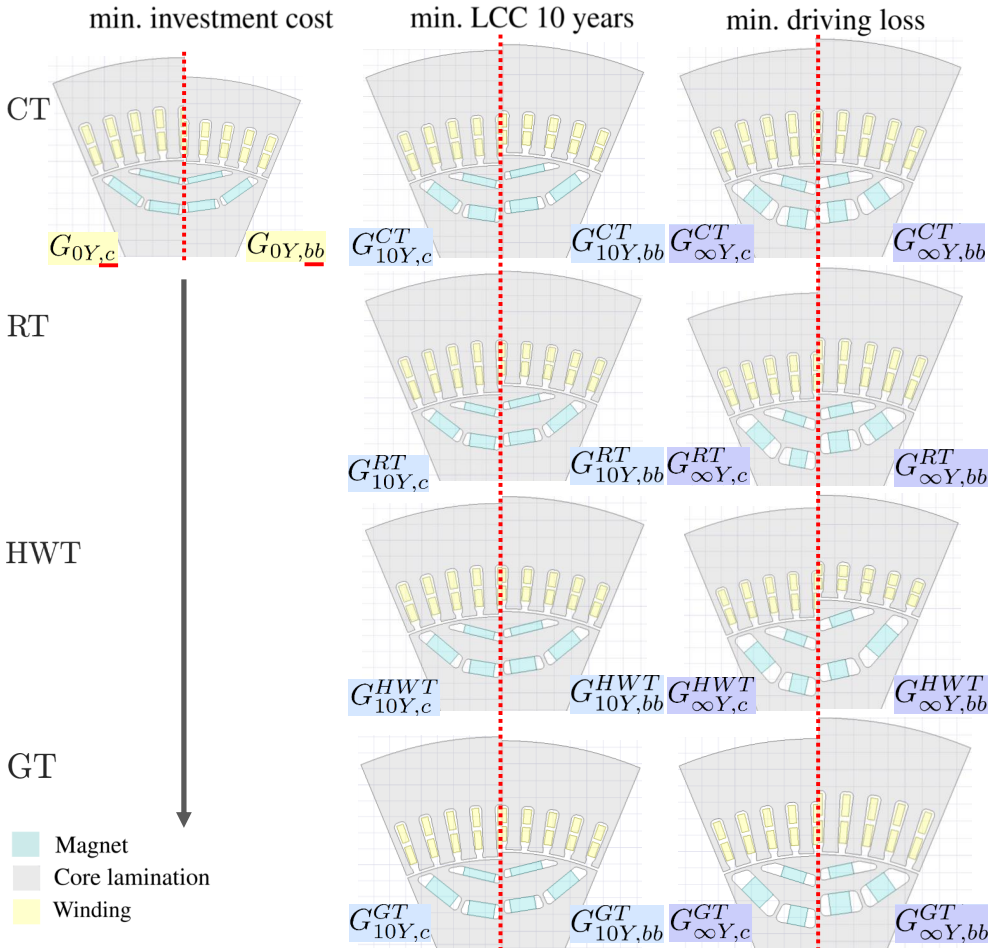

Figure 10.6 Comparison of IPM geometries resulting from the optimizations with **continuous** k_w **(left sides) versus fix** k_w **(right sides) in the scaling**. The size of each IPM reflects its diameter including scaling. The cases of minimization of investment cost (yellow label), minimization of driving energy loss (purple labels) and minimization of LCC with 10 years of driving (blue labels), are included for the **SCMD** driving distributions.

copper losses being relatively more important for city driving and core losses being relatively more important for rural- and highway driving. For the most mixed driving distribution, SCMD-GT, the IPM cross sections are similar in shape but slightly larger compared to their counterparts with rural driving distribution.

Overall, the IPM geometry is seen to vary significantly with the driving distribution for minimization of driving energy losses (rightmost column). However, for minimization of LCC (middle column), there are only slight differences in the IPM geometries for different driving distributions. While the IPM geometries for the most pronounced city driving (CADC-CC) and the most pronounced highway driving (CADC-HWC) still stand out somewhat, the other IPMs (for CADC-RC and all SCMD) are very similar.

10.3 Customized IPM geometries versus same geometry for all driving types

Previously in this chapter, several IPM designs optimized for different driving distributions have been presented. The LCC of these IPMs are further investigated in this section. In particular, this section quantifies whether there are significant benefits with customizing the IPM compared to using a single IPM design for all driving types. This is done by comparing the LCC of an IPM optimized for a specific driving distribution to the LCC of an IPM optimized for mixed driving but used for the driving distribution in question.

The IPM optimized for mixed driving is taken as the IPM optimized for SCMD-GT. Still, the IPM optimized for mixed driving depends on the objective; minimization of investment cost, minimization of LCC for 10 years of driving or minimization of driving energy losses, as well as the two scaling cases (continuous k_w or fix k_w). Thus, the IPM designs $G^{GT}_{10Y,c}$, $G^{GT}_{10Y,bb}$, $G^{GT}_{\infty Y,c}$, $G^{GT}_{\infty Y,bb}$ are solutions for mixed driving. Additionally, the designs $G_{0Y,c}$, $G_{0Y,bb}$, which are independent of the driving distribution, are also included for reference. To give an overview of how strongly the driving energy losses differ with the optimization objective, the efficiency maps of the IPM and converter are shown in Figure 10.7. For brevity, only the case of fix k_w in the scaling is included, but the results for continuous k_w are similar.

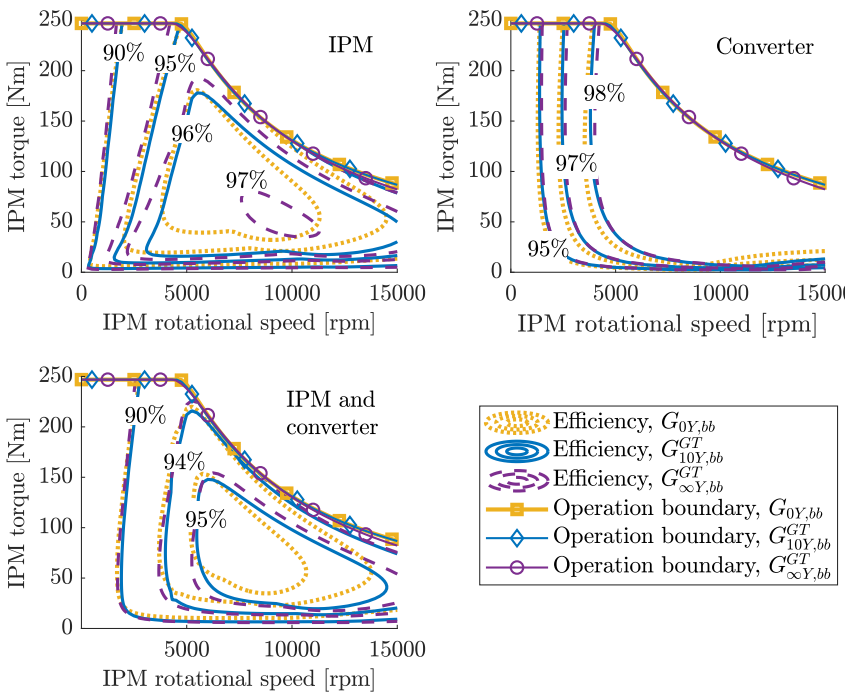

Figure 10.7 Efficiency maps for the IPM, converter and IPM and converter combined for the IPM designs resulting from minimization of investment cost, minimization of LCC with 10 years of driving and minimization of driving energy losses (SCMD-GT distribution).

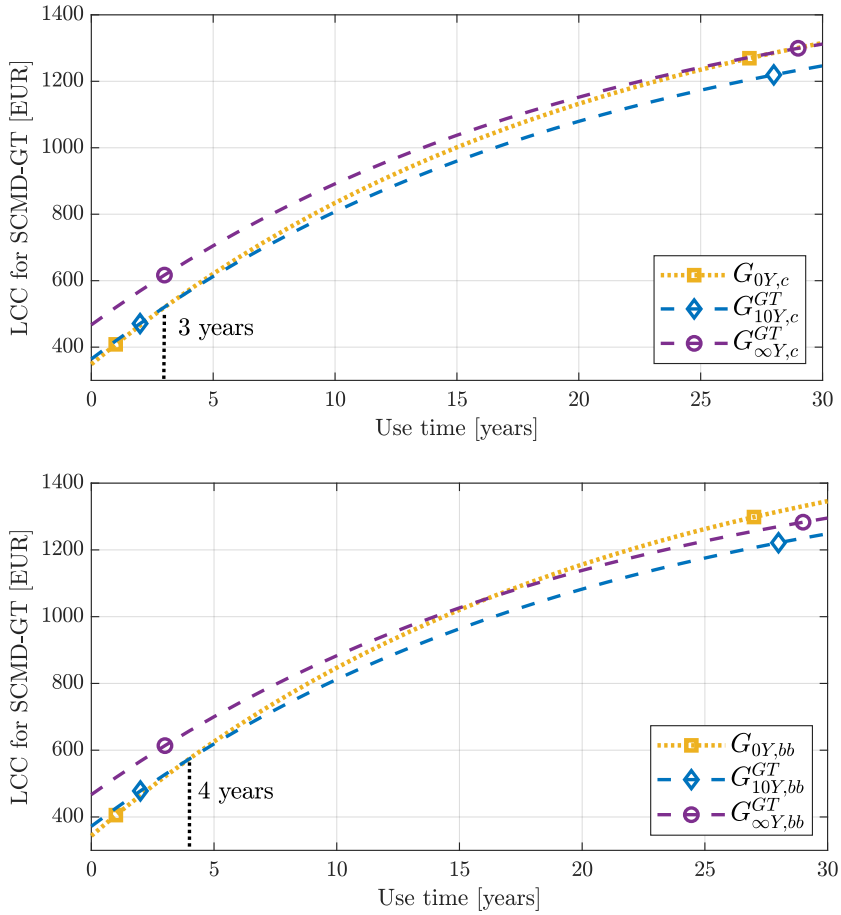

Figure 10.8 LCC depending on the use time, for SCMD-GT driving distribution (15 000 km/year), for the IPM designs optimized for minimum investment cost, minimum LCC at 10 years of driving and minimum driving energy losses, for continuous k_w in the scaling (upper plot) and fix k_w in the scaling (lower plot).

Figure 10.7 shows significant differences between the different IPMs, especially in the high speed region. The largest differences are seen in the IPM efficiency at high speeds, which indicates a large difference in core losses. The converter efficiency also varies among the IPMs, due to differences in current rating and power factor among the IPM designs. The combined efficiency of the IPM and converter of the three IPM designs is similar in the low speed region but quite different in the high speed region, which is particularly clear looking at the size of the contour for 95%-efficiency in Figure 10.7 (bottom left plot).

A comparison of the LCC for these three IPMs, for SCMD-GT, is presented in Figure 10.8. Figure 10.8 shows how the LCC changes over time, from the investment cost (at 0 years of use) to increasing values as the cost of the driving energy losses accumulates

over the years. Overall, the results for continuous k_w and fix k_w (i.e. top plot versus bottom plot) are very similar. As expected, the IPM optimized for low investment cost ($G_{0Y,c}$ or $G_{0Y,bb}$ depending on the treatment of k_w) indeed show the lowest LCC for the first few years. However, the IPM optimized for low LCC at 10 years of driving ($G_{10Y,c}$ or $G_{10Y,bb}$ becomes the best option after 3-4 years of driving. The LCC of the IPM optimized for low driving energy losses ($G_{\infty Y,c}$ or $G_{\infty Y,bb}$) increase less strongly with the use time, but the lower losses does not compensate the higher investment cost within a reasonable time frame, as it is out-competed in terms of LCC by $G_{10Y,c}$/$G_{10Y,bb}$ even at 30 years of use time.

A quantification of the improvement offered by custom-making the IPM for a specific driving type, compared to using an IPM optimized for mixed driving, is provided in Figures 10.9-10.10, for the different driving distributions in CADC and SCMD. Figure 10.9 and Figure 10.10 show the results for continuous k_w and fix k_w respectively.

The overall result, both for continuous k_w and fix k_w, is that customization of the IPM geometry gives a significant reduction of the LCC for CADC-CC, a slight reduction of LCC for CADC-HWC and virtually no reduction for the other driving distributions. This can be seen by comparing solid curves with their dashed counterparts (with same marker shape and color) in Figure 10.9 and Figure 10.10. In other words, the driving type needs to have either a very pronounced city-characteristic or a very pronounced highway-characteristic for customization of the IPM geometry to pay off in terms of LCC. For rural or mixed driving, with only partial inclination towards the city- or highway-type of driving, the IPM can be kept the same without negatively impacting the LCC.

This might indicate that the IPM can reach high efficiency over a quite wide range of the operating region at low torques and medium-high speeds in a cost effective way, meaning that differemt driving distributions that are well contained within that operating region (regardless of how they are distributed within that region) would not benefit from IPM customization. To a certain extent, the high efficiency area of the IPM and converter can be enlarged with relative ease. Then, it seems that only the most specialized driving distributions leads to the need to change the positioning of the high efficiency area and subsequently a benefit with customizing the IPM. Notably, all the driving distributions based on large amounts of logged driving, i.e. the SCMD-distributions, were here found to fall in the category of mixed driving where customization of the IPM is not necessary.

Further, it can be noted that, for all the included driving distributions, minimization of the investment cost results in an IPM that is quickly out-competed in terms of LCC by an IPM targeting minimum LCC at 10 years of driving. Typically, the break-even between these two IPM design occurs after 2-4 years of driving (at 15 000 km/year). In particular for the pronounced highway driving in CADC-HWC, an investment cost minimization gives very poor results in terms of LCC. This can be understood from the low efficiency at high speeds for this IPM version, which can be seen in Figure 10.7. On the other hand, minimization of the driving energy losses results in IPM designs that have too high investment cost which is not compensated for by the loss reduction. However, the relative importance of loss reduction compared to investment cost will naturally depend on the amount of driving, which was kept constant (at 15 000 km/year) during the optimizations.

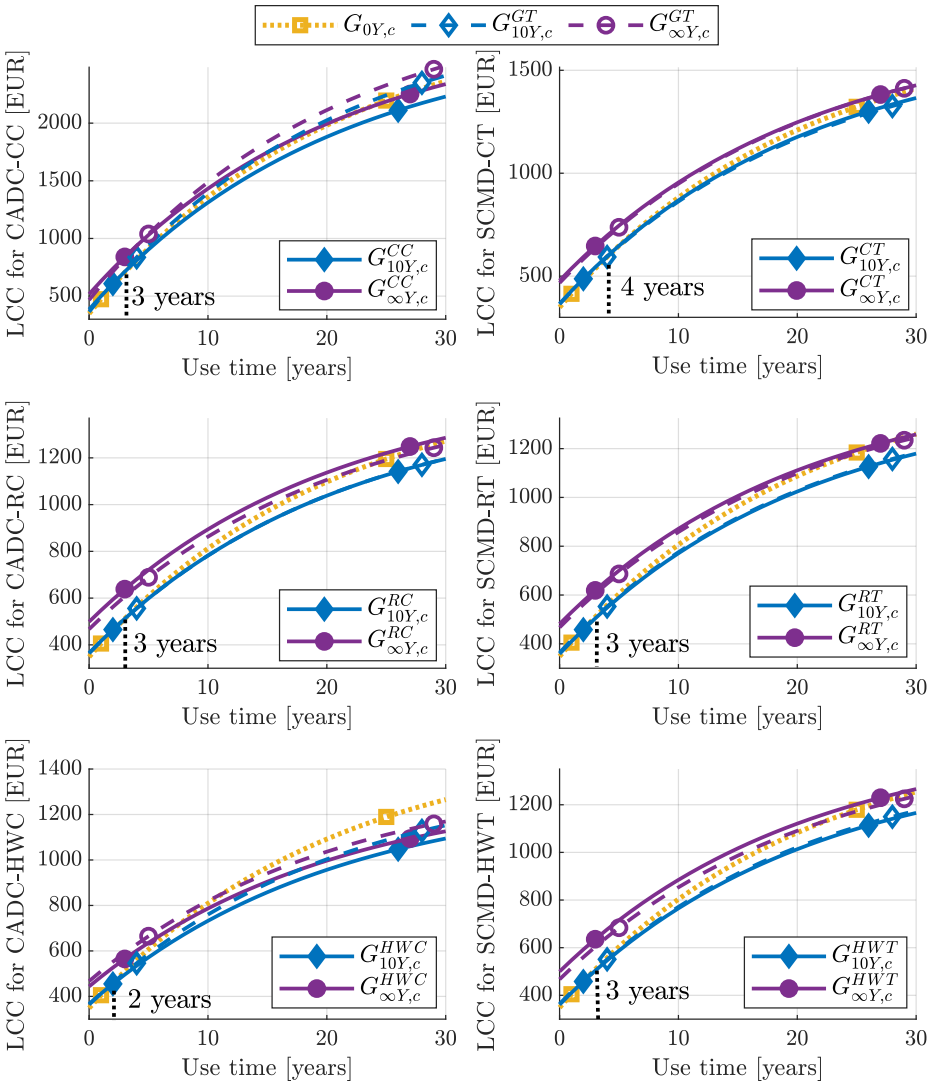

Figure 10.9 The LCC versus use time, for the CADC (left column) and the SCMD (right column) driving distributions (15 000 km/year), including both the IPM optimized for the specific driving type (solid curves) and the IPM optimized for mixed driving (dashed curves). The IPM versions come from minimization of investment cost (dotted curve), minimization of LCC at 10 years of driving and minimization of driving energy losses, with **continuous k_w in the scaling**.

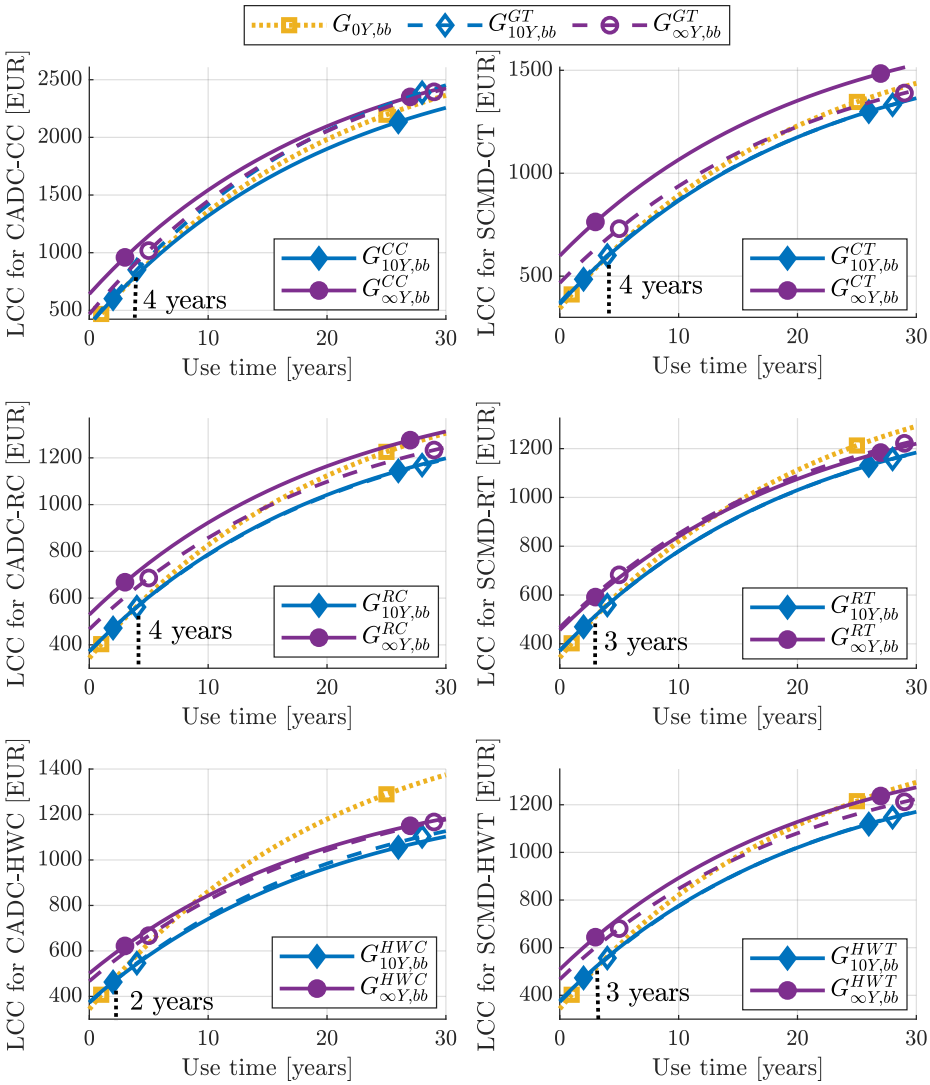

Figure 10.10 The LCC versus use time, for the CADC (left column) and the SCMD (right column) driving distributions (15 000 km/year), including both the IPM optimized for the specific driving type (solid curves) and the IPM optimized for mixed driving (dashed curves). The IPM versions come from minimization of investment cost (dotted curve), minimization of LCC at 10 years of driving and minimization of driving energy losses, with **fix** k_w **in the scaling**.

10.3.1 Sensitivity to amount of driving

While the IPMs resulting from minimization of either only the investment cost or only the driving energy losses were both found to be poor options in terms of LCC for all the driving types at 15 000 km/year they might be more interesting if the amount of driving is significantly lower or higher. Therefore the LCC is also presented for the CADC for 5 000 km/year and 45 000 km/year, in Figure 10.11.

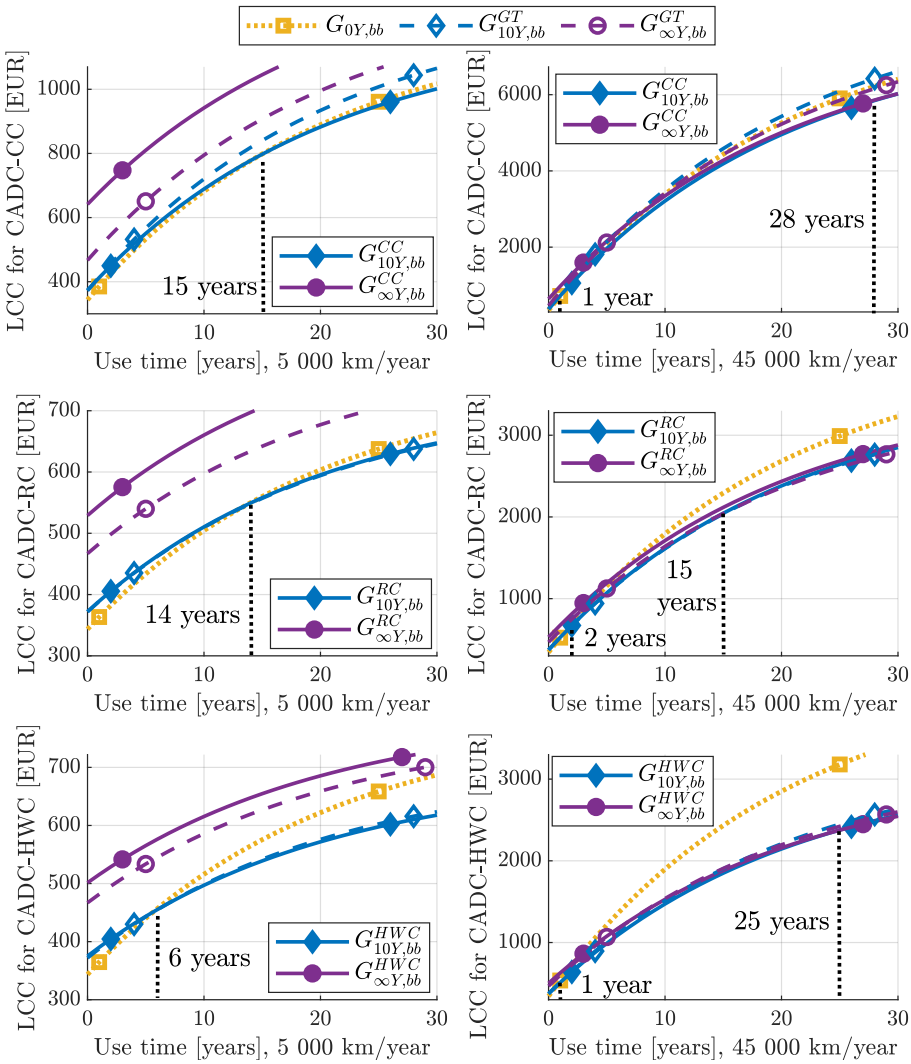

Figure 10.11 LCC versus use time, for CADC with **5 000 km/year** (left) and **45 000 km/year** (right), including both the IPM optimized for the specific driving type (solid curves) and the IPM optimized for mixed driving (dashed curves). The IPM versions come from minimization of investment cost (dotted curve), minimization of LCC at 10 years of driving and minimization of driving energy losses, with fix k_w in the scaling.

The left column in Figure 10.11 shows that the IPM from minimization of the investment cost becomes a viable option for low amount of city or rural driving, but remains a poor option for highway driving. The right column in Figure 10.11 shows that larger amount of driving increases the benefit with customizing the IPM design for city or highway driving. The IPMs from minimization of the driving energy losses still take over 15 years of driving to close the gap in LCC compared to the IPMs from minimization of LCC for 10 years of driving.

10.4 Selection of IPMs for different driving cases

Based on the results in this chapter, three IPM designs can be selected as particularly interesting depending on the driving scenario. For brevity, only designs with an actual winding configuration, i.e. fix k_w in the scaling, are considered here. The IPM $G^{CC}_{10Y,bb}$ is a good option for very pronounced city driving, especially for large amounts of driving. For example a city taxi would benefit from such an IPM design. The $G^{HWC}_{10Y,bb}$ is a good option for large amounts of pronounced highway driving, for example daily highway commuting. Still, the $G^{GT}_{10Y,bb}$ covers most cases of traditional passenger car usage, and offers a low LCC for a wide range of mixed driving.

For the comparison in this section, the IPM geometries of $G^{CC}_{10Y,bb}$, $G^{GT}_{10Y,bb}$ and $G^{HWC}_{10Y,bb}$ have been re-evaluated with higher mesh- and time-resolution in the FEA. The time resolution was increased to 270 steps per electric period and the fine mesh settings, where a segment of the IPM geometry corresponding to one pole is modelled with around 15 500 mesh elements (see Section 6.1 for further description), compared the medium mesh and time resolution of 180 steps per electric period which were used in the optimization procedure. The scaling is also removed and instead the actual machine dimensions are used and the sweep of i_d, i_q combinations are set based on the current rating of each IPM. This also means that the air-gap (0.8 mm) and slot opening width (2 mm) are kept identical in all three machines. Finally, the thickness of the ribs in the rotor are set according to the look-up table for the actual rotor dimensions.

Following these model changes, the size of the IPMs need to be adjusted slightly, to find the feasible version (i.e meeting performance requirements as well as thermal and mechanical constraints) with the lowest LCC. This has been done by updating the IPM dimensions and recomputing the scaling factors. After two iterations of updating the IPM dimensions, the scaling can be removed (as all scaling factors were within 0.9997-1.0003). The IPMs are, after the described modifications, referred to as:

- G_{city} (based on $G^{CC}_{10Y,bb}$)
- G_{mix} (based on $G^{GT}_{10Y,bb}$)
- $G_{highway}$ (based on $G^{HWC}_{10Y,bb}$)

The modifications in IPM dimensions are minor, around 1 mm change in stator outer diameter and stack length and less than 0.2 A change in current rating. The LCC increases with 2-12 EUR depending on the driving distribution and IPM design, which is expected since the core losses increase and performance reduces slightly with the higher model

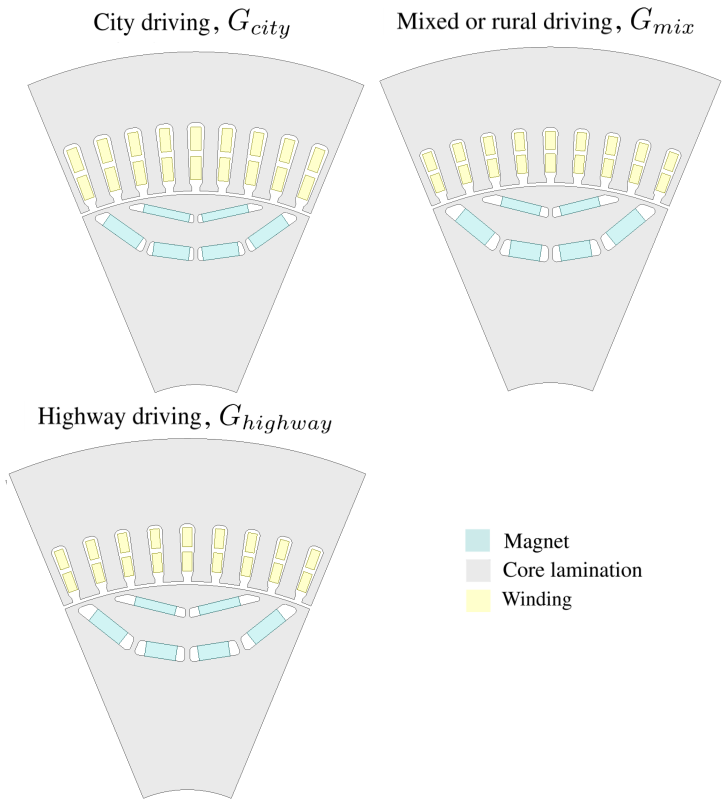

Figure 10.12 Cross sections for the three selected IPM designs based on minimization of LCC with 10 years of pronounced city driving (CADC-CC), mixed driving (SCMD-GT distribution) and pronounced highway driving (CADC-HWC).

resolution. Still, the difference in LCC between the included IPMs remains very similar. This indicates that the differences between the IPMs are not sensitive to the resolution in the model.

The geometries of the selected IPM designs are shown in Figure 10.12 and further description of these three IPM designs and their characteristics are given in Table 10.5. The efficiency maps of the IPMs are presented in Figure 10.13. The geometry of G_{city} shows larger slots and its slightly wider and shallower flux barriers with a larger share of magnet compared to the others. The geometries of G_{mix} and $G_{highway}$ are very similar, but $G_{highway}$ is somewhat lager in diameter and has slightly thinner magnets. It can be noted, from Table 10.5, that G_{city} has the highest amount of copper while $G_{highway}$ has the lowest PM amount among the included IPMs. As intended, all IPMs have very similar peak torque. Furthermore, the torque ripple is relatively low, even though torque ripple constraints where not included in the optimization.

Table 10.5 Key parameters for the selected IPM designs (G_{city}, G_{mix} and $G_{highway}$), suitable for (in order) pronounced city driving, mixed driving and pronounced highway driving.

	G_{city}	G_{mix}	$G_{highway}$
Investment cost [EUR]*	375.4	370.2	372.6
Current rating [A]	317.5	335.9	352.4
Peak torque [Nm]	246.8	246.9	246.8
Peak power [kW]**	138.8	137.2	137.1
Power at top speed [kW]**	138.8	136.0	129.7
Torque rippple [%]***	7.3	5.1	5.7
Stator outer diameter [mm]	216.5	219.5	231.9
Stack length [mm]	154.7	142.6	128.0
Current density [A/mm^2]***	17.7	26.3	26.1
Maximum stress [MPa]****	302	312	323
PM weight [kg]	1.6	1.6	1.3
Copper weight [kg]	4.7	3.2	3.3
IPM weight [kg]	39.5	37.1	37.5

* Including IPM and converter, ** At 370 V (DC)
*** RMS, at peak torque, **** In rotor rib, at top speed

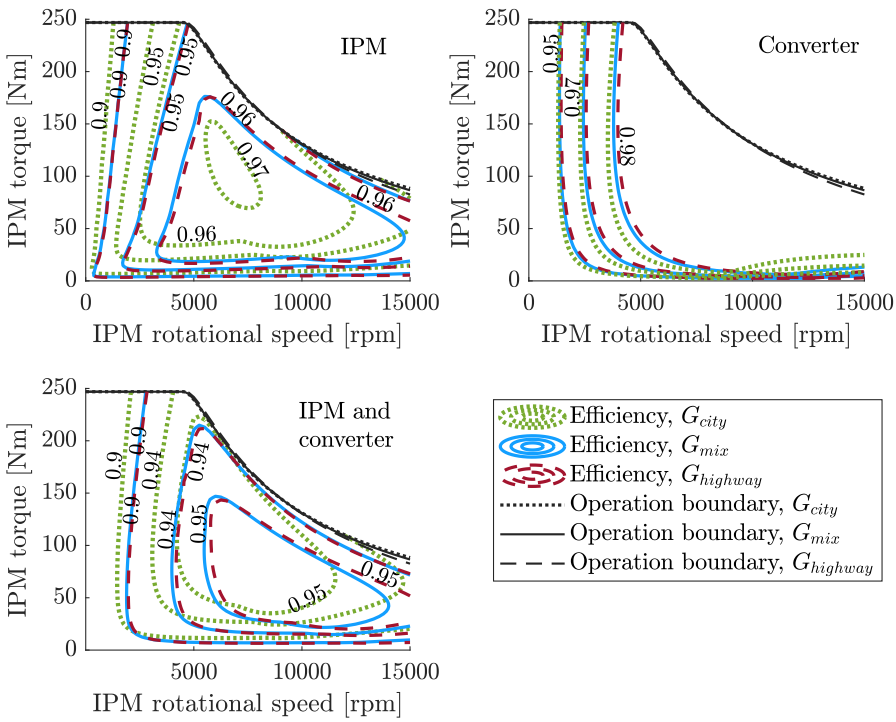

Figure 10.13 Efficiency maps for the IPM, converter and IPM and converter combined, for the IPM designs based on minimization of LCC for 10 years of mixed driving (G_{mix}), pronounced city driving (G_{city}) and pronounced highway driving ($G_{highway}$).

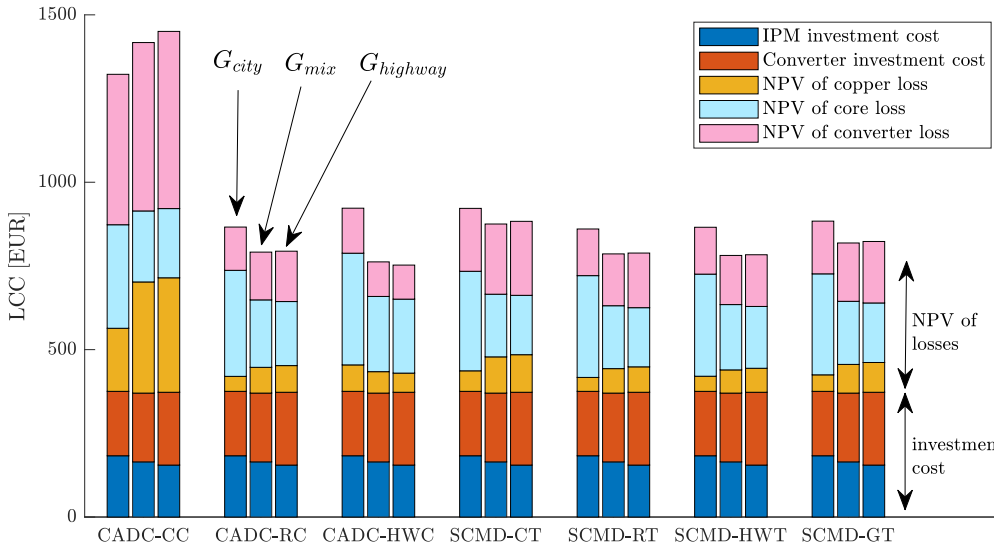

Figure 10.14 LCC of three selected IPMs designs for 10 years of driving (15 000 km/year) of the driving distributions related to CADC and SCMD. The contribution of the investment cost and loss components to the total LCC is shown, for the IPM and the converter.

The efficiency maps in Figure 10.13 show that G_{city} has a clear shift in the high efficiency region of the IPM towards lower speed and higher torques while the other two IPMs have quite similar efficiency, except at very high speeds where $G_{highway}$ is more efficient than G_{mix}. G_{city} has the highest peak IPM efficiency, over 97%, but the contours of 96% efficiency for G_{mix} and $G_{highway}$ reach further into the area of low torques and medium-high speeds which is especially important for BEV applications. The converter efficiency map also differs among the IPM designs, as shown in Figure 10.13. Although, the converter efficiency varies less than the IPM efficiency, the trend remains, with G_{city} having better efficiency than the other two IPMs at low speeds while $G_{highway}$ has the best efficiency at high speeds. The efficiency maps of the IPM and converter combined naturally also follow the same trend. Overall, the three selected IPMs differ in the placement of the high efficiency region while the operation boundary remains very similar.

Finally, Figure 10.14 presents the LCC of the three selected IPMs for 10 years of driving (at 15 000 km/year) of the different driving distributions related to CADC and SCMD. It can be seen that G_{city} has the lowest LCC for CADC-CC but the highest LCC for all the other driving distributions. G_{mix} and $G_{highway}$ are quite close in LCC for most of the driving distributions, but G_{mix} is typically slightly better. Notably, $G_{highway}$ has the lowest NPV of core losses among the IPMs, for all the driving distributions, but it is only in CADC-HWC that it has the lowest LCC. Compared to G_{mix}, G_{city} shows an LCC reduction of around 7% in CADC-CC and $G_{highway}$ shows an LCC of around 1% in CADC-HWC.

For further understanding of the LCC results in Figure 10.14, it can be noted that all three IPMs are very similar in terms of investment cost, although the balance between the investment cost of the IPM and the converter differs. Further, the difference in driving energy losses among the included IPM designs can be understood by comparing the efficiency contours (of the IPM and converter combined) with the energy distribution of each driving combination, as shown for CADC in Figure 10.15 and for SCMD in Figure 10.16.

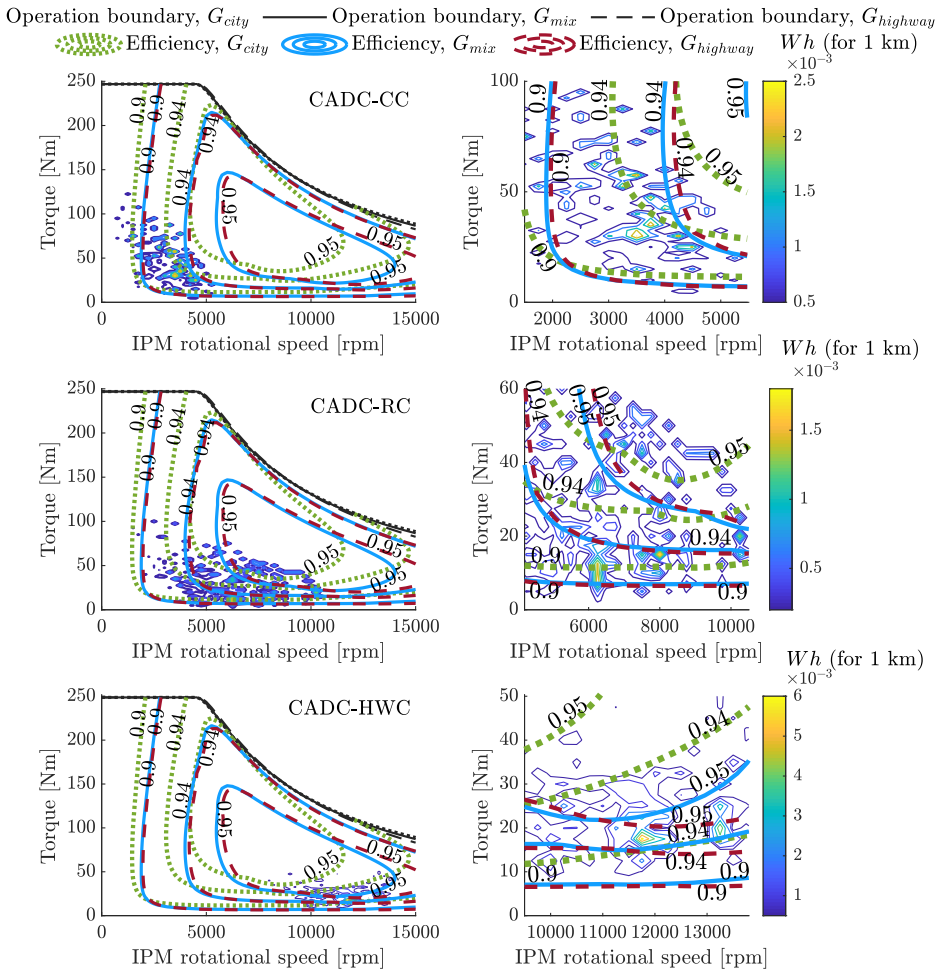

Figure 10.15 Efficiency maps (of the IPM and converter combined) for the IPM designs based on minimization of LCC for 10 years of mixed driving (G_{mix}), pronounced city driving (G_{city}) and pronounced highway driving ($G_{highway}$). Overlays of the driving energy distributions are shown for the city cycle (top row), rural cycle (middle row) and highway cycle (bottom row), for the motoring operation (left column) and zoomed in on the most energy dense area (right column).

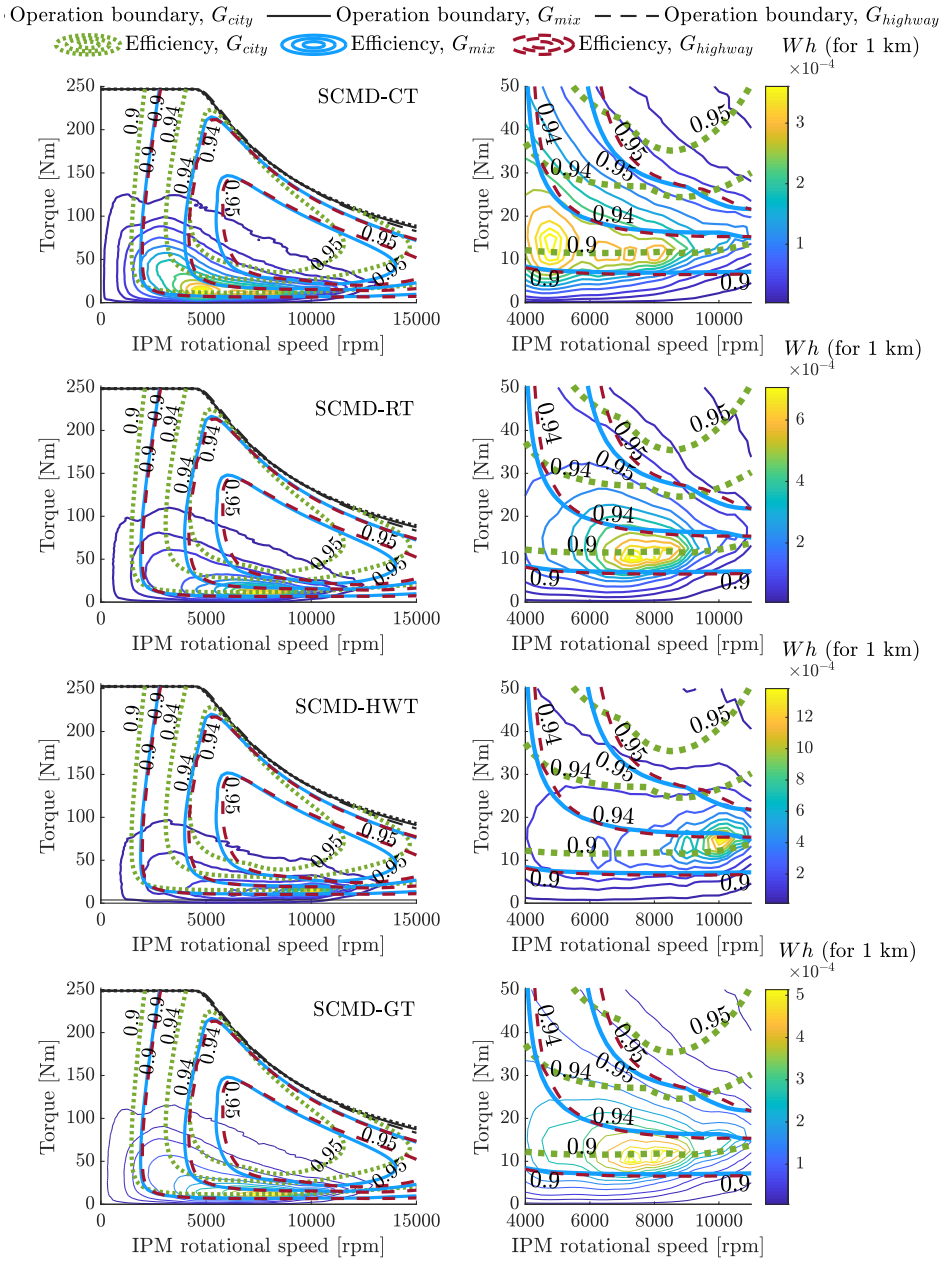

Figure 10.16 Efficiency maps (of the IPM and converter combined) for the IPM designs based on minimization of LCC for 10 years of mixed driving (G_{mix}), pronounced city driving (G_{city}) and pronounced highway driving ($G_{highway}$). Overlays of the driving energy distributions are shown for the city type, rural type, highway type and general type (in order, top to bottom), for the motoring operation (left column) and zoomed in on the most energy dense area (right column).

The higher efficiency of G_{city} in CADC-CC distribution can be seen in Figure 10.15, as the efficiency contours of G_{city} clearly cover more of the CADC-CC energy distribution than the corresponding contour for the other two IPMs designs. Similarly, the higher efficiency of $G_{highway}$ CADC-HWC distribution can seen, as the efficiency contours of $G_{highway}$ are significantly better than the ones of G_{mix} for speeds above 11 500 rpm (corresponding to around 120 km/h).

However, as shown in Figure 10.16, all the SCMD driving distributions are quite well contained in operating region of 4 000-11 000 rpm and 5-25 Nm, where the efficiency contours of G_{mix} and $G_{highway}$ are very similar. It should also be noted that G_{city} is not the best option for the SCMD city type (SCMD-CT), which has somewhat higher speed and lower torques than CADC-CC. Although the SCMD differ in terms of the placement of the most energy dense operating region G_{mix} covers all of them with a good efficiency.

Chapter 11

Conclusion and future work

11.1 Conclusions

In this thesis, a method to customize the IPM design towards a specific combination of city, rural and highway driving is proposed, with focus on the potential to reduce the LCC of the IPM and power electronic converter for an example BEV. The customization was made using an optimization method where both the size and shape of the IPM geometry is varied to minimize the LCC for a given driving scenario. In the optimization, driving is represented with a time distribution over the entire torque versus speed plane of the IPM. As several drive cycles can be aggregated into a single distribution in the IPM torque versus speed plane, this allows a large number of drive cycles to be included without affecting the computational time. The optimization was repeated for three official drive cycles, CADC (city, rural and highway cycles), as well as four different driving combinations based on a large number of logged driving, referred to as SCMD (city, rural, highway and mixed driving distributions).

The computational speed of the optimization is reduced by utilizing scaling of IPM FEA results to automatically select the best feasible version of each IPM geometry, considering performance requirements as well as thermal and mechanical constraints. Further, the rotor geometry was parametrized in an effective way by using piece-wise-linear approximation of the natural q-flux lines as a basis for describing the flux barrier shape. Overall, this reduces the number of variables needed and increases the share of feasible geometries without too strong restrictions on the design freedom in the optimization. Furthermore, the influence of time- and mesh resolution on the core losses in the electromagnetic FEA was investigated. The resulting core loss convergence curves were used to select a suitable comprise between the numerical accuracy in core loss and the computational time, which was very important for the IPM optimization. The final IPM designs resulting from the optimizations were also evaluated with higher mesh- and time-resolution and it was verified that the differences among the final glsplipm were not sensitive to the resolution in the FEA.

Additionally, the IPM peak performance requirement in this thesis was set to manage all the included driving scenarios with the example BEV. It was found that a high FW-performance was beneficial to meet this performance requirement. The FW-performance

was further investigated for IPM rotors with two layers of flux barriers, with emphasis on the influence of the flux barrier shape and importance of mechanical constraints. It was found that the balance between saliency and normalized magnet flux linkage (which together govern the FW-characteristics of the IPM) changes with the shape of the flux barriers. More arc-shaped flux barriers improve the saliency while V-shaped barriers give higher magnet flux linkage for a given magnet amount. If mechanical aspects were neglected, all the included barrier shapes resulted in similar FW-performance. However, when rotor stress constraints were introduced, the V-shaped flux barrier suffered comparatively less and gave higher FW-performance than flux barriers with more arc-like shape. Still, the higher saliency associated with more arc-like flux barrier shapes was seen to improve the IPM efficiency in the operating region of low torques and high speeds, which is highly important for BEV applications.

Further, it was found that including geometry dependence in the mechanical constraints (i.e. adjusting the thickness of the rotor ribs with the flux barrier design) gave a significant change in the optimized rotor geometry. Careful handling of the mechanical constraints was found to be of similar importance for the FW-performance as the choice of flux barrier shape. Therefore, the geometry dependent mechanical constraints are used in the optimization of the entire IPM geometry.

For the CADC city cycle, the optimization resulted in an IPM design with larger slots, higher amount of copper and relatively shallow flux barriers that are well-filled with magnets. Comparatively, the IPM custom-made for the CADC highway cycle has smaller slots and lower copper and magnet amounts. Targeting city driving in the optimization resulted in an IPM with lower resistive losses and improved IPM efficiency at low speeds and high torques, while optimizing the IPM for highway driving reduced the core losses and improved IPM efficiency at high speeds. The IPM optimized for mixed driving has a geometry that is similar in shape but with somewhat smaller cross section and higher magnet amount, compared to the IPM customized for highway driving. The IPM optimized for mixed driving has a large and well-placed operating region with high efficiency and offers low LCC for most of the included driving distributions.

Overall, the results of the IPM geometry optimization for different combinations of driving showed that there is potential to reduce the LCC by customizing the IPM geometry, but only for pronounced city or highway driving. The LCC (of the IPM and converter) was found to be 7% lower for the CADC city driving cycle and 1% lower for the CADC highway driving cycle, when using the customized IPM compared to the IPM optimized for mixed driving. Still, for a wide range of mixed and rural driving, the customization of the IPM does not offer any significant reduction in LCC. Notably, none of the driving distributions based on large amounts of logged driving included here were specialized enough for customization of the IPM to reduce the LCC significantly. This indicates that the traditional use of passenger cars typically has a variation of driving types that can be well met with an IPM designed for general driving and the potential for further improvement by custom-making the IPM is limited. However, the benefit of custom-making the IPM design is likely higher for BEV applications with more specialized driving type and larger amounts of driving.

11.2 Future work

As the IPM optimization against drive cycles was only done for one rotor topology and winding configuration within this thesis, it would be very interesting to investigate other IPM topologies. That would increase the design freedom and likely increase the potential to reduce LCC by customizing the IPM design. For example, since the optimizations here showed a trend of shallow flux barrier placement when targeting city driving, it seems likely that a rotor topology with one or two V-shaped flux barrier(s) would improve the results for city driving.

Furthermore, the IPM geometry optimizations here focused on minimizing LCC for a case requiring high FW-performance. It would be interesting to investigate how the results are affected if an objective with a stronger environmental connection, such as a life cycle assessment, and/or different peak torque requirements are considered. The sensitivity of the results to the converter model would also be interesting to investigate further. For example, the influence of replacing the IGBT-based converter model here with a more modern silicon-carbide converter (which is expected to increase in automotive applications in the future [71]) could be investigated. Additionally, the IPM current rating could be changed into a discrete variable in the optimization, to match the converter ratings that are available on the market.

The IPM model used in this thesis can be refined and expanded in many ways to improve the accuracy of the results. However, the improved accuracy of more detailed modelling needs to be balanced against the increased computational burden when used for IPM geometry optimization. From a thermal perspective, it would be interesting to refine the LPN and include magnet temperature and losses in the constraints of the optimization, preferably with magnet segmentation as a design variable. From a structural perspective, it would be beneficial to include a larger range of rotor diameters and also different top speeds, and including the gear ratio as a design variable. From an electromagnetic perspective, the core loss modelling could be refined and constraints on demagnetization as well as noise and vibration levels could be considered. But, possibly the most important, aspect that could be improved is the modelling of system aspects, in particular the changes in battery voltage and temperature of the IPM during drive cycles. This will also affect the operating point and losses of the IPM, in a way that is dependent on the design of the IPM.

However, both the battery voltage and IPM temperature are quantities that depend on the respective order of the drive cycles. This which makes it difficult to aggregate a large number of drive cycles into a distribution in the torque versus speed plane of the IPM. Still, it might be possible to include dimensions for temperature and battery voltage and, using the vehicle model, identify how each operating point (i.e. a certain torque and speed) distributes over temperature and voltage during driving.

Naturally, it would be ideal to verify the IPMs optimized in this thesis experimentally. However, construction of several prototype IPMs and measurements, especially covering the entire operating region and capturing losses accurately, would be very costly and has not been possible to realize within this thesis project.

The optimization method presented here could also, with some further development, be applied to cases where there are two EMs in the BEV. For example the combination of an IPM with low driving energy losses and another EM with low investment cost

would be interesting to investigate. Thanks to the use of scaling and meta-models in the EM design optimization, it could be computationally feasible to co-optimize two EMs. Co-optimization, where the design of both EMs and their relative contribution to the total performance requirement are covered in the optimization, can be expected to give a better system solution than optimizing the EMs separately.

Finally, it is suggested to investigate the value of custom-making the IPM geometry for the intended driving type for BEV applications with more specialized driving types and/or larger amounts of driving than passenger cars currently have (for example taxis, buses or trucks). While it is difficult to generalize the results here to other applications, it is still considered likely that custom-making the IPM design offers larger benefits for such applications. The use of passenger cars might also transition towards larger amounts of driving and more specialized driving in the future, for example if self-driving vehicles and car sharing services develop further.

References

[1] I. P. I. E. Agency, "Global ev outlook, catching up with climate ambitions," International Energy Agency (IEA), 2023, https://iea.blob.core.windows.net/assets/dacf14d2-eabc-498a-8263-9f97fd5dc327/GEVO2023.pdf.

[2] E. Parliament, "Eu ban on the sale of new petrol and diesel cars from 2035 explained," European Parliament, 2023, https://www.europarl.europa.eu/news/en/headlines/economy/20221019STO44572/eu-ban-on-sale-of-new-petrol-and-diesel-cars-from-2035-explained.

[3] M. Yilmaz, "Limitations/capabilities of electric machine technologies and modeling approaches for electric motor design and analysis in plug-in electric vehicle applications," *Renewable and Sustainable Energy Reviews*, vol. 52, pp. 80–99, 2015.

[4] B. Praslicka, C. Ma, and N. Taran, "A computationally efficient high-fidelity multiphysics design optimization of traction motors for drive cycle loss minimization," *IEEE Transactions on Industry Applications*, vol. 59, no. 2, pp. 1351–1360, 2023.

[5] G. Lei, J. Zhu, Y. Guo, C. Liu, and B. Ma, "A review of design optimization methods for electrical machines," *Energies*, vol. 10, no. 12, p. 1962, 2017.

[6] M. Salameh, I. P. Brown, and M. Krishnamurthy, "Fundamental evaluation of data clustering approaches for driving cycle-based machine design optimization," *IEEE Transactions on Transportation Electrification*, vol. 5, no. 4, pp. 1395–1405, 2019.

[7] K. Kant, J. L. Kirtley, L. V. Iyer, and G. Schlager, "Finite element simulation-based design optimization of permanent magnet motors considering drive cycle," *SAE International Journal of Electrified Vehicles*, vol. 10, no. 2, pp. 157–166, 2021.

[8] A. G. Sarigiannidis, M. E. Beniakar, and A. G. Kladas, "Fast adaptive evolutionary pm traction motor optimization based on electric vehicle drive cycle," *IEEE Transactions on Vehicular Technology*, vol. 66, no. 7, pp. 5762–5774, 2016.

[9] L. Chen, X. Chen, J. Wang, and P. Lazari, "A computationally efficient multiphysics optimization technique for permanent magnet machines in electric vehicle traction applications," in *2015 IEEE International Electric Machines & Drives Conference (IEMDC)*. IEEE, 2015, pp. 1644–1650.

[10] A. Fatemi, N. A. Demerdash, D. M. Ionel, and T. W. Nehl, "Large-scale electromagnetic design optimization of pm machines over a target operating cycle," in *2015 IEEE energy conversion congress and exposition (ECCE)*. IEEE, 2015, pp. 4383–4390.

[11] G. Choi and T. Jahns, "Design of electric machines for electric vehicles based on driving schedules," in *2013 International Electric Machines & Drives Conference*. IEEE, 2013, pp. 54–61.

[12] S. Stipetic, D. Zarko, and M. Popescu, "Ultra-fast axial and radial scaling of synchronous permanent magnet machines," *IET Electric Power Applications*, vol. 10, no. 7, pp. 658–666, 2016.

[13] B. Chen, C. Monissen, M. Ayyildiz, G. Birmes, J. Andert, and S. Pischinger, "A study on scaling laws for thermal parameters of permanent magnet synchronous machines," in *2021 24th International Conference on Electrical Machines and Systems (ICEMS)*. IEEE, 2021, pp. 35–41.

[14] G. Dilevrano, P. Ragazzo, S. Ferrari, G. Pellegrino, and T. Burress, "Magnetic, thermal and structural scaling of synchronous machines," in *2022 IEEE Energy Conversion Congress and Exposition (ECCE)*. IEEE, 2022, pp. 1–8.

[15] K. Ramakrishnan, S. Stipetic, M. Gobbi, and G. Mastinu, "Optimal sizing of traction motors using scalable electric machine model," *IEEE Transactions on Transportation Electrification*, vol. 4, no. 1, pp. 314–321, 2017.

[16] E. A. Grunditz, T. Thiringer, and N. Saadat, "Acceleration, drive cycle efficiency, and cost tradeoffs for scaled electric vehicle drive system," *IEEE Transactions on Industry Applications*, vol. 56, no. 3, pp. 3020–3033, 2020.

[17] B. Ban, S. Stipetic, and T. Jercic, "Minimum set of rotor parameters for synchronous reluctance machine and improved optimization convergence via forced rotor barrier feasibility," *Energies*, vol. 14, no. 10, p. 2744, 2021.

[18] N. Schneider, M. Kanamaru, H. Sano, and T. Yamada, "Solving geometry conflicts in ga optimizations with large numbers of geometric parameters," in *2022 International Conference on Electrical Machines (ICEM)*. IEEE, 2022, pp. 1034–1040.

[19] M. Gamba, G. Pellegrino, and F. Cupertino, "Optimal number of rotor parameters for the automatic design of synchronous reluctance machines," in *2014 international conference on electrical machines (ICEM)*. IEEE, 2014, pp. 1334–1340.

[20] Y. Yang, S. M. Castano, R. Yang, M. Kasprzak, B. Bilgin, A. Sathyan, H. Dadkhah, and A. Emadi, "Design and comparison of interior permanent magnet motor topologies for traction applications," *IEEE Transactions on Transportation Electrification*, vol. 3, no. 1, pp. 86–97, 2016.

[21] A. Wang, Y. Jia, and W. Soong, "Comparison of five topologies for an interior permanent-magnet machine for a hybrid electric vehicle," *IEEE transactions on Magnetics*, vol. 47, no. 10, pp. 3606–3609, 2011.

[22] K. Kamiev, J. Montonen, M. P. Ragavendra, J. Pyrhönen, J. A. Tapia, and M. Niemelä, "Design principles of permanent magnet synchronous machines for parallel hybrid or traction applications," *IEEE Transactions on Industrial Electronics*, vol. 60, no. 11, pp. 4881–4890, 2012.

[23] X. Liu, H. Chen, J. Zhao, and A. Belahcen, "Research on the performances and parameters of interior pmsm used for electric vehicles," *IEEE Transactions on Industrial Electronics*, vol. 63, no. 6, pp. 3533–3545, 2016.

[24] Y. Hu, S. Zhu, C. Liu, and K. Wang, "Electromagnetic performance analysis of interior pm machines for electric vehicle applications," *IEEE Transactions on Energy Conversion*, vol. 33, no. 1, pp. 199–208, 2017.

[25] R. Sundaria, A. Lehikoinen, A. Hannukainen, A. Arkkio, and A. Belahcen, "Mixed-order finite-element modeling of magnetic material degradation due to cutting," *IEEE Transactions on Magnetics*, vol. 54, no. 6, pp. 1–8, 2018.

[26] T. Nakata, M. Sanada, S. Morimoto, and Y. Inoue, "Automatic design of ipmsms using a genetic algorithm combined with the coarse-mesh fem for enlarging the high-efficiency operation area," *IEEE Transactions on Industrial Electronics*, vol. 64, no. 12, pp. 9721–9728, 2017.

[27] A. Andersson, "Electric machine control for energy efficient electric drive systems," Ph.D. dissertation, Chalmers University of Technology, Sweden, 2018.

[28] H. Jin, J. Park, D. Kum, and J. Lee, "Magnetic flux waveform estimation for fast efficiency map calculation in permanent magnet synchronous motors," *International Journal of Applied Electromagnetics and Mechanics*, vol. 56, no. 3, pp. 373–386, 2018.

[29] E. A. Grunditz, "Design and assessment of battery electric vehicle powertrain, with respect to performance, energy consumption and electric motor thermal capability," Ph.D. dissertation, Chalmers University of Technology, Sweden, 2016.

[30] T. Gillespie, *Fundamentals of vehicle dynamics*. SAE international, 2021.

[31] J. Y. Wong, *Theory of ground vehicles*. John Wiley & Sons, 2022.

[32] J. Hendershot and T. Miller, *Design of Brushless Permanent-Magnet Machines*. Motor Design Books LLC, 2010.

[33] W. Soong and T. Miller, "Theoretical limitations to the field-weakening performance of the five classes of brushless synchronous ac motor drive," in *1993 Sixth International Conference on Electrical Machines and Drives (Conf. Publ. No. 376)*. IET, 1993, pp. 127–132.

[34] W. L. Soong and T. Miller, "Field-weakening performance of brushless synchronous ac motor drives," *IEE Proceedings-Electric Power Applications*, vol. 141, no. 6, pp. 331–340, 1994.

[35] S. Morimoto, Y. Takeda, T. Hirasa, and K. Taniguchi, "Expansion of operating limits for permanent magnet motor by current vector control considering inverter capacity," *IEEE transactions on industry applications*, vol. 26, no. 5, pp. 866–871, 1990.

[36] R. Lin, S. D. Sudhoff, and C. Krousgrill, "Analytical method to compute bridge stresses in v-shape ipms," *IET Electric Power Applications*, vol. 12, no. 7, pp. 938–945, 2018.

[37] R. D. Bremner, "Bridge stresses and design in ipm machines," in *IEEE EUROCON 2009*. IEEE, 2009, pp. 655–662.

[38] S. Stipetic, J. Goss, D. Zarko, and M. Popescu, "Calculation of efficiency maps using a scalable saturated model of synchronous permanent magnet machines," *IEEE Transactions on Industry Applications*, vol. 54, no. 5, pp. 4257–4267, 2018.

[39] E. A. Grunditz and T. Thiringer, "Electric vehicle igbt power module sizing and drive cycle energy efficiency for various switching frequencies-based on a scalable module model," in *2018 20th European Conference on Power Electronics and Applications (EPE'18 ECCE Europe)*. IEEE, 2018, pp. P–1.

[40] J. W. Kolar, H. Ertl, and F. C. Zach, "Influence of the modulation method on the conduction and switching losses of a pwm converter system," *IEEE Transactions on Industry Applications*, vol. 27, no. 6, pp. 1063–1075, 1991.

[41] A. Wintrich, U. Nicolai, W. Tursky, and T. Reimann, *Application manual power semiconductors*. ISLE Verlag Ilmenau, Germany, 2011, vol. 7, no. 6.

[42] E. Commission, "Life-cycle costing," European Commission, 2023, https://green-business.ec.europa.eu/green-public-procurement/life-cycle-costing_en.

[43] N. Andréasson, A. Evgrafov, and M. Patriksson, *An introduction to continuous optimization: foundations and fundamental algorithms*. Courier Dover Publications, 2020.

[44] D. GmbH, *Methods for optimization and robustness analysis*. Dynardo GmbH, 2020.

[45] K. Schittkowski, "Nlpql: A fortran subroutine solving constrained nonlinear programming problems," *Annals of operations research*, vol. 5, pp. 485–500, 1986.

[46] M. Mitchell, *An introduction to genetic algorithms*. MIT press, 1998.

[47] S. Ray and D. A. Lowther, "Multi-objective optimization applied to the matching of a specified torque-speed curve for an internal permanent magnet motor," *IEEE Transactions on Magnetics*, vol. 45, no. 3, pp. 1518–1521, 2009.

[48] W. Zhao, F. Zhao, T. A. Lipo, and B.-I. Kwon, "Optimal design of a novel v-type interior permanent magnet motor with assisted barriers for the improvement of torque characteristics," *IEEE Transactions on Magnetics*, vol. 50, no. 11, pp. 1–4, 2014.

[49] L. Jolly, M. Jabbar, and L. Qinghua, "Design optimization of permanent magnet motors using response surface methodology and genetic algorithms," *IEEE Transactions on Magnetics*, vol. 41, no. 10, pp. 3928–3930, 2005.

[50] J. Will and T. Most, "Metamodell of optimal prognosis (mop)-an automatic approach for user friendly parameter optimization," *Weimarer Optimierungsund Stochastiktage*, vol. 6, 2009.

[51] D.-K. Lim, K.-P. Yi, S.-Y. Jung, H.-K. Jung, and J.-S. Ro, "Optimal design of an interior permanent magnet synchronous motor by using a new surrogate-assisted multi-objective optimization," *IEEE Transactions on Magnetics*, vol. 51, no. 11, pp. 1–4, 2015.

[52] J. Clausen, "Branch and bound algorithms-principles and examples," *Department of Computer Science, University of Copenhagen*, pp. 1–30, 1999.

[53] M. Tutuianu, A. Marotta, H. Steven, E. Ericsson, T. Haniu, N. Ichikawa, and H. Ishii, "Development of a world-wide worldwide harmonized light duty driving test cycle (wltc)," *Technical Report*, 2013.

[54] M. André, "The artemis european driving cycles for measuring car pollutant emissions," *Science of the total Environment*, vol. 334, pp. 73–84, 2004.

[55] L. Sileghem, D. Bosteels, J. May, C. Favre, and S. Verhelst, "Analysis of vehicle emission measurements on the new wltc, the nedc and the cadc," *Transportation research part D: transport and environment*, vol. 32, pp. 70–85, 2014.

[56] S. Karlsson, "The swedish car movement data project final report." 2013.

[57] S. Karlsson and L.-H. Kullingsjö, "Gps measurement of swedish car movements for assessment of possible electrification," in *2013 World Electric Vehicle Symposium and Exhibition (EVS27)*. IEEE, 2013, pp. 1–14.

[58] P. Plötz, N. Jakobsson, F. Sprei, and S. Karlsson, "On the distribution of individual daily vehicle driving distances," in *European Electric Vehicle Congress Brussels, Belgium, 3rd-5th December 2014*, 2014.

[59] T. Analysis, "Vehicles kilometres 2022," Transport Analysis, 2022, https://www.trafa.se/en/road-traffic/driving-distances-with-swedish-registered-vehicles/.

[60] Cogent, "Altogether more powerful - non-oriented electrical steel," Cogent Power, 2016, https://cogent-power.com/cms-data/downloads/Cogent%20NO%20brochure%202016.pdf.

[61] A. Krings, "Iron losses in electrical machines-influence of material properties, manufacturing processes, and inverter operation," Ph.D. dissertation, KTH Royal Institute of Technology, 2014.

[62] V. Abramenko, J. Bárta, I. Lolová, I. Petrov, and J. Pyrhönen, "Design of a low-power direct-on-line synchronous reluctance motor based on the modified natural flux line curve approach," *IEEE Transactions on Industry Applications*, vol. 57, no. 6, pp. 5894–5906, 2021.

[63] R. R. Moghaddam, "Synchronous reluctance machine (synrm) in variable speed drives (vsd) applications," Ph.D. dissertation, KTH Royal Institute of Technology, Sweden, 2011.

[64] Y. Wang, G. Bacco, and N. Bianchi, "Geometry analysis and optimization of pm-assisted reluctance motors," *IEEE Transactions on Industry Applications*, vol. 53, no. 5, pp. 4338–4347, 2017.

[65] A. Tokat, E. Jansson, K. Bergsro, and T. Thiringer, "Improvement of the continuous performance of a traction machine for a battery electric vehicle through magnet segmentation," in *2022 International Conference on Electrical Machines (ICEM)*. IEEE, 2022, pp. 1348–1354.

[66] W. Soong and T. Miller, "Practical field-weakening performance of the five classes of brushless synchronous ac motor drive," in *1993 Fifth European Conference on Power Electronics and Applications*. IET, 1993, pp. 303–310.

[67] G. Bacco and N. Bianchi, "Design criteria of flux-barriers in synchronous reluctance machines," *IEEE Transactions on Industry Applications*, vol. 55, no. 3, pp. 2490–2498, 2018.

[68] B. Ban, A. Andersson, and S. Stipetić, "Design and torque ripple reduction methods for synchronous reluctance machine applied in electric power take-off actuation," in *2022 International Conference on Electrical Machines (ICEM)*. IEEE, 2022, pp. 476–482.

[69] S.-H. Han, W. L. Soong, and T. M. Jahns, "An analytical design approach for reducing stator iron losses in interior pm synchronous machines during flux-weakening operation," in *2007 IEEE Industry Applications Annual Meeting*. IEEE, 2007, pp. 103–110.

[70] W. L. Soong, S. Han, T. M. Jahns, and N. Ertugrul, "Reducing iron loss in interior pm machines under field-weakening conditions," in *2007 IEEE Industry Applications Annual Meeting*. IEEE, 2007, pp. 111–118.

[71] B. Fahimi, L. H. Lewis, J. M. Miller, S. D. Pekarek, I. Boldea, B. Ozpineci, K. Hameyer, S. Schulz, A. Ghaderi, M. Popescu *et al.*, "Automotive electric propulsion systems: A technology outlook," *IEEE Transactions on Transportation Electrification*, 2023.

[72] J. Lindström, "Development of an experimental permanent-magnet motor drive," Licentiate Thesis, Chalmers University of Technology, Sweden, 1999.

[73] G. Kylander, "Thermal modelling of small cage induction motor," Ph.D. dissertation, Chalmers University of Technology, Sweden, 1995.

[74] E. A. Grunditz, T. Thiringer, J. Lindström, S. T. Lundmark, and M. Alatalo, "Thermal capability of electric vehicle pmsm with different slot areas via thermal network analysis," *eTransportation*, vol. 8, p. 100107, 2021.

Appendix A

Quality of driving data

While large amounts of real-world driving data offers a detailed description of the operation that a IPM experiences in a BEV application, there are also challenges in terms of data quality when using measurements. In particular a large amount of measured data, as in the case of the database from the "Swedish Car Movement Project" (SCMD) used here, renders it practically impossible to do a visual inspection of all the measured data. Still, it is crucial that faulty data and outliers that might be present are removed. This section describes the efforts regarding quality of the driving data selected from the database.

It was observed that the database includes a lot of very short trips, as shown in Figure A.1. In this work, only trips with a duration > 30 seconds are included.

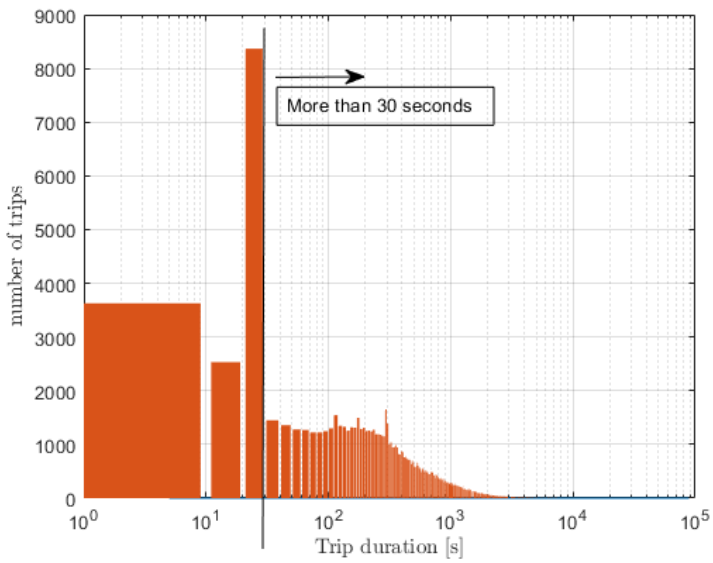

Figure A.1 Distribution of durations for the trips logged in the driving database.

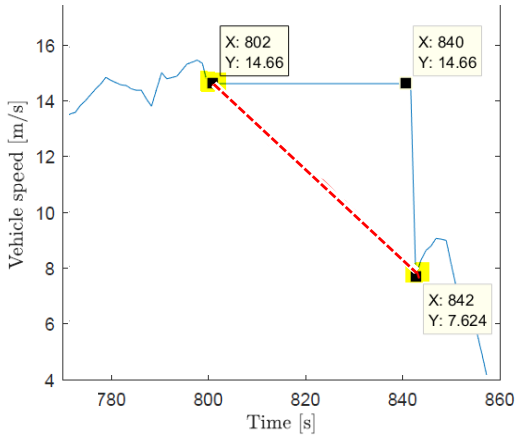

Figure A.2 Example of a missing data event for a trip logged in the driving database, with the database signal (blue) and the modified version (dashed red).

Further, limits on the vehicle speed at the start and end of the logging was added. While it would have been preferred to cover all trips completely, i.e. starting and ending at 0 speed, that is not typically the case in the database. In particular, it seems that it takes some time for the measurement equipment to start logging, as the beginning of the trips is usually missed. Within this work, trips with a velocity < 35 km/h when the logging starts and a velocity < 10 km/h when the logging ends have been included. Additionally, trips with very low speeds are not considered further. Here, only trips that reach > 3 km/h at some point during the trip are included.

The measured driving also contains missing data events, like the one shown in Figure A.2. In the database, such events are padded using zero-order-hold (i.e. keeping the velocity constant until the signal is regained). However, this will usually lead to a very strong, unrealistic, acceleration or deceleration when the lost signal is regained. From the perspective of IPM operation, such acceleration spikes should not be allowed to affect the IPM peak torque requirement.

Thankfully, these missing data events are relatively straightforward to identify as the velocity remains identical over a number of consecutive data samples. Here, an identical velocity (> 1 km/h) in four consecutive samples qualifies as a missing data event. These events are repaired by replacing the zero-order-hold with a linear interpolation, as shown in Figure A.2. However, if a trip has more than 0.5% of the total data missing, or if either the highest acceleration or velocity times acceleration of the trip occurs in relation with a repaired missing data event, the entire trip is disregarded.

Events where the velocity spikes for a very short time, typically a single data sample, or swings from a positive spike to a negative spike in two consecutive data samples occasionally occur in the logged data. An example of such an event is given in Figure A.3. These events are not considered to be realistic, but likely caused by some disturbance in the measurement. These events are repaired by removing the data sample where the spike occurs and instead interpolating the remaining data. However, the identification of these spikes need to be done with care, since relatively short and strong accelerations can

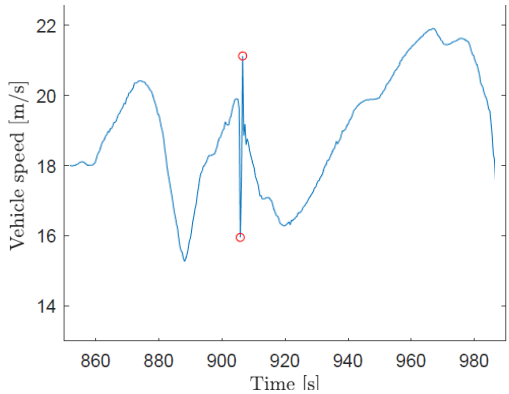

Figure A.3 Example of a suspected measurement noise event in the driving database.

be a part of real driving. Here, thresholds for considering the velocity spikes unrealistic are set based on the standard deviation in the acceleration of the entire trip in question. For spikes that occur in a single data sample, the threshold is set it 4 times the standard deviation in acceleration of that trip, while for the swings (where a single sample high acceleration is directly followed by a single sample strong deceleration) the threshold is 2.5 times the standard deviation in acceleration.

Furthermore, a moving average filter (averaging two samples) is used on the velocity, before the acceleration is computed (using the mid-point Euler approach). The logged trips in the database are associated with different vehicles. Here, only vehicles with ≥ 35 logged trips are included. In the database, 450 vehicles meet the criteria described so far.

Thereafter a subset of the 450 remaining vehicles are selected, based on their peak performance requirement (i.e. highest acceleration in different speed intervals). Since the IPM peak performance requirement significantly affects the IPM design, it was desired to avoid individual vehicles that stand out in terms of peak performance. With 382 vehicles (85%) included, the peak performance requirements became quite stable, meaning that removing an additional vehicle did no longer alter the required power versus speed curve. All trips logged for these 382 vehicles forms the full selection of measured driving data.

To verify that the data repair and filtering described above does not alter actual driving events significantly, a small set of four trips with high data quality are used as reference. These four trips took place around Gothenburg, with a Volvo Cars test vehicle where measurement signals at 100 Hz were available. To mimic the resolution in the database, a 2.5 Hz version of the trips are created (by simply using every 40th sample from the 100 Hz measurement) and then the data repair and filtering is applied. As expected, no outliers are identified in the high-quality data trips, meaning that no data repair actions are taken. However, the effect of the moving-average filter remains, and Figure A.4 shows the original 100 Hz measurements together with the filtered 2.5 Hz data (where the time shift of the filter has been compensated for). Comparing the filtered data to the measured data shows that the the driving dynamics are well preserved. One of the trips includes a rather extreme deceleration event (bottom row in Figure A.4, with zoomed in version in the right column), where the driver suddenly brakes very strongly and the vehicle goes

from 19 m/s to 0 in around 2 s. This event is intended to mimic an extreme, but realistic, situation where the driver brakes to avoid an accident. Even this extreme braking event is rather well preserved and only slightly smoother in the filtered data.

To conclude, the actions taken to ensure selection of high quality data mainly targets outliers in acceleration. While these actions are important for the resulting peak performance requirements, they are not expected to affect the overall energy distribution of the driving significantly.

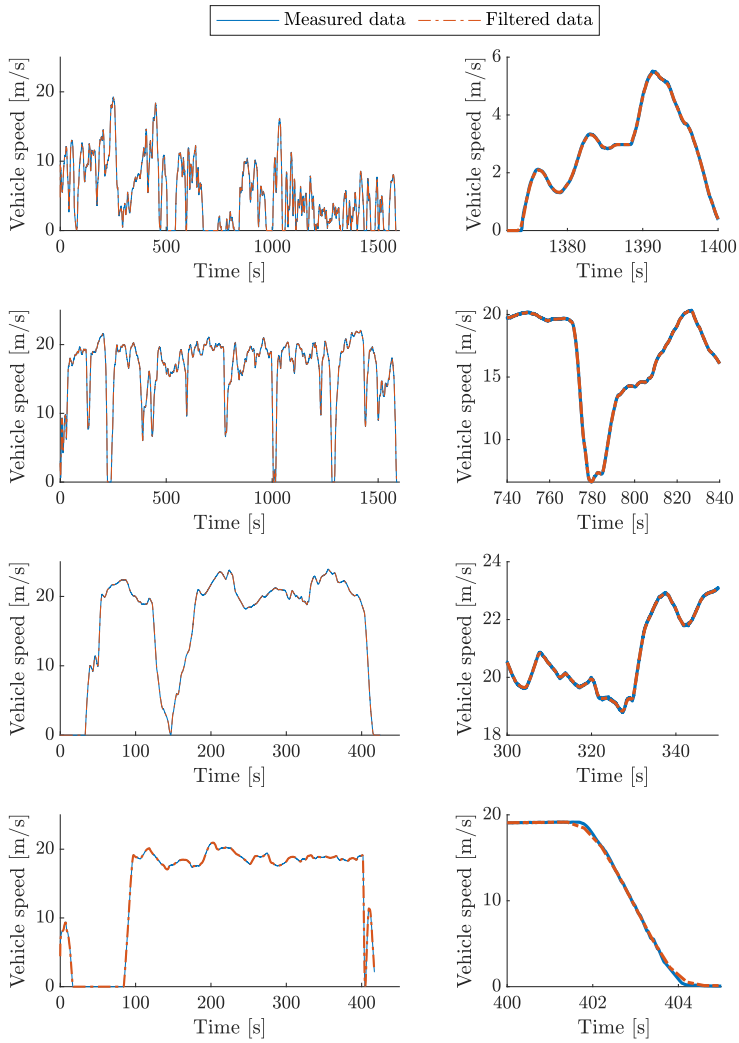

Figure A.4 Influence of the moving average filter, using four trips with high-quality data as reference, showing the full trip (left column) and a zoomed in view (right column).

Appendix B

Thermal LPN model

Thermal LPN models describe the heat flows and temperatures in a system, in this case an IPM. Fundamentally, a lumped model assumes that the system being modelled can be split into a number of different pieces, where each piece can be approximated with uniform thermal properties and heat generation (i.e. losses) which allows the piece to be lumped into a node in the LPN. Thermal phenomena, such as heat conduction, convection and heat capacity, are then expressed using thermal resistances and thermal capacitances connected to the nodes. The values of the different thermal resistances and capacitances in the LPN can be computed using analytical formulations (described in Section 2.4).

This appendix describes the specific LPN model that, within the thesis (Section 5.3), is referred to as the detailed LPN. However, within this appendix it is simply referred to as the LPN. The thermal LPN model here closely follows [29], which in turn was largely based on [72] and [73]. As [29] gives a thorough description of the creation of the LPN, this Appendix gives an overview and describes any differences in the LPN compared to [29].

The LPN implemented here is shown in Figure B.1, as a network with 11 nodes (black) and the cooling circuit (red). The LPN has been implemented in Simscape Thermal, except for the cooling circuit which is implemented in Simscape Thermal-Liquid, (both from Simulink, Mathworks). The network around the PMs is further described in the coming Section B.1.

The nodes (and their subscripts) in the LPN are: rotor yoke ($_{royo}$), rotor stripe ($_{rost}$), PMs of the inner flux barrier ($_{PMi}$), PMs of the outer flux barrier ($_{PMo}$), stator yoke ($_{yo}$), stator teeth ($_{te}$), stator tooth tips ($_{toti}$), active winding ($_{aw}$), end winding ($_{ew}$), frame/housing ($_{fr}$), bearing ($_{be}$) and cooling channel ($_{coch}$). The thermal resistances are denoted as $R_{th,to-yo}$ where the first subscript $_{th}$ refers to thermal and a second subscript describes the two nodes between which the thermal resistance is placed. The thermal capacitances are denoted as $C_{th,yo}$ and the losses are denoted as P_{yo}, in both cases the second subscript denotes the node. In Figure B.1, the circuit elements that involve convective heat transfer are shown with grey fill and the ones that involve a contact air film are indicated with dashed outlines.

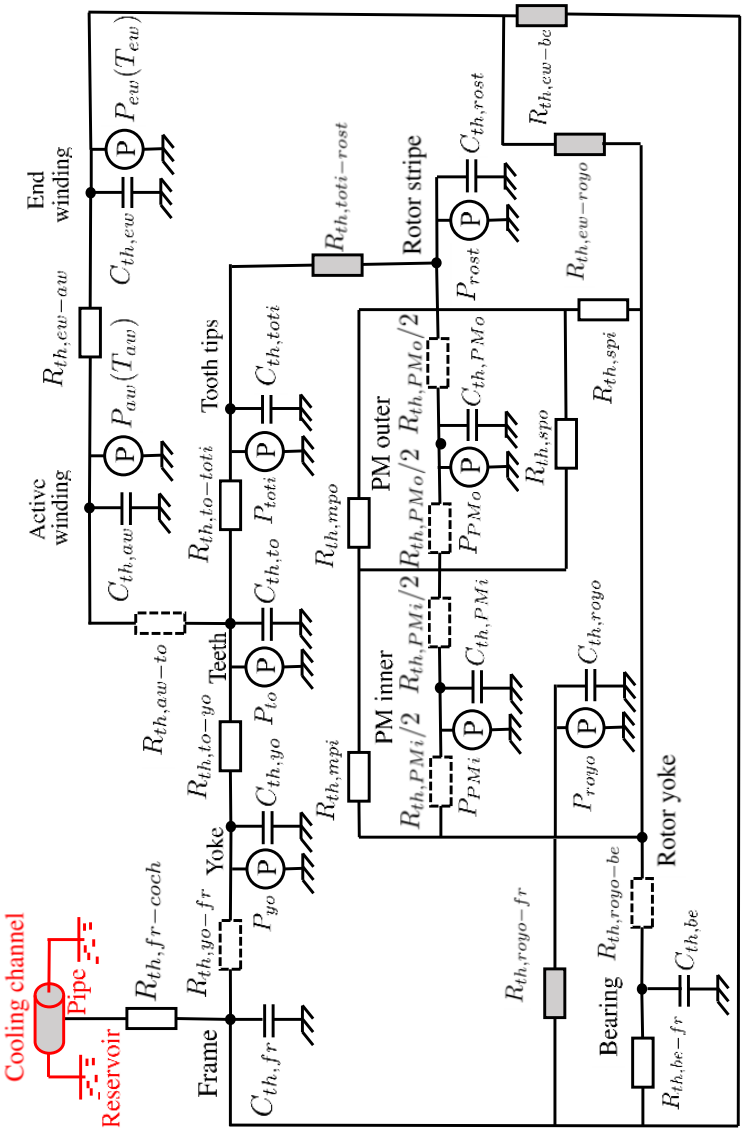

Figure B.1 LPN model of the IPM, showing the cooling circuit (red) and a network of nodes corresponding to different geometrical parts of the IPM (black), with thermal resistances, capacitances and power losses connected to the nodes. For thermal resistances, grey shade indicate that convection is involved and dashed outline indicate that a contact air-film is included.

Table B.1 Material properties used for thermal LPN

Material	Density $[kg/m^3]$	Thermal conductivity $[W/mK]$	Specific heat capacity $[J/kgK]$
Core lamination	7600	31	557
Winding (copper)	8933	401	385
Slot impregnation (unsaturated polyester)	1350	0.2	1700
Frame (Aluminium)	2790	168	883
Air	0.9458	0.03095	-
Magnets (NdFeB)	7500	7.5	410
Shaft (carbon-silicon steel)	7817	51.9	446

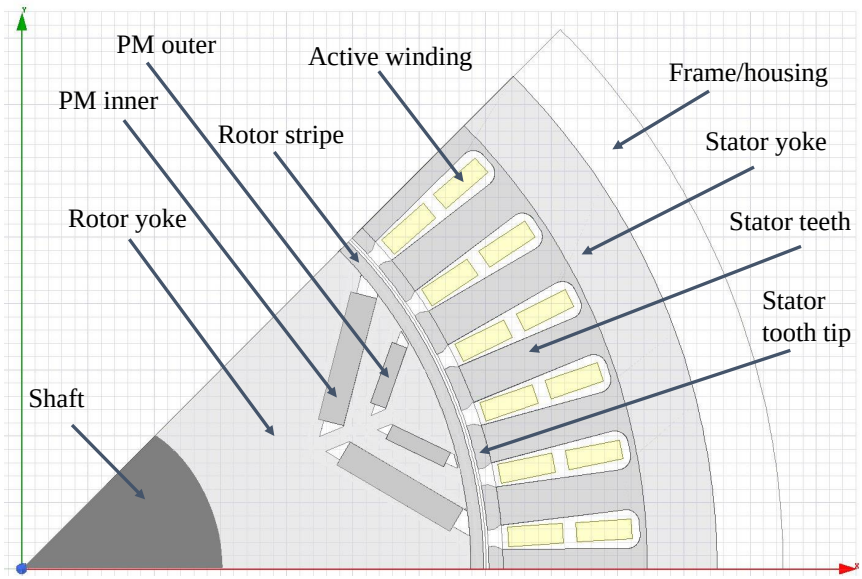

Figure B.2 Split of the IPM geometry into parts corresponding to nodes in the LPN.

The geometrical parts corresponding to the LPN nodes are shown in the cross-section of the IPM in Figure B.2. The material properties are shown in Table B.1.

B.1 Analytical calculation of thermal resistances

The thermal resistance for some parts (i.e. the frame, stator yoke and rotor stripe) can directly be computed using the expression for heat conduction in a hollow cylinder, (2.23). For other parts, the general expressions for heat conduction and convection, (2.22), need to be used along with the geometry of each involved part.

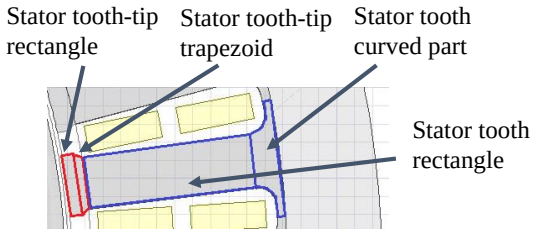

Figure B.3 Split of the stator tooth and tooth tip into sub-parts for calculation of thermal resistance.

B.1.1 Thermal resistance in stator teeth and tooth tips

The thermal resistance of a stator tooth is computed by (2.22), considering a straight part in series with a curved part (shown with blue outlines in Figure B.3). All stator teeth in the IPM are assumed to conduct heat in parallel. Similarly, the thermal resistance of a stator tooth tip is computed as a straight part in series with a trapezoid part (red outlines in Figure B.3), and all the stator tooth tips are in parallel.

B.1.2 Thermal resistance of the winding

The active winding node is taken as a mix of the copper winding and the slot impregnation material (unsaturated polyester), as in [29] the thermal conductivity of this mix, in the circumferential direction (i.e. towards the stator teeth) is taken as 2.75 times thermal conductivity of the impregnation material, which is an approximation from [73] for windings with 45% fill factor. A slot liner and contact air film, with thickness 0.2 mm and 10 μm respectively, are considered. The slot shape is approximated with a rectangular shape (with the same cross sectional area and average width as the actual slot). Further description and the related set of equations are given in [29]. The thermal resistance between the active winding and the end winding node, related to the heat flow in the axial direction, is done as in [29], considering only the copper material.

B.1.3 Heat transfer across the air-gap and via internal air

The thermal resistance associated with convection across the air-gap is calculated, based on empirical expressions involving the Nusselt number (which is in turn approximated from the Taylor's number, which depends on the rotor speed), for laminar/transitional/turbulent flow ranges. Further description and the involved expressions are given in [29].

The modelling of heat transfer to the internal air of the IPM (apart from the air-gap) is done using empirical expressions for the heat transfer coefficients, between the internal air and the inner frame, the rotor end shield and the end winding surface, depending on the rotor surface velocity, as presented in [29]. However, modelling of the internal air flows is a complicated matter and the empirical expressions used here should be considered a rather rough approximation.

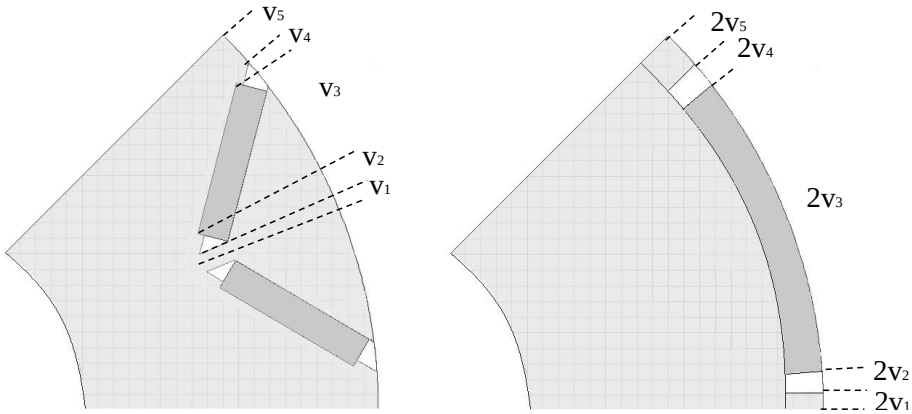

Figure B.4 Approximation of the magnet for heat conduction in the rotor.

B.1.4 Thermal resistances in the rotor

For the purposes of computing thermal resistances, a transformation of the flux barriers and PMs into arc-like shapes is used. This transformation is the same as in [29, 74] and is illustrated in Figure B.4. Note that the transformation has been done individually for the inner and outer barrier. For each barrier layer, there are three parallel thermal paths across the barrier: through the magnets (PM-path, corresponding to $2v_3$ in Figure B.4), through the middle rib (middle path, related to $2v_1$) or outside the barrier (side path, related to $2v_5$). The thermal resistances associated with each of these paths are shown in Figure B.1 where they are denoted as, in order, $R_{th,PMo}$, $R_{th,mpo}$ and $R_{th,spo}$ (where the second subscript indicates which path it refers to and the final letter $_o$ indicates the outer barrier). The same thermal paths are also shown in Figure B.5, which also illustrated the modelled combinations of thermal paths across both barriers (i.e. from the rotor stripe node to the rotor yoke node or vice versa).

Two nodes are used for the PMs, one for those in the inner barrier and one for those in the outer barrier. Both magnet nodes are thermally in-between the rotor-stripes node and the rotor-yoke node. As illustrated in Figure B.5 it has been assumed that heat from the rotor stripe can reach the rotor yoke, either by passing outside both barriers or by taking a parallel path through the magnets or the mid-rib of the inner barrier. However, if the latter path is taken, that heat must also pass the outer barrier (through the magnets, mid-rib or between the two barriers). Together, this results in the network of thermal resistances shown in Figure B.5, which is also incorporated in the larger LPN (Figure B.1).

B.2 Analytical calculation of thermal capacitances

The thermal capacitances of each node are simply computed using (2.24), based on the masses and specific heat of the materials associated with the node. The cross sectional areas, that are used for the calculation of the masses of different parts, are exported for a given IPM geometry using the electromagnetic FEA software.

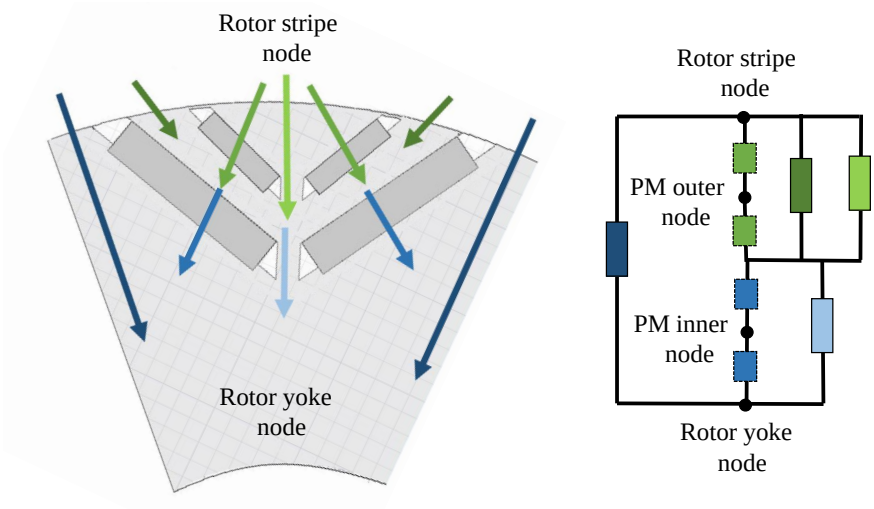

Figure B.5 Illustration of the LPN part describing the rotor with two layers of flux barriers and magnets, shown geometrically (left) and as a small LPN (right).

B.3 Cooling channel model

Following [29], the cooling system has been taken as a cooling channel with rectangular cross section (5x30 mm) in four laps circumferentially around the frame. The frame thickness has been set, as in [29], to 11 mm, and the cooling channel is radially placed in the middle of the frame. The cooling channel is implemented using the Pipe-block (from Simscape, Thermal-Liquid), which includes modelling of the heat transfer at the pipe wall, using Nusselt numbers in the laminar and turbulent regimes, as well as friction, using the Darcy-Weisbach law. The settings for pipe length, cross sectional area and hydraulic diameter of the Pipe-block are set according to the design of the cooling channel. The surface roughness of the cooling channel is set, as in [29], to 5 μm. The other settings of the Pipe-block are kept at their default values. The flow rate and temperature of coolant is set using a Mass Flow Rate-block and Reservoir-block (both from Simscape, Thermal-Liquid). The temperature of the reservoir is kept constant throughout the simulation.

B.4 Losses

The heat generation at the different nodes are based on the losses from the electromagnetic FEA, computed as described in Chapter 4. The core losses are separated into the different parts corresponding to the LPN nodes, directly in the FEA software. The winding losses are computed based on the DC-resistance (electrical resistance) of the active winding and the end-winding separately. The temperature dependence of the resistances are considered as in (2.14). Other losses, such as bearing losses, have been neglected here.